

University of Southampton Research Repository

Copyright © and Moral Rights for this thesis and, where applicable, any accompanying data are retained by the author and/or other copyright owners. A copy can be downloaded for personal non-commercial research or study, without prior permission or charge. This thesis and the accompanying data cannot be reproduced or quoted extensively from without first obtaining permission in writing from the copyright holder/s. The content of the thesis and accompanying research data (where applicable) must not be changed in any way or sold commercially in any format or medium without the formal permission of the copyright holder/s.

When referring to this thesis and any accompanying data, full bibliographic details must be given, e.g.

Thesis: Author (Year of Submission) "Full thesis title", University of Southampton, name of the University Faculty or School or Department, PhD Thesis, pagination.

Data: Author (Year) Title. URI [dataset]

University of Southampton

Faculty of Engineering and Physical Science

Electronics and Computer Science

An Investigation into the Next Generation of Ultra High Voltage DC Power Supplies

by

Russell Edwin Patrick Frost

ORCID ID 0000-0002-3286-2209

Thesis for the degree of Doctor of Philosophy

February 2020

University of Southampton

Abstract

Faculty of Engineering and Physical Science

Electronics and Computer Science

Thesis for the degree of Doctor of Philosophy

An Investigation into the Next Generation of Ultra High Voltage DC Power
Supplies

by

Russell Edwin Patrick Frost

In recent years, there has been a growing interest, in both academia and industry, for a new generation of power supplies that are capable of producing high currents at ultra-high voltages. Unlike existing technology, these power supplies must have a high power density, making them relatively compact. This work details an investigation into potential technologies that could later be developed into working designs.

First, an extensive literature review is undertaken that considers existing high voltage power supplies, and assesses the relative merits of each of them. This is in order to determine which of them shows the greatest potential for further development. It is decided that, of the selected technologies, the insulated core transformer and the cascade transformer have the greatest capacity for further improvement. Both of these types of power supply contain many common components, as they are both variations on the conventional transformer, adapted to overcome problems associated with insulation.

A design for a power supply, based on either of these technologies, is proposed; along with a program to develop the high voltage components. As part of this program, a series of simulation studies are undertaken in order to establish which of the chosen technologies is suitable for use in such a design. In addition to this, practical experiments are carried out that establish that printed circuit board based transformer windings are suitable for use in high voltage applications.

Finally, it is concluded that, while both technologies are suitable for power supplies that operate at voltages up to a megavolt, only the cascade transformer should be used for voltages above this.

Table of Contents

Table of Contents.....	i
List of Tables.....	v
List of Figures	vii
Research Thesis: Declaration of Authorship	xix
Acknowledgements	xxi
Additional Thanks	xxii
Definitions, Abbreviations, and Initialisms.....	xxiii
Chapter 1 Introduction.....	1
1.1 Aims	2
1.2 Contributions	3
1.3 Contents	4
Chapter 2 Review of Existing Technology	7
2.1 Van De Graaff Generator	7
2.2 Voltage Multiplier.....	9
2.2.1 Voltage Doubler	10
2.2.2 Dynamitron.....	11
2.3 Transformer.....	13
2.3.1 Rectification.....	15
2.3.2 Cascade Transformers.....	16
2.4 Insulated Core Transformer.....	17
2.5 Resonant Transformer	18
2.6 Nested High Voltage Generator	20
2.7 Summary and Discussion.....	21
Chapter 3 System Design	23
3.1 Rectifier and Modulator	24
3.1.1 Connections to Transformer Stage	25
3.2 Transformer Stage	26
3.3 Rectifier	27
3.4 Insulation	27

3.4.1 Solid Dielectrics.....	29
3.4.2 Liquid Dielectrics	29
3.4.3 Gaseous Dielectrics and Vacuum	30
3.4.3.1 Sulphur Hexafluoride	32
3.4.3.2 Vacuum	33
3.5 Semiconducting Devices	34
3.6 Magnetic Materials	35
3.6.1 Laminated Iron	36
3.6.2 Powdered Iron Core	37
3.6.3 Amorphous Alloy	37
3.6.4 Nanocrystalline.....	38
3.6.5 Ferrites	38
3.6.6 Conclusions.....	39
3.7 Core Losses	39
3.7.1 Comparison of Loss Calculation Methods	43
3.8 Thermal Considerations	45
3.9 Outline of Conceptual Design.....	45
Chapter 4 Secondary Windings	47
4.1 Advantages of Using PCB Windings	47
4.2 Current Limitations	50
4.3 Voltage Limitations	52
4.3.1 Simulation	54
4.3.1.1 Cross Section	55
4.3.1.2 Narrow Straight.....	57
4.3.1.3 Tight Curve	59
4.3.1.4 Wide Curve.....	60
4.3.1.5 Imperfections	62
4.3.2 Experimental Setup.....	63
4.3.3 Experimental Data Analysis	65
4.3.4 Straight Section	67
4.3.5 Tight Curve.....	71
4.3.6 Wide Curve	74

4.3.7 Comparison of Results	76
4.4 Variations	78
4.4.1 Gap Distance	78
4.4.2 Frequency	80
4.4.3 Pressure	83
4.5 Discussion and Potential Developments	84
Chapter 5 Insulated Core Transformers	87
5.1 An Evaluation of ICT Layouts	87
5.1.1 Basic ICT Layout	88
5.1.2 Flux Diverters	91
5.1.3 Clamped Return Path	94
5.1.4 Partial Clamp Return Path	96
5.1.5 Van De Graaff Layout	98
5.1.6 Comparison of Different ICT Arrangements	100
5.2 Flux Path Layout	101
5.3 Additional Improvements to Core	104
5.3.1 Increase in Stage Sizes	104
5.3.2 Increasing Flux Path Length	106
5.4 Benefits of Cross Core Technology	108
5.5 Stored Energy	112
5.6 Circuit Equivalent Model (CEM) of Flux Loss	112
5.6.1 Stack Height	115
5.6.2 Different Stage Sizes	116
5.6.3 Extended Flux Path	117
5.6.4 Evaluation of the Circuit Equivalent Model	118
5.7 Increasing the Current Output	119
5.8 Possible Future Developments	121
5.9 Limitations of Simulations	122
5.10 Possible Improvements and Concluding Comments on ICTs	123
Chapter 6 Cascade Transformers	125
6.1 Design Methodology	125

6.1.1	Flux Equation	126
6.1.2	Transformer Losses	126
6.1.3	Simulation Design	127
6.2	2D Simulations	129
6.2.1	Optimal Winding Location	130
6.2.2	Concentric Transformers	137
6.2.3	Comparison	144
6.3	3D Simulations	145
6.3.1	Cascade Transformers	145
6.3.2	Concentric Transformer	147
6.3.3	Rotated Concentric Designs	149
6.3.4	Square Wave Driven Design	154
6.3.5	Power Loss	155
6.4	Future Scope of Design	156
6.5	Summary	157
Chapter 7	Conclusions	159
7.1	Conclusions	160
7.2	Future Work	161
List of References	163
Appendix A	Published Paper	173
Appendix B	Derivation of Equation 4.3	183
B.1	Straight sections	183
B.2	Curved Sections	184
B.3	Total Length	185
Appendix C	Experimental Breakdown Voltages	187

List of Tables

Table 1.1	The intended specifications for a power supply developed in this project.....	2
Table 3.1	Parameters for core loss calculations.	44
Table 3.2	Loss predictions according to different methods.....	44
Table 5.1	Flux linkage in a basic transformer core.	89
Table 5.2	Flux linkage in a basic ICT with two primary windings.....	91
Table 5.3	Flux linkage in a 10 layer ICT with flux diverters.....	93
Table 5.4	Flux linkage in an ICT with flux diverters and two primary windings....	94
Table 5.5	Flux linkage in an ICT with flux return clamp and two primary windings	96
Table 5.6	Flux linkage in an ICT with partial flux return clamp and two primary windings.	98
Table 5.7.	Flux linkage in a 10 layer Bell Dong ICT.	100
Table 6.1	Power supply voltages generated using different layouts and idealised voltage doubling.....	144
Table 6.2	The total output voltage of power supplies based on Layout 9, with different angles of rotation between transformer stages, assuming perfect voltage doubling.....	152
Table 6.3	Core losses under different forms of excitation.....	155
Table 6.4	Winding losses under different forms of excitation.	156
Table 6.5	Total losses calculated by summing the 3D simulation core losses in Table 6.3 and the winding losses in Table 6.4.....	156

List of Figures

Figure 2.1. The operation of a Van De Graaff Generator.	8
Figure 2.2. Circuit diagram of a three stage voltage multiplier.	9
Figure 2.3. Circuit diagram of a) a half wave voltage doubler and b) a full wave voltage doubler.	11
Figure 2.4. Internal workings of a Dynamitron. Capacitances are formed between the corona rings (inside) and electrodes (outside).	12
Figure 2.5. The operation of a transformer. Change in current in the primary winding induces a change in flux density in the core, which in turn induces a voltage across the secondary windings.	13
Figure 2.6. (LEFT) The circuit diagram of a full wave rectifier. (RIGHT) Voltage Waveforms in a full wave rectifier.	15
Figure 2.7. Circuit diagram of a cascade transformer with three stages.	17
Figure 2.8. A diagram of an ICT, consisting of windings wrapped around sections of core material that are insulated from each other.	18
Figure 2.9. Circuit diagram of a resonant transformer.	19
Figure 2.10. Schematic of the cross section of a nested high voltage generator.	21
Figure 3.1 A block diagram of the proposed power supply.	24
Figure 3.2 A block diagram of the modulator stage.	25
Figure 3.3 Circuit diagram of a three phase rectifier.	25
Figure 3.4 Boundaries between insulating materials placed between two plane electrodes.	28
Figure 3.5 The Paschen Curve of air with electrodes held 5 cm apart.	31
Figure 3.6. The transformer core that was simulated in MagNet. The limbs and yokes all have an outside length of 240 mm, and an inside length of 160 mm. There is a primary winding wrapped around both of the yokes, and secondary windings wrapped around the limbs.	43

Figure 4.1	The winding arrangement used by Cross in his ICT design. Note that each winding consists of one turn. Several windings share a PCB, with their rectified outputs connected in series.....	49
Figure 4.2	A PCB based winding arrangement that consists of a winding, with numerous turns, circling a core. There is only one winding per PCB and one rectification circuit.....	49
Figure 4.3	A PCB based winding arrangement that consists of two windings, each with numerous turns, circling a core, allowing either 'plain disk' or 'interleaved' connection.....	50
Figure 4.4	The relationship between skin depth and current frequency in copper. The skin depth at a frequency of 100 kHz is highlighted in red, and the frequency at which the skin depth drops below the typical thickness of the plating on a PCB is highlighted in black.....	52
Figure 4.5	The PCB windings divided into straight and curved sections. Sections tested are indicated in blue.	53
Figure 4.6	Track layout for a test sample testing the electrical breakdown strength of sections of the secondary windings where straight lengths of track run parallel to each other.....	53
Figure 4.7	Track layout for two test samples testing the electrical breakdown strength of sections of the secondary windings that curve around the core at the centre of the winding.	54
Figure 4.8	Track layout for two test samples testing the electrical breakdown strength of sections of the secondary windings that curve around the core on the outside of the winding.	54
Figure 4.9.	Idealised cross section of a sample. The FR4 board is shown in brown, the solder mask in green, and the copper tracks in orange.	55
Figure 4.10.	Electric field around the cross section of an idealised sample.	55
Figure 4.11.	Close up of the electric field around the track of an idealised sample.....	56
Figure 4.12.	The elevations at which the simulations in the following sections take place. The elevation of the red line is 10 μm , while the blue line is 30 μm	57
Figure 4.13.	The electric field around the straight samples, at an elevation of 10 μm above the surface of the FR4 board.	57

Figure 4.14. The electric field strength around the end of the tracks, 10 μm above the surface of the FR4 board. The black lines represent the flux function between the tracks.....	57
Figure 4.15. The electric field around the straight samples, at an elevation of 30 μm above the surface of the FR4 board.	58
Figure 4.16. The electric field strength around the end of the tracks, 30 μm above the surface of the FR4 board.	58
Figure 4.17. The electric field around the samples that represent the inside turns of the winding, at an elevation of 10 μm above the surface of the FR4 board.....	59
Figure 4.18. A close up of the electric field around the curve of the samples that represent the inside turns of the winding, at an elevation of 10 μm (TOP), and 30 μm (BOTTOM), above the surface of the FR4 board.....	60
Figure 4.19. The electric field around the samples that represent the outside turns of the winding, at an elevation of 10 μm above the surface of the FR4 board.....	61
Figure 4.20. A close up of the electric field around the curve of the samples that represent the outside turns of the winding, at an elevation of 10 μm (TOP), and 30 μm (BOTTOM), above the surface of the FR4 board.....	61
Figure 4.21. An imperfection placed on the bottom track of the straight sample, with a radius of 1 μm	62
Figure 4.22. The electric field around the straight samples, at an elevation of 10 μm above the surface of the FR4 board, with an imperfection on the edge of the bottom track.	62
Figure 4.23. A close up of the electric field around the imperfection shown in Figures 4.21 and 4.22.	63
Figure 4.24. Experimental setup.....	63
Figure 4.25 Diagram of the experimental setup.	64
Figure 4.26 PDF showing an example of standard distribution (BLUE) and Weibull distribution (ORANGE). In both cases, the graphs are based on randomly generated data.....	65

Figure 4.27	An example of a Weibull plot. The data points are the same as those used to generate the Weibull PDF in Figure 4.26. The line of best fit is shown in red, and the 95% certainty lines are shown in black.	66
Figure 4.28	Corona discharge is visible in the form of the blue light between the two straight lengths of track that are printed 0.5 mm apart.	67
Figure 4.29	Breakdown occurring between two straight sections of track, printed 0.5 mm apart.	67
Figure 4.30	The voltage and current waveforms of the output of the amplifier when corona becomes clearly visible. Note the sudden increase in current when the voltage reaches 4 kV and corona begins to occur.	68
Figure 4.31	The voltage and current waveform of the output of the amplifier when a breakdown occurs. Note the rapid rise in current as a conductive path of plasma appears when breakdown occur.	68
Figure 4.32	An example of the holes that appeared in the solder mask after breakdown occurs. The tracks in this sample are printed 1.5 mm apart.	69
Figure 4.33	Weibull plot recording the breakdown voltages that occurred between two straight lengths of track printed 0.5 mm apart.	70
Figure 4.34	PDF comparing the voltage, at which flashover occurred, before and after the solder mask was damaged. The samples in this dataset represented the straight sections of track, printed 0.5 mm apart.	70
Figure 4.35	Corona discharge seen occurring, in the form of blue light, between two curved tracks printed 0.5 mm apart.	71
Figure 4.36	Flashover occurring between two curved tracks printed 0.5 mm apart.	71
Figure 4.37	The voltage and current waveforms of the output of the amplifier when corona becomes clearly visible and flashover occurs. Note the sudden increase in current when the voltage reaches 4.136 kV and corona becomes clearly visible; also, the sharp rise in current when the insulation breaks down.	72
Figure 4.38	Weibull plot recording the breakdown voltages that occurred between two curved tracks printed 0.5 mm apart. Data points that imply a second breakdown mechanism are circled, with a possible reference line shown in green.	73

Figure 4.39	PDF comparing the voltage, at which flashover occurred, before and after the solder mask was damaged. The samples in this dataset represented the curved sections of track closest to the core, printed 0.5 mm apart.73
Figure 4.40	Corona discharge seen occurring between two curved tracks, printed 0.5 mm apart.....74
Figure 4.41	Flashover occurring between two curved tracks printed 0.5 mm apart.74
Figure 4.42	The voltage and current waveforms of the output of the amplifier when corona becomes clearly visible and flashover occurs. Note the sudden increase in current when the voltage reaches 3.6 kV and corona becomes clearly visible; also, the sharp rise in current when the insulation breaks down.75
Figure 4.43	Weibull plot recording the breakdown voltages that occurred between two curved tracks printed 0.5 mm apart. Data points that imply a second breakdown mechanism are circled, with a possible reference line shown in green.....76
Figure 4.44	PDF comparing the voltage, at which flashover occurred, before and after the solder mask was damaged. The samples in this dataset represented the curved sections of track closest to the core, printed 0.5 mm apart.76
Figure 4.45	(TOP) A PDF comparing the breakdown voltages of the three different shaped samples before the solder mask was damaged. (BOTTOM) A PDF comparing the breakdown voltages of the same samples after the solder mask was damaged.77
Figure 4.46	The simulated electric field between two tracks, printed 1.5 mm apart, on a PCB. The voltage difference between the two tracks is 1 kV.79
Figure 4.47	Corona discharge visible between tracks printed 1.5 mm apart.79
Figure 4.48	Breakdown of tracks printed 1.5 mm apart.79
Figure 4.49	The breakdown voltages of two straight tracks printed 1.5 mm apart..79
Figure 4.50	(TOP) A PDF comparing the breakdown voltages of samples with straight tracks before the solder mask was damaged. (BOTTOM) A PDF comparing the breakdown voltages of samples with straight tracks after the solder mask was damaged.80

Figure 4.51	The breakdown voltages of PCBs, with a solder mask, tested at different frequencies.....	81
Figure 4.52	The breakdown voltages of PCBs, with a damaged solder mask, tested at different frequencies.....	81
Figure 4.53	Breakdown occurring across a sample, with tracks printed 0.5 mm apart, at a pressure of 40 Pa.....	83
Figure 5.1	Layout of the most basic ICT stack. The cores are arranged on top of each other with the windings surrounding them.....	88
Figure 5.2	The flux flow around a 10 layer ICT.	88
Figure 5.3	Layout of a 10 stage ICT powered by two primary windings. Each winding is connected, in parallel, to the winding opposite, with the two primary windings at the top and the bottom.	90
Figure 5.4	The flux flow around a 20 layer ICT with primary windings at the top and bottom.	90
Figure 5.5	Flux diverters surrounding a stack of insulated cores.	92
Figure 5.6	Flux flow around a 10 stage ICT with flux diverters.	92
Figure 5.7	The flux flow around a 20 layer ICT with flux diverters, and primary windings at the top and bottom.	93
Figure 5.8	Layout of clamped flux return path ICT.	95
Figure 5.9	The flux flow around a 20 layer ICT with a flux return clamp, and primary windings at the top and bottom.	95
Figure 5.10	Layout of a partial flux return clamped ICT.	97
Figure 5.11	The flux flow around a 20 layer ICT with a partial flux return clamp, and primary windings at the top and bottom.	97
Figure 5.12	2D representation of the original Van De Graaff, or Bell Dong, ICT layout.	99
Figure 5.13	Flux flow within a Bell Dong Layout.	99
Figure 5.14	(LEFT) Minimum flux linkage found in each ICT as a percentage of the primary winding flux linkage and (RIGHT) maximum flux linkage in each design.....	101

Figure 5.15	The traditional layout of the Cross type ICT.....	102
Figure 5.16	The proposed alternative layout of the Cross type ICT.....	103
Figure 5.17	The minimum flux found in ICTs, arranged using both the traditional double stack layout and the proposed single stack layout, with a number of insulated cores ranging from 1 to 50.....	103
Figure 5.18	The flux linkage in the first 100 windings of a clamped return path ICT with various stage sizes, calculated using FEA.....	105
Figure 5.19	The flux contours in and around a clamped return path ICT with the 200 windings grouped around insulated cores in stages of 20.	105
Figure 5.20	A clamped return path ICT with a stage size of 20. The distance between the insulated core stack and the return path is 1.5 m.	106
Figure 5.21	The flux linkage in the first 100 windings of a clamped return path ICT, with a distance of 1.5 m between the insulated core stack and the flux return path, with various stage sizes.....	107
Figure 5.22	Minimum flux found in two clamped return path ICT, with 100 pairs of windings, with the stages grouped into different stage sizes, calculated using FEA.	107
Figure 5.23	The flux contours around a clamped return path ICT with a stage size of 20. The distance between the insulated core stack and the return path is 1.5 m.	108
Figure 5.24	Circuit diagram of the secondary windings.	109
Figure 5.25	The peak voltage found in each secondary winding of an ICT, with 50 secondary circuits, with and without a flux compensation capacitor. .	110
Figure 5.26	The 100 kHz voltage across the 50th pair of secondary windings, when excited by a sinusoidal signal with an amplitude of 400 V.	111
Figure 5.27	The 100 kHz voltage across the 50th pair of secondary windings, when excited by a square signal with an amplitude of 400V.	111
Figure 5.28	Magnetic flux loss in a core can be modelled as an electrical circuit. .	113
Figure 5.29	A gap in a magnetic core modelled as a resistance in a circuit.	114
Figure 5.30	A simplification of the magnetic circuit shown in Figure 5.29.....	114

Figure 5.31	The flux circuit equivalent model of a clamped return path ICT.	115
Figure 5.32	The minimum flux in an ICT, with different numbers of insulated cores, calculated using the circuit equivalent model, and finite element analysis.	116
Figure 5.33	The normalised flux linkage in the first 100 windings of a clamped return path ICT with various stage sizes, calculated using the CEM.	116
Figure 5.34	The normalised flux linkage in the first 100 windings of a clamped return path ICT, calculated using CEM and FEA.	117
Figure 5.35	The normalised flux linkage in the first 100 windings of a clamped return path ICT with an extended flux path, with stage sizes of 1 and 20, calculated using both the CEM and FEA.	118
Figure 5.36	The flow of flux in a clamped return path ICT, as modelled by the Flux Circuit Equivalent Model.	119
Figure 5.37	The layout of a multiphase ICT.	120
Figure 5.38	The minimum flux found in ICTs, arranged using both the traditional double stack layout and the proposed single stack layout, with a number of insulated cores ranging from 1 to 100.	121
Figure 5.39	Flux flow around a clamped return path ICT (LEFT) outside of a ferrous container and (RIGHT) inside of a ferrous container.	123
Figure 6.1.	(TOP) A conceptual design of each three stage cascade transformer. Two phases share this cascade, A on the right and B on the left, with each having its own set of primary, secondary, and auxiliary windings. All of the secondary windings around each core are grouped into two phases. Voltage doublers are connected across each group of secondary windings. Note that only things inside the grey dotted line are actually modelled. (BOTTOM) The idealised voltage waveforms of the groups of secondary windings, and the outputs of the voltage doublers.	128
Figure 6.2.	The idealised voltage waveforms of the grouped secondary windings, and voltage doublers, relative to ground.	129
Figure 6.3.	The dimensions of the cascade transformer modelled in this section. Each core has a cross section of 40 mm by 40 mm.	130
Figure 6.4.	The windings around the core, as used in Layout 1.	131

Figure 6.5	(LEFT) The two dimensional geometry of Layout 1. Note that associated pairs of primary and auxiliary windings are located on opposite sides of the secondary windings they are driving. (RIGHT) The magnetic flux flow, around Layout 1, 0.045 ms after the start of the simulation.131
Figure 6.6	The computed voltages across the secondary windings of Layout 1. The voltages in the secondary windings surrounding the bottom core are shown in blue, windings around the middle core are shown in red, and windings around the top core are shown in green.132
Figure 6.7	(LEFT) The two dimensional geometry of Layout 2. Note that associated pairs of primary and auxiliary windings are located on opposite yokes to each other. That is to say, in the bottom and middle cores, the primary winding driving the left hand secondary stack, and the auxiliary winding associated with the right hand stack, are wound around the lower yoke. The reverse is true for the upper yoke. (RIGHT) The magnetic flux flow around Layout 2, 0.045 ms after the start of the simulation.133
Figure 6.8	The computed voltages across the secondary windings of Layout 2. The voltages in the secondary windings surrounding the bottom core are shown in blue, windings around the middle core are shown in red, and windings around the top core are shown in green.133
Figure 6.9	(LEFT) The two dimensional geometry of Layout 3. Note that each auxiliary surrounds the primary winding that is driving it. (RIGHT) The magnetic flux flow around Layout 3, 0.045 ms after the start of the simulation.134
Figure 6.10	The computed voltages across the secondary windings of Layout 3. The voltages in the secondary windings surrounding the bottom core are shown in blue, windings around the middle core are shown in red, and windings around the top core are shown in green.134
Figure 6.11	(LEFT) The two dimensional geometry of Layout 4. The auxiliary windings encompass the primaries, which are in turn wound around the centres of the horizontal yokes. (RIGHT) The magnetic flux flow around Layout 4, 0.045 ms after the start of the simulation.135
Figure 6.12	The computed voltages across the secondary windings of Layout 4. The voltages in the secondary windings surrounding the bottom core are shown in blue, windings around the middle core are shown in red, and windings around the top core are shown in green.136

Figure 6.13	(LEFT) The two dimensional geometry of Layout 5. There is a primary and auxiliary winding at the top and bottom of each stack of secondary windings. (RIGHT) The magnetic flux flow around Layout 5, 0.045 ms after the start of the simulation.	136
Figure 6.14	The computed voltages across the secondary windings of Layout 5. The voltages in the secondary windings surrounding the bottom core are shown in blue, windings around the middle core are shown in red, and windings around the top core are shown in green.	137
Figure 6.15.	The dimensions of the concentric transformer modelled in this section. Each core has a cross section of 40 mm by 40 mm.	138
Figure 6.16	The two dimensional geometry of Layout 6.	138
Figure 6.17	The magnetic flux flow around Layout 6, 0.045 ms after the start of the simulation.	139
Figure 6.18	The computed voltages across the secondary windings of Layout 6. The voltages in the secondary windings surrounding the bottom core are shown in blue, windings around the middle core are shown in red, and windings around the top core are shown in green.	139
Figure 6.19	The two dimensional geometry of Layout 7.	140
Figure 6.20	The magnetic flux flow around Layout 7, 0.045 ms after the start of the simulation.	140
Figure 6.21	The computed voltages across the secondary windings of Layout 7. The voltages in the secondary windings surrounding the bottom core are shown in blue, windings around the middle core are shown in red, and windings around the top core are shown in green.	141
Figure 6.22	The two dimensional geometry of Layout 8.	141
Figure 6.23	The magnetic flux flow around Layout 8, 0.045 ms after the start of the simulation.	142
Figure 6.24	The computed voltages across the secondary windings of Layout 8. The voltages in the secondary windings surrounding the bottom core are shown in blue, windings around the middle core are shown in red, and windings around the top core are shown in green.	142
Figure 6.25	The two dimensional geometry of Layout 9.	143

Figure 6.26	The magnetic flux flow around Layout 9, 0.045 ms after the start of the simulation.	143
Figure 6.27	The computed voltages across the secondary windings of Layout 9. The voltages in the secondary windings surrounding the bottom core are shown in blue, windings around the middle core are shown in red, and windings around the top core are shown in green.	144
Figure 6.28	A 3D rendering of the Layout 4.	145
Figure 6.29	The computed voltage across the secondary windings in each stage of Layout 5 when simulated in 3D. The voltages in the secondary windings surrounding the bottom core are shown in blue, windings around the middle core are shown in red, and windings around the top core are shown in green.	146
Figure 6.30	A 3D rendering of the Layout 5.	146
Figure 6.31	The computed voltage across the secondary windings in each stage of Layout 5 when simulated in three dimensions. The voltages in the secondary windings surrounding the bottom core are shown in blue, windings around the middle core are shown in red, and windings around the top core are shown in green.	147
Figure 6.32	A 3D rendering of Layout 8.	147
Figure 6.33	The computed voltage across the secondary windings in each stage of Layout 8 when simulated in three dimensions. The voltages in the secondary windings surrounding the bottom core are shown in blue, windings around the middle core are shown in red, and windings around the top core are shown in green.	148
Figure 6.34	A 3D rendering of the Layout 9.	148
Figure 6.35	The computed voltage across the secondary windings in each stage of Layout 9 when simulated in three dimensions. The voltages in the secondary windings surrounding the bottom core are shown in blue, windings around the middle core are shown in red, and windings around the top core are shown in green.	149
Figure 6.36	A variation on Layout 9 in which each stage is rotated 90° from the previous one.	150

Figure 6.37	The computed voltage across the secondary windings in each stage of Layout 9 with each stage rotated 90° from the one below it. The voltages in the secondary windings surrounding the bottom core are shown in blue, windings around the middle core are shown in red, and windings around the top core are shown in green.....	151
Figure 6.38	A variation on Layout 9 in which each stage is rotated 120° from the previous one.....	151
Figure 6.39	The computed voltage across the secondary windings in each stage of Layout 9 with each stage rotated 120° from the one below it. The voltages in the secondary windings surrounding the bottom core are shown in blue, windings around the middle core are shown in red, and windings around the top core are shown in green.....	152
Figure 6.40	A variation on Layout 9 in which each stage is rotated 120° from the previous one and each yoke is the same length.	153
Figure 6.41	The computed voltage across the secondary windings in each stage of Layout 9 with each stage rotated 120° from the one below it and each yoke is the same length. The voltages in the secondary windings surrounding the bottom core are shown in blue, windings around the middle core are shown in red, and windings around the top core are shown in green.....	153
Figure 6.42	The voltage across the secondary windings in each stage of Layout 9 when excited by a square wave. The voltages in the secondary windings surrounding the bottom core are shown in blue, windings around the middle core are shown in red, and windings around the top core are shown in green.....	154
Figure 6.43	A 3D rendering of the concentric transformer with six stages.....	156
Figure 6.44	The computed voltage across the secondary windings in each stage of a concentric transformer with six stages. Core 1 is the innermost stage, as shown in Figure 6.43, while Core 6 is the outermost stage in the design	157

Research Thesis: Declaration of Authorship

Print name:

Russell Edwin Patrick Frost

Title of thesis:

An Investigation into the Next Generation of Ultra High Voltage DC Power
Supplies

I declare that this thesis and the work presented in it are my own and has been generated by me as the result of my own original research.

I confirm that:

1. This work was done wholly or mainly while in candidature for a research degree at this University;
2. Where any part of this thesis has previously been submitted for a degree or any other qualification at this University or any other institution, this has been clearly stated;
3. Where I have consulted the published work of others, this is always clearly attributed;
4. Where I have quoted from the work of others, the source is always given. With the exception of such quotations, this thesis is entirely my own work;
5. I have acknowledged all main sources of help;
6. Where the thesis is based on work done by myself jointly with others, I have made clear exactly what was done by others and what I have contributed myself;
7. Parts of this work have been published as:-

R. E. P. Frost, J. A. Pilgrim, P. L. Lewin and M. Spong, "An Investigation into the Next Generation of High Density, Ultra High Voltage, Power Supplies," 2018 IEEE International Power Modulator and High Voltage Conference (IPMHVC), Jackson, WY, USA, 2018, pp. 156-161.

R. E. P. Frost, P. L. Lewin and M. Spong, "An Investigation into the Suitability of Insulated Core Transformer Technology for an Ultra High Voltage Power Supply," in IEEE Transactions on Dielectrics and Electrical Insulation, vol. 26, no. 2, pp. 501-507, April 2019.

Signature:

Date:

Acknowledgements

First and foremost, I would like to thank God, without whom I am nothing and through whom all things are possible.

The first mortal who should be thanked is my supervisor Prof. Paul Lewin. Aside from the technical guidance and rational grounding that he provided, both of which were essential to keeping this thesis on course, he also gave encouragement and support. In addition to this, he was very generous with his time and wit, even when he had little to spare; for the former I will always be grateful, for the latter I have mixed feelings. In particular, I would like to thank him for seeing in me a small spark of potential and choosing to invest in it. The late nights, stress and anxiety, which I have suffered since then, go to show that maybe he was onto something.

I would also like to thank my second supervisor Dr James Pilgrim for the regular meetings we had, it is unfortunate that we never got round to arranging a third one.

Thanks go to my corporate sponsor, Matt Spong, for all of his help and technical input over the last three years. I look forward to working with you in the future.

A special thank you is owed to Nicki Lewin, for taking me under her wing and putting me back on my feet again when I needed it most. I hope her garden flourishes.

I am also very grateful to the lab technicians, without whose time and expertise, the practical work described in this thesis would not have been possible. In particular, I would like to thank Barry Bailey, Richard Howell, Charlie Reed, and Neil Palmer. A special commendation is deserved by Liz Tillotson, for her considerable talents that were able to help organise the un-organisable.

In addition to them, I would also like to thank the research community of the Tony Davies High Voltage Laboratory for generously providing help and advice when it was needed. In particular I would like to thank: Nik Hakimi Nik Ali; Allison Shaw; George Callender; Cristian Dobranski; Alex Lliopoulos; Duncan Bell; and Kevin Godard.

I am enormously grateful to the staff and volunteers at the Chaplaincy, for providing a home away from home for the last six years. Sisters Catherine and Valentina, Rev. Lawrence Fellick, and Rev. Trish Davis have all been excellent chaplains, and I wish each of them luck in their future ministry. I am continually impressed by the dedication of the amazing team of volunteers that make the place the welcoming international hub that it is. In

particular I feel I should mention: Max Lang; Paul Bailey; David Hibbs; Dr Frank Bolton; Rev. Keith Hawton; Margaret Hawton; Sister Ann Marie Isabel D'Souza; and the Scope team for the warm atmosphere they exhume. Finally, thank you Dr Anna Pilgrim for the amazing transformation you've brought since joining the team.

Many thanks go to Dr Oliver Clark-Darby and Dr Samantha Kanza for keeping me sane over many coffee breaks and extended lunches. Likewise, the members of SUPAC are notable for detracting from my mental health over the last three years.

I am deeply indebted to (soon to be) Dr Arianna Grasso, for the adventures we shared. May we have many more in the future!

The Student Christian Movement deserves a special mention for becoming a wonderful and supportive family to me. Membership has been a blessing, and being given the opportunity to lead you was an honour.

Finally, I would like to thank my parents, Andrew and Paula Frost, and my girlfriend, Gabby North, for all the love and support they have given me. And also Owen.

Additional Thanks

For this, extended, version of this thesis, I would like to thank my examiners: Prof. Steve Gabriel; and Prof. Manu Haddad. This work is greatly improved by their input. I would also like to thank Olly again, for proof reading some of the more boring bits.

Definitions, Abbreviations, and Initialisms

α_1 and α_2	Angles of Diffraction between Dielectrics
B_{max}	Maximum Flux Density
B_{min}	Minimum Flux Density
C_p and C_s	Capacitance of Primary and Secondary Circuits, respectively, of a Resonant Transformer
E_{stored}	Stored Energy
K_1	Equivalent Steinmetz Parameter Derived in (6.9)
K_2	Equivalent Steinmetz Parameter Derived in (6.11)
K_v	4.44 for Sine Wave Excitation or 4 for Square Wave Excitation
L_p and L_s	Inductance of Primary and Secondary Circuits, respectively, of a Resonant Transformer
N_L	Number of Winding Layers
N_p	Number of Primary Turns
N_s	Number of Secondary Turns
P_{cu}	Power Loss in Windings
P_{fe}	Iron Loss in Core
P_{loss}	Total Power Loss
P_{total}	Total System Power
R_a and R_b	The Reluctance of the Gap between the Limbs of an ICT and the Reluctance of the Gap between Cores, Respectively
R_{ac}	Resistance of Wire under AC
R_μ	Reluctance
S_c	Cross Sectional Area of a Core
T_r	Signal Period
V_{bd}	Breakdown Voltage
V_{core}	Volume of Core
V_{in}	Input Voltage
V_{out}	Output Voltage
V_{ripple}	Voltage Ripple

Y_i	Y Coordinate of a Data Point Plotted on a Weibull Plot
c_{sq}	Waveform Coefficient for a Square Wave with a 50% Duty Cycle
d_0	Initial Thickness of Material
f_{eq}	Equivalent Frequency Used in the MSE
f_r	Repetition Frequency
l_g	Length of Gap between Insulated Cores
l_l	Length of Magnetic Flux Path
n_w	Total Number of Data Points Used in Weibull Plot
r_0	Radius of a Wire
t_c	Thickness of Core
t_t	Thickness of Track
ϵ_0	Permittivity of Free Space
ϵ_r	Relative Permittivity
μ_0	Permeability of Free Space
ΔB	Difference between Maximum and Minimum Flux
ΔT	Permissible Change in Temperature
\hat{S}	Charge Density
Φ	Magnetic Flux
A and B	Experimentally Determined Values that Relate the Breakdown Voltage of a Gas to the Product of the Distance between Electrodes and Gas Pressure
C	Capacitance
E	Electric Field Strength
I	RMS Current
K, α and β	Steinmetz Parameters
k_v	A Constant that Converts Frequency to Angular Velocity in Faraday's Law (4.44 for Sinusoidal Waves, and 4 for Square Waves)
L	Inductance of Winding
N	Number of Turns in a Winding
P	Absolute Pressure
Q	Charge
R	DC Resistance of a Conductor

S	Cross Sectional Area of a Winding
V	Voltage
V_{max}	Maximum Voltage
Y	Youngs Modulus
b	Width of Belt
c	Waveform Coefficient
d	Distance
f	Frequency
g	Distance of Gap between Turns
i	Instantaneous Current
j	Rank of a Data Point
k	Constant Determined by the IPC-2221
l	Length of a Conductor
n	Number of Stages
r	Distance Between Core and Inside Winding
v	Velocity
w	Width of a PCB Track
γ	Secondary Electron Emission Coefficient
δ	Skin Depth
ε	Permittivity
η	Efficiency
σ	Conductivity of a Material
AWG	Arbitrary Waveform Generator
CDF	Cumulative Density Function
CEM	Circuit Equivalent Model
CTT	Cross Transformer Technology
DAB	Dual Active Bridge
EMF	Electromotive Force
FD	Flux Diverter
FEA	Finite Element Analysis

GSE	Generalised Steinmetz Equation
HVAC	High Voltage Alternating Current
HVDC	High Voltage Direct Current
HVLC	High Voltage Low Current
ICT	Insulated Core Transformer
IGSE	Improved Generalised Steinmetz Equation
IIGSE	Improved Improved Generalised Steinmetz Equation
IPMHVC	International Power Modulator and High Voltage Conference
ITER	International Thermonuclear Experimental Reactor
MMF	Magneto Motive Force
MSE	Modified Steinmetz Equation
NHVG	Nested High Voltage Generator
PC	Personal Computer
PCB	Printed Circuit Board
PDF	Probability Density Function
SE	Steinmetz Equation
SST	Solid State Transformer
WCSE	Waveform Coefficient Steinmetz Equation

Chapter 1

Introduction

High voltage direct current (HVDC) electricity has been generated and used since the 1870s. Although it was quickly superseded in many applications by high voltage alternating current (HVAC), which has many advantages that makes it more suitable for power transmission and distribution, such as compatibility with transformers and ease of design of switchgear. However, technological developments over the last century have led to HVDC making a resurgence in electrical power transmission, as it has several advantages over AC that make it suitable for transmitting power over long distances. The first of these is that DC power does not have a reactive element, as AC does, meaning it does not suffer from voltage distortion based on the inductance and capacitance of the line. This makes it more suitable for undersea cables, which inherently have extremely high capacitances. Another benefit of DC transmission is that it can be used to connect two different AC transmission networks that operate at different frequencies. As power loss in transmission lines is proportional to the square of the current passing through them, HVDC interconnectors are being developed that work at increasingly high voltages to reduce power loss. The drawback of this is in generating these high voltages. Current AC/DC interconnectors have huge geographic footprints to accommodate the circuitry required to rectify, invert and boost the voltage between the two power systems. This in turn leads to higher costs due to the value of land. There is, therefore, scope for the development of new technologies that can perform these functions in a much smaller space.

Another use of HVDC power is in particle accelerators. These have uses in many applications, including: medical imaging; silicon etching; and nuclear and plasma experiments. Early particle accelerators required little power to function. What was of interest was the operational voltage rather than the current. However, as the role of these particle accelerators has grown more complex, their power requirements have grown accordingly. Compare, for example, the “Westinghouse Atom Smasher”, constructed in 1937, which had a working voltage of 3 MV but a current of less than a milliamp [1]; with the

commercially available Tandetrans, developed by High Voltage Europa in the 1990s [2]. These produce the same voltage and a current nearly twenty times greater than that of the Atom Smasher, while being a fraction of the size and cost. Now a similar increase in the demands placed on new power supplies is taking place. Projects, such as the International Thermonuclear Experimental Reactor (ITER) [3], have power requirements in the order of megawatts, which must be supplied at extremely high voltages, and demanding space requirements.

What is essentially required is a means of generating high currents at extremely high DC voltages, with a geographic footprint of less than five by five metres. At present, practical DC power supplies, which operate at voltages in the order of megavolts, have a low power density; meaning that their size scales disproportionately in relation to their current output. The reason for this is that machines, based on technologies primarily intended for the production of high voltages, are not suited for high current loads. In contrast, technologies with a high power density typically don't scale to high voltages without drastically increasing in size. It is therefore clear that a way of combining these two archetypes must be discovered, to develop a new type of power supply capable of producing high currents at voltages greater than a megavolt, with reduced size compared to existing designs. The research conducted in this thesis is intended to contribute to the development of the next generation of high power density, HVDC power supplies.

1.1 Aims

The ultimate goal of this project is to develop a functioning power supply that is capable of meeting Specification 1, as described in Table 1.1, and could potentially be developed at a later date to meet Specification 2. However, this falls outside the scope of work that could possibly be completed while studying for a PhD. The work carried out in this thesis therefore represents the first steps in realising this wider, long term goal.

Table 1.1 The intended specifications for a power supply developed in this project.

	Voltage (MV)	Current (A)	Ripple (%)	Stored Energy (kJ)
Specification 1.	1	2	0.5	Less than 2
Specification 2.	5	5	0.5	Minimal

The aims of this thesis are as follows:

1. To critically examine existing HVDC power supply technology and identify advantages and shortcomings associated with each one.

2. To determine which of these technologies have the greatest potential to meet Specification 1, and which technologies in the future could potentially be developed to meet Specification 2.
3. To identify technical challenges associated with each technology and investigate ways of overcoming them.
4. To propose a theoretical design, that meets Specification 1, on which a prototype can be developed.

1.2 Contributions

The first major contribution of this work was in evaluating magnetic flux loss inherent to different configuration of insulated core transformer (ICT) layout. From this, an optimal layout was established that can be used to improve subsequently developed ICTs. In addition to this, assorted methods of reducing, or compensating for, flux loss in an ICT were investigated; including Cross Core Technology (CTT) [4] which has been used commercially by Kaiser Systems [5]. The voltage limitations of an ICT based design were also established, thus better defining the applications for which this technology can be used. These contributions were published in the IEEE Transactions on Dielectrics and Electrical Insulation special issue on high voltages and power modulation April 2019 (see Appendix A).

In addition to this, simulations and experiments were conducted to appraise the ability of windings, etched onto the surfaces of printed circuit boards (PCBs), to withstand the voltage and current demands placed upon them during continuous use in a high voltage, high frequency transformer. Testing was carried out under a wide range of potential operating conditions. These results are beneficial to anyone wishing to use such a winding construction method for high voltage applications in the future. This contribution is intended to be submitted to the International Power Modulator and High Voltage Conference in June 2020 (IPMHVC 2020) [6], and later modified for publication in a special issue of the IEEE Transactions on Dielectrics and Electrical Insulation [7].

The inherent flux loss in various arrangements of cascade transformers were also examined in simulation, leading to the determination of the optimum winding locations for such devices. In conjuncture with this, a new type of power supply was proposed that is based on the cascade transformer, but has been modified to reduce size. A draft paper describing this work is in preparation for publication in a journal at a later date.

Finally, a design was proposed for a power supply that is capable of meeting Specification 1, as described in Table 1. This design can be developed further into a working prototype of such a power supply.

1.3 Contents

The work in this thesis is divided into Chapters as follows:

Chapter 1: Introduction – A brief introduction outlining the background, aims and contributions of this thesis.

Chapter 2: Review of Existing Technology – A literature review was carried out that examined existing HVDC power supply technology presently in use around the world. The relative merits and drawbacks of each design are discussed and conclusions are drawn about their suitability for this project. Finally, the most promising technologies are selected for further scrutiny in the rest of this work.

Chapter 3: System Design – The basic outline of a design for a power supply, featuring one of the technologies that showed promise in the previous chapter, is described. The work that must be carried out, in the remainder of this thesis, to validate this design is also identified. In the latter half of the Chapter, additional technical problems are identified and possible solutions are discussed.

Chapter 4: Secondary Windings – An investigation was carried out into the possibility of using transformer windings etched onto the surfaces of PCBs. This investigation begins by examining the current carrying capacity of PCB tracks. Simulations and experiments are then undertaken to determine the withstand voltage of PCB insulation under different operating conditions.

Chapter 5: Insulated Core Transformers – A detailed investigation into flux leakage in ICTs was undertaken. This looks at various ways of reducing flux loss in ICTs, with special attention being given to the design proposed by Cross [4]. Finally, conclusions are made about the likelihood of a design, based on ICT technology, being able to meet the specifications described in Table 1.1.

Chapter 6: Cascade Transformers –A number of cascade layouts are examined with the intention of reducing flux leakage and maximising output voltage. During the course of this, a new type of power supply is proposed that would function in the same way as a cascade transformer, but has a smaller space requirement owing to its reduced size. Two and three dimensional simulations are used to evaluate the performance of these designs.

Chapter 7: Conclusions – The work in this thesis is summarised and conclusions are drawn from the work presented. Future projects that could be developed from this work are then discussed.

Chapter 2

Review of Existing Technology

Technologies already exist which can produce voltages near, or in excess of, 1 MV. Each was developed separately and has relative merits and disadvantages. A number of these technologies are discussed in this chapter before concluding remarks are made on which hold the most promise.

Other ideas, including the modification of pulsed power supplies [8]–[14] and technologies based on kinetic energy systems [15]–[18], were not investigated as there was insufficient evidence that they could be developed into a power supply that met the specifications outlined in Table 1.1

2.1 Van De Graaff Generator

The Van De Graaff Generator was first invented in 1931 [19], [20] to power particle accelerators [1], [21], [22], but is still used today as a source of high voltages for education and experiments [23]. It essentially consists of a rounded HV electrode mounted on top of an insulating support, and a belt, made from an insulating material, that hangs taut inside the support. There is a pulley inside the electrode, around which the belt is wrapped, and a second, motor driven, pulley at the base of the insulated column. The bottom of the belt is sprayed with electric charge, at a potential of tens of kilovolts from ground, using either corona discharge points or direct contact. This voltage is typically generated using a rectified transformer. The charge is then carried to the HV electrode, by the belt, where it is removed by discharging points that are connected to the inside of the electrode. This is shown in Figure 2.1. The HV electrode acts as a capacitor, storing the charge delivered to it by the belt.

As

$$V = \frac{Q}{C} \quad (2.1)$$

where V is the potential of the HV electrode; Q is the charge built up inside the electrode; and C is the capacitance of the electrode, hence the voltage of the device is proportional to the built up charge. The rate at which the electrode voltage increases can, therefore, be calculated using

$$\frac{dV}{dt} = \frac{I}{C} \quad (2.2)$$

where I is the time based derivative of Q , otherwise known as the current, and can be calculated using [24]

$$I = \dot{S}bv \quad (2.3)$$

where \dot{S} is the charge density of the belt; b is the width of the belt; and v is the velocity of the belt.

As the voltage is generated by a constant build-up of charge in the top electrode, without a way of returning the charge to earth, the voltage in a Van De Graaff Generator can theoretically become infinite. In practice, with a small load current, a voltage of several megavolts is often achieved.

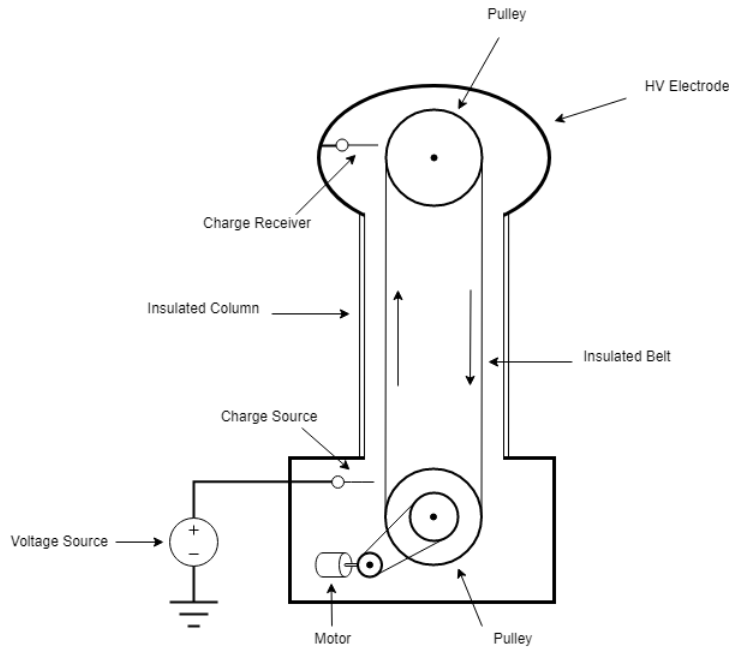


Figure 2.1. The operation of a Van De Graaff Generator.

The biggest drawback of Van De Graaff Generators is their low current output [25]. This is typically a few milliamps [19], roughly a thousandth of that required for this project. This low current capacity makes this power supply ideal for educational purposes, as it reduces the danger of serious electric shock. However, it is not suitable for the work outlined in this project. In theory, the current output could be increased by either finding a belt material capable of handling a higher charge density, widening the belt (or using multiple belts), or

increasing the motor speed. However, in practice, it is unlikely that any number of changes will increase the output power by three orders of magnitude.

Even if the Van De Graaff Generator could be modified to produce a sufficient current, it would still have several drawbacks. First, as the top electrode acts as a single capacitor, storing the charge that is drawn by the load current, it will necessarily store an unacceptably large amount of energy. Another inconvenience is that the mechanically driven belt and pulley system will necessarily reduce the electrical efficiency of the device by introducing additional sources of loss, such as friction. In addition to this, moving parts introduce another potential way for faults to occur, thus reducing the reliability of the design. For these reasons, a solid state design would be ideal.

2.2 Voltage Multiplier

A voltage multiplier is a configuration of electrical components that takes in an AC voltage, rectifies it and increases its amplitude. The first voltage multiplier was invented in 1920 by Grainacher, but was later improved by Cockcroft and Walton, in 1932, with the invention of the Cockcroft-Walton Generator, Figure 2.2 [24].

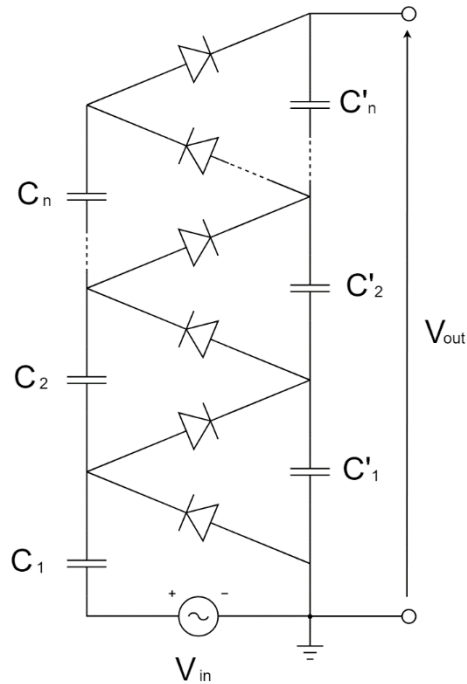


Figure 2.2. Circuit diagram of a three stage voltage multiplier.

With reference to Figure 2.2, in the first positive half cycle of operation, the inputted alternating current charges capacitor C_1 , to a potential equal to V_{max} , where V_{max} is the peak input voltage. Then, in the first negative half cycle, capacitor C'_1 is charged. In the second positive half cycle, capacitor C_2 is charged; then C'_2 in the negative. This process, of charging pairs of capacitors over each cycle, is continued until capacitors C_n and C'_n are

charged. At this point, the voltage across the whole ladder will be n times the peak input voltage, where n is the number of stages.

The Cockcroft-Walton Generator has been applied to many applications including particle accelerators [19] and X-ray [26] emitters. As it is constructed wholly from discrete, solid state components, it is reliable, efficient and highly adaptable. Due to its relative simplicity and diversity of application, it has remained in constant and frequent use since its inception.

The Cockcroft-Walton Generator suffers from two significant disadvantages. Firstly, being constructed mostly from capacitors, it necessarily stores a large amount of energy. This is discussed in greater detail in Section 5.5, where it is compared to the ICT. The second is that it suffers from significant voltage drop under load. This is because, in a similar fashion to the Van De Graaff Generator, power drawn from a Cockcroft-Walton Generator comes from discharging capacitors. In accordance with (2.1) as the charge in a capacitor decreases, the voltage across it also decreases.

The most obvious way of alleviating the latter problem is to increase the capacitances used in the design. However, work has gone into developing other solutions that don't increase the stored energy. The first of these solutions is to increase the frequency of operation. This has the additional advantage that the required capacitance, for a given load current, is inversely proportional to the excitation frequency. This method has been used to successfully create a Cockcroft-Walton based power supply capable of producing 400 kV at 400 mA [27]. Another solution is to create multiple multiplier circuits that operate out of phase with each other. This has been shown to reduce voltage loss across a Cockcroft-Walton Generator, with work going into determining the optimal numbers of phases and their ideal phase shifts [26].

2.2.1 Voltage Doubler

A voltage doubler is simply a voltage multiplier, based on the Cockcroft-Walton design, that consists of only one stage. These are a useful and economical way of rectifying the voltage produced by an AC power supply, as they double the produced voltage while storing the same energy, and using half as many diodes, as a conventional voltage rectifier (see Figure 2.6). In addition to this, a voltage doubler provides short circuit protection for the output circuit. Providing Class-Y safety capacitors are used, if there is an overvoltage then the capacitors will fuse open circuit, thus disconnecting the AC source from the output circuit. Voltage doublers would make a useful addition to a practical design as they would effectively half the voltage required from the rest of the design, although this comes at the expense of doubling the required input current.

The two most commonly used types of voltage doubler are the half wave voltage doubler, also known as the Greinacher Circuit, and the full wave voltage doubler, also known as the Delon Circuit [28]. These can be seen in Figure 2.3 a) and 2.3 b) respectively. The main functional difference between these two designs is that the half wave voltage doubler produces an output voltage that is double the amplitude of the input voltage, as measured from the 0 V input terminal. This means that the output circuit can be earthed to the same potential as the input. On the other hand, the full wave circuit has an equal output voltage above and below the 0 V input terminal. This means that, although the output voltage is twice the peak of the input voltage, when measured between the output terminals, the outputs are effectively floating and cannot be earthed to the same potential as the input circuit. This makes it problematic for use in high voltage applications, where earthing must be a serious design consideration.

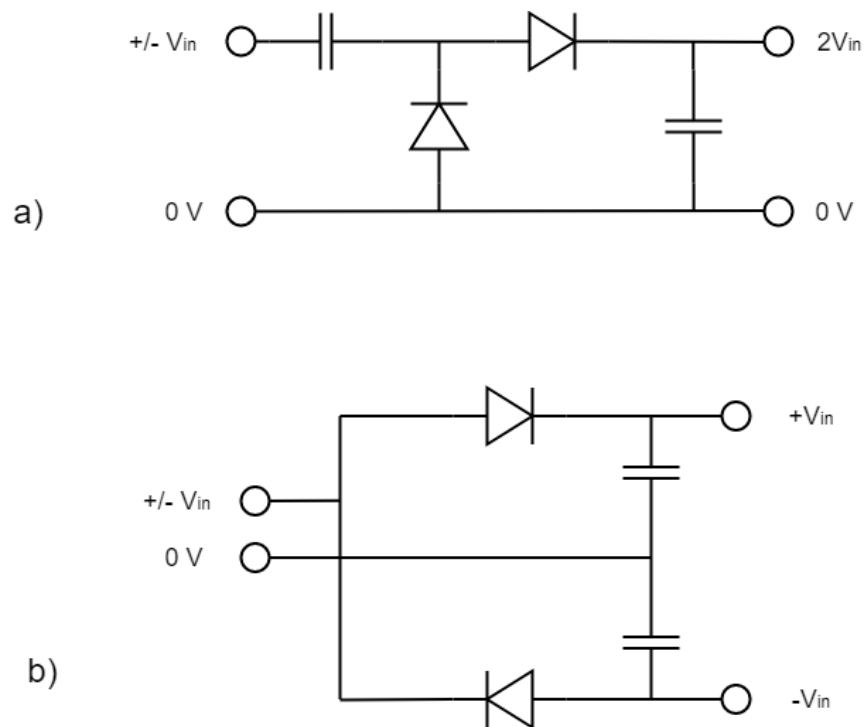


Figure 2.3. Circuit diagram of a) a half wave voltage doubler and b) a full wave voltage doubler.

2.2.2 Dynamitron

The Dynamitron is a topology of power supply that is commonly used in particle accelerators [29]–[34]. It is based on a variation of the Cockcroft-Walton Generator, and is capable of producing voltages, in the order of megavolts. It is advantageous in comparison to Van De Graaff Generators, which produce similar voltages, for high power applications in that it is capable of producing relatively high currents, typically several tens of milliamps.

The equivalent circuit diagram of a Dynamitron is shown in Figure 2.4. A column consisting of semi-circular corona rings, connected via a series of rectifiers, is inserted into a shielded

tube lined with two semi cylindrical electrodes. The mutual capacitance between the electrodes and corona rings energise all of the rectifier stages equally, thus raising the voltage across the whole design in a manner similar to the workings of a Cockcroft-Walton Generator.

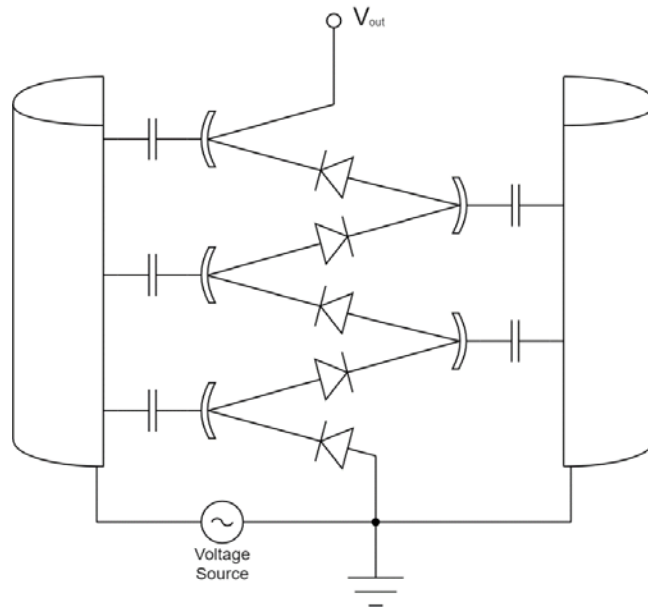


Figure 2.4. Internal workings of a Dynamitron. Capacitances are formed between the corona rings (inside) and electrodes (outside).

Because these capacitances are much less than those used in a Cockcroft-Walton Generator, where discrete capacitors are used, for each stage to achieve the same impedance, Dynamitrons must operate at a much higher frequency. As the capacitors are mutually coupled, rather than being series coupled, as in a conventional Cockcroft-Walton Generator, the voltage drop under load is not related to the number of rectifier stages [30]. This means that Dynamitrons can have many more stages than a Cockcroft-Walton Generator, and therefore generate much higher voltages. Indeed, voltages of several megavolts are far from uncommon for commercially available machines [2].

The Dynamitron is a relatively simple design with no moving parts; factors that contribute to the high reliability of the design. This, in combination with its high efficiency and relatively high achievable power output, has made the Dynamitron a very popular choice for people requiring a power source for a particle accelerator; with numerous Dynamitrons installed in research facilities (both academic and industrial) around the world. Particle accelerators, powered by Dynamitrons, can be bought off the shelf. One of the largest of these companies is High Voltage Engineering Europa, who have recently developed a 6 MV 20 mA particle accelerator powered by their “Tandetron” [2], [33]. Again, the design is limited by the current a single device can supply.

2.3 Transformer

One of the oldest voltage changing technologies, the transformer is now so ubiquitously used it makes up the voltage changing component of all AC power grids worldwide, as well as being the central component of almost all power supplies. It is incredibly versatile and, in addition to being able to step up or step down any AC voltage, it electrically isolates the output circuitry from the input.

Transformers are constructed from two, or more, coils of wire that pass energy between themselves in the form of magnetic flux. The flux is induced, through Faraday's Law of Induction [35], by an alternating current in one of the coils. The coils, typically, share a core made out of a soft magnetic material [36]–[38], which has a higher magnetic permeability than the insulating material around it; allowing it to channel the flux between the coils. In most designs, the core forms a complete magnetic flux path to avoid leakage inductance. This arrangement is shown in Figure 2.5. Core materials are often optimised so that they operate efficiently; either at high flux densities, as in transmission and distribution transformers, or at high frequencies, as in switch mode power supplies.

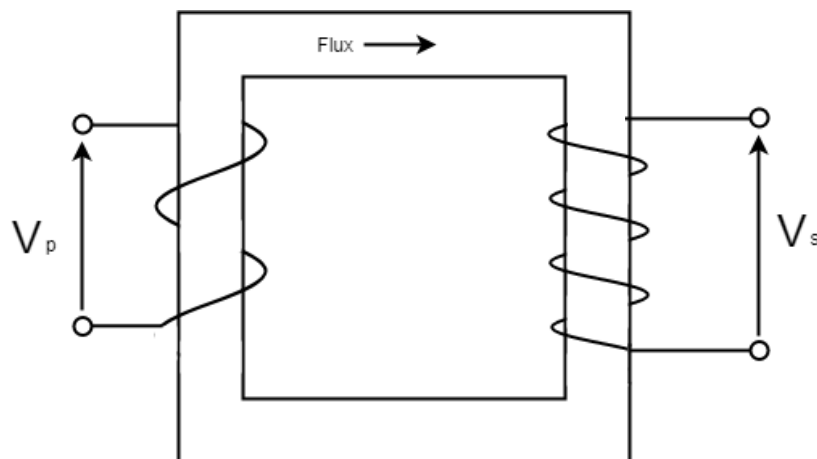


Figure 2.5. The operation of a transformer. Change in current in the primary winding induces a change in flux density in the core, which in turn induces a voltage across the secondary windings.

The versatility of transformers comes from the fact that they have a higher current handling capability than almost any other kind of voltage changing technology. While most other technologies described in this chapter produce currents in the order of milliamps, there are innumerable transformers in use in transmission networks that continually handle kiloamps at hundreds of kilovolts.

Theoretically, the only limiting factor in a transformer design is the flux density in the core, though in reality power lost in the windings and core must also be taken into account.

Transformers, with cores that have high flux saturation levels, can have tremendously high power densities.

Despite the ubiquity of transformers in applications requiring voltages in the order of hundreds of kilovolts, there are relatively few transformers that continuously operate in the region of megavolts. There are, of course, exceptions to this rule. For example, there are currently several transformers operating at 1 MV in the Chinese and Russian transmission networks [39]. The power density of transformers decreases at these voltages because of the difficulties associated with insulating transformers. While other technologies, such as the Van De Graaff Generator and Cockcroft-Walton Generator, distance the high voltage components from the low voltage terminal, all of the windings of a transformer must be wound closely around a metal core. This reduces the allowable space for electrical insulation, as each winding must be insulated, up to their total voltage, from the core as well as the other windings. Extremely high voltage transformers must, therefore, have large gaps between their conducting components. This, in turn, increases their size. For this reason, transformers are arguably better suited for high currents than high voltages.

In addition to its high power density, and high current handling ability, the transformer has several advantages that make it appealing for this project. First, as its principal components are inductive, rather than capacitive, very little energy is stored during HVLC operation. Also, the ubiquitous use of transformers, for almost all types of application, has led to the optimisation of their design. Transmission transformers are expected to operate, with efficiencies in excess of 99.998%, for fifty years or more. This is evidence that transformers can be designed to be highly reliable and efficient. There is also a significant body of literature explaining the craft of transformer design [36]–[38], streamlining any prototyping phase of a project based on transformer technology.

The main disadvantage of the transformer, apart from the scaling issues at extremely high voltages, is that it produces an AC voltage that must be rectified using additional power electronics. This issue is discussed in detail in the following section.

The size of the transformer core is dependent on a number of parameters, as will be explained in greater detail in Section 6.1, one of which is the operational frequency. Broadly speaking, the size of the core is inversely proportional to the frequency of winding excitation; meaning that the size of the core, and therefore the transformer, can be minimized by using a high operational frequency. Recent developments have been made in developing a new generation of transformer, known as the solid state transformer (SST), that uses power electronics to switch at a frequency much faster than conventional transmission and distribution transformers. They have been produced and shown to be able to handle distribution loads [40]–[42]. As they operate at much higher frequencies, than conventional

transmission and distribution transformers, the cores of SSTs are typically made out of specialist materials to avoid saturation [36]. A brief description of some of these materials is given in Chapter 3.

2.3.1 Rectification

As the transformer outputs an AC voltage, a rectifier must be used in order to process this waveform before it can be used in a DC application. A simple full wave, single phase, rectifier circuit is shown in Figure 2.6. The negative half cycle of the waveform is inverted, resulting in a DC current with a 100% voltage ripple. This ripple is reduced by charging a capacitor from which a more consistent DC voltage can be drawn, also shown in Figure 2.6.

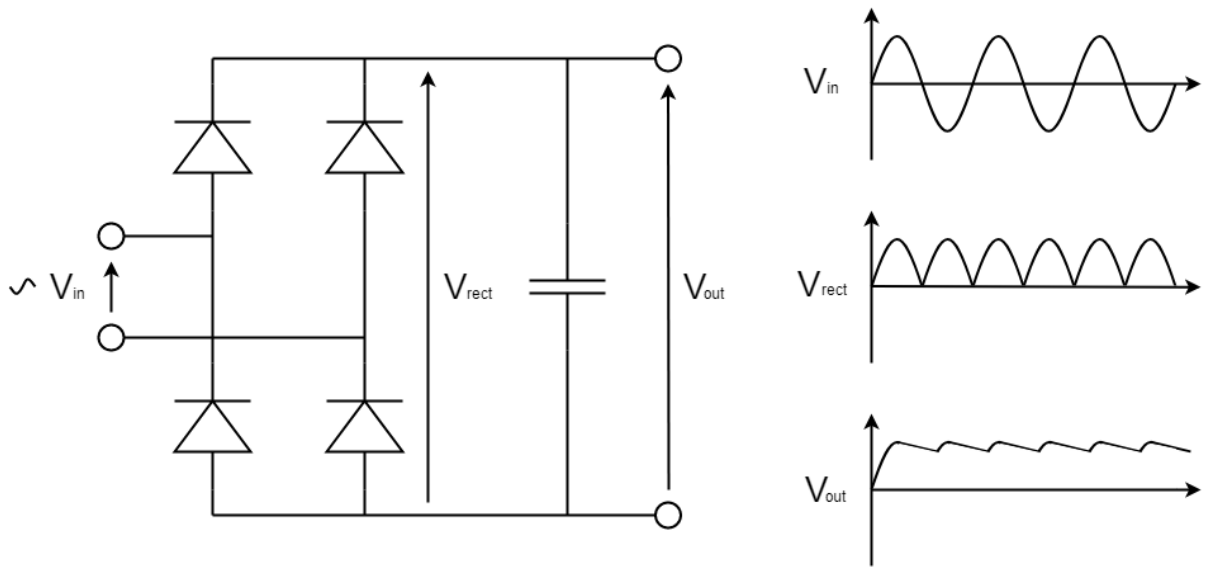


Figure 2.6. (LEFT) The circuit diagram of a full wave rectifier. (RIGHT) Voltage Waveforms in a full wave rectifier.

The capacitance C needed, to reduce voltage ripple V_{ripple} of a full wave rectifier, of a single-phase AC voltage source, to a given level, can be calculated using [24]

$$C = \frac{I}{fV_{ripple}} \quad (2.4)$$

where f is the operating frequency. To meet the requirements outlined in Table 1.1, using power grid frequency, and allowing a voltage ripple of 5,000 V at 2 A, the necessary capacitance is 8 μ F. Energy stored in a capacitor E_{stored} can be calculated using

$$E_{stored} = \frac{1}{2} CV^2 \quad (2.5)$$

where V is the peak voltage in the capacitor. At one megavolt, the capacitor would have to store 4 MJ of energy. This is far in excess of the 2 kJ or less as specified in the first chapter of this thesis. This value can be reduced, by designing the transformer to function at a higher

frequency, as the stored energy is inversely proportional to the frequency. If the same voltage and current values are used, the transformer would have to operate at a frequency of 200 kHz in order to reduce the stored energy to 1 kJ.

An alternative to this would be to use a voltage doubler. This would have the advantage of halving the voltage requirement from the transformer itself, thus reducing the stresses on the transformer insulation and greatly reducing the overall size of the design. In comparison to this, the doubling of the required load current is a more straight forward matter.

2.3.2 Cascade Transformers

The cascade transformer was developed to solve the problems associated with insulating a single transformer against an extremely high voltage. It does this by connecting multiple transformers in series so that each one transforms only a fraction of the total voltage [24]. The circuit diagram of a three stage cascade transformer is shown in Figure 2.7. Each stage consists of a transformer with three windings: a primary; a secondary; and an auxiliary. The primary and the secondary both have the same number of windings, meaning they experience the same flux linkage and operate with the same electrical characteristics. The auxiliary of each transformer is connected to the primary of the next transformer in the cascade, with the auxiliary of the top transformer being left open circuit, or else omitted entirely. The primary of the bottom transformer is connected to a voltage source. The secondary windings have a number of turns N_s that can be calculated using

$$N_s = \frac{V_{out}N_p}{nV_{in}} \quad (2.6)$$

Where N_p is the number of turns in the primary and auxiliary windings; V_{in} is the voltage in the primary windings; n is the number of stages; and V_{out} is the total output voltage of the design. The secondary windings can then be connected in series to produce the total output voltage. In theory, each transformer should behave identically; although flux leakage in each transformer, as well as power losses in the windings and cores, will have a cumulative effect on each transformer.

It is a much simpler process to insulate whole transformers from each other than it is to insulate the windings from the core of a single transformer, because the location of each transformer has little effect on the other transformers in the cascade.

Cascade transformers have been used before to produce voltages in the region of 1 MV [43], [44].

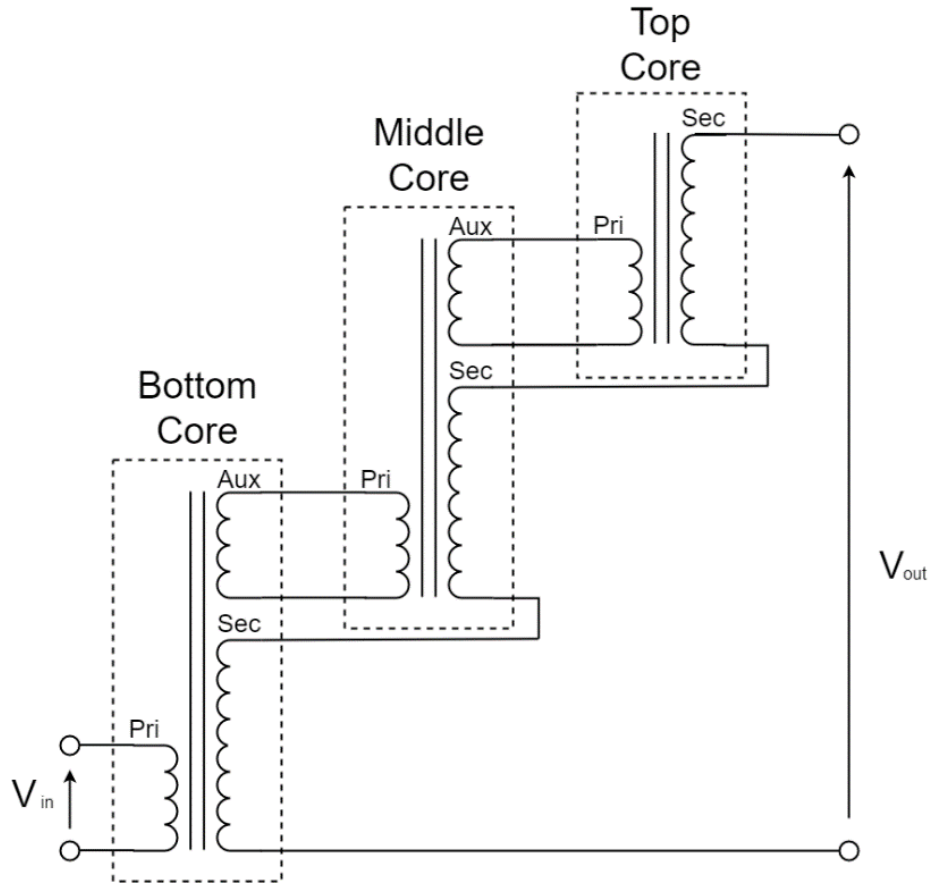


Figure 2.7. Circuit diagram of a cascade transformer with three stages.

2.4 Insulated Core Transformer

Insulated core transformers (ICTs), like cascade transformers, represent an attempt to overcome the problems associated with insulating transformers against extremely high voltages. A detailed account of the history and development of the ICT is given in Chapter 5, so here only a basic outline of its operation will be given.

As stated previously, the greatest difficulty in designing transformers, for high voltage applications, is insulating the windings from the core; as the core, being conductive, must have the same potential throughout its entire volume. The ICT attempts to solve this problem by breaking the core into a number of sections, each electrically insulated from the others [4], [45]. This is shown in Figure 2.8. In this way, each winding only needs to be insulated against a fraction of the total transformer voltage. The biggest drawback to this is that insulating sections of the core will necessarily disrupt the flux path. Special care must, therefore, be taken when designing an ICT to reduce the effects of flux loss on the design. Although there have been a number of attempts to do this in different ways (many of which

are examined in Chapter 5), it is generally desirable to minimise the lengths of the gaps between the flux carrying sections of core and to have a large core cross sectional area.

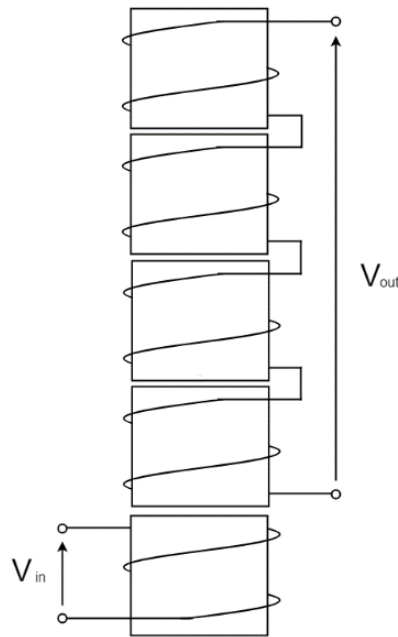


Figure 2.8. A diagram of an ICT, consisting of windings wrapped around sections of core material that are insulated from each other.

There currently exist ICTs that are capable of producing hundreds of milliamps at a megavolt [5] using voltage doublers. So, in order to develop this design, it is only necessary to increase the current output by around an order of magnitude.

2.5 Resonant Transformer

A resonant transformer is a transformer in which the excitation voltage is provided by the inherent properties of the windings, rather than being driven by an outside source [46]–[51]. The circuit schematic of one of these transformers can be seen in Figure 2.9. The primary circuit consists of an inductor, which makes up the primary winding and a capacitor. Together, these components form an oscillating circuit which is periodically energised by an external power source. Historically, this has been achieved using a conventional transformer, the peak voltage of which would be enough to bridge a spark gap, although thanks to developments in solid state technology, the energy burst can be provided by power transistor switching. The primary oscillating circuit is typically tuned to resonate at radio frequencies. As operation, under such high frequencies, would cause insurmountable power losses in most core materials, the core is often omitted entirely; resulting in the two windings being coupled through air. For this reason, this device is also known as an air cored transformer.

The secondary circuit also consists of an inductor and capacitor; though in this case, the capacitance is often parasitic, rather than being the product of a discrete component. This second resonant circuit is tuned to the same frequency as the first, allowing energy to be passed between the two circuits. The resonant transformer has a much lower coupling coefficient than a conventional transformer, owing to the lack of a magnetic core channelling the flux between the windings.

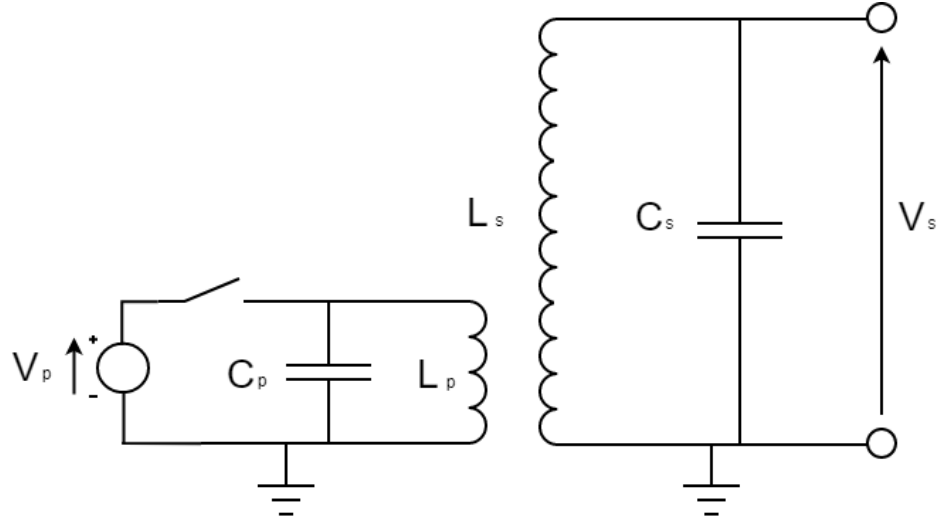


Figure 2.9. Circuit diagram of a resonant transformer.

Unlike a conventional transformer, the voltage ratio between the primary and secondary windings is not based wholly on the turns ratio of the windings. Instead, it is dependent on the frequency of operation. The frequency f of an oscillating circuit can be calculated using [52]

$$f = \frac{1}{2\pi\sqrt{LC}} \quad (2.7)$$

Where L is the inductance of the winding, and, given the energy stored in a capacitor can be calculated using (2.5), it can be seen using conservation of energy that

$$V_s = V_p \sqrt{\frac{C_p}{C_s}} = V_p \sqrt{\frac{L_s}{L_p}} \quad (2.8)$$

where C_p and C_s are the capacitances of the primary and secondary circuits respectively; and L_p and L_s are the inductances of the primary and secondary circuits respectively.

This type of transformer is advantageous in that it can easily be tuned to produce extremely high voltages and does not suffer from core losses, as would be the case with a conventional transformer. However, due to the low coupling coefficient between the windings, the current in the primary windings must necessarily be much greater to compensate for the high flux leakage. The winding losses caused by this high current may

outweigh the benefits gained by not using a magnetic core. In addition to this, the heat generated in the primary circuit, from this high current, could damage the transformer; thus reducing its reliability.

2.6 Nested High Voltage Generator

The Nested High Voltage Generator (NHVG) is a configuration developed in the early nineties in order to decrease the diameter of DC particle accelerators by splitting the total voltage evenly between a number of insulated stages, each with their own power source. The stages are placed inside each other, so that the stage with the highest potential is at the centre of the design, while the stage with the lowest potential is on the outside. In this way, each stage only needs to be insulated from the one immediately inside it, thus allowing for linear scaling of the insulation. This means that no part of the design needs to be insulated against the total system voltage, greatly reducing the stress on the insulation.

There are a number of ways that the internal stages may be powered. These include: (a) batteries, which may be charged between system uses; (b) a mechanical drive shaft passing through each stage turning a generator inside of each one; and (c) a transformer cascade [53]. However, the method that is most commonly used is electrical induction from a primary winding, wound around the base stage, acting as an air core transformer, as seen in Figure 2.10 [53]–[59]. In this way, the NHVG is topologically similar to the ICT, without the magnetic core channelling the magnetic flux. Instead, the magnetic flux must reach the secondary windings through the insulation between stages.

The operation of the electrically induced NHVG is as follows: The primary winding is excited, at a high frequency, via an external AC voltage source. This, in turn, induces an alternating current in each of the secondary windings, via magnetic induction, that is then rectified using voltage doublers. The rectified voltages are then connected in series to produce the total system voltage.

This configuration can be constructed either of metal cylinders suspended in insulating oil, in which case the oil makes up the total of the insulation, or from plastic cylinders that are suspended in oil, in which case the insulation consists of an oil/plastic mix. Historically, the oil/plastic mix has been avoided in larger designs, with most existing NHVGs consisting of stages constructed from metal cylinders. Magnetic flux must pass through azimuthal gaps in the cylinders in order to reach the secondary windings. It is because of these gaps that the NHVG is unsuited to being insulated using pressurised gas, and why oil must be used instead. The biggest source of loss, in an oil insulated electrically induced NHVG, is caused by eddy currents induced in the metal cylinders surrounding each stage. It has been suggested that this loss could lead to the overall efficiency of the design being reduced to

50% [6]. This would effectively turn a 2 MW power supply into a 4 MW power supply and produce a rather daunting 2 MW of excess heat. For this reason, it would be worth examining the plastic/oil insulated NHVG.

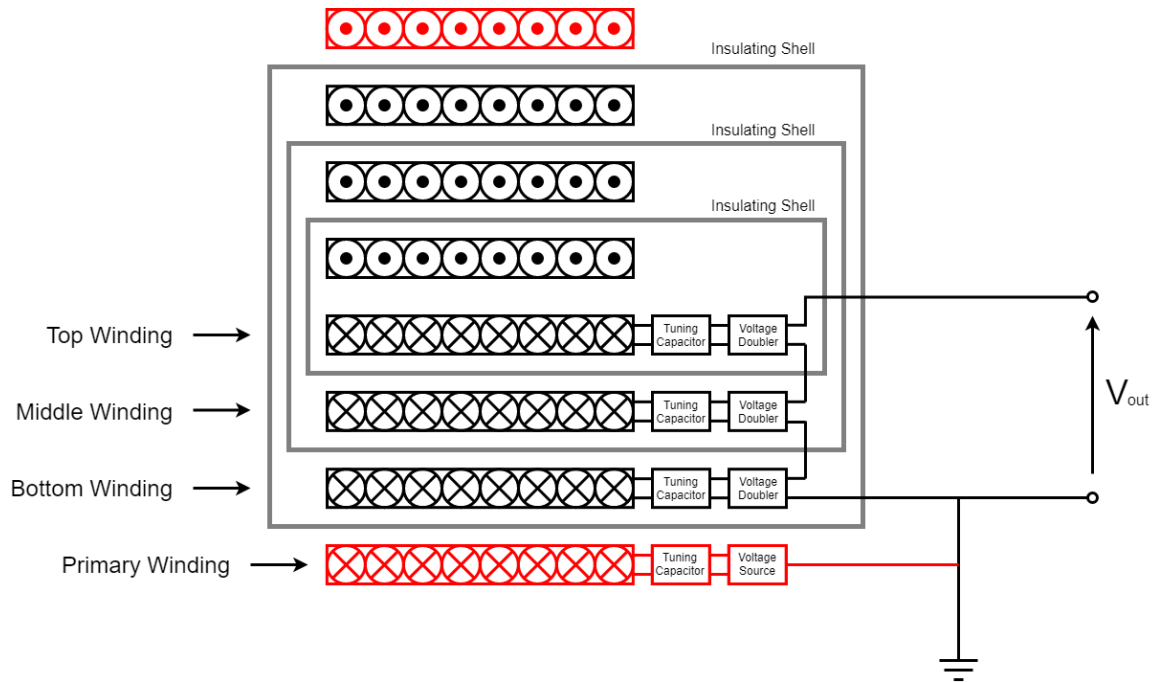


Figure 2.10. Schematic of the cross section of a nested high voltage generator.

It would stand to reason that by replacing the metal stage housings with plastic ones, these eddy current losses could be reduced. However, a faraday cage must exist around each stage to prevent excessive magnetic flux radiation. This could be maintained either by coating the plastic in a thin conductive layer less than one skin depth thick, or embedding metal rods into the plastic housing. As both of these techniques are presently untested, additional time and resources would have to be spent developing this technology before it can be used in a practical power supply.

2.7 Summary and Discussion

A number of different technologies, and their variations, have been identified and described in the previous sections. With the notable exception of those based on the conventional transformer, all of these technologies are able to produce voltages greatly in excess of 1 MV; with it being a trivial matter to scale up their design to produce 5 MV. However, the power demands, of this project, are more challenging to overcome. It is important to decide which of these technologies have the potential to be developed, to meet the specifications outlined in the previous chapter, as the rest of this thesis is centred on identifying a design methodology for developing a working prototype.

It is clear that the Van De Graaff Generator is unsuitable for this project as the difference between currents that have been produced by this machine in the past, and what is required in this work, is insurmountable. Similarly, the voltage multiplier and Dynamitron lack the ability to operate effectively under high loads. Although it is conceivable that the design shown in [27] could be expanded upon to produce the electrical characteristics required in this project, doing so would certainly exceed the stored energy requirements outlined in the previous chapter, probably in addition to the size requirements.

The resonant transformer shows promise, as it is known to be capable of producing voltages in the order of megavolts. To the author's knowledge, there is no work, existing in the public domain, that has investigated the potential current output of resonant transformers; although there is no component, inherent to the operation of the technology, that would significantly limit current produced by a resonant transformer. For this reason, it may be assumed that a design based on resonant transformer technology could be viable for the purposes of this project. It appears that the most space efficient way of implementing this, and the way that is best suited for the loads required in this project, would be using a NHVG configuration. However, additional research and development must be carried out to prevent this technology operating with an unacceptably low level of efficiency.

The conventional transformer is the only technology that is known to easily meet the current requirements of this project, although it is less suited for higher voltages as it is difficult to insulate. A voltage doubler could be used to change the system requirements from 1 MV and 2 A, to 500 kV and 4 A; this is closer in line with the electrical parameters that transformers are more commonly designed to meet. The problems associated with insulation could be further alleviated by using a cascade to reduce the voltage across each individual transformer. This topology also shows the greatest potential for development of a 5 MV, 5 A power supply based on the transformer.

The ICT has similar electrical characteristics and works in a similar way to the cascade transformer, as they both share many of the same components and technical challenges. This makes it convenient for a single program of development to be carried out, investigating both technologies. For this reason, it was decided that this thesis would focus on the development of the insulated core and the cascade transformer designs. Although the resonant transformer also displays the potential to meet the requirements outlined previously, it shares relatively few components in common with the other two technologies and should only be considered if the other approaches prove impractical.

Chapter 3

System Design

The technologies that show the most promise, for the purposes of this project, are the cascade transformer and the ICT. Both of these technologies are variations of the conventional transformer and, accordingly, have many components in common. Both designs consist of a primary winding, one or more soft magnetic cores and numerous secondary windings. Operationally, both designs output AC power that must be rectified externally. For these reasons, a similar design methodology can be applied to both technologies. This Chapter outlines an overall design for the power supply and details work that must be carried out, in the remainder of this thesis, to evaluate the suitability of the selected technologies.

Several design principles became apparent in the previous chapter. First, multiple parallel voltage sources, acting in different phases, produce a smaller voltage ripple than a single voltage source, or multiple parallel voltage sources acting in phase [26]. Secondly, stored energy and voltage ripple, in a capacitor based system, are inversely proportional to operational frequency. Finally, voltage doublers store no more energy than a conventional rectifier capacitor but have the added advantage that they electrically isolate the output circuit from the ICT or cascade transformer. In addition to this, they effectively change the requirement of the rest of the design, from producing 2 A at 1 MV to producing 4 A at 500 kV. This is ideal as the technologies that were selected for closer scrutiny in the remainder of this project are those that produced the highest current, rather than the highest voltage.

Based on these observations, the design shown in Figure 3.1 is proposed. Mains electricity is first rectified, thus producing a regulated DC voltage that can be inverted, at a much higher frequency, by numerous modulator units acting at different phases. These high frequency AC voltages are then used to power the transformer stages, which consist of either cascade transformers or ICTs. The final stage will double, and then rectify, the voltage produced by the transformer stage. These voltage doublers can then be connected in parallel to create a single DC output.

Using multiple phases, connected in parallel units, also has the advantage of reducing the load on each individual transformer stage; thus reducing power loss and minimising electrical and thermal aging of components. Each of the stages outlined above will be explained in greater detail in the remainder of this chapter. In addition to this, a number of real world technical challenges, such as its electrical insulation, will be discussed.

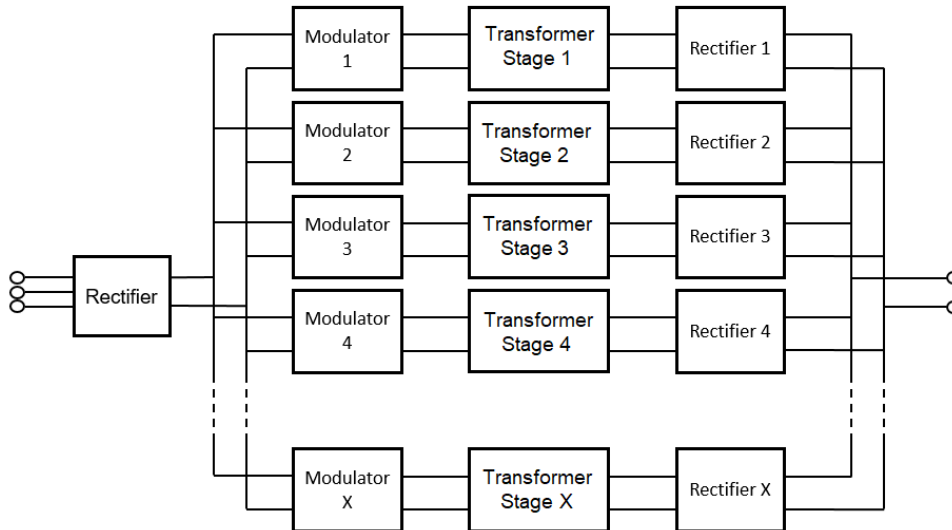


Figure 3.1 A block diagram of the proposed power supply.

3.1 Rectifier and Modulator

The rectifier and modulator will be designed to provide a high current, low voltage primary supply. The cascade transformer or ICT used to increase the voltage, will be designed to operate at a frequency in the order of tens of kilohertz. 100 kHz was selected as the target operating frequency, as this was shown to be possible by James Cross when he developed his own ICT [4]. Achieving this regulated input would require an external power supply, the design of which is beyond the scope of this thesis. Despite this, a brief overview of the operation of such a power supply will be given here, with a schematic diagram shown in Figure 3.2.

First, the mains power should be rectified in a manner similar to that described in Section 2.3.1. The circuit for a three phase rectifier can be seen in Figure 3.3, and requires only two more diodes than the single phase full wave rectifier. Once the voltage has been rectified, it is processed by a voltage regulator, which removes the voltage ripple and produces a constant DC voltage. This voltage can then be inverted to an AC frequency, much greater than 50 Hz, with any number of phases. In addition, the voltage amplitude can be varied electronically in accordance with the requirements of the transformer stage and rectifier stages of the overall design. Inversion can be performed either using a simple switching circuit, in which case square waves will be produced, or using Dual Active Bridges

(DABs) that are capable of creating sine waves. Although square waves would be simpler to create, they would induce greater losses in the transformer stage. In addition, DABs are not without fault as they are constructed from significantly more transistors than a square wave generator, thus suffering from greater losses at the switching stage. In addition to this, DABs do not create pure sinusoids. Instead, the waveforms they generate contain harmonic frequencies that could only be removed using, naturally lossy, low pass filters. As a detailed design for the modulation stage is outside the scope of this work, so too is a decision on the exact nature of the inversion used. The work in the remainder of this thesis will investigate the effects of both sinusoidal and square wave excitation.

Existing high frequency drive technology tends to be designed for low voltage, high current loads. For this reason, it was decided that the outputs of the modulators should have an amplitude of 400 V, which can be used in the primary windings of the transformer stages.

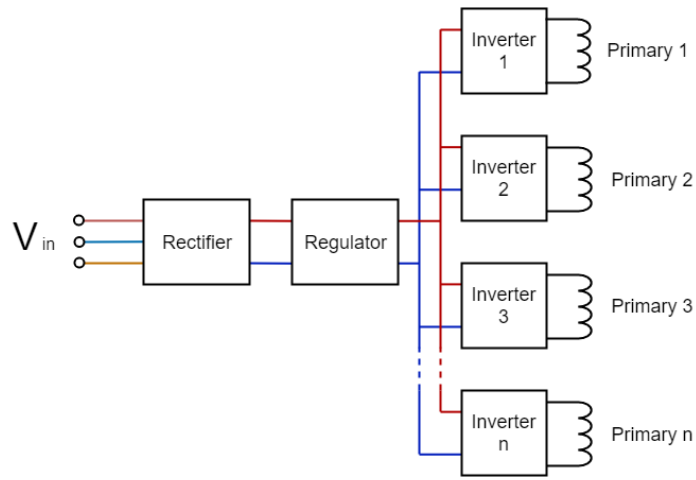


Figure 3.2 A block diagram of the modulator stage.

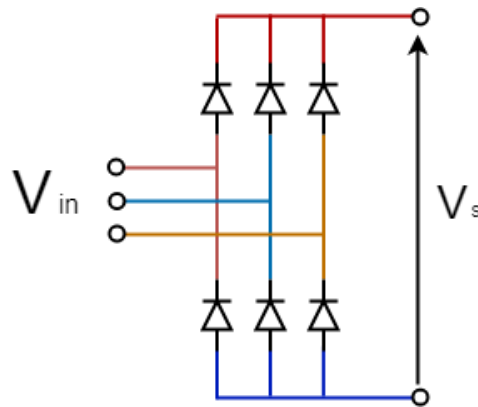


Figure 3.3 Circuit diagram of a three phase rectifier.

3.1.1 Connections to Transformer Stage

A further challenge lies in electrically connecting the transformer stages to the modulators. The design is intended to supply 2 MW with an input voltage of 400 V. This means that,

even if it is assumed that the power supply is 100% efficient, the connectors will have to carry a minimum of 5 kA. Even divided between multiple phases, this is a significant current and transporting it between the modulators and transformers is not a trivial task. This problem is further complicated by the fact that the current will be oscillating at 100 kHz, so will induce a skin effect in the connectors.

The high currents in the connectors will cause two problems. Firstly, the resistance in the connectors will lead to high power loss. Secondly, these losses will heat the connectors, possibly damaging them. Due to the skin effect, increasing the thickness of the cables will have limited effect. In addition to this, as the thickness of the conductors increases, they become less flexible, making them more difficult to route around the design.

One possible solution to this would be to form these connections out of multiple thin wires that can be connected in parallel. This would increase the cross sectional area of the connectors, while keeping the diameter of each wire relatively small. This solution would have the additional advantage of increasing the surface area of the connectors, thus increasing thermal dissipation. This is the same principle used in overhead power lines.

This problem is so rooted in the practicalities of the power supply installation that a definitive solution cannot be decided upon at such an early stage of system design.

3.2 Transformer Stage

Both the cascade transformer and ICT are adaptations of the conventional transformer, which works by linking the currents in different windings through mutual inductance, and therefore share many design principles. Both technologies were developed with the intention of overcoming the problems associated with insulating the windings from the total transformer voltage by dividing the core into sections that each has its own potential. Magnetic flux must pass between these sections so that the whole design can operate like a conventional transformer with a single core.

The ICT simply relies on magnetic flux bridging the small insulated gaps between sections of core; while the cascade transformer connects its sections of core electrically. Both methods suffer from flux leakage, which must be minimised in order to maintain a high output voltage, as will be seen in Chapters 5 and 6.

Due to their functional similarity, both technologies are constructed from many of the same components. This means that both the ICT and the cascade transformer can be developed in parallel before a single solution is decided upon based on a detailed comparison of the two technologies. Specifically, the components that both technologies share in common are the material of the core, and the primary and secondary windings.

Possible core materials are discussed briefly, later this chapter. The primary, and potentially auxiliary, windings are a relatively trivial matter to create due to the small number of turns that are required. In contrast to this, the secondary windings are a much more complex task to develop as, to create a voltage ratio of 1,000,000:400, there must be 1,250 times as many secondary turns as there are primary turns. Chapter 4 will consider the possibility of making these secondary windings from printed circuit boards (PCBs).

3.3 Rectifier

The role of the rectifier stage is to double the voltage of the transformer stage, and rectify it to produce a DC output. This will be achieved using voltage doublers, which were described in the previous chapter. In addition to the voltage smoothing effects of the capacitors in each individual voltage doubler, by connecting the output of each rectification stage in parallel, the voltage ripple can be further reduced, as described in [26].

The disadvantage of capacitor based voltage rectifiers is the energy they store. However this can be reduced by increasing the operational frequency of the power supply. Voltage doublers also have the advantage that their capacitor arrangement electrically isolates the output terminals from the rest of the power supply. This is a useful safety feature as, providing appropriately rated capacitors are selected, the capacitors can fail-open in the event of a short circuit; thus preventing the fault current from passing through the load.

3.4 Insulation

The breakdown strength of a material is a measure of the electric field it can withstand without discharge. Electric field strength can be expressed as the electrical potential across a given length, hence the SI unit for electric field strength is volts per meter (Vm^{-1}). In a uniform electric field, insulated by a single insulating material, it is a trivial matter to calculate the maximum safe voltage to apply across a gap of a given distance. Most practical systems, however, do not create a uniform field, and cannot be insulated by a single material. Sharp edges and protrusions on the surface of conducting components will distort the electric field, increasing its strength in the near vicinity. This increased field strength makes breakdown more likely to occur in these areas. For this reason, care should be taken when designing the conductive components of a high voltage system to avoid sharp edges that may cause corona, or even full breakdown.

Under alternating current, the electrical displacement field is the same across the whole gap between two parallel electrodes, regardless of the insulation materials used. Because of this, the electric field in each material is effected by its own electric permittivity and the

permittivity in the materials around it. In the simple case where the boundary between two insulating materials runs perpendicular to the electric field, as seen in Figure 3.4a, the electric field strengths in the two materials are related by [24], [60]

$$\frac{E_1}{E_2} = \frac{\varepsilon_2}{\varepsilon_1} \quad (3.1)$$

where E_1 and E_2 are the electric field strength in the first and second material respectively; and ε_1 and ε_2 are the permittivities in the same materials. From this, it can be seen that, if a material with a high permittivity displaces a portion of a low permittivity insulator in an electric field, rather than increasing the breakdown strength across the whole length of the field, the new material will actually increase the stress placed on the lower permittivity material.

In addition to this, if the boundary between two insulating materials intersects a uniform electrical displacement field at an angle other than 90° , as shown in Figure 3.4b, then the electric field in each material will be distorted such that it will be refracted at the boundary at an angle that can be calculated as follows [24], [60], [61]

$$\frac{\tan \alpha_1}{\tan \alpha_2} = \frac{\varepsilon_1}{\varepsilon_2} \quad (3.2)$$

where α_1 and α_2 are the angles of diffraction of the electrical displacement vector in each material. It is important to note that, if the angle between interface and electrode is less than 90° on the side of the material with the lower permittivity, then the point of intersection will theoretically have an infinite electric field intensity; thus making this point particularly prone to breakdown [62]. If the boundary between the two materials is parallel to the electric field, as shown in Figure 3.4c, then the electric field will be the same over both materials. These principles must be taken into account when designing solid spacers that must be placed inside gasses or liquids. Different types of insulating material have different properties that make them suitable for different situations. These are explored briefly in the following sections.

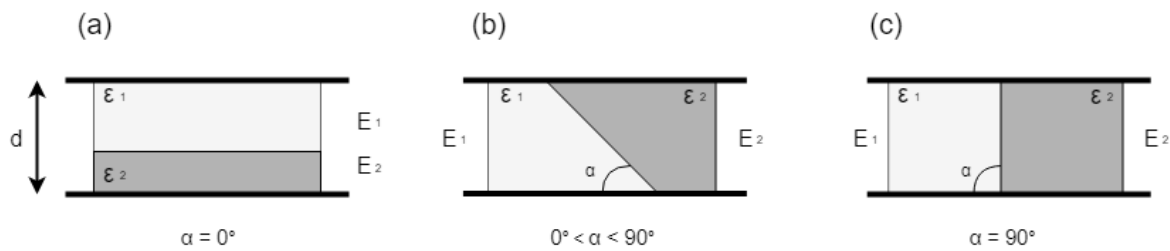


Figure 3.4 Boundaries between insulating materials placed between two plane electrodes.

3.4.1 Solid Dielectrics

It is practically inevitable that solid insulators will be used in a high voltage system, as they are required to hold the electrical components in position. They typically have a very high dielectric breakdown strength, and in some materials, this can be as high as $1,000 \text{ MVm}^{-1}$ [60]. However, their poor heat handling qualities, combined with the fact that they are non-restoring, mean that they are usually used sparingly in conjunction with liquids and gasses. Their high permittivity, in comparison to other insulating materials, mean that careful consideration must be taken when designing spacers to avoid tracking occurring along their surface [24], caused by the principles mentioned in the previous subsection.

Solids are prone to a number of different breakdown mechanisms [24], though the most common is thermal [60]. The breakdown voltage in a solid insulator increases in line with the insulators thickness; unless the material is heated to a critical temperature, in which case the conduction of the material is determined by its temperature [24], [60], [63]. A second failure mechanism, which must be accounted for, is electromechanical breakdown. This is caused by compression forces, acting on the material, caused by electrostatic attraction between surface charges that appear when a voltage is applied across the insulator. The highest voltage that can safely be applied across a solid insulator can be calculated using [24]

$$V = 0.6d_0 \sqrt{\frac{Y}{\epsilon_0 \epsilon_r}} \quad (3.3)$$

where V is the applied voltage; d_0 is the initial thickness of the material; Y is the Young's Modulus of the material; and ϵ_0 and ϵ_r are the permittivity of free space and the relative permittivity of the material respectively. From this, it can be seen that care must be taken when designing spacers to avoid overloading them.

3.4.2 Liquid Dielectrics

Liquids, typically oils, are also used as insulators in high voltage equipment. In addition to having a high breakdown strength, often in the order of 100 MVm^{-1} [60], they are also ideal for cooling as they have high heat capacities and are partially self-restoring after breakdown. For these reasons, oil-insulated transformers, cables and switchgear have made up an integral part of power transmission and distribution networks around the globe for decades. In this capacity, they have proven themselves to be highly reliable providing they are correctly maintained. The relative permittivity of oil can vary between 2 and 73, depending on the type of oil used and the frequency of operation [60]. This is greater than gasses, which typically have a relative permittivity of 1, and likely to be closer to that of the

solid insulating components; thus reducing the charge accumulation on the surface of the spacers.

Despite these advantages, oil insulation suffers from a number of drawbacks. Firstly, the damage it can cause to the environment means that there are strict regulations associated with its disposal and storage. Particular care must be taken to avoid leaks as spilled oil is a hazard and can damage the surrounding equipment. In addition to this, the breakdown strength of oil can be greatly affected by contaminants such as moisture and metal particles. Just 0.01% [60] water contamination in transformer oil reduces its electrical strength by 80%. Oil is also highly flammable, making it particularly susceptible to disastrous and irreparable failure. One final property of oil, that makes it unsuitable for the prototyping nature of this project, is that it can degrade certain materials through ingress and its thermal and electrical properties can change due to chemical processes associated with aging such as oxidation.

3.4.3 Gaseous Dielectrics and Vacuum

Gases are commonly used to insulate high voltage systems for a number of reasons. Although they typically have a lower dielectric breakdown strength than many solids and liquids [60], they can be pressurised to increase their breakdown strength [64]. Gasses are ideal for prototyping as they are cleaner than oils, thus reducing the degradation on parts that must be repeatedly inspected, altered, or removed from the device. In addition to this, gasses are self-restoring [24], though toxins generated in repeated breakdown may affect the integrity of the medium over time if an enclosed system is used. Many gasses, particularly air and its constituent parts, are non-hazardous and do not cause damage to the environment, making them easy to dispose of. However, there is growing concern in the public consciousness for gasses, such as Sulphur Hexafluoride (SF_6), that are highly damaging to the environment [65]. This has led to an increased research focus into environmentally friendly alternatives to SF_6 . To date, no other gasses have been found that perform as well as SF_6 . If harmful or damaging gasses are to be used, additional work must be carried out to prevent leaks and to reclaim gas when opening any sealed container.

The most abundantly available insulating gas is air, which theoretically has a dielectric breakdown strength at atmospheric pressure of 3 MVm^{-1} ; though in practice it is common for a design engineer to include a significant margin of error to account for factors such as humidity, so in practice the breakdown strength is normally considered to be closer to 1 MVm^{-1} [24]. Other commonly used gases include Nitrogen, CO_2 , and Argon. It has been shown that the breakdown strength of both of these gasses can be increased by mixing them with SF_6 , though neither mixture performs as well as pure SF_6 [66]–[68].

The breakdown strength V_{bd} of most gases can be increased in accordance to Paschen's Law [24], [60], [64], which can be defined as

$$V_{bd} = \frac{Bpd}{\ln(Apd) - \ln(\ln(1 + 1/\gamma))} \quad (3.4)$$

where pd is the product of the absolute pressure of the gas and the distance between the cathode and anode; A and B are experimentally determined values that depend on the gas; and γ is the secondary electron emission coefficient of the electrodes. Plotting this equation for a given set of values results in a curve, known as the Paschen Curve. The Paschen Curve for air is shown in Figure 3.5, from which it can be seen that V_{bd} rises above a minimum value as the pressure is increased or decreased. The effects of reducing the gas pressure are discussed in Section 3.4.3.2. There are limits to Paschen's Law. First, a gas will liquefy if the pressure is increased beyond a certain point. And second, Paschens Law was developed based on DC breakdown between two parallel plate electrodes meaning that, although it remains a useful guide, it cannot be relied upon to give accurate breakdown predictions in practical AC systems.

It is also worth noting that gas insulation systems suffer, much like liquid insulation, from reduced breakdown strength when mixed with foreign contaminants, such as metal particles and moisture [69]–[71].

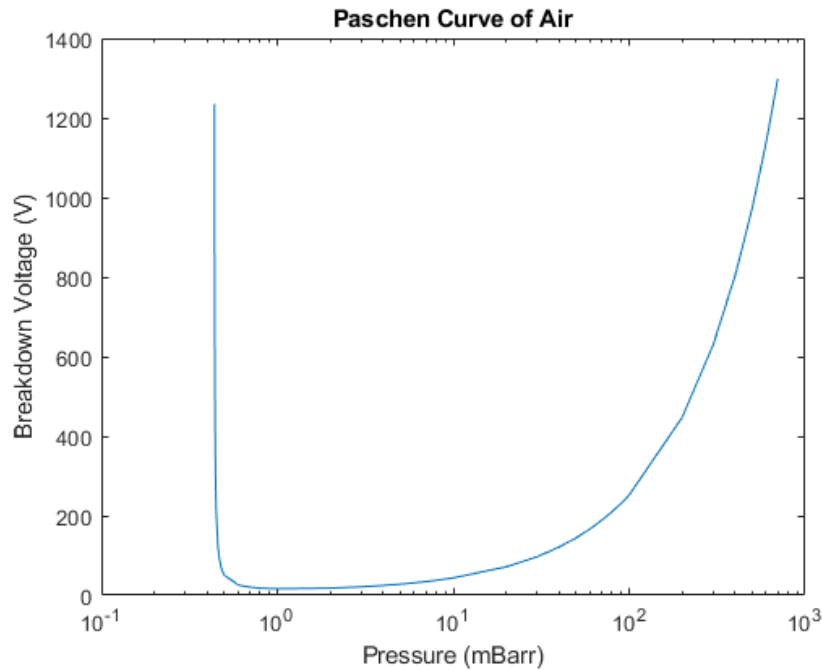


Figure 3.5 The Paschen Curve of air with electrodes held 5 cm apart.

3.4.3.1 Sulphur Hexafluoride

Sulphur Hexafluoride is a dense and highly electronegative gas [72], meaning that its particles bond with free electrons, effectively absorbing them. This property makes it an ideal material for insulating HV apparatus. It has been used in AC applications for a long time [73], where the positive half cycle of operation detaches the surplus electrons from the gas ions, preventing electron saturation in the insulation. In a DC field, the electrons do not have an opportunity to be separated from the positive ions, thus leading to substantial charge accumulation in the gas [62], [71]. This makes design of DC SF_6 insulated systems more challenging, partly because the electron saturation reduces the dielectric breakdown strength of SF_6 by approximately 20% in a uniform electric field [74], but more importantly, because of the free charge accumulation on the surfaces of the solid insulating spacers, making flashover more likely to occur at lower voltages [62], [71].

Because of the additional stress put upon solid spacers in a DC system, additional care must be taken when designing them [62], [73]. While, in an AC system, it is possible to represent insulating media entirely based in its permittivity; in a DC field, conduction plays a dominant role, meaning that conductivity must be considered. This is further complicated by the charge accumulation, formed on the surface of solid insulators, effectively changing the properties of the boundary between epoxy and SF_6 . It is, therefore, important to consider the volume and surface conduction when designing a spacer [75]. A method of modelling the properties of the boundary was given by Volpov [75], who also proposed a series of design rules for spacers in HVAC and HVDC SF_6 insulated systems [62]. It has also been suggested that applying a thin dielectric coating, such as polyethylene, to the surface of a spacer might be an effective way of increasing the DC breakdown voltage [62], [73].

In the latter part of the last century, 500 kV DC transmission lines were developed that were insulated using SF_6 gas [76]–[78]. It was also predicted that SF_6 could be used to insulate DC systems up to 1 MV, though 1.2 MV was considered unrealisable without additional advances in technology [73]. At time of writing, this estimation is being proven correct in the form of the International Thermonuclear Experimental Reactor (ITER) which is currently under construction. This neutral beam injector is designed to operate for up to an hour and requires a power supply capable of producing 40 A at 1 MV DC. This voltage is created using a five stage, oil insulated, cascade transformer. The rectification circuits of this, as well as the 75 m transmission line, are all insulated using SF_6 pressured to 600 kPa [44], [71]. In light of this, SF_6 could be an appropriate insulating material for the requirements of this project, providing special consideration is taken when designing the solid components of the insulation.

3.4.3.2 Vacuum

It was seen in Section 3.4.3 that the breakdown strength of gasses can be predicted using Paschens Law and that, as the pressure is increased above a certain value, the breakdown voltage increases as well. However, it can also be seen that reducing this pressure below this critical value also increases the breakdown voltage. The reason for this relates to the mechanisms that cause breakdown to take place.

In order for breakdown to occur between two electrodes, a free electron, energised by the electric field, must leave the cathode and collide with an insulating atom. There is then a chance that this collision will impart sufficient energy to the atom to free one or more electrons. These electrons, as well as the original electron, can then be energised again by the electric field and cause more collisions, freeing more electrons and causing an avalanche effect until a continuous plasma is formed between the electrodes. As the pressure of the insulating gas drops below a critical value, the number of particles that can be turned into positive ions, freeing one or more negative electron(s) in the process, and thus becoming capable of carrying a charge between the electrodes also reduces [24], [60].

In theory, breakdown should be impossible in absolute vacuum as there are no available charge carriers capable of passing between the cathode and electrode. In practice, however, small unavoidable discrepancies in the surface of the cathode distort the electric field around them. Eventually, this causes particles to be ejected from certain cathode spots, which are capable of carrying charge, thus leading to metal vapour plasma [79]. A means of calculating “field enhancement factor”, based on the size and shape of these discrepancies, is given in [80].

Vacuum is a very effective form of insulation and has many advantages over gas insulation. Perhaps most notable, for experimental and prototyping purposes, is the fact that it does not damage the electrical components; in the same way that some oil and gases can. Also, as no media, other than air, is involved, the insulating container can be opened and closed without the need to flush and store insulating gases. This reduces the operational cost of vacuum insulation, as only an initial expense for vacuum equipment is required. High breakdown strengths can be achieved using relatively low vacuum, limiting the necessary initial cost of equipment.

There are two major disadvantages of using vacuum in a practical power supply; the first of these is that it is a very good thermal insulator. There are three ways for thermal energy to leave a body. These are: (a) conduction through solid materials; (b) convection into liquids and gasses in contact with the surface of the body; and (c) radiation in the form of electromagnetic waves. Vacuum, by essentially being the absence of any surrounding liquid or gas, limits the forms of heat transfer to conduction and radiation. As radiation is the least

effective form of heat transfer, additional apparatus may need to be put in place to conduct heat away from the active power supply components. This would significantly increase the complexity of a prototype power supply design. The second disadvantage is that many materials outgas in a low pressure environment [81]; meaning that the area around them becomes conductive in a vacuum. Included in the list of materials that outgas are most plastics, and other solid insulators. Great care must, therefore, be taken when selecting materials to be used in a vacuum insulation system.

3.5 Semiconducting Devices

Since the middle of the 20th century, most electronic devices have been made from silicon. Silicon has been used ubiquitously in power electronic devices for the last sixty years, with research being carried out to improve devices' maximum operating voltage, current and frequency. Silicon devices are now available that are capable of producing nearly 2 A, with a blocking voltage of 6.5 kV, at nearly 1 kHz [82]. However, new technologies, such as solid state transformers, require higher current densities and higher frequencies than silicon can provide.

Because of these limitations, there has been a focus over the last few decades on developing “post-silicon” devices that are capable of meeting these requirements [82]. The most well developed material, for this purpose is silicon carbide. It has been shown that silicon carbide has a ten times stronger breakdown field than silicon, and “three orders of magnitude improved turn off characteristics over silicon devices with comparable voltage ratings” [83]. This means that they can be made smaller and produce less excess heat than silicon devices.

Silicon carbide devices come in the same categories as silicon ones, such as metal oxide silicon field effect transistors (MOSFETs) and insulated gate bipolar transistors (IGBTs).

Silicon carbide MOSFETs have been developed that operate at 15 kV, with a turn off time of 150 ns and the total energy lost during turn off being only 0.81 mJ [83]. This makes them very efficient at high frequencies. However, due to their higher DC resistance, they are unsuitable for higher voltages or current densities [84].

Silicon Carbide IGBTs have a lower blocking resistance making them better suited to operating at higher currents. They can be optimised to have either a high blocking voltage (p-IGBT) or a high operating frequency (n-IGBT), depending on the doping used. Even n-IGBTs have a turn off time of around 500 ns making them more than three times slower than MOSFETs [84]. Drive systems, operating at 20 kHz, have been developed using IGBTs [40]. It has been found that IGBTs have lower power loss than MOSFETs at

frequencies up to 7 kHz [85] and that IGBTs are better suited for voltages above 15 kV [40], [82], [83].

Silicon Carbide MOSFETs and diodes have been shown to be effective at driving and rectifying a 110 kV HV generator that operates at frequencies up to 500 kHz [86]. This is several times faster than is required for this project. As the driving circuit will operate at voltages of less than 1 kV, sufficiently sized MOSFETs (or numerous MOSFETS connected in parallel) should be ideal for the modulation stage [87]. Silicon carbide diodes will also be ideal for the rectification stage as they have been shown to operate at high frequencies and voltages.

3.6 Magnetic Materials

All soft magnetic materials consist of microscopic particles that each have their own magnetic field. When a magnetic field is applied to the material, the particles will rotate so that their magnetic fields align with the field applied to them. The ability of the particles to align with the applied field is known as permeability. On a macro level, this is effectively the ability of the material to form internal magnetic fields. A material with a higher permeability will divert more of the applied magnetic field through itself, rather than the air around it. Magnetic permeability is the ratio between the magnetic flux density B and the magnetic field intensity H . In all practical materials, permeability is not a linear relationship, but varies with magnetic field intensity.

When all of the magnetic fields of the particles are aligned, the material is saturated. At this point, increasing the strength of the applied field will have no additional effect on the material, and the effective permeability of the material is the same as that of free space. The field strength at which saturation occurs is known as the saturation inductance.

The resistance of the particles to aligning with the magnetic field is known as hysteresis, and is one of the biggest sources of core loss in the material. The second biggest source of core loss are eddy currents, which form in the core as a result of the alternating magnetic field. An electrically resistive core material is ideal for reducing these currents, and by extension the losses in the core. Over the last two hundred years, materials have been developed with exceptionally low hysteresis losses, for a given range of frequencies. However, as most magnetic materials are electrically conductive, eddy currents remain a problem at higher frequencies. Methods of compensating for this are examined in the following subsections.

The purpose of the core of a transformer is to channel magnetic flux between the primary and secondary windings. High permeability and saturation inductance are desirable

properties, as this reduces the required size of the core. This means that less material is needed to construct the core, in turn, lowering the price of the transformer. It is also desirable for the material to have low losses, as losses lead to energy wasted in the form of heat, which could damage the transformer and other components. A detailed investigation into core losses is undertaken in the next section.

There are two broad categories of materials used in transformer cores [38]. The first of these are iron alloys, which have been used in practical applications since the beginning of the nineteenth century. Variations of these include laminated cores, powdered cores, amorphous alloys, and nanocrystalline materials. These tend to have a high saturation inductance, but an incredibly low resistivity that is often only a little higher than that of a good electrical conductor. The second type of material are ferrites, which are a form of magnetic ceramic material. These tend to have a lower saturation inductance than iron, but typically have a much higher resistivity. This makes them better suited to high frequency applications [38].

3.6.1 Laminated Iron

Laminated iron cores were developed in the middle of the nineteenth century, with the intention of compensating for the low resistivity of iron ($0.7 - 0.8 \mu\Omega m$) [63], while maintaining the high relative permeability, which can be as high as 1,000,000 [63]. To do this, thin slices of electrically insulated magnetic material are held together. This creates a clear magnetic flux path while reducing the distance eddy currents can travel in the core.

The material most commonly added to iron in laminated cores is silicon. The silicone is added to reduce the conductivity of the iron and, thus, reduce the eddy current losses even further. However, silicon reduces the saturation inductance and makes the material more brittle, so it is unusual for the alloy to consist of more than 3% silicon [38], [88].

Nickel is also often added to iron for use in transformer cores. Different alloys are created by mixing different ratios of the two elements, depending to the physical properties required of them. For example, Permalloy which consists of 80% nickel and 20% iron. Permalloy is typically used in DC applications due to its high permeability. Invar, which is 36% nickel and 64% iron, has a greater resistivity and so is better suited for high frequency applications. Because of this, Invar is often used in audio applications, where frequencies of up to 20 kHz are required [38].

Although silicon steel is normally isotropic, it can be grain orientated to reduce the core losses at high inductances. However, grain orientation makes the material anisotropic, meaning that care must be taken when constructing the transformer to ensure that the grains line up with the direction of the flux path [36], [38], [88].

3.6.2 Powdered Iron Core

Powdered Iron cores consist of grains of iron, which are typically 20 – 100 μm thick, set in insulating resin [88]. The grains are intended to be smaller than the skin depth of the excitation field [38]. The resin forms a distributed gap that reduces the effects of eddy currents. On a macro scale, the resistance of powdered iron is around 1 Ωm [36], making these cores ideal for use at frequencies of several hundred megahertz [88]. They also have a relatively high saturation inductance, as high as 1.5 T [36].

The biggest drawback of powdered iron is that the distributed gap also reduces the permeability of the core to just a few hundred times that of air [36], [38]. Despite this, it is commonly used in switch mode power supplies, radio frequency chokes and filters, and variable inductors [88].

Carbon can be mixed with the iron to increase the saturation inductance, at the expense of the permeability [38].

3.6.3 Amorphous Alloy

Amorphous alloys are formed by melting together a ferromagnetic element (iron, nickel or cobalt), with a metallic element (silicon, boron or carbon) that is introduced to reduce the melting point of the alloy [38]. This molten alloy is then cooled so fast that a crystalline order does not have a chance to form. The cooling rate is typically around 1,000,000 $^{\circ}C s^{-1}$ [63] and the material is formed into thin strips, between 10 – 50 μm thick [38], which can then be tape wound. When cooled, amorphous alloys have a structure similar to that of glass, hence they are often referred to as metallic glass [36]. The lack of crystalline structure reduces the hysteresis of the material [38]. This, combined with the relatively high resistivity of 1.2 – 2 $\mu\Omega m$, means that amorphous materials suffer from very low losses [38].

The saturation induction of amorphous alloys can be as high as 1.8 T [38], and the relative permeability can be as high as 150,000 [38]. However, these values are not stable throughout all possible operating conditions. The saturation inductance may reduce by as much as 30% if the temperature is increased from 25 $^{\circ}C$ to 250 $^{\circ}C$ [36]. Additionally the relative permeability may reduce to less than 1,000 at frequencies over 1 MHz [38].

Iron based amorphous alloys are typically used for low frequency transformers and high power inductors, as they typically have low losses compared to grain orientated steel and have a similar saturation [36], [38]. Nickel based alloys have a very high relative permeability, but this comes at the expense of the saturation induction, which can be reduced to as little as 1 T. These are typically used in low to medium frequency transformers [36]. Finally, cobalt is used as the base material if very high permeability is required.

However, cobalt based amorphous alloys have a saturation inductance of less than 1 T. As they tend to be expensive, cobalt is generally used only in specialist applications [36].

3.6.4 Nanocrystalline

Nanocrystalline cores combine the high saturation of silicon steel, with the low loss at high frequencies of ferrites [36], [38]. They are formed of ribbons with a thickness of 15 – 25 μm [36], [38]. The ribbons consist of small crystalline structures, with diameters in the order of 10 nm [63] (hence the name nanocrystalline), that are able to align themselves with the magnetic field with relatively little resistance. This makes nanocrystalline materials very efficient at high frequencies.

Nanocrystalline materials can have a relative permeability up to 150,000, a saturation inductance of 1.5 T, and typically operate at frequencies up to 150 kHz [36], [38]. For these reasons, nanocrystalline cores are usually smaller than cores made of other materials that have similar power requirements. This, in turn, reduces their losses even further. Additionally, nanocrystalline materials are known to be very temperature stable [36]. For these reasons, nanocrystalline cores have been judged to be the most suitable core material for the new generation of solid state distribution transformers [40].

3.6.5 Ferrites

The physical properties, and production process, of ferrites resemble those of ceramic materials [38], [88]. There are four stages to its production. First it is produced as a powder with the required chemical composition, then it is pressed and sintered, before finally being ground into the desired shape [63]. Ferrites have a very high resistivity, typically in the order of 10,000 Ωm [36], [38], which leads to very low eddy current losses making them ideal for very high frequency operation. Indeed, zinc ferrites have been used in applications up to 1.5 MHz [88].

Ferrites have a relatively low saturation inductance, typically between 0.25 T and 0.45 T [38], and a relative permeability in the order of 10,000 [88]. They are typically used in filters, pulse transformers, and power transformers that operate between 10 kHz and 100 kHz [88]. Due to their low saturation inductances, ferrites have limited use in high current applications [36].

The most common ferrite variant is manganese-zinc, which has a relatively low resistivity of 0.1 – 10 Ωm , but a high relative permeability and high saturation inductance. This is ideal for use at frequencies below 1 MHz. The other common variety is nickel-zinc, which is better

suited for use at frequencies above 1 MHz due to its resistivity, which is in the order of 10,000 – 1,000,000 Ωm [36], [38].

3.6.6 Conclusions

A final decision regarding what material to use will have to be based on many other factors, including the mechanical requirements of the core, the operating temperature and the insulation material. It would be impossible to know what these requirements are before a draft design is established. However, a brief comparison of potential materials, based on known magnetic requirements, can still be made at this early juncture.

Laminated iron and silicon iron are extensively used in high voltage applications at power grid frequencies. They are structurally sound, however their high losses at higher frequencies make them unsuitable for this project. Similarly, powdered cores are structurally sound and suffer lower losses at high frequencies, but they are not ideal due to their low permeability that make them unsuitable for high current applications.

Nanocrystalline materials appear to have the best magnetic properties as they are constructed from numerous layers of thin tape, but they are known to have poor structural strength. This is impractical, as the high voltages involved in this project will require a lot of space for insulation that will require a large core. Amorphous alloys share many of the same advantages and disadvantages.

Ferrites also show a great deal of promise for this project. As they are ceramic materials, they are more structurally stable than tape wound cores. This comes at the expense of the saturation inductance, which is significantly less than any other material examined in this section. This means that more material is needed to prevent saturation. Although this increases loss, and is more expensive, the extra material will further increase the structural stability of the core.

Material manufacturers list the magnetic properties of their materials on data sheets. Additionally, several sources have published tables that list generic values for materials, and compare them in tables [36], [37]. These are a useful tool for design engineers wishing to quickly evaluate which material is most suited for their application.

3.7 Core Losses

In order to accurately predict the power loss in a transformer core P_{iron} , three different approaches are often used [89]. The first of these is the loss separation technique, which splits the sources of loss into eddy current loss and hysteresis loss and sums them together. The second is the hysteresis approach, which only calculates static losses and neglects

dynamic losses. Methods based on these approaches often require numerous parameters based on detailed information of the core material. This information is difficult to obtain without extensive experimentation. This makes them impractical for design engineers who often need to consider a wide range of materials for a purpose, and typically do not have access to physical samples until the prototyping stage of project development. For these reasons, work in this Chapter will focus on methods based on a third, empirical, approach. The most commonly used equation is [90]

$$P_{fe} = V_{core} K f^\alpha B_{max}^\beta \quad (3.5)$$

where V_{core} is the volume of the core. This has the advantage of only needing three coefficients, K , α and β , that are obtained from curve fitting core loss data given in manufacturer datasheets.

Because of (3.5)'s resemblance to a similar equation devised by Steinmetz in 1892 [91], which does not include a frequency dependant component, this equation is commonly known as the Steinmetz Equation (SE). Unfortunately, although it is commonly used in transformer design, the SE is applicable only for sinusoidally excited cores. As indeed is, typically, the loss data provided by manufacturers. In addition to this, the Steinmetz parameters are typically only valid for a limited range of frequencies [89].

Despite these limitations, the SE remains a useful tool, in no small part, because of its simplicity and the ease with which loss data can be calculated using only three, easily ascertained, variables. For these reasons, a number of attempts have been made to devise ways in which the Steinmetz parameters can be used to predict power loss in magnetic cores driven by arbitrary waveforms. One of the earliest contributions was the Modified Steinmetz Equation (MSE) [92], [93] which replaces the sinusoidal frequency with an equivalent frequency f_{eq} , and is defined as

$$P_{fe} = V_{core} K f_{eq}^{\alpha-1} \dot{B}^\beta f_r \quad (3.6)$$

where

$$f_{eq} = \frac{2}{\Delta B^2 \pi^2} \int_0^T \left(\frac{dB}{dt} \right)^2 dt \quad (3.7)$$

$$\Delta B = B_{max} - B_{min} \quad (3.8)$$

$$\dot{B} = \frac{\Delta B}{2} \quad (3.9)$$

and

$$f_r = \frac{1}{T_r} \quad (3.10)$$

where B_{min} is the minimum flux density in the core; and T_r is the period of the excitation voltage.

The MSE has been shown to be an effective tool for estimating iron loss. However, it suffers from a number of problems. Specifically, that it can produce differing results depending on how the driving waveform is defined. In addition to this, when used to predict losses in a sinusoidally excited transformer core, the results are not in agreement with the SE. Because of these problems, the Generalised Steinmetz Equation (GSE) was proposed [94]. The GSE was derived from the SE, and can be defined as

$$P_{fe} = V_{core} \frac{k_1}{T_r} \int_0^T \left| \frac{dB}{dt} \right|^\alpha |B(t)|^{\beta-\alpha} dt \quad (3.11)$$

where

$$k_1 = \frac{K}{(2\pi)^{\alpha-1} \int_0^{2\pi} |\cos\theta|^\alpha |\sin\theta|^{\beta-\alpha} d\theta} \quad (3.12)$$

Although it is more consistent, it has been shown to be less accurate than the MSE. For this reason, the Improved Generalised Steinmetz Equation (IGSE) [95] was then developed, which breaks the flux waveform into major and minor loops and solves each of these before summing the total losses together. It also replaces the dependence on transient flux density, used in the GSE, with the peak flux density. The IGSE is extremely complex and time consuming in its implementation. It was originally intended for use in high performance CAD programs [95]. However, a simplified version which was developed for use by design engineers, is defined as

$$P_{fe} = V_{core} \frac{k_2}{T_r} \int_0^T \left| \frac{dB}{dt} \right|^\alpha |\Delta B|^{\beta-\alpha} dt \quad (3.13)$$

$$k_2 = \frac{K}{2^{\beta-\alpha} (2\pi)^{\alpha-1} \int_0^{2\pi} |\cos\theta|^\alpha d\theta} \quad (3.14)$$

To simplify (3.13) still further, the creators of the IGSE performed the integration component of k_2 and curve fit the results, thus simplifying (6.11) to

$$k_2 = \frac{K}{2^{\beta-\alpha} \pi^{\alpha-1} \left(0.2761 + \frac{1.7061}{\alpha+1.354} \right)} \quad (3.15)$$

Which has been shown to be accurate, to (3.14), within 0.15% [95]. The IGSE is considered to be one of the most accurate methods of calculating flux loss under non-sinusoidal excitation. The imaginatively named Improved Improved General Steinmetz Equation (IIGSE) [96] was developed from the IGSE. This increased the accuracy of the IGSE when calculating power loss, in cores that experienced extended periods of steady flux, by taking into account the relaxation process of the boundary walls of a magnetic material. However,

as the IIGSE requires five additional non Steinmetz variables, this technique is unsuitable for most design purposes.

The Waveform Coefficient Steinmetz Equation (WcSE) was developed as a simple method of estimating core losses [97]. This technique creates a waveform coefficient c , which is defined as the ratio between the average value of a given non-sinusoidal and sinusoidal waveform.

$$P_{fe} = V_{core} c K f^{\alpha} B_{max}^{\beta} \quad (3.16)$$

It is shown in [97] that the waveform coefficient between a sinusoidal voltage and a square wave voltage, with the same peak flux density and a 50% duty cycle, is

$$c_{Sq} = \frac{\pi}{4} \quad (3.17)$$

For this to work, both signals must have the same peak flux density. As a square wave voltage only needs an amplitude of $2/\pi$, of an equivalent sine wave, to induce a flux wave with the same voltage; the core losses induced by a square wave with the same peak voltage as a sine wave also need to be scaled up. As such, (3.16) could be re-written as

$$P_{fe} = V_{core} c_{Sq} k f^{\alpha} \left(\frac{\pi}{2} B_{max} \right)^{\beta} \quad (3.18)$$

Which is equivalent to using the value of $k_v = 4$, rather than 4.44, to calculate the peak flux.

All of the methods mentioned above suffer from two distinct limitations. The first is that they do not take into account DC biasing in the core. The second is that they use a single set of Steinmetz parameters across all conditions, even though these are known to change with frequency. This latter problem was examined in [89], which proposes a new method for calculating loss in a square wave excited core with a duty ratio other than 0.5. The method essentially splits the excitation waveform into two sections, associated with the positive and negative phase of the square wave, and solves them independently using WcSE before summing the resulting losses. Each section is treated as half of a waveform with a 50% duty cycle and a different frequency. Reference [89] then proposes curve fitting loss data, in the manufacturer's datasheet, to define α and β as functions of frequency.

As DC biasing is not anticipated in this design, this issue can be neglected. In addition, as this thesis is concerned only with evaluating the viability of technology based on the cascade transformer rather than development of a full working prototype, no real world materials will be investigated in the level of detail that would require variable values of the Steinmetz parameters.

3.7.1 Comparison of Loss Calculation Methods

None of the equations, described in the previous subsection, can be verified without a comparison to results obtained from physical experimentation. However, this is outside of the scope of this work. Instead, each of these equations were compared to each other, and to MagNet finite element analysis software package.

MagNet, like all other commercial software packages, do not publish details about how values are calculated. However, it is known that MagNet calculates core losses during post processing, based on the SE constants. It is likely that MagNet bases its calculations on one of the equations described in the previous subsection. MagNet is able to apply this equation to each finite element, rather than to the core as a whole. Doing this makes MagNet more accurate than applying equations by hand could ever be.

A transformer was designed, based on arbitrary values, and losses were calculated using the SE, MSE, GSE, IGSE, and WcSE. The excitation voltage was also decided on arbitrarily. MagNet was used to simulate this transformer in both 2D and 3D. The parameters used in this investigation can be seen in Table 3.1, and a picture of the transformer can be seen in Figure 3.6. The results obtained, using the different methods, are listed in Table 3.2.

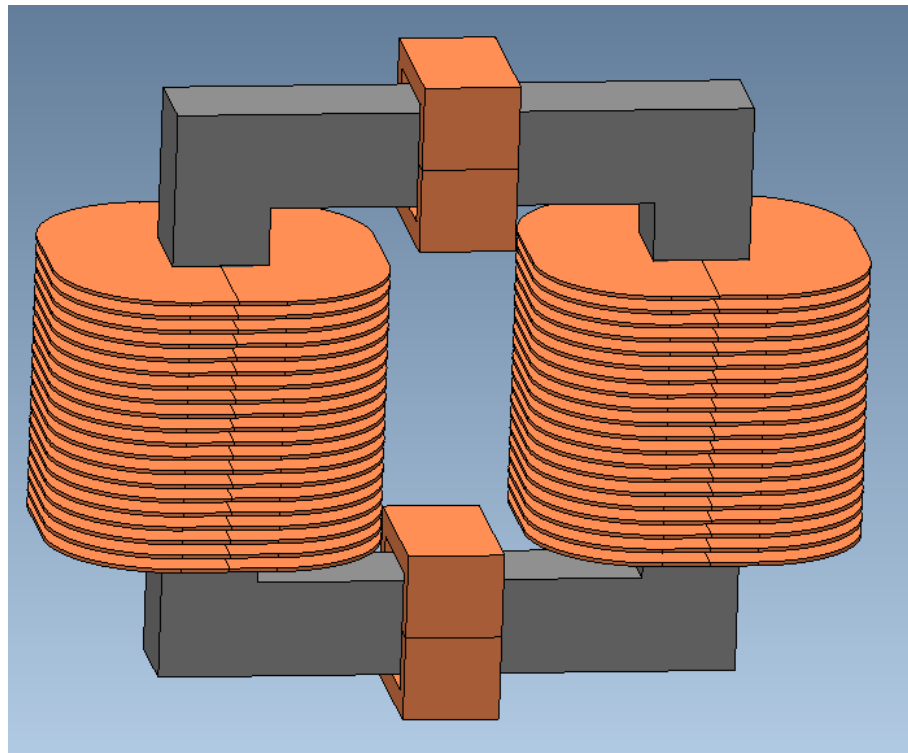


Figure 3.6. The transformer core that was simulated in MagNet. The limbs and yokes all have an outside length of 240 mm, and an inside length of 160 mm. There is a primary winding wrapped around both of the yokes, and secondary windings wrapped around the limbs.

Table 3.1 Parameters for core loss calculations.

Parameters	Values
Flux Path Length	0.8 m
Core Width	40 mm
K	2.3
α	1.32
β	2.1
Maximum Voltage	400 V
Maximum Current	250 A
Frequency	100 kHz
Relative Permeability	1,000

Table 3.2 Loss predictions according to different methods.

Sine Wave Excitation	
2D Simulation	80.8 W
3D Simulation	54.9 W
SE	49.5 W
Square Wave Excitation	
2D Simulation	186 W
3D Simulation	118 W
SE	113 W
MSE	24.8 W
GSE	45.0 W
IGSE	126 W
WcSE	89.3 W

Table 3.2 shows a wide range of results attained using the different methods. Several observations are worth noting. First, in both cases, the two dimensional simulation produced results that are approximately 60% higher than those of the three dimensional simulation. Secondly, the Steinmetz equation produced a result that was quite close to the three dimensional simulation in both cases. Indeed, even when predicting square wave losses, the basic SE was closer to the results predicted by the 3D simulation than any of the other equations. Of the equations designed for non-sinusoidal excitation, the IGSE obtained the closest result to the 3D simulation. However, this is still less accurate than the unaltered SE. For these reasons, only the original SE, and losses calculated using simulations, will be used in the remainder of this thesis.

3.8 Thermal Considerations

As discussed in previous sections, the effects of a build-up of thermal energy could have catastrophic effects in the insulating and semi-conductor components of a power supply. For this reason, care must be taken to keep the operational temperature of the design to a minimum. It is possible that only passive cooling will be required. However, it is equally possible that a more detailed study will reveal that systems must be put in place to actively remove heat from some components. In either case, a detailed investigation into this issue is beyond the scope of this thesis, and mention of this issue is only made for the sake of completeness.

3.9 Outline of Conceptual Design

This chapter has discussed ways in which a 1 MV, 2 A power supply could be constructed, as well as listing a number of technical challenges that must be overcome in designing such a supply. Now, an overall design is established, upon which the remainder of this project will be based.

Not discussed in this chapter, is the challenge of connecting the

The power supply will be driven by an external power source that is capable of exciting multiple phases at a peak voltage of 400 V. The exact number of required stages is left to be decided when designing a prototype of this design. These voltages will then be amplified to 500 kV in a transformer stage. This transformer stage will consist of either ICTs or cascade transformers connected in parallel. In either case, the number of primary turns will be four, meaning that the secondary circuit will consist of 5,000 turns. These turns will be divided across 50 secondary windings, each consisting of 100 turns. The outputs of these windings are each connected to a voltage doubler, which are then connected in series to produce a voltage of 1 MV. Finally, these stacks are connected in parallel to reduce voltage ripple and so that the total load current can be drawn. The transformer stages and rectifier stage will be insulated using either SF_6 gas or vacuum, to be decided based on the outcome of the research carried out in this thesis.

The matter of cooling the power supply is left to the prototyping stage of project development. The remaining chapters of this thesis will focus on: (a) establishing a suitable design for the secondary windings; (b) ascertaining whether vacuum insulation would be compatible with such an arrangement; and (c) determining the suitability of ICT and cascade transformer technology for a high density HV power supply.

Chapter 4

Secondary Windings

Based on initial analysis, it was decided in the previous chapter that power supply designs based on the conventional, solid-cored transformer would be assessed throughout the remainder of this thesis. This chapter outlines a design for the secondary windings of a power supply; specifically one based on PCB technology, similar to that used in the CTT [4], [5]. The assumption is made that the secondary windings and conversion to DC output will be the same regardless of the design of the core.

First, the relative merits of constructing the windings from PCBs, rather than wound wire as is conventionally used, is discussed. This leads to an examination of the current and thermal limitations of PCBs. An extensive investigation into the voltage handling capabilities of a PCB winding has been undertaken. This consists of a combination of simulations and experiments.

Finally, conclusions are drawn about the relative merits and limitations of using PCB based technology to construct the secondary windings, and suggestions for future investigation into this field are proposed.

The primary and auxiliary windings will need to handle very high currents, and will have few turns. This makes them unsuitable for construction from PCBs. Instead, they will be constructed using conventional winding methods. As a significant body of work already exists, detailing the design of conventional windings, this thesis will not investigate this subject further. For this reason, the remainder of this chapter will be devoted, exclusively, to PCB based transformer windings, for use in the secondary windings.

4.1 Advantages of Using PCB Windings

PCBs consist of a number of conductive areas, typically made of copper or gold, etched onto the surface of a board. These conductive areas are usually subdivided into two categories. These are pads, where electronic components are mounted to the board, and tracks, which

effectively connect the pads. The thickness of the conductive area is determined by the copper weight, and is usually measured in $ozft^{-2}$ [98], with 1 $ozft^{-2}$ being equivalent to a copper thickness of 35 μm . Though the board can be made from a number of materials, the most commonly used is fiberglass. Specifically, FR-4 [98] is often used due to its strong rigidity and heat resistance. Over each surface of the board, a thin insulating film, known as a solder mask, is often applied. This is primarily intended to protect the copper and prevent solder bridges occurring during the construction process. This is typically made from a polymer, such as Carapace [99]. Other materials are now being used to manufacture PCBs with interesting properties, for example: polyamide is used in flexible PCBs [98]; and Teflon is being used for circuits designed for ultra-high frequency applications [100]. As well as surface tracks, many PCBs now have tracks routed inside the board itself, creating internal layers. It is not uncommon for PCBs to have upwards of 16 layers, including the two surface layers [101].

The conventional method, of making transformer windings, is to wrap lengths of wire around the core. In theory, this should be a straight forward process, and there are indeed a number of merits to this technique, namely that the windings can be made to be very space efficient, and can be added to the transformer after the core has been fully constructed if a bobbin is not used. However, there are also drawbacks to the application of conventional windings. Firstly, it is an exact and time consuming process to wrap windings around a transformer core; this is usually carried out by machines designed to maintain exact spacing. Another issue is insulating the windings. Each wire must be insulated from those around it, to avoid shorting the windings, this must be applied to the wire before the transformer is fabricated, thus adding an additional stage and greater complexity to the power supply construction. Finally, if there is a fault in any part of the windings, the whole assembly must be disassembled and replaced, before the power supply can be used again. These issues should not present a serious problem in well-established technologies, where designs have evolved to be highly reliable. Indeed, transmission and distribution transformers use conventional windings and are expected to function, with 99.998% efficiency, for fifty years or more. However, the work in this project is intended to be used in the development of a prototype for a new type of power supply. The requirement is that windings can be handled as discrete components, and added to, or removed from, the design with relative ease.

An inductor can be made by printing the tracks of a PCB in a spiral, this method is often used to create the antenna in radio-frequency identification circuits, and a transformer consists of two or more inductors sharing magnetic flux. In this way, the windings of a transformer can be made by winding the tracks of a PCB in a spiral around a hole, allowing the PCB to be placed around the transformer core. PCB based windings are already commonly used in high frequency power electronic converters [50], [51], [102] and were

used by Cross, in his design for an ICT [4], [5], as they are very thin; thus allowing many of them to be stacked on top of each other in a relatively small space. Further to this, if the insulating medium is not electronegative, and thus is suitable for DC components, the HV secondary electronics can be mounted directly to the same PCB that the windings are printed on, thus reducing the overall complexity of the design. In addition to these features, PCBs are also quite rugged and relatively economical to produce. These are all features that lend themselves well to the prototyping nature of this project.

Cross's original design consisted of numerous LV windings printed on each board. The outputs of these windings would then be rectified and the voltage doubled, and then connected in series to produce a HV output. This arrangement is shown in Figure 4.1. The main reason for this was likely that it allows for the use of off-the-shelf, low voltage surface mount diodes and capacitors. However, now that HV surface mount components are widely available, two alternative designs are proposed that use only one set of HV components and either one or two sets of windings per board. These are shown in Figures 4.2 and 4.3 respectively

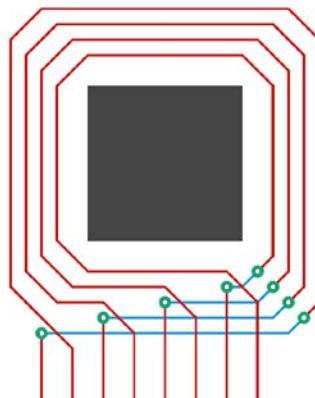


Figure 4.1 The winding arrangement used by Cross in his ICT design. Note that each winding consists of one turn. Several windings share a PCB, with their rectified outputs connected in series.

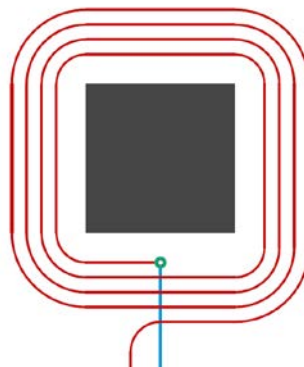


Figure 4.2 A PCB based winding arrangement that consists of a winding, with numerous turns, circling a core. There is only one winding per PCB and one rectification circuit.

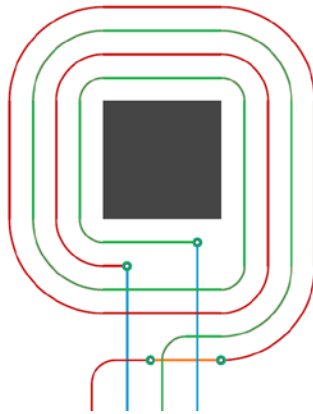


Figure 4.3 A PCB based winding arrangement that consists of two windings, each with numerous turns, circling a core, allowing either 'plain disk' or 'interleaved' connection.

The design in Figure 4.2 is the simplest design, consisting as it does of a single coil printed onto both surfaces of the board. The coil component of this design has only two connections, which are connected directly to the voltage doubler. The design shown in Figure 4.3 is slightly more complex, as the winding element consists of two interleaved windings. These windings can either be connected in series (interleaved) or parallel (plain disk), depending on whether a high voltage or current is needed. There is, however, a design issue that must be addressed; when the two windings are connected in series, parallel turns will need to be insulated from half of the overall voltage of the board. That is to say, in a board that is designed to produce 10 kV, parallel windings will need to be insulated against 5 kV. The Cross design, as shown in Figure 4.1, also has drawbacks. As it consists of numerous separate windings, each consisting of one turn, each winding must pass through the board using a via. This will increase the inductance of the board by an unknown amount. In addition to this, each single-turn winding will need its own secondary HV circuit. This will significantly increase the number of secondary circuits needed, in turn increasing the required space on the board.

The secondary windings must be able to withstand voltage and current loads conditions during continuous operation and under short term fault conditions (e.g. primary voltage surges or short circuit on the secondary). The ability of PCBs to withstand these will be discussed in the following sections.

4.2 Current Limitations

There are two problems associated with the current in the windings of a transformer. Firstly, there is the matter of power loss associated with electrical currents in conductors. Power

lost in a conductor P_{cu} is directly proportional to the square of the current passing through it, as can be seen in

$$P_{cu} = I^2 R \quad (4.1)$$

where I is the RMS of a sinusoidal current, or the peak of a square current, in the conductor; and R is the total resistance of the conductor. The power lost in the transformer windings, by definition, reduces the efficiency of the device.

The second, and more pressing, problem is that the power lost in the windings is converted into heat. Sufficient heat could damage the components of the circuit. In order to avoid this, generated heat must be removed from the system or, at least, kept to a minimum.

The resistance of a wire R can be calculated, under a direct current, as

$$R = \frac{l}{S\sigma} \quad (4.2)$$

where l is the length of the windings in meters; S is the cross sectional area of the windings; and σ is the conductivity of the windings in Siemens. For each PCB secondary winding, l can be calculated using

$$l = 4Nt_c + 2\pi N \left\{ r + \frac{(N/N_L - 1)(g+w)}{2} \right\} \quad (4.3)$$

where N is the number of turns; t_c is the thickness of the transformer core; r is the distance between the core and the inside track; N_L is the number of layers of windings; g is the distance of the gap between turns; and w is the width of each track (See appendix B for derivation). The cross sectional area can be calculated using

$$S = t_t w \quad (4.4)$$

where t_t is the thickness of the tracks. An alternating current induces a magnetic field inside the wire, which in turn acts against the excitation current, in what is known as the skin effect. This effectively increases the effective resistance of the wire R_{ac} such that [35]

$$R_{ac} = R \left\{ 1 + \frac{(r_0/\delta)^4}{48 + 0.8(r_0/\delta)^4} \right\} \quad (4.5)$$

where r_0 is the radius of the wire; and δ is the skin depth which can be calculated using

$$\delta = \frac{1}{\sqrt{\pi f \mu_0 \sigma}} \quad (4.6)$$

where μ_0 is the permeability of free space. The relationship between skin depth and frequency, in copper, is shown in Figure 4.4. At a frequency of 100 kHz, the skin depth of

copper is 210 μm , which is several times the thickness of the conductive layer of a PCB. Indeed, the skin depth of copper is not reduced to 35 μm until a frequency greater than 3.58 GHz is applied. Therefore, the skin effect can be neglected when calculating the loss in the secondary windings.

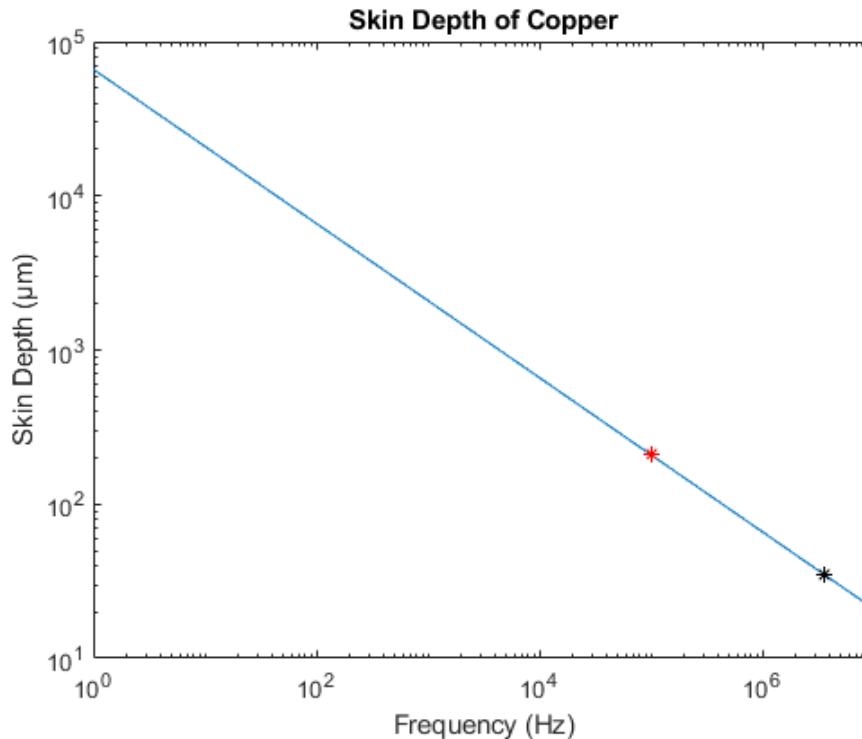


Figure 4.4 The relationship between skin depth and current frequency in copper. The skin depth at a frequency of 100 kHz is highlighted in red, and the frequency at which the skin depth drops below the typical thickness of the plating on a PCB is highlighted in black.

4.3 Voltage Limitations

The Secondary Windings are expected to operate at a high voltage, at least 10 kV across each PCB would be ideal, which will lead to a high potential difference between individual turns (100 V if 100 turns are used). It is, therefore, necessary to ascertain if the boards are capable of handling these high voltages. To do this, a number of practical experiments have been undertaken.

As PCBs typically use a solder mask to help insulate the tracks; breakdown experiments between tracks will necessarily be destructive because of the damage caused to the solder mask by electrical breakdown. Performing a breakdown experiment across a whole winding would be costly and inefficient, as it would be expensive to manufacture a sufficient number of PCBs to gain meaningful data. Instead, it was decided to examine individual elements of the windings separately, as shown in Figure 4.5. This would allow for a more precise view of the breakdown characteristics of the windings.

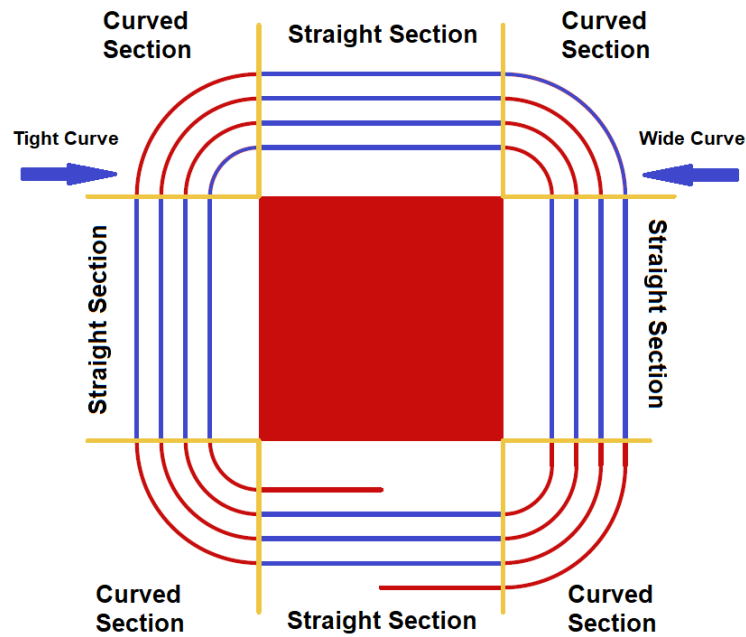


Figure 4.5 The PCB windings divided into straight and curved sections. Sections tested are indicated in blue.

Each winding can be seen as a collection of straight sections of track, running parallel to each other, separated by curved sections of track. Each curved section has a constant radius and is separated from the tracks on either side by a constant distance.

The first areas to be examined are the straight sections. These are modelled in this investigation by two straight tracks, each with a thickness of 0.5 mm, running parallel to each other and 0.5 mm apart. The ends of these tracks conform to the Base electrode profile, which essentially consists of a straight section connected to a rounded edge that has a constant radius. The Base profile was selected, in preference to the Rogowski and Bruce profiles, as it has been shown to have the largest area of uniform field when applied to plate electrodes [103]. The track layout of these samples is shown in Figure 4.6.



Figure 4.6 Track layout for a test sample testing the electrical breakdown strength of sections of the secondary windings where straight lengths of track run parallel to each other.

In order to examine areas where the track is curved, it is necessary to understand that these sections effectively consist of numerous quarter circles, with the tracks closest to the core having the smallest radius, and the tracks on the outside of the winding having a larger radius. In this way, these areas were modelled with two different types of sample. The first,

which can be seen in Figure 4.7, represents the tracks with the smallest radius; while the second, shown in Figure 4.8, represents tracks on the outside of the design. In both cases, the same track endings are used, to help place electrodes and reduce the chances of discharge at the ends of the track, and positioned in the same locations relative to each other. These track endings also conform to the Base profile.

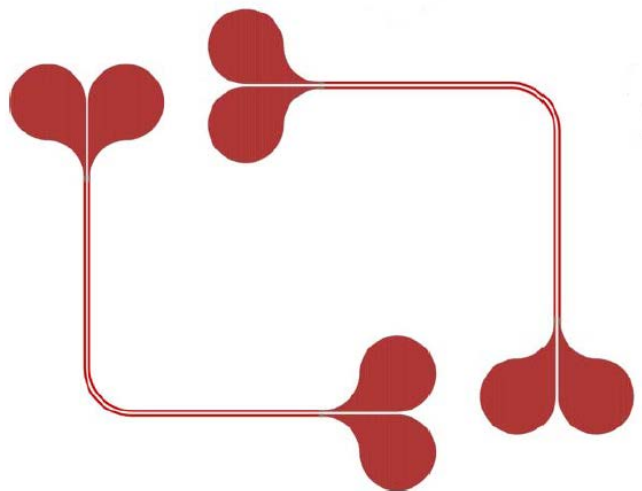


Figure 4.7 Track layout for two test samples testing the electrical breakdown strength of sections of the secondary windings that curve around the core at the centre of the winding.

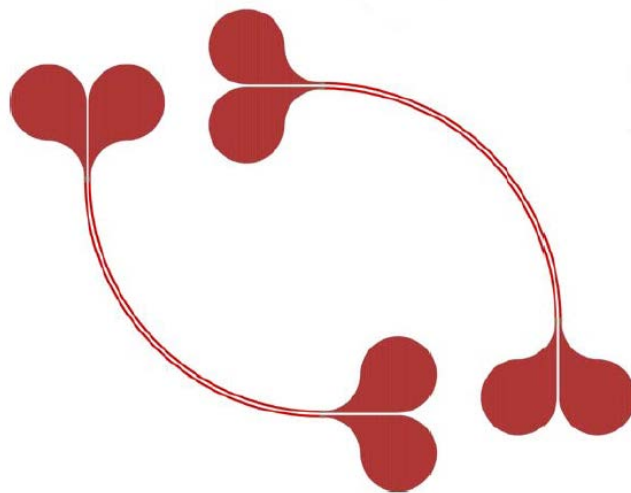


Figure 4.8 Track layout for two test samples testing the electrical breakdown strength of sections of the secondary windings that curve around the core on the outside of the winding.

4.3.1 Simulation

Before practical experiments were carried out, simulations were performed to calculate the electrical field strength between the tracks of each sample. This was important in ascertaining whether or not there were any inconsistencies in the field between the two tracks that could lead to more breakdowns occurring in certain areas.

The results of the 3D simulations were unclear. This is because the geometry of the area of interest is 500 μm wide, but only 55 μm high. Even using localised fine meshing, 3D simulations were found to be unsuitable for simulating relatively high detail in small areas of relatively large volume. For this reason, the remainder of the simulations were carried out in 2D and so only 2D simulations are shown in this section. The simulations were static, meaning a 1KV DC voltage was applied to one track whilst the other one was grounded.

The first simulations carried out were of the cross section of two tracks. This was useful in predicting how breakdown would occur between the tracks of a PCB-based winding. The different sample shapes were then simulated, to determine what effect the curvature of the windings would have on the electric field between the tracks. Finally, a small discrepancy was added to one of the tracks on a straight section of winding, to see how imperfections in the manufacturing process might affect breakdown.

4.3.1.1 Cross Section

In theory, the tracks should have a rectangular profile and be covered with an evenly distributed solder mask, as shown in Figure 4.9. If this were the case, the electric field around the tracks would resemble that shown in Figure 4.10. A close up on the edge of one of the tracks is shown in Figure 4.11.

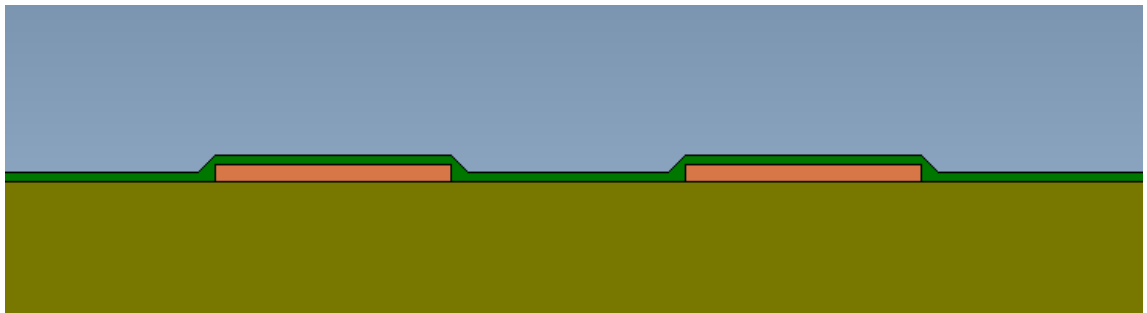


Figure 4.9. Idealised cross section of a sample. The FR4 board is shown in brown, the solder mask in green, and the copper tracks in orange.

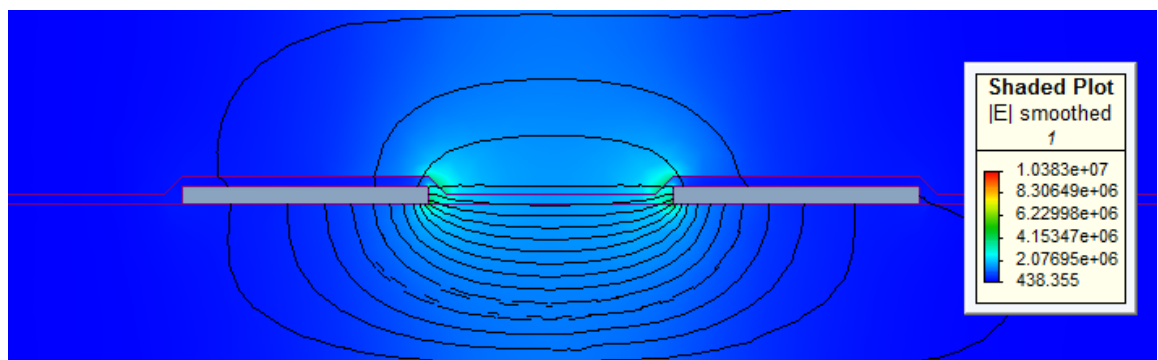


Figure 4.10. Electric field around the cross section of an idealised sample.

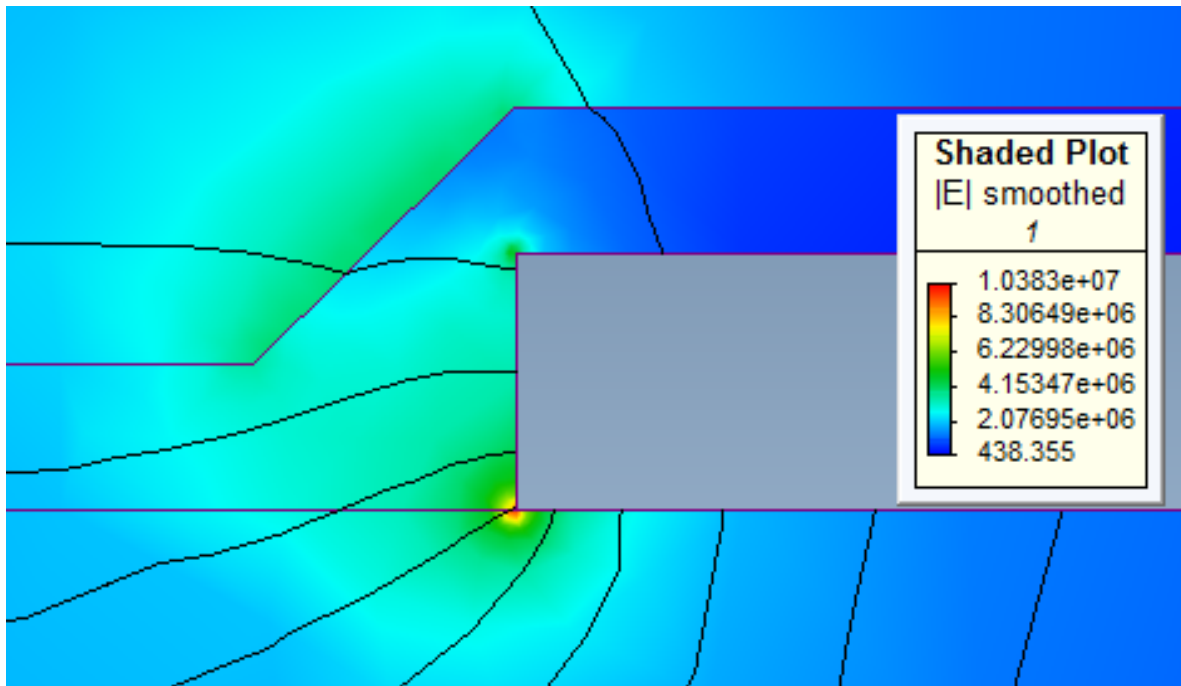


Figure 4.11. Close up of the electric field around the track of an idealised sample.

In this case, the greatest field strength is at the triple point between the board, the solder mask, and the track. This is as one would expect based on the literature [24]. There is also an area of high electric field around the top corner of the track. As the solder mask has a higher dielectric constant than the air around it, this leads to an enhanced field on the surface of the diagonal edge of the solder mask. In this case, the enhanced field is approximately twice as strong as the average field strength.

In practice, it is unlikely that PCB tracks will have such a neat profile. As the nature of the manufacturing process is unknown, it is impossible to predict exactly what the profile of the tracks will look like. Therefore, it is impossible to predict with any certainty the precise breakdown mechanism that will occur between the tracks. The electric field shown in Figures 4.10 and 4.11 should be used merely as an indication of what the field will look like. As the shape of the tracks is unknown, it is not certain that the points of high electric field strength, which appear at the top and bottom of the tracks, will exist in a practical sample. However, the high electric field on the surface of the diagonal solder mask is still expected, as its existence is dependant solely on the existence of the track, and not its exact profile.

The following sections will examine the affect that the sample shape has upon the electric field. To do this, two top down views of each sample will be examined, with elevations of $10\text{ }\mu\text{m}$ and $30\text{ }\mu\text{m}$ above the FR4 board. These correspond to the red and blue dotted lines respectively, as shown in Figure 4.12. These elevations were selected to show the electric field inside the solder mask above the board; and in the cross section of the track, solder mask, and air.



Figure 4.12. The elevations at which the simulations in the following sections take place. The elevation of the red line is 10 μm , while the blue line is 30 μm .

4.3.1.2 Narrow Straight

The first sample to be simulated was the one that represented straight sections of the track. An image of the electric field, 10 μm above the surface of the FR4 board, is shown in Figure 4.13. From this it can be seen that the electric field, between the straight sections of track, is constant. The field at the end of the tracks decreases gradually in strength as the copper conductors curve further apart. Figure 4.14 shows the ends of these samples in close detail.

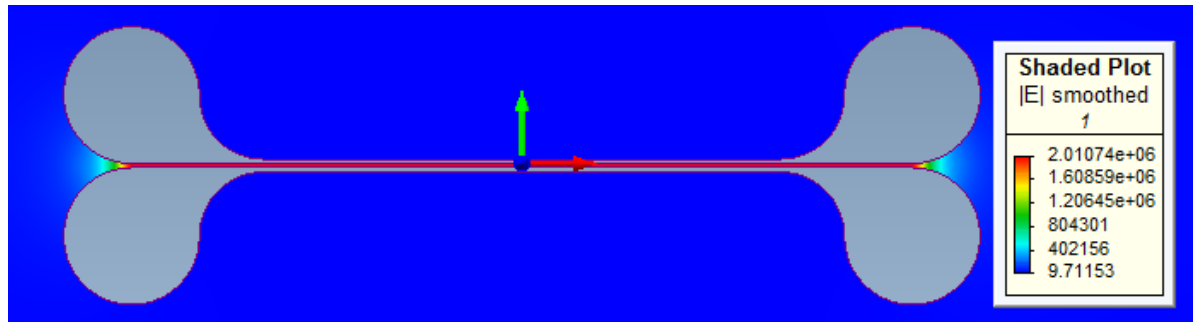


Figure 4.13. The electric field around the straight samples, at an elevation of 10 μm above the surface of the FR4 board.

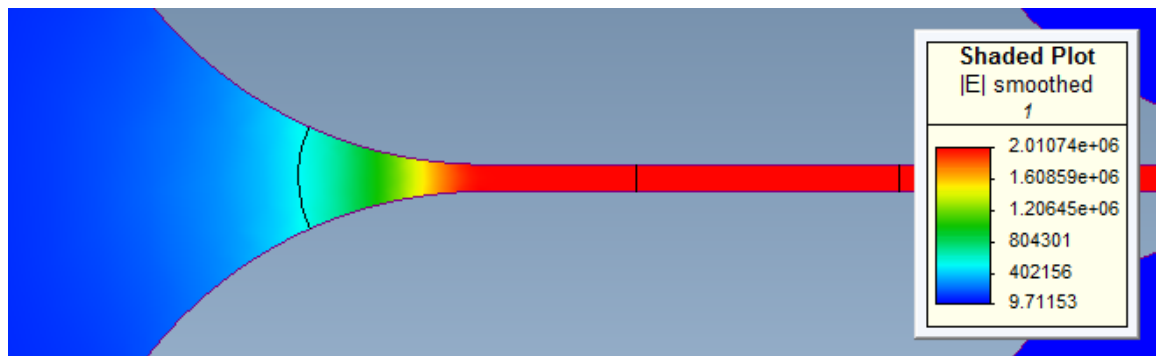


Figure 4.14. The electric field strength around the end of the tracks, 10 μm above the surface of the FR4 board. The black lines represent the flux function between the tracks.

The flux lines in Figure 4.14 show that the electric field around the curved sections of track bulge outwards, away from the high field density between the tracks, as one would expect. Also, the electric field, between the straight sections of the track, runs normal to the direction of the gap. This shows that the electric field between the tracks is uniform. The observed electric field strength, of approximately 2 MVm^{-1} , is in accordance with what should be

expected from a 1 kV potential across a 0.5 mm gap. Breakdown is unlikely to take place at this elevation, as the dielectric strength of solder masks is much greater than that of air.

Figure 4.15 shows the electric field simulated 30 μm above the FR4 board. Here the gap between the tracks is partially bridged by solder mask that, in accordance with the theory outlined in Section 3.4, suffers from a much lower electric field strength than the air around it. Similarly, Figure 4.16 shows the electric field strength in the solder mask, around the curved area of the electrodes. It should be noted that the magnitude of the electric field in the solder mask decreases at the same rate as the air around it. However, the magnitude of the electric field is much smaller.



Figure 4.15. The electric field around the straight samples, at an elevation of 30 μm above the surface of the FR4 board.

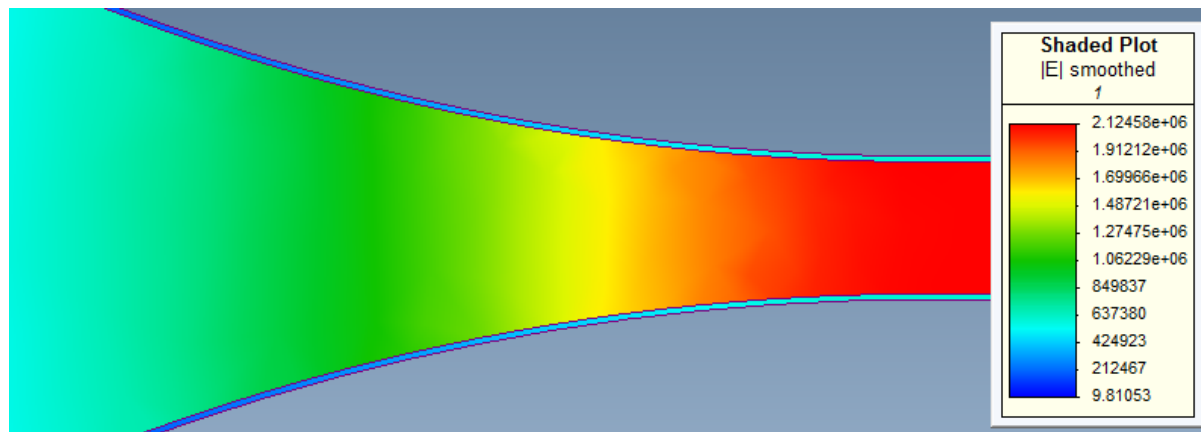


Figure 4.16. The electric field strength around the end of the tracks, 30 μm above the surface of the FR4 board.

It is difficult to predict the breakdown voltage of this sample, due to the complex nature of the insulation. If the breakdown strength of air is taken as 3 MVm^{-1} , theoretically breakdown should occur at 1.5 kV, notwithstanding the solder mask. However, in practice, the solder mask will prevent breakdown bridging the two tracks. It will only be when partial discharge in the air between the tracks damages the solder mask that breakdown will occur.

4.3.1.3 Tight Curve

The next simulation sample was one that represented the inside turns of the winding. A simulation of the whole model is shown in Figure 4.17. This model shows that the average electric field strength is almost identical to that of the straight lengths of track. This is intuitive, as the same potential difference is spread over the same distance. Also, as in the previous case, the electric field bulges out from the gap at the ends of the samples.

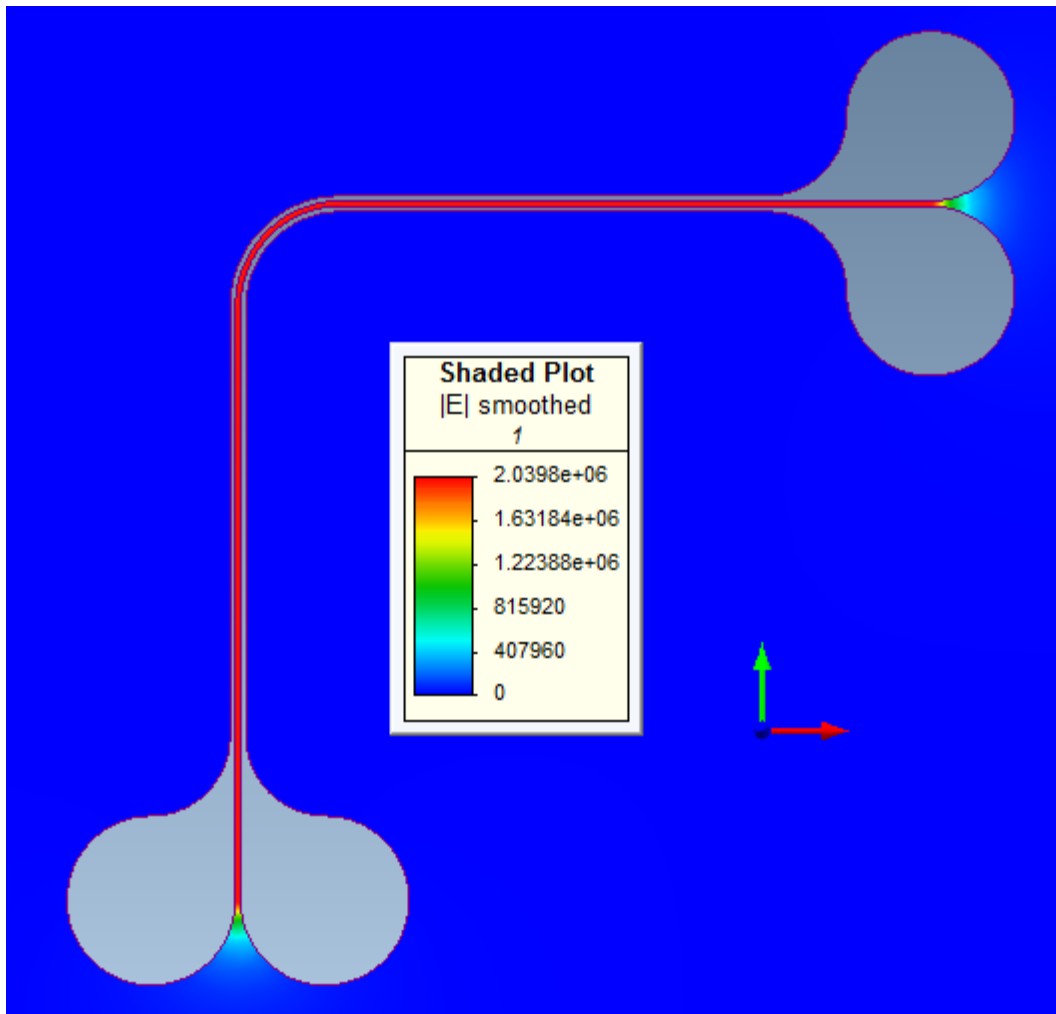


Figure 4.17. The electric field around the samples that represent the inside turns of the winding, at an elevation of 10 μm above the surface of the FR4 board.

Figure 4.17 shows that the electric field between the tracks appears consistent. However, Figure 4.18 demonstrates there is a slight difference in electric field strength between the inside and outside tracks of the curved section of the sample. This would imply that breakdown is more likely to take place on the inside edge of the curve, just outside of the solder mask. Although, as the difference in field strength is so small, it is likely that other factors will have a greater effect on the breakdown location. These other factors, such as manufacturing discrepancies, will be discussed later in this section.

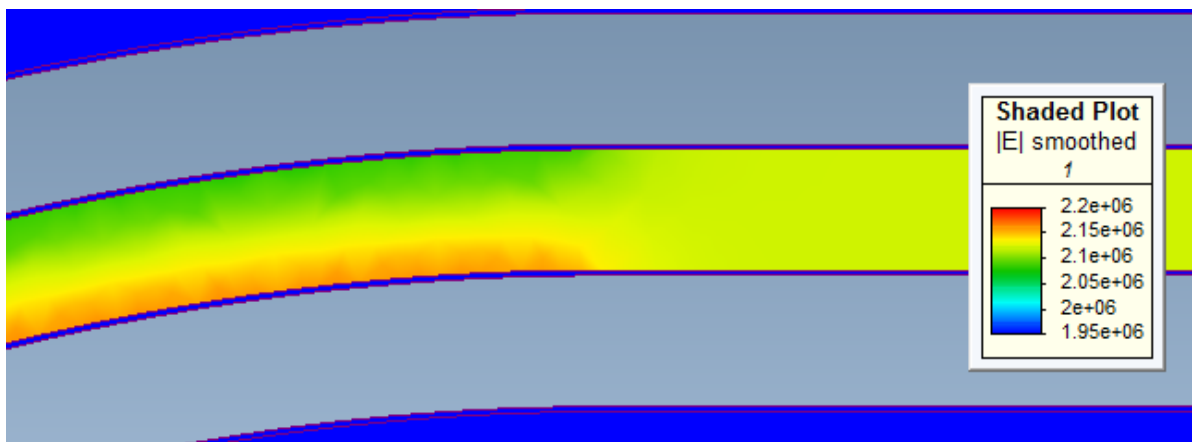
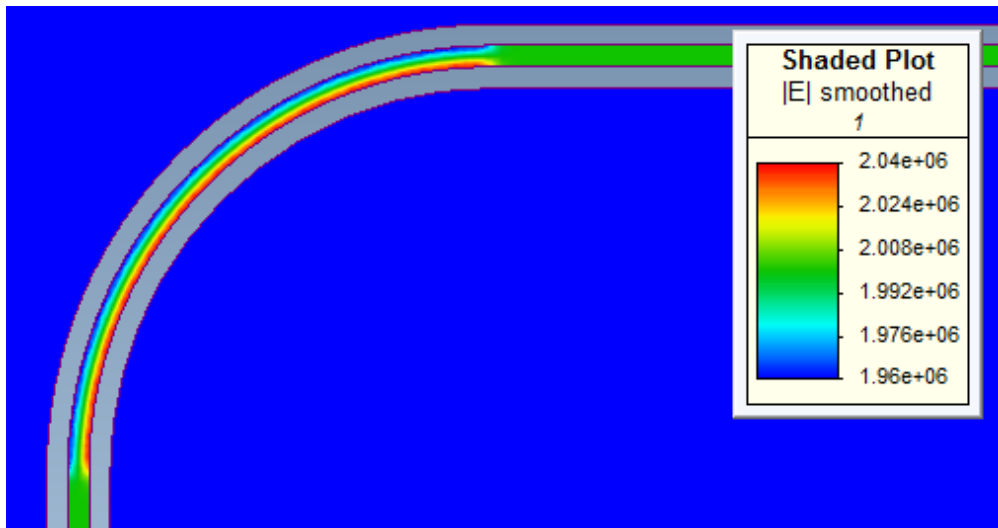


Figure 4.18. A close up of the electric field around the curve of the samples that represent the inside turns of the winding, at an elevation of 10 μm (TOP), and 30 μm (BOTTOM), above the surface of the FR4 board.

4.3.1.4 Wide Curve

The last simulation shows a curve that represents the turn at the outside of the winding. This can be seen in Figure 4.19. As in the previous two samples, the average electric field strength in the gap between the tracks is approximately 2 MVm^{-1} . The electrical field also bulges out around the ends of the track in a similar manner.

Figure 4.20 shows that again, like the previous sample, there is a slight discrepancy between the electric field on either side of the gap between the tracks. This is caused by the curve of the tracks. Unlike the last sample, the curve continues along the whole length of the tracks, apart from at the very ends. As the radius of the curve is much greater, the discrepancy is much smaller. This suggests that breakdown is equally likely to occur at any point along the curved length of the sample. Again, as the increase in the field strength is very small around the inside of the curve, it is more likely that breakdown will be brought about by manufacturing discrepancies.

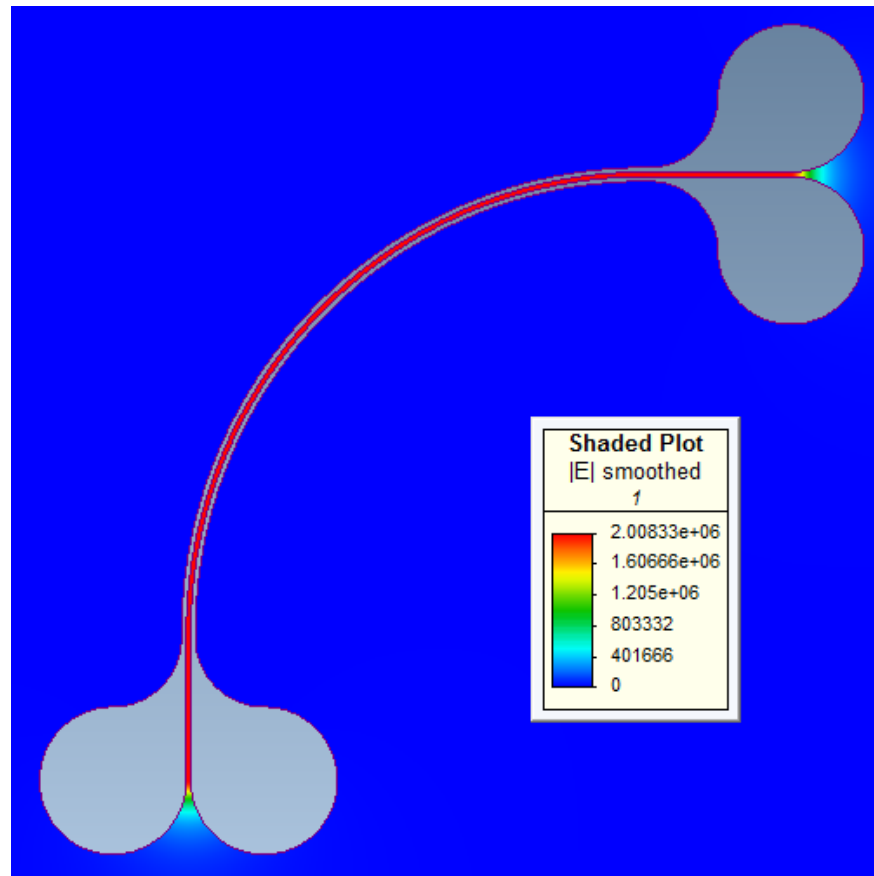


Figure 4.19. The electric field around the samples that represent the outside turns of the winding, at an elevation of 10 μm above the surface of the FR4 board.

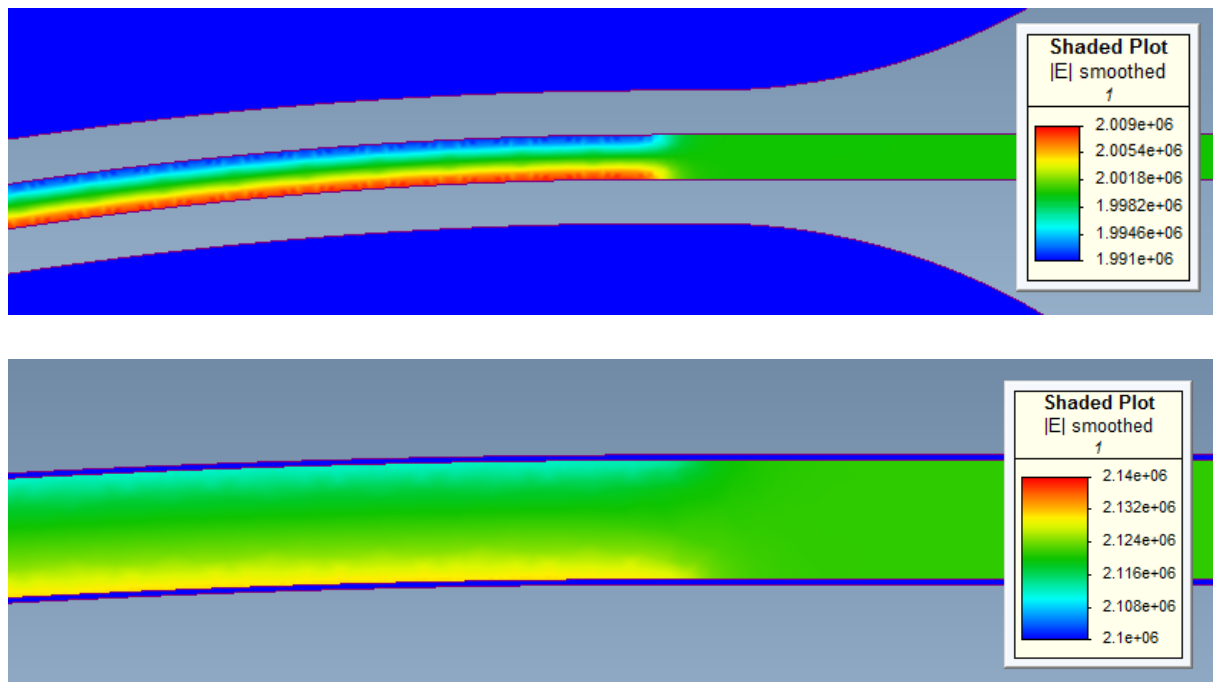


Figure 4.20. A close up of the electric field around the curve of the samples that represent the outside turns of the winding, at an elevation of 10 μm (TOP), and 30 μm (BOTTOM), above the surface of the FR4 board.

4.3.1.5 Imperfections

As has already been stated, the manufacturing process of PCBs is likely to lead to imperfections in the samples. These may be invisible to the human eye, but have a significant effect on the breakdown mechanism.

Figure 4.21 shows a small imperfection placed on the bottom track of the straight sample. The imperfection is semi-circular and has a radius of $1\text{ }\mu\text{m}$, making it invisible to the naked eye. When the bottom track is charged to 1 kV, the distortion caused by the electric field between the tracks is imperceptible on a macro level. This is demonstrated in Figure 4.22. However, from Figure 4.23 it can be seen that the field around the imperfection is greatly distorted. The field directly above the imperfection is 1.5 times stronger than the average field between the tracks. Therefore, breakdown is most likely to occur at this point between the tracks.

It is likely that the characteristics of all breakdowns between the tracks of a PCB are the product of microscopic imperfections in manufacturing.

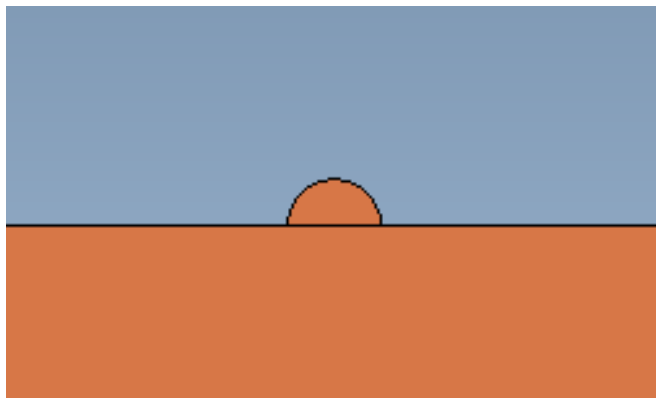


Figure 4.21. An imperfection placed on the bottom track of the straight sample, with a radius of $1\text{ }\mu\text{m}$.



Figure 4.22. The electric field around the straight samples, at an elevation of $10\text{ }\mu\text{m}$ above the surface of the FR4 board, with an imperfection on the edge of the bottom track.

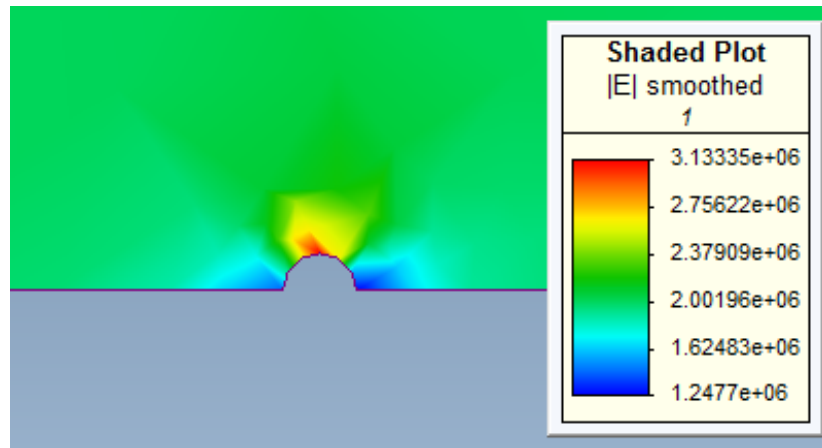


Figure 4.23. A close up of the electric field around the imperfection shown in Figures 4.21 and 4.22.

4.3.2 Experimental Setup

An experiment was devised that would subject the samples, discussed in the previous Section, to an increasing AC voltage. The experimental setup can be seen in Figure 4.24, a diagram of this setup is shown in Figure 4.25. The output of an arbitrary waveform generator (AWG), which was controlled via a PC, was connected to a Trek Model 10/10B High Voltage Amplifier. The HV output of the amplifier was connected to one electrode of the sample, the other electrode of which was connected to ground. The output of the AWG and the voltage monitoring terminal of the amplifier were connected to different terminals of an oscilloscope, to allow the voltage of the system to be monitored in real time, and to make sure the system was working correctly. The voltage and current monitoring terminals of the amplifier were connected to a PicoScope 2000, which in turn was connected to the PC so that it could record the voltage and current across the sample. The PicoScope had a sampling frequency of 10 MSs^{-1} . Finally, a camera was placed above the sample that would film the breakdown.

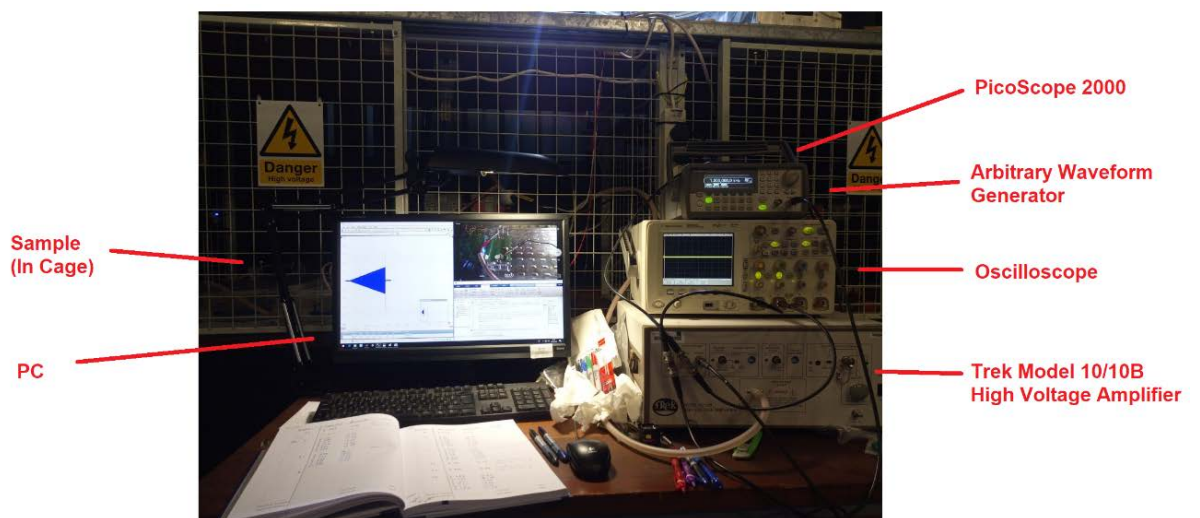


Figure 4.24. Experimental setup.

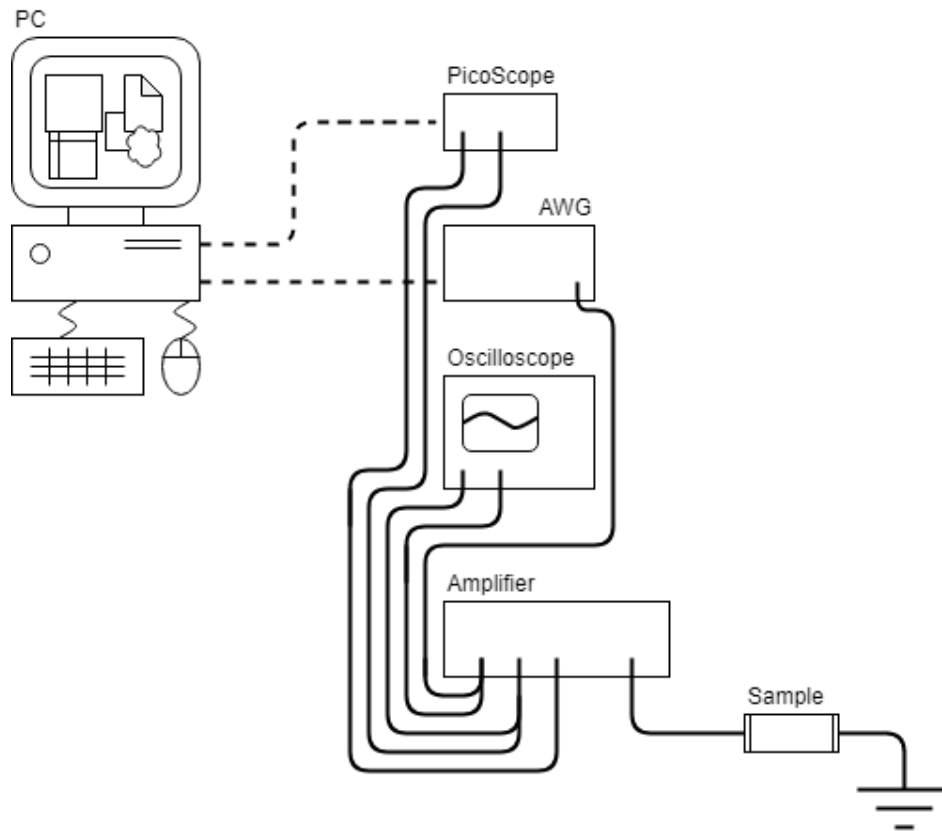


Figure 4.25 Diagram of the experimental setup.

When a sample was tested, an electrode was connected to each track. A MatLab script was written that would instruct the AWG to produce a sinusoidal signal, with a frequency of 1 kHz and a peak amplitude of 100 V, and then increase the signal amplitude, in steps, by 0.1 V every 0.02 seconds. The amplifier has a gain of 1,000, meaning that the voltage applied to the sample increases by 500 V every second. Once the voltage reached was sufficient to cause a breakdown across the sample, the current rise would trigger the circuit breaker of the amplifier and turn the HV output off. The voltage at which the breakdown occurred, as well as the voltage and current waveforms and a video of the breakdown, were recorded.

After each sample broke down, they were tested again to ascertain whether there was a noticeable difference in breakdown voltage. This was to ensure that the solder mask had indeed been damaged, and to evaluate what contribution the solder mask made to the dielectric breakdown strength of the sample.

Before any breakdown experiments were carried out, the voltage monitoring terminal and the HV output of the amplifier were compared, with no discrepancies found between the two. The samples were prepared by applying an insulating lacquer across the gaps in the exposed copper terminals at the ends of the tracks. This prevented flashover occurring through the air between the terminals, rather than through the solder mask between the tracks. Each experiment was performed on 25 different samples, in order to get a sufficient number of data points to perform Weibull analysis.

It should be noted that this experimental procedure does not conform to either IEEE or IEC standards for dielectric breakdown testing. Furthermore, no effort was made to measure or maintain the atmospheric air pressure, humidity or temperature, despite the experiments being carried out over several months in different weather conditions. For these reasons, the results obtained in this chapter cannot be considered the definitive breakdown voltages of PCBs, but nonetheless serve as a useful indication of these values. No deliberate steps were taken to measure corona discharge.

4.3.3 Experimental Data Analysis

It is generally accepted that electrical breakdown, much like mechanical breakdown, does not fit a standard distribution; which is characterised by an event probability decreasing symmetrically on either side of a peak mean value. This is shown, on a probability density function (PDF) in Figure 4.26. Instead, breakdown data has been shown to, much more accurately, fit the Weibull Distribution [104]–[109]. This is characterised, on a PDF, by a gradually rising leading edge and a rapidly falling tailing edge, also shown in Figure 4.26. The reason for this is that, although there are a wide range of voltages at which breakdown could occur, breakdown is practically guaranteed at a given maximal voltage.

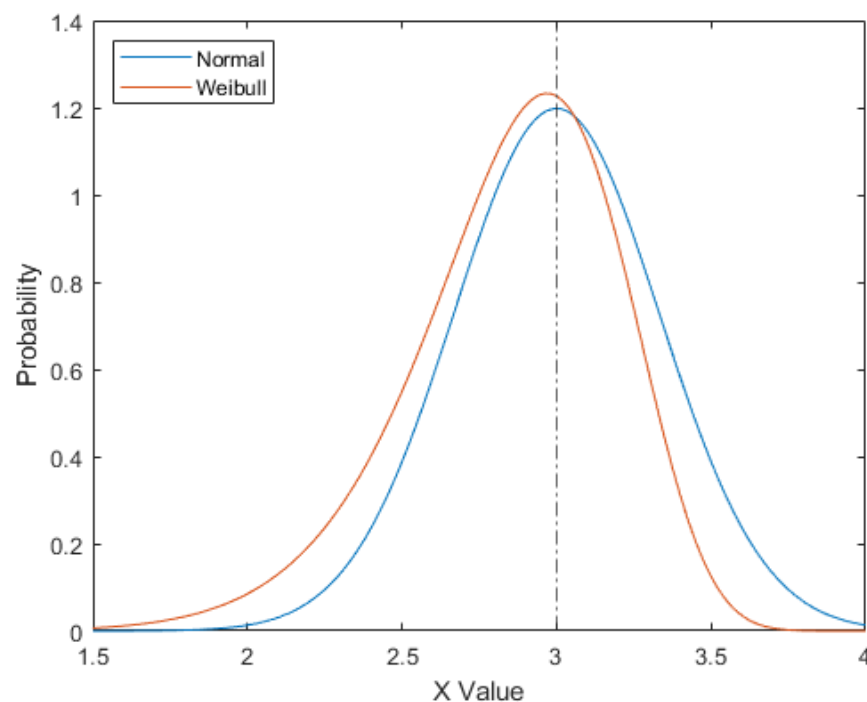


Figure 4.26 PDF showing an example of standard distribution (BLUE) and Weibull distribution (ORANGE). In both cases, the graphs are based on randomly generated data.

It is widely recognised that at least 25 data points are required to perform Weibull analysis. These data points can be plotted on a Weibull Plot, as shown in Figure 4.27, which is essentially a cumulative density function (CDF) plot. The horizontal axis represents failure

times, in \log_{10} scale, and the vertical axis represents cumulative probability. The data points are positioned on the vertical scale according to

$$Y_j = \ln \left(-\ln \left(1 - \frac{j-0.3}{n_w+0.4} \right) \right) \quad (4.7)$$

where j is the rank of each data point; and n_w is the total number of data points. The Weibull plot is designed such that, if the data does indeed match Weibull distribution, then the data points will fall in an approximately straight line. Once all breakdowns have been plotted, a line of best fit can be applied to the data points; as can probability lines, which show the boundaries that data points must fall into in order for Weibull distribution to be considered valid for a given level of certainty. Typically 95% is used. From this Weibull plot, two parameters can be estimated: the Scale Parameter, the voltage at which the line of best fit crosses 63.2% probability; and the Shape Parameter, which is the reciprocal of the gradient of the line of best fit. Strictly speaking, Weibull distribution is also characterised by a third parameter, known as the Location Parameter but, for the purposes of breakdown analysis, the Shape and Scale Parameters are sufficient and the location parameter is typically omitted.

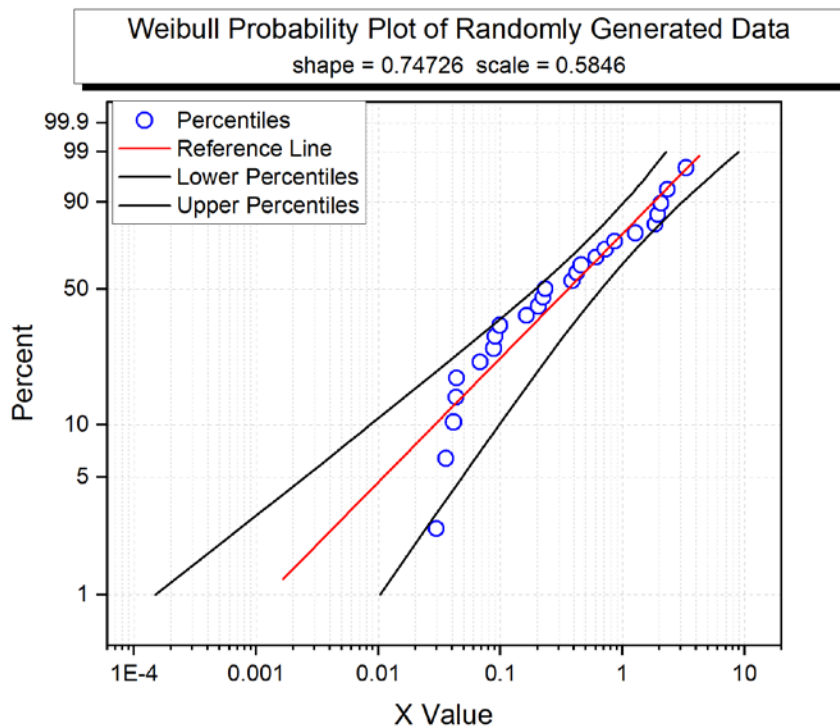


Figure 4.27 An example of a Weibull plot. The data points are the same as those used to generate the Weibull PDF in Figure 4.26. The line of best fit is shown in red, and the 95% certainty lines are shown in black.

4.3.4 Straight Section

The first samples to be tested were the ones representing straight sections of track. Each sample was, in turn, connected to the experimental setup described in the section 4.3.2, before an increasing voltage was put across them. At around 4 kV, corona discharge would become clearly visible between the two tracks of the sample, as shown in Figure 4.28, with full breakdown typically occurring around 4.7 kV (Figure 4.29). For the sake of clarity, it is possible that corona discharge was induced below 4 kV. However, as this was not visible to the camera used, and it does not appear to have effected the measured results, this potential corona discharge is omitted from further discussion.

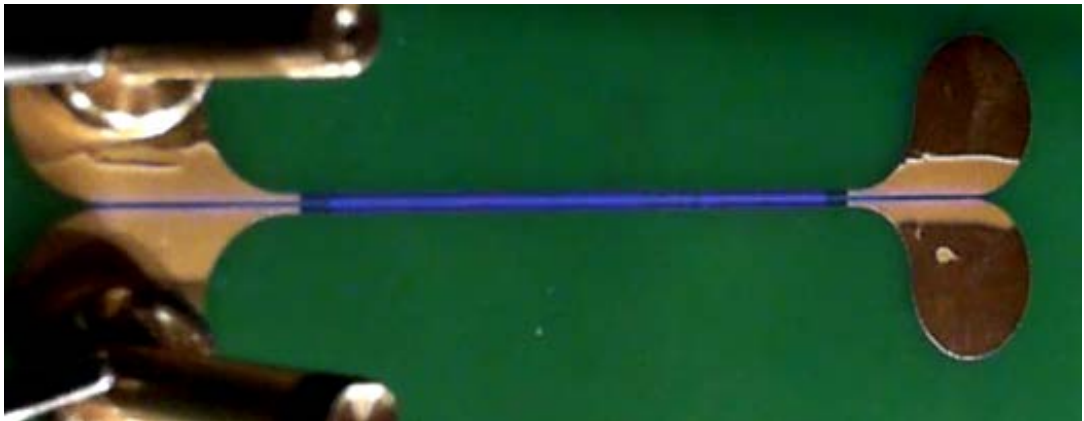


Figure 4.28 Corona discharge is visible in the form of the blue light between the two straight lengths of track that are printed 0.5 mm apart.

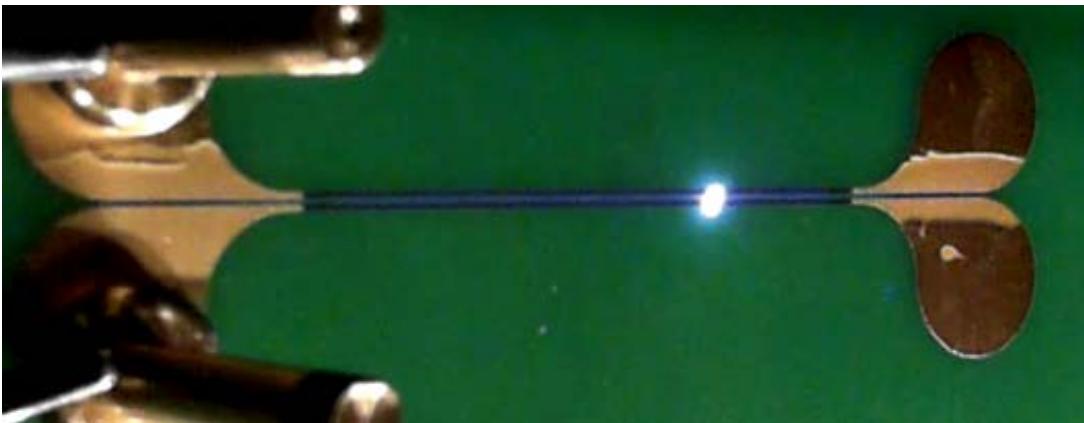


Figure 4.29 Breakdown occurring between two straight sections of track, printed 0.5 mm apart.

The effects of the visible corona discharge are evident in the current output of the amplifier; in Figure 4.30, it can be seen that when the voltage rises to 4 kV, the current rapidly increases to 3 mA. This is because electrical charge is passing between the tracks, thus forming a small electrical current.

Similarly, the breakdown between the tracks can also be seen in the voltage and current output of the amplifier. Figure 4.31 shows the same data as shown in Figure 4.30, only

zoomed into the time at which breakdown occurs. In this case, the instant at which breakdown occurs can be seen as a rapid increase in current. Once the current reaches a threshold of 13.75 mA, the circuit breaker in the amplifier opens, thus disconnecting the power across the sample. The voltage across the sample can be seen to decrease over the following power cycles, as the capacitors in the amplifier discharge, before the voltage and current disappear completely.

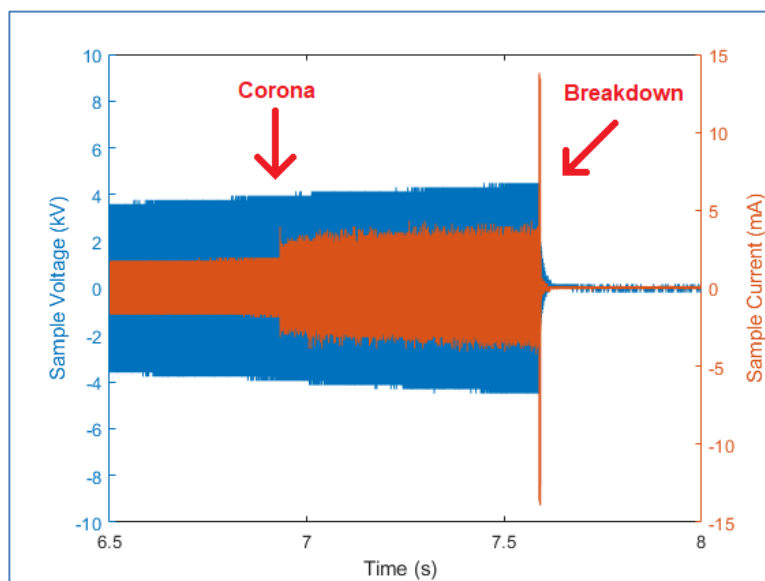


Figure 4.30 The voltage and current waveforms of the output of the amplifier when corona becomes clearly visible. Note the sudden increase in current when the voltage reaches 4 kV and corona begins to occur.

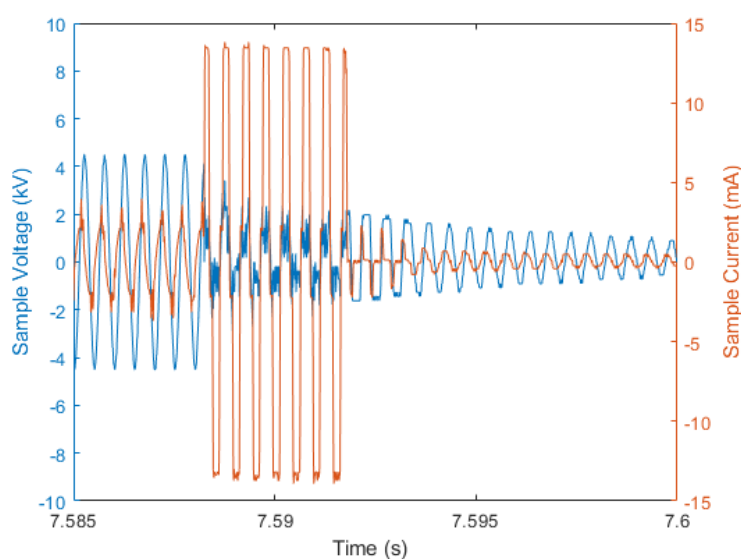


Figure 4.31 The voltage and current waveform of the output of the amplifier when a breakdown occurs. Note the rapid rise in current as a conductive path of plasma appears when breakdown occur.

After each experiment, two holes appeared in the solder mask where the breakdown occurred, like the ones shown in Figure 4.32. It is clear that the solder mask is irreparably damaged during the course of the first breakdown, thus forming a complete air path between the tracks. The electric current passes through this air path in all subsequent experiments. This is in contrast to what was simulated, where it was predicted that a conduction path would form between in the fibreglass board and the solder mask.

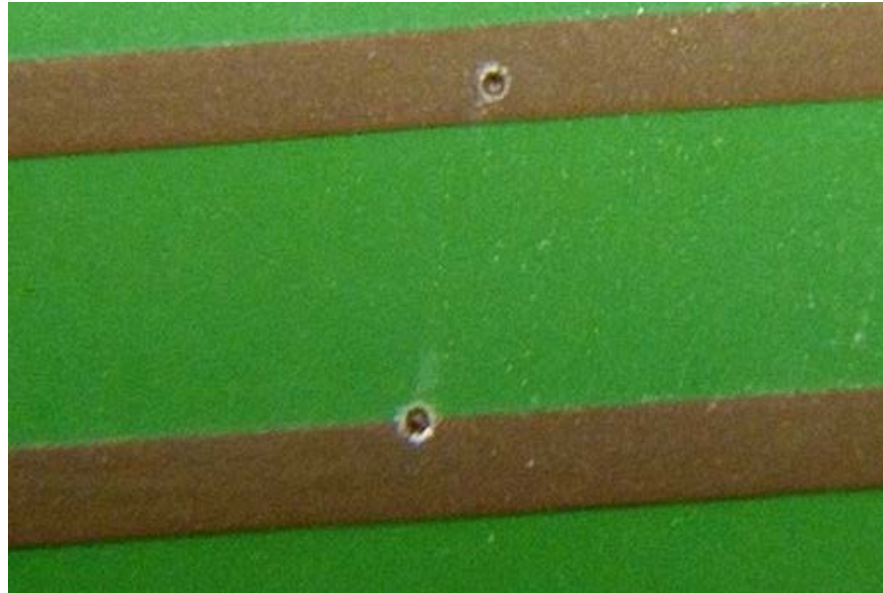


Figure 4.32 An example of the holes that appeared in the solder mask after breakdown occurs. The tracks in this sample are printed 1.5 mm apart.

The experiment was repeated, on each sample, after the first breakdown. This was to test the breakdown voltage when there was no solder mask, and also to ensure the solder mask had properly broken down. In the vast majority of cases, the sample would breakdown in the same place as in the first experiment, just at a lower voltage. Occasionally, the voltage would continue to rise to close to the voltage of the original breakdown before breakdown occurred in the same place. This implies that the solder mask was only partially damaged in the first breakdown experiment. However, even more occasionally, the second breakdown would occur in a second location or breakdown would occur in two separate places in the first experiment, implying that the solder mask on the sample may have been damaged prior to the experiment being undertaken.

The voltages of each breakdown are recorded in Appendix C and plotted, using a Weibull plot, in Figure 4.33. From the Weibull plot, it can be seen that the scale parameter of this dataset is 4.72, and the shape parameter is 16.7, meaning that breakdowns typically occurred with a peak voltage between 4.5 kV and 5 kV with relatively little deviation. This is certainly greater than the 100 V expected between adjacent windings in a single spiral design, but short of the 5 kV expected between windings in an interleaved design.

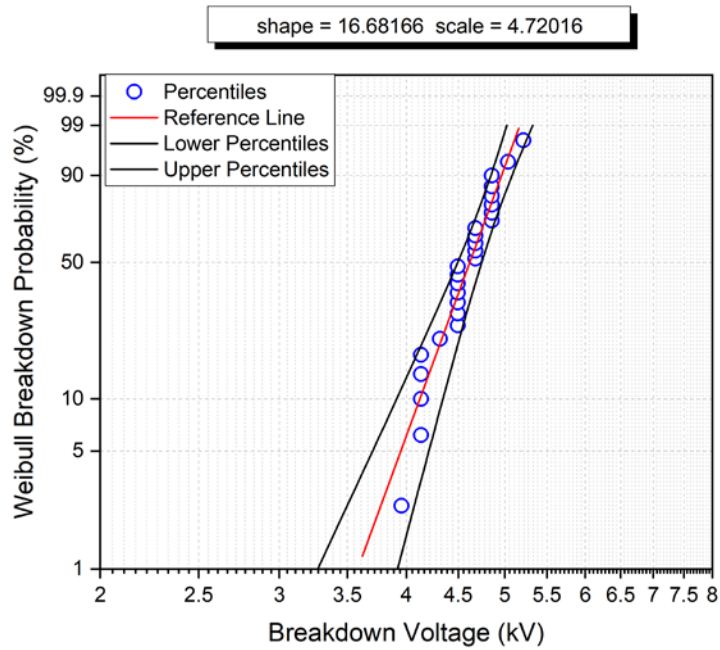


Figure 4.33 Weibull plot recording the breakdown voltages that occurred between two straight lengths of track printed 0.5 mm apart.

The breakdown voltages of the tracks, before the first breakdown across each sample, were then compared to the breakdown voltages after the solder mask was damaged. This can be seen in Figure 4.34. Under both circumstances, the range of voltages at which breakdown occurs is quite narrow; and the solder mask appears to increase the breakdown voltage by approximately 1.5 kV.

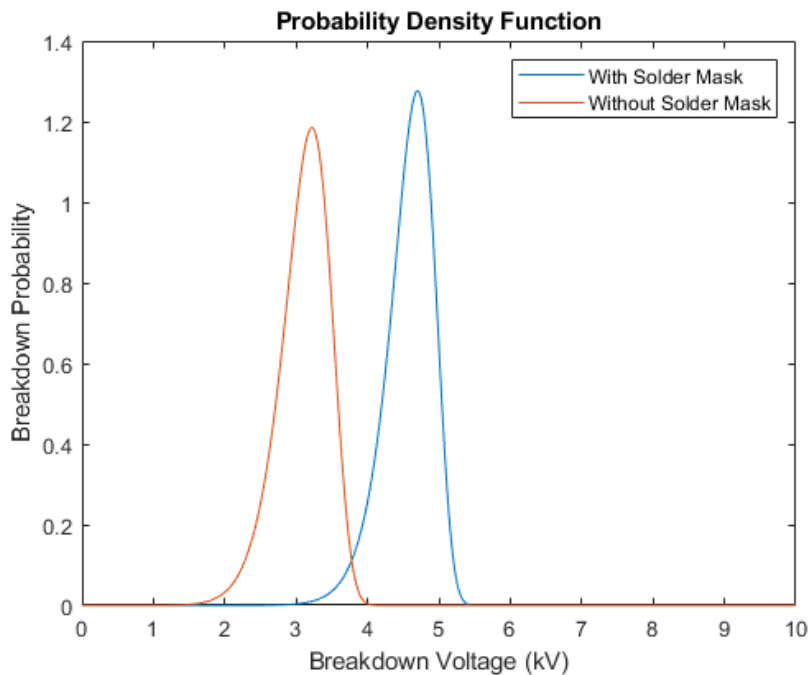


Figure 4.34 PDF comparing the voltage, at which flashover occurred, before and after the solder mask was damaged. The samples in this dataset represented the straight sections of track, printed 0.5 mm apart.

4.3.5 Tight Curve

The process outlined in the previous section was then performed on the samples replicating the curved sections of track closest to the core. In this case, corona (see Figure 4.35) typically became clearly visible around 4.1 kV with breakdown (shown in Figure 4.36) occurring between 5 – 6 kV. Flashovers happen at, seemingly, random locations along the tracks, with no area having a higher breakdown frequency than any other. This is in contrast with the simulation performed in Section 4.3.1.1 that predicted that breakdown was more likely to occur at the bend in the tracks. However, as the discrepancy in the field at this point is so small, it is more likely that breakdown was caused by manufacturing imperfections in the tracks.

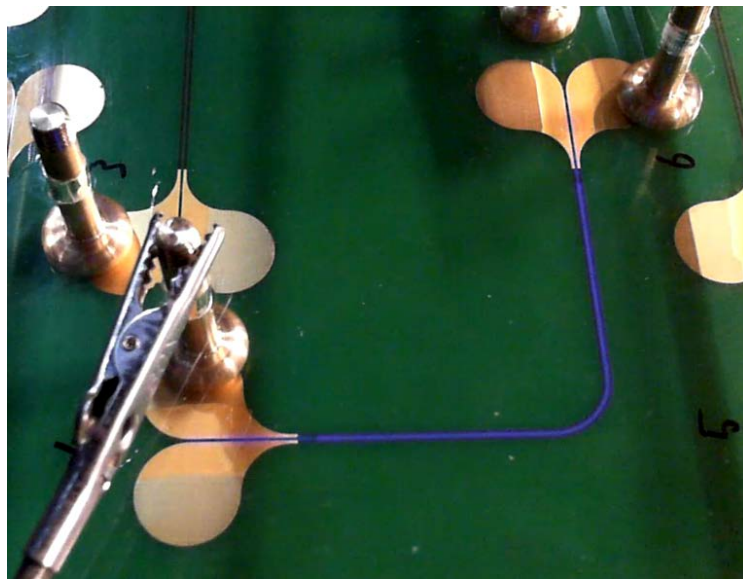


Figure 4.35 Corona discharge seen occurring, in the form of blue light, between two curved tracks printed 0.5 mm apart.

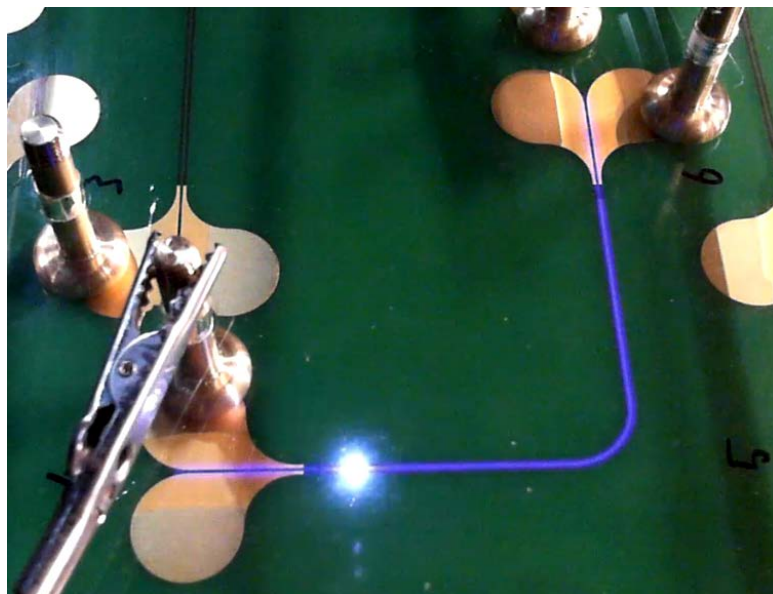


Figure 4.36 Flashover occurring between two curved tracks printed 0.5 mm apart.

As in the previous section, the effects of corona discharge and breakdown are evident in the current output of the amplifier; in Figure 4.37, it can be seen that when the voltage rises to 4.14 kV, the current rapidly increases to 5 mA. When breakdown occurs, there is a sharp rise in current before the circuit breaker in the amplifier opens and disconnects the current.

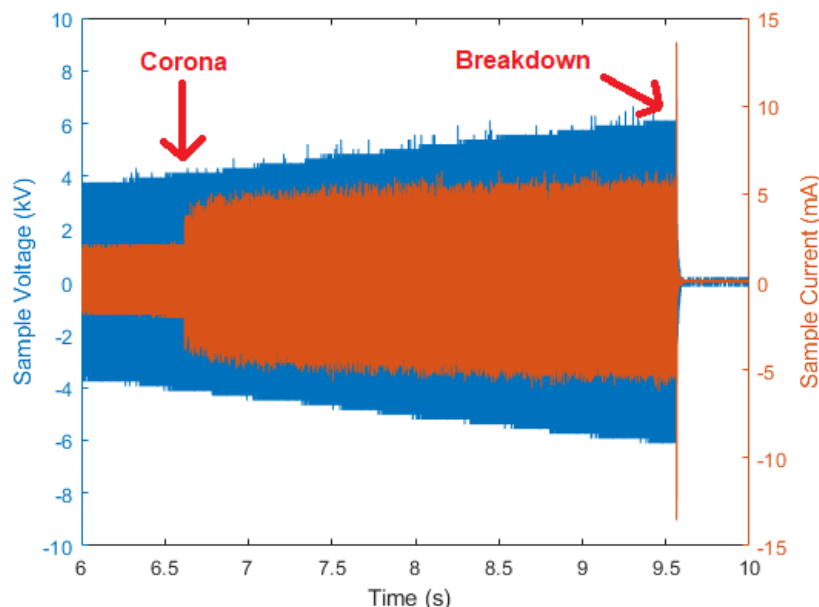


Figure 4.37 The voltage and current waveforms of the output of the amplifier when corona becomes clearly visible and flashover occurs. Note the sudden increase in current when the voltage reaches 4.136 kV and corona becomes clearly visible; also, the sharp rise in current when the insulation breaks down.

As was the case when the tracks were straight, after each experiment, two holes appeared in the solder mask where the breakdown occurred, implying that the same breakdown mechanism happened in both cases.

The voltages of each breakdown are recorded in Appendix C and plotted, using a Weibull plot, in Figure 4.38. From the Weibull plot, it can be seen that the scale parameter of this dataset is 5.88, and the shape parameter is 7.80, meaning that breakdowns typically occurred with a peak voltage of roughly 5.9 kV with a wide deviation. Again, this is greater than the 100 V expected to occur between adjacent windings in a single spiral design, but not consistently greater than the 5 kV expected to occur between windings in an interleaved design. Four samples broke down at a noticeably lower voltage than the rest of the dataset; these have been circled in Figure 4.38. It is possible that these outliers are indicative of a second breakdown mechanism, shown by the green line in Figure 4.38, although it is more likely that the lower breakdown voltage is the result of damage sustained by the solder mask while storing samples.

The breakdown voltages of the tracks, before the first breakdown across each sample, were then compared to the breakdown voltages after the solder mask was damaged. This can

be seen in Figure 4.39. Without the solder mask, breakdown occurs consistently between 3 kV and 4 kV with little deviation. This latter point is in contrast to the wide range of breakdown voltages when the solder mask was intact. The breakdowns that occurred after the solder mask had been damaged were similar, in terms of voltage, to those that occurred between the straight tracks.

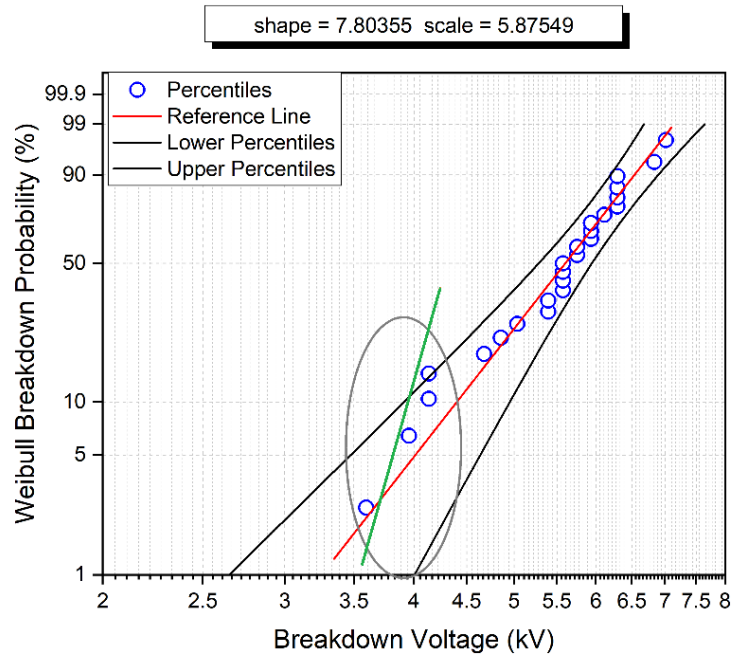


Figure 4.38 Weibull plot recording the breakdown voltages that occurred between two curved tracks printed 0.5 mm apart. Data points that imply a second breakdown mechanism are circled, with a possible reference line shown in green.

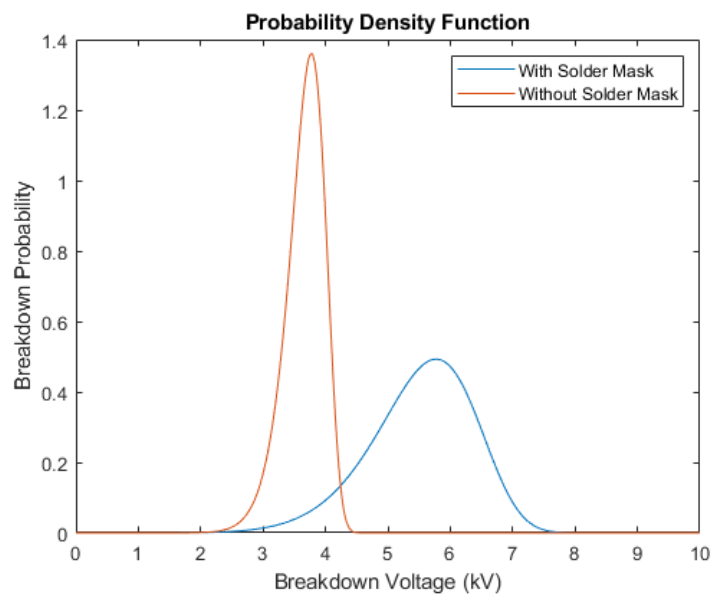


Figure 4.39 PDF comparing the voltage, at which flashover occurred, before and after the solder mask was damaged. The samples in this dataset represented the curved sections of track closest to the core, printed 0.5 mm apart.

4.3.6 Wide Curve

The process carried out in the previous two sections was then performed on the samples replicating the curved sections of track furthest from the core. In this case, corona (see Figure 4.40) typically became clearly visible around 3.4 kV with breakdown (Figure 4.41) occurring around 5.6 kV. Flashovers happen at, seemingly, random locations along the tracks, with no area having a higher breakdown frequency than any other. This is in line with the simulation performed in Section 4.3.1.4.

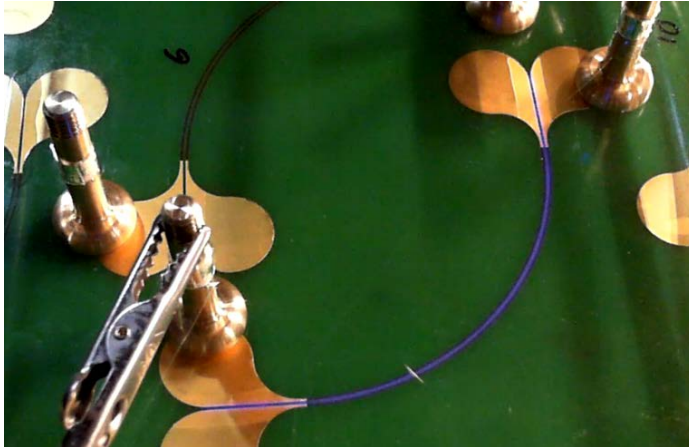


Figure 4.40 Corona discharge seen occurring between two curved tracks, printed 0.5 mm apart.

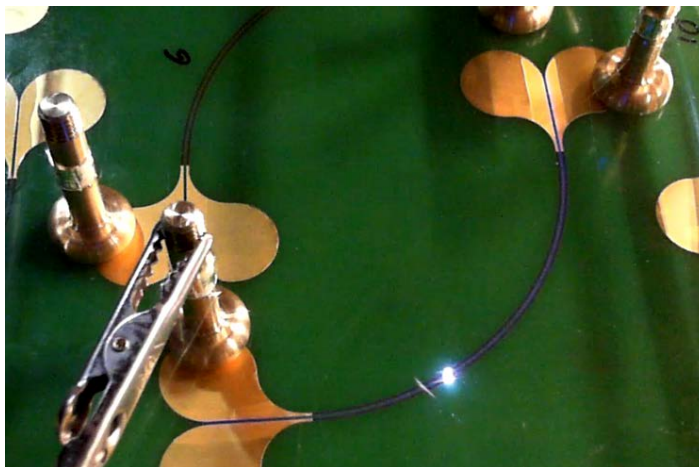


Figure 4.41 Flashover occurring between two curved tracks printed 0.5 mm apart.

As in the previous sections, the effects of corona discharge and breakdown are evident in the current output of the amplifier; shown in Figure 4.42, it can be seen that when the voltage rises to 3.6 kV, the current rapidly increases to 5 mA. When breakdown occurs, there is a sharp rise in current before the circuit breaker in the amplifier triggers and disconnects the current.

As in the previous cases, after each experiment, two holes appeared in the solder mask where the breakdown occurred, implying that the same breakdown mechanism happened

in both cases. The experiment was repeated on each sample after the first breakdown. This was to test the breakdown voltage when there was no solder mask, and also to ensure the solder mask had properly broken down.

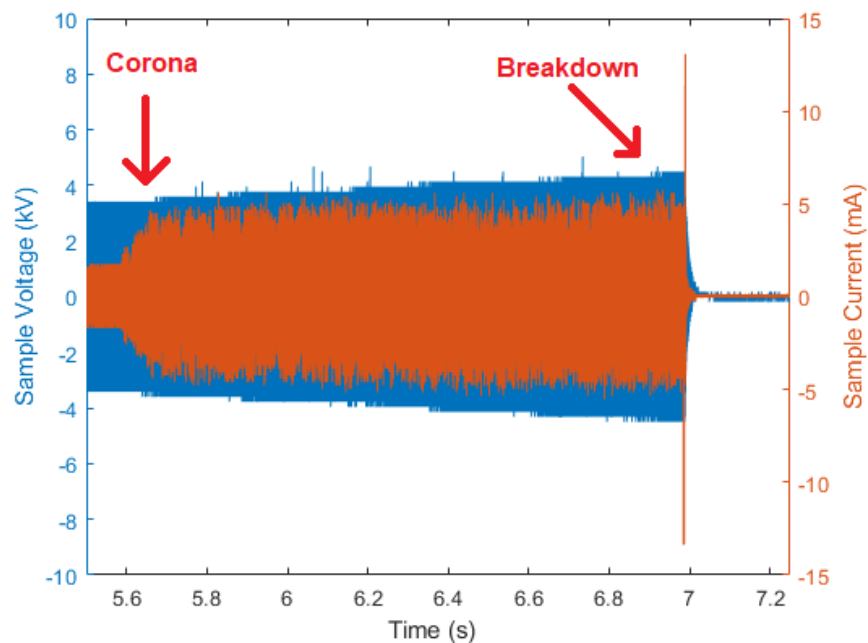


Figure 4.42 The voltage and current waveforms of the output of the amplifier when corona becomes clearly visible and flashover occurs. Note the sudden increase in current when the voltage reaches 3.6 kV and corona becomes clearly visible; also, the sharp rise in current when the insulation breaks down.

The voltages of each breakdown are recorded in Appendix C and plotted, using a Weibull plot, in Figure 4.43. From the Weibull plot, it can be seen that the scale parameter of this dataset is 5.64, and the shape parameter is 5.90, meaning that breakdowns typically occurred with a peak voltage around 5.6 kV with quite a lot of deviation. Seven samples broke down at a noticeably lower voltage than the rest of the dataset; these have been circled in Figure 4.43. It is possible that these outliers are indicative of a second breakdown mechanism, shown by the green line in Figure 4.43, although it is more likely that the lower breakdown voltage is the result of damage sustained by the solder mask while storing samples.

The first breakdown voltages across each sample, were then compared to the breakdown voltages after the solder mask was damaged. This can be seen in Figure 4.44. Without the solder mask, breakdown occurs consistently between 2.5 kV and 4 kV with little deviation. This latter point is in contrast to the wide range of breakdown voltages when the solder mask was intact. In terms of voltage, the breakdowns that occurred after the solder mask had been damaged were similar to those that occurred between the straight tracks and the tracks with the wide curve.

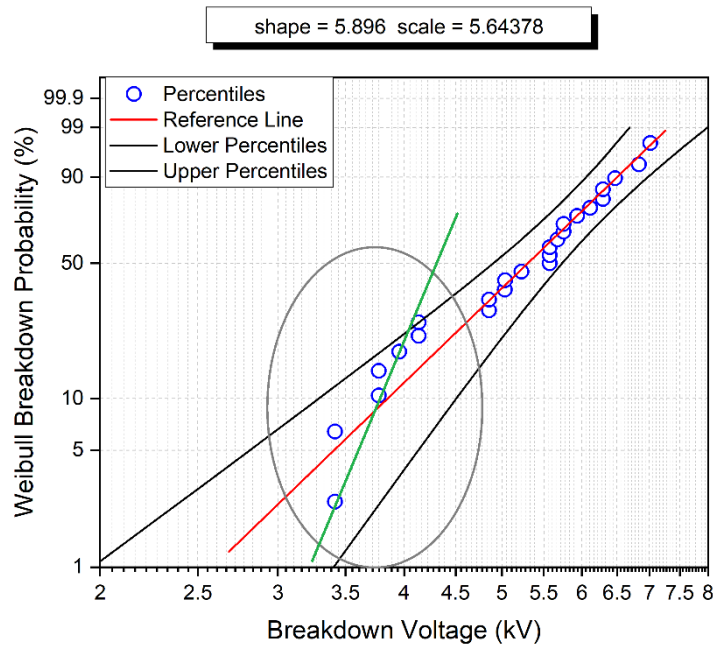


Figure 4.43 Weibull plot recording the breakdown voltages that occurred between two curved tracks printed 0.5 mm apart. Data points that imply a second breakdown mechanism are circled, with a possible reference line shown in green.

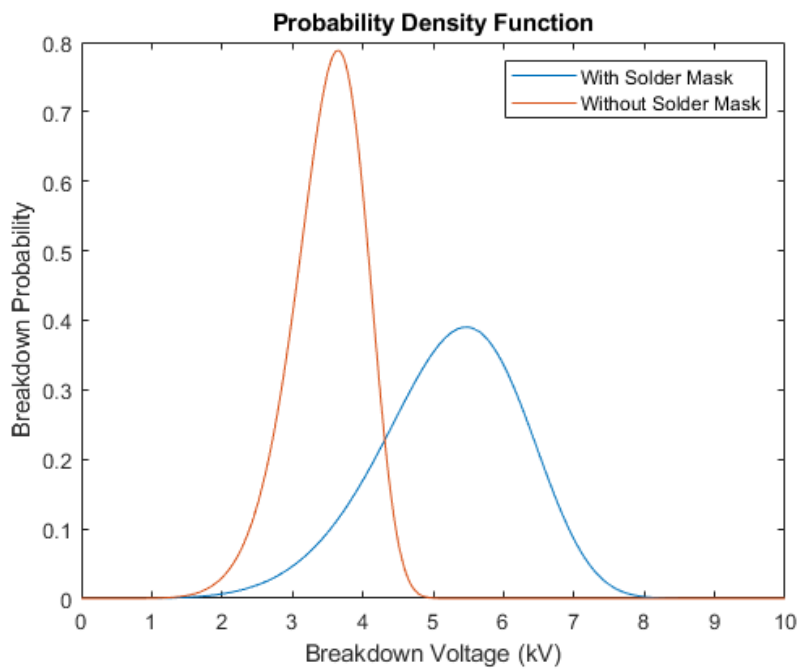


Figure 4.44 PDF comparing the voltage, at which flashover occurred, before and after the solder mask was damaged. The samples in this dataset represented the curved sections of track closest to the core, printed 0.5 mm apart.

4.3.7 Comparison of Results

Two PDFs were created to compare the results listed in the previous three sections; both with and without a solder mask. These can both be seen in Figure 4.45.

Before the solder mask was damaged, the samples consisting only of straight tracks broke down at a reasonably consistent voltage. By contrast, the tracks that featured a curve had a much wider variation of breakdown voltage. This is likely caused by a combination of the inconsistencies in the fabrication quality of the samples, and the lengths of each sample. It is inevitable that the samples contained microscopic imperfections around the edges of the tracks, and in the thickness of the solder mask. The curved samples, being longer than the straight samples, contained more imperfections and, therefore, more potential causes of breakdown. This, in turn meant there was a larger distribution of breakdown voltages.

On the other hand, once the solder mask is damaged, breakdown occurred at a more consistent voltage in all types of sample. This is most likely because the initial breakdown creates two holes in the solder mask between the tracks, meaning there is a clear air path between the electrodes. This means that subsequent breakdowns take place through air only, and is not subject to the inconsistencies in the solder mask. In addition to this, as breakdown of a sample is most likely to occur at a point with the greatest imperfections in the track and soldermask, these points will be similar to each other, thus leading to comparable breakdown phenomena.

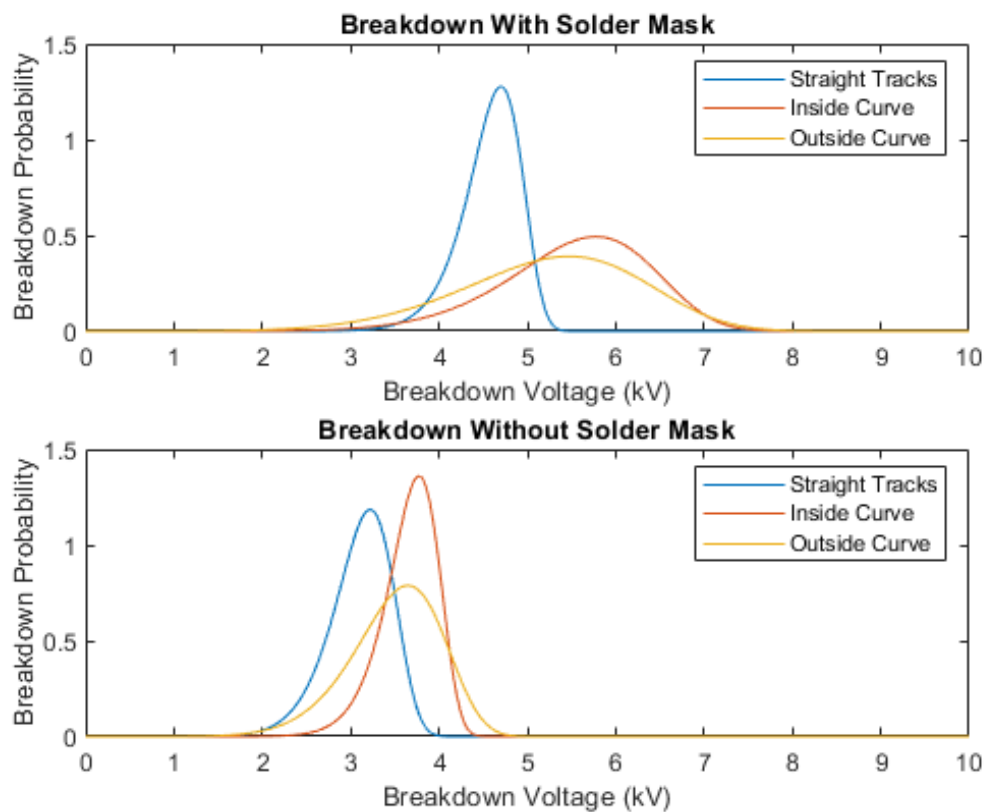


Figure 4.45 (TOP) A PDF comparing the breakdown voltages of the three different shaped samples before the solder mask was damaged. (BOTTOM) A PDF comparing the breakdown voltages of the same samples after the solder mask was damaged.

4.4 Variations

Having performed a number of experiments to evaluate the breakdown characteristics of PCB based windings, with a gap of 0.5 mm between tracks, in atmospheric pressure air; it was decided to vary the experimental parameters in another set of experiments.

4.4.1 Gap Distance

The first variation that was made, was to increase the distance between the tracks. Experiments, carried out in the literature [107], [110], [111], concluded that there is an approximately linear relationship between breakdown voltage and the distance between tracks, under impulse testing, between 0.2 mm and 0.8 mm. In this work, a second set of breakdown experiments were conducted on samples that were identical to those in Section 4.3.4, except that the gap between the tracks was increased to 1.5 mm.

These samples were simulated, as shown in Figure 4.46, to estimate the electric field that would exist between the tracks. The electric field strength for a given voltage is shown to be a third that of the case when the tracks are 0.5 mm apart.

The samples were connected to the same experimental setup as described in Section 4.3.2, with a frequency of 1 kHz, and the voltage increasing at 500 V per second. Similar to when the tracks were closer together, corona discharge (Figure 4.47) often became clearly visible before breakdown, typically when the voltage was 6.1 kV. With full breakdown, as shown in Figure 5.48, occurring around 6.5 kV. The Weibull plot for this experiment is shown in Figure 4.49.

As in previous sections, the experiment was conducted again after the first breakdown in order to test the breakdown voltage without the solder mask. In each case, the second breakdown occurred in the same place as the first. The voltages of the first and second breakdowns are compared to those, when the tracks were 0.5 mm apart, in Figure 4.50. This shows that, when the gap is increased to 1.5 mm, the solder mask becomes less effective at increasing the breakdown voltage; as the difference in breakdown voltage is less than 0.5 kV, as opposed to the 1.5 kV difference seen when the gap was only 0.5 mm wide. However, the solder mask appears to reduce the deviation in breakdown voltage. This is in contrast to the results seen with the narrower gap. It is intuitive that the increased breakdown path should also increase the variation in breakdown voltage. It is also possible that the solder mask has a more consistent breakdown threshold, leading to the reduced deviation when the tracks are 1.5 mm apart, and this is simply overcome by the much higher field strength when the tracks are closer.

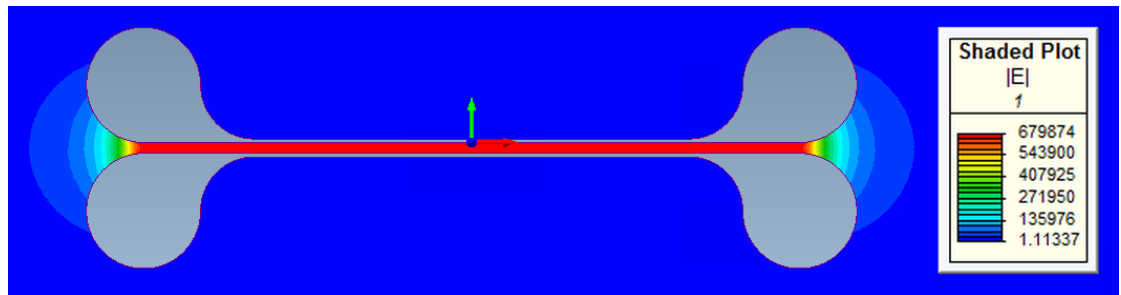


Figure 4.46 The simulated electric field between two tracks, printed 1.5 mm apart, on a PCB. The voltage difference between the two tracks is 1 kV.

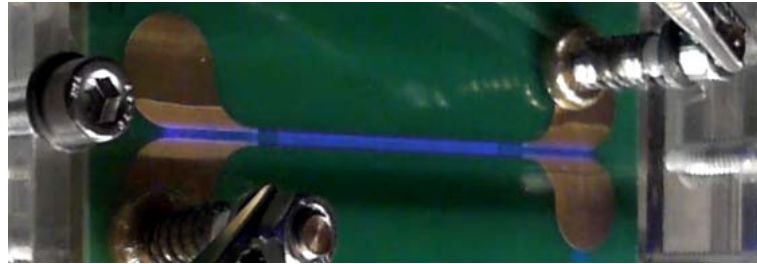


Figure 4.47 Corona discharge visible between tracks printed 1.5 mm apart.

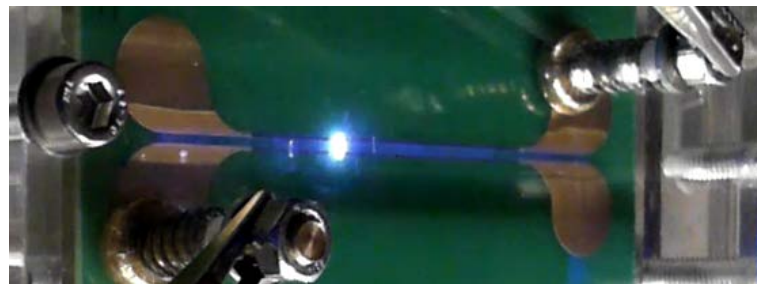


Figure 4.48 Breakdown of tracks printed 1.5 mm apart.

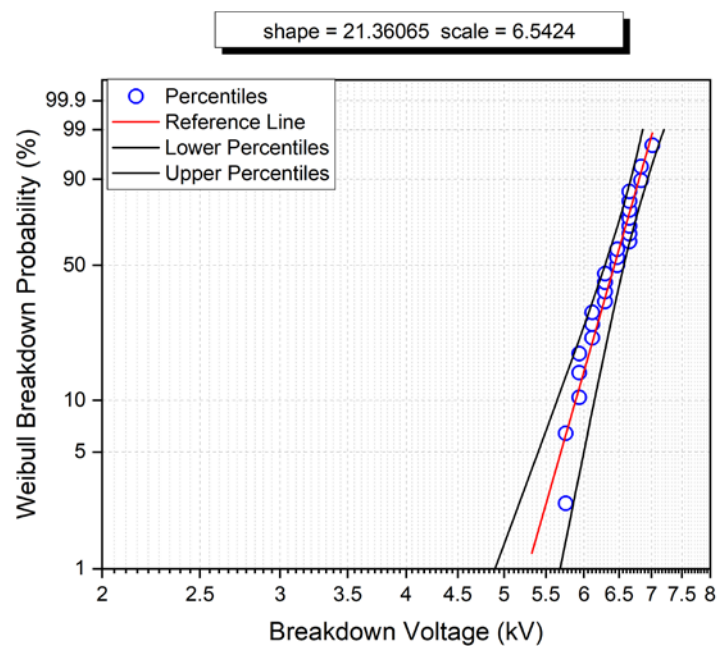


Figure 4.49 The breakdown voltages of two straight tracks printed 1.5 mm apart.

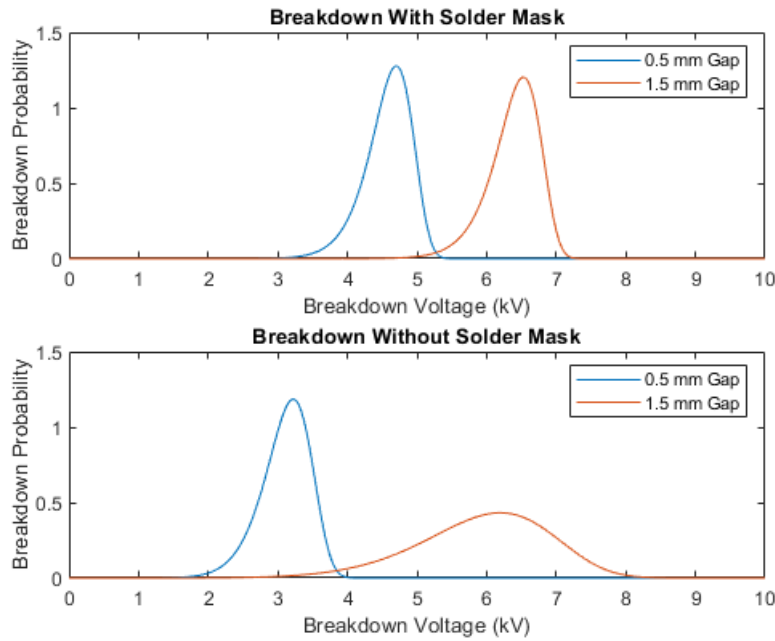


Figure 4.50 (TOP) A PDF comparing the breakdown voltages of samples with straight tracks before the solder mask was damaged. (BOTTOM) A PDF comparing the breakdown voltages of samples with straight tracks after the solder mask was damaged.

4.4.2 Frequency

The experiments, documented so far in this work, were performed at a frequency far lower than that expected in an actual power supply design. For this reason, it was decided that more experiments should be conducted in order to predict the effect that frequency has on breakdown voltage.

Experiments were performed, at a number of different frequencies, with the intention of extrapolating this data with the goal of estimating the approximate breakdown voltage at 100 kHz. The frequencies 100 Hz, 2 kHz, and 5 kHz were selected to cover one and a half orders of magnitude. At each frequency, five breakdown tests were performed, in order to provide a reasonable sample size. The results of these experiments are shown in Figure 4.51.

Figure 4.51 shows a slight downwards trend, in breakdown voltage with respect to frequency, equivalent to a decrease in breakdown voltage of 481 V per order of magnitude. If this data were to be extrapolated linearly, a breakdown voltage of 3.70 kV would be expected at an operational frequency of 100 kHz. However, the data does not closely match the trend line. Indeed, the correlation coefficient is only -0.42, meaning that the data shows a poor correlation between the frequency and breakdown voltage. As experiments were conducted several months apart, differences in breakdown voltage are more likely the result of environmental issues, such as air humidity, than in changes of frequency.

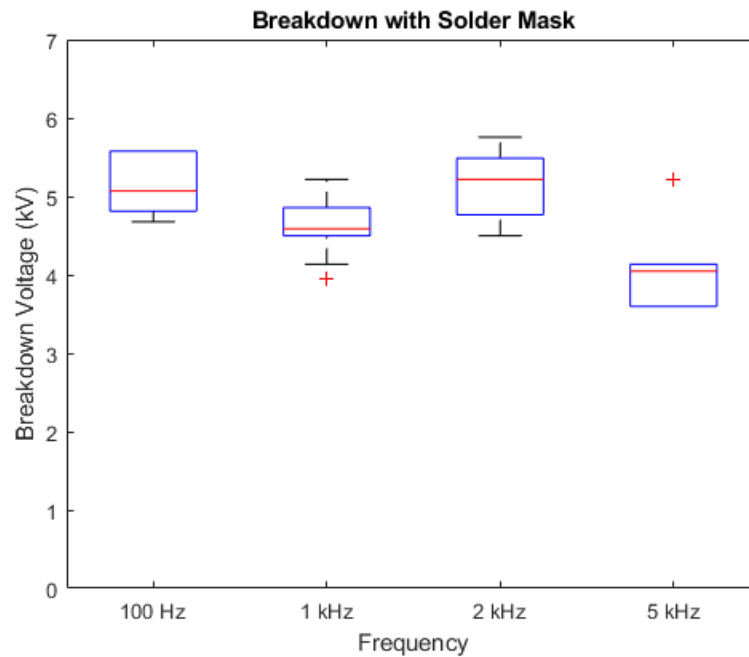


Figure 4.51 The breakdown voltages of PCBs, with a solder mask, tested at different frequencies.

The same analysis was performed on samples that had already broken down, the results from which can be seen in Figure 4.52. This implies that there is no relationship between power frequency and breakdown voltage when insulated only by air. Although the trend line suggests a slight increase in breakdown voltage, this equates to an increase of only 73 V per order of magnitude. This coupled with the fact that the correlation coefficient for this data is only 0.44 means that it should not be concluded there is a relationship between frequency and breakdown voltage, below 5 kHz, when the solder mask has broken down.

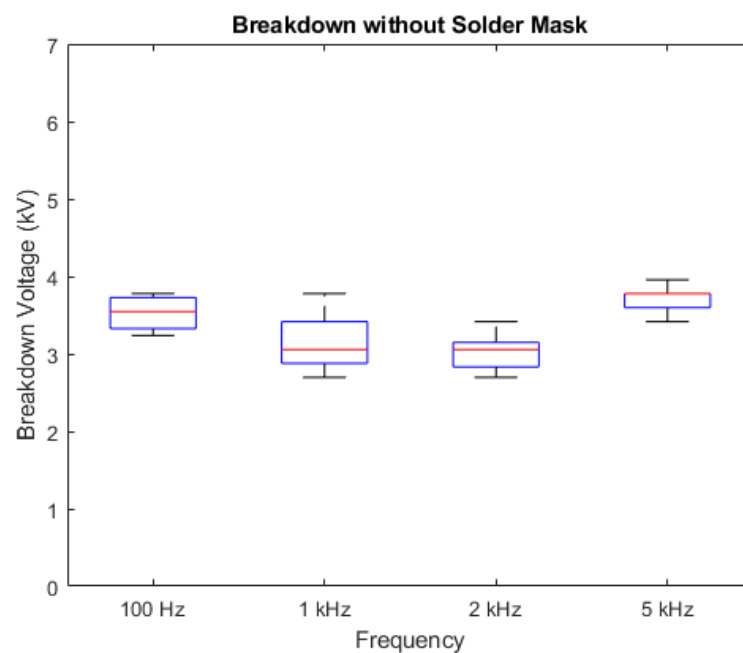


Figure 4.52 The breakdown voltages of PCBs, with a damaged solder mask, tested at different frequencies.

In order to interpret these results, it may be worth discussing existing theory regarding the relationship between frequency and breakdown. In an electric field between two electrodes, negatively charged electrons are drawn towards the positive anode, while positive ions are drawn towards the cathode. As these charged particles accelerate towards their respective electrodes, they will collide with neutral particles. If the charged particles have sufficient velocity, they may dislodge an electron from the neutral particle, thus forming two new charged particles that will begin accelerating in the electric field. Both of these particles will begin ionising neutral particles which, in turn, will ionise yet more neutral particles; thus forming an avalanche effect.

As electrons are much smaller than positive ions, they accelerate at a much faster rate. This means that, assuming both particles start with zero velocity, after a given length of time, an electron will have moved much further than the positive ion. This greater velocity means that more electrons than positive ions are responsible for ionising collisions.

The difference in velocity is so great that, compared to the electrons, the positive ions appear to be stationary. As the electrons move towards the anode, they leave in their wake a cone of positive ions with the highest density of ions closest to the anode. The accumulation of positive ions leads to an increase in field strength in the gap between the electrodes. In turn, this increases the current in the gap and is ultimately what leads to breakdown. This is the case for both DC and low frequency fields.

As the frequency increases, there will come a point at which the positive ions cannot reach the cathode before the polarity of the field is reversed and the cathode becomes the anode. When this happens, the positive ions will begin moving towards the new cathode. However, before the positive ions can reach the new cathode, the polarity will be reversed again, and the positive ions will begin moving back to the original cathode. The positive ions are effectively trapped between the two electrodes.

As the avalanche continues, this forms a space charge with a growing density between the two electrodes increasing the field current and leading to breakdown. This means that, although the potential may be the same as for the DC case, the local potential gradient is greater, leading to breakdown occurring at a reduced voltage. The frequency at which breakdown voltage begins to decrease is known as the first critical frequency.

If the frequency is increased further, the breakdown voltage decreases as more and more positive ions are trapped between the electrodes. This is until a second critical frequency is reached. At this point, the polarity is reversed so often that the electrons become trapped between the electrodes. As they are no longer swept into the anode, the electrons travel back and forth between the electrodes and ionise twice as many particles in one cycle than they would at a lower frequency. This means that there are now twice as many positive ions

forming a space charge in the gap, which reduces the breakdown voltage to its lowest point. As the frequency is raised above the second critical frequency, the number of negative electrons in the gap also increases and cancels out the positive space charge. This means that as the frequency is increased, the breakdown voltage begins to increase again.

The seminal work on this topic was carried out by Reukema in 1928, and published in 1929. His investigation, conducted on brass spheres with a diameter of 62.5 mm and separated by distances between 5.8 mm and 25.4 mm, found a 13% drop in breakdown voltage between 20 kHz and 60 kHz. He also predicted that the second critical frequency would be around 6 MHz [112].

In theory, for a given distance, if one knew the velocity a particle would reach in a uniform electric field, one could calculate the critical frequencies. However, as the electric field around the samples used in this investigation is far from uniform, calculating the critical frequencies is unlikely to be so straight forward.

The fact that the results obtained in these experiments do not show any strong correlation with frequencies below 5 kHz is in line with results published in the literature [112], [113]. A more detailed experimental study is needed to determine the effect that frequency has on breakdown voltage between parallel tracks of a PCB.

4.4.3 Pressure

A sample was placed in a vacuum chamber, and the pressure reduced to 40 Pa. According to Paschen's Law [24], [60], [79], [114], this should yield the same breakdown voltage as atmospheric pressure, for copper electrodes. The sample was then subjected to the same experiment as that outlined in Section 4.3.2. As soon as a voltage was applied to the sample, breakdown occurred, as seen in Figure 4.53.



Figure 4.53 Breakdown occurring across a sample, with tracks printed 0.5 mm apart, at a pressure of 40 Pa.

Rather than a simple flashover, as could be seen when breakdown occurred in atmospheric pressure air, Figure 4.53 shows a blue hue around the electrodes and conductive areas of the samples. This implies that outgassing has occurred and that current is passing through a conductive gas surrounding the board. The source of the outgassing is unclear. It may be the solder mask, insulating lacquer applied to the exposed contacts, or even the FR4 of the board itself. Further experimentation is required to satisfactorily explain this phenomenon.

4.5 Discussion and Potential Developments

The work in this chapter has focussed primarily on windings fabricated using copper tracks printed onto the surface of fiberglass boards, as these are the cheapest and most commonly produced PCBs. It has been shown that a single tracked winding is unlikely to short in atmospheric pressure air, although an insulating material with a higher dielectric breakdown strength would likely be required to prevent breakdown between the core and each winding. There are many more variations of PCBs that may be explored in greater detail in future work.

The first variation that could be made would be to print tracks inside the PCB. It is possible to print tracks on internal layers of a PCB, with many companies offering 16 or more internal layers [98]. By only printing tracks on the surface of the boards, one is limited to only two layers of windings. As the surface area, of a spiral winding, is related to the square of the number of turns in each layer, doubling the number of layers the turns are spread over could more than half the surface area. This is beneficial as it would reduce the parasitic capacitance, as well as significantly reducing the overall size of the board; this is useful as manufacturers charge by area. Only two layers are used in this work for the sake of simplicity. However, it would be worth considering using more layers if developing a prototype based on this design.

Further work should also examine the suitability of different materials for the construction of the PCBs. For example, Teflon is used in high frequency PCB construction [100], this has the advantage that it is known to not outgas at, even, high vacuum. It is also not uncommon for PCBs used in high power applications to be manufactured with an aluminium sheet at their centre [98]. This helps conduct heat away from the circuit, and may be useful for the purposes of this project.

As discussed in the previous chapter, conventional wisdom advises against using SF_6 to insulate HVDC components. Therefore, if this convention is to be adopted and SF_6 is used to insulate the core and windings, the HVDC components must be kept in a separate insulating enclosure from the windings. A good insulator for DC applications is vacuum. If the HV circuitry can be mounted on a PCB, this would significantly simplify the design, and

significantly reduce the cost, of the HVDC component of the design. A detailed investigation should be conducted into evaluating the performance of PCBs in vacuum. This should take into account the outgassing associated with different board materials and heat dissipation from components operating under load.

Finally, a working prototype of a winding should be fabricated and tested under different conditions, including, but not limited to, high pressure SF_6 .

Chapter 5

Insulated Core Transformers

In this Chapter, the suitability of ICTs to function in a practical power supply, is evaluated. First, different layouts for an ICT are reviewed, to determine the best way of constructing an ICT. This layout is then optimised to reduce flux loss as much as is practically possible. As the voltage generated across a winding is directly proportional to the flux linkage passing through it, it is desirable to keep flux loss to a minimum in order to maximise the output of the design. Then, Cross Transformer Technology (CTT) is discussed, in order to consider the benefits it may bring to this project. A new method is proposed that reduces the complexity of calculating the flux loss in an ICT.

The chapter concludes by discussing the limitations of the work carried out in the previous sections, and then proposing a way in which to adapt existing ICT technology to fulfil the specifications of this project. Finally, it is decided whether or not a design based on ICTs would be suitable for a 5MV, 5A Power supply. The work in this chapter focuses, entirely, on investigating flux loss in ICTs, and does not examine problems associated with eddy currents and heat generation, that would occur in a practical ICT design.

5.1 An Evaluation of ICT Layouts

ICTs can be arranged into different formations; a number of these are suggested here and then compared in simulation. Each simulation is carried out on a core with ten secondary windings around twenty insulated core slices. Each winding consists of 100 turns in order to ensure consistent flux linkage. Each section of insulated core has a cross sectional area of 80 mm by 80 mm, and is 9 mm thick; there is 1 mm of insulation between each segment of core. A current of 400 Amps will drive the primary winding. The results of these simulations will then be discussed in order to deduce the most effective ICT layout for ensuring consistent flux linkage.

5.1.1 Basic ICT Layout

The most basic layout for a practical ICT is simply to stack each section of insulated core on top of each other, with a primary winding driving the whole stack from the bottom, as shown in Figure 5.1. This design was simulated, using a Static 2D solve, in order to calculate the flux linkage in each winding, with the results being shown in Table 5.1. The flux flow in this design is shown in Figure 5.2.

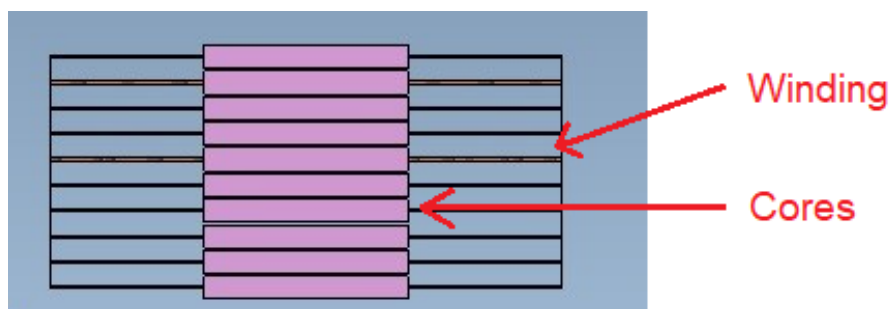


Figure 5.1 Layout of the most basic ICT stack. The cores are arranged on top of each other with the windings surrounding them.

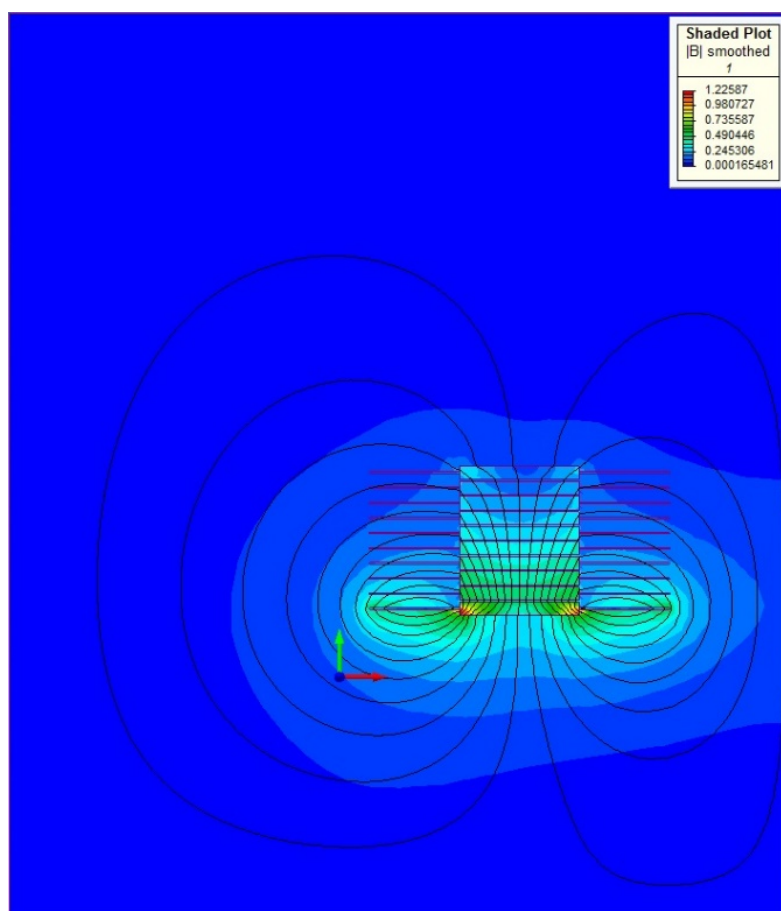


Figure 5.2 The flux flow around a 10 layer ICT.

Table 5.1 Flux linkage in a basic transformer core.

Winding Number:	Flux Linkage (Wb-t):	Normalised Flux linkage:
1	0.342401782	100%
2	0.298770948	87%
3	0.260393463	76%
4	0.22763104	66%
5	0.199110369	58%
6	0.173920212	51%
7	0.15138311	44%
8	0.130954109	38%
9	0.112185041	33%
10	0.094698916	28%

This design suffers jointly from the lack of a flux return path, as well as the distance of some of the furthest secondary windings from the primary. The flux is reluctant to travel up the stack, to the higher windings, as in doing so it will have a longer return path through the air. One possible solution to this might be to add another primary winding at the top of the stack. This would create a flux path that goes straight through the stack with a flux return path going through the air outside the stack.

The biggest drawback to this idea is that it effectively doubles the number of secondary windings needed. This is because one of the key principles of an ICT is that each secondary winding only needs to be insulated from the winding next to it and not from the full operating voltage of the device. In order to be powered from the mains, a primary winding must necessarily be grounded. If a grounded winding were to be placed next to a secondary winding at the very top of the stack, that secondary winding would have to be insulated against the full operating voltage of the device. To overcome this, a second stack of insulated cores must be constructed from the second primary winding, with each core operating at an increasing voltage until the final core operates at the same voltage as the top core of the first stack. At this point, both stacks can meet in the middle, creating a single stack grounded at both the top and the bottom.

The layout of the double primary ICT is shown in Figure 5.3, with the flux flow shown in Figure 5.4. The flux linkage measured in each winding shown in Table 5.2.

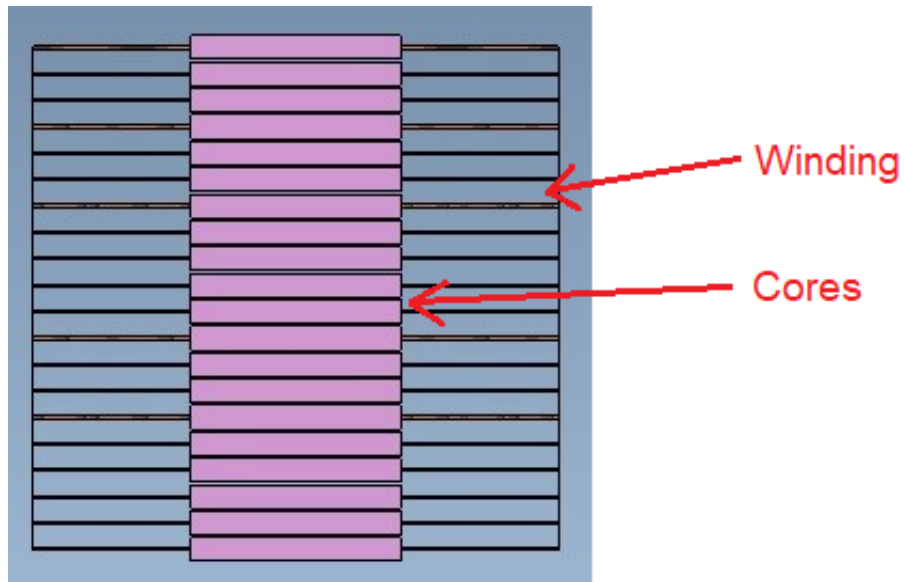


Figure 5.3 Layout of a 10 stage ICT powered by two primary windings. Each winding is connected, in parallel, to the winding opposite, with the two primary windings at the top and the bottom.

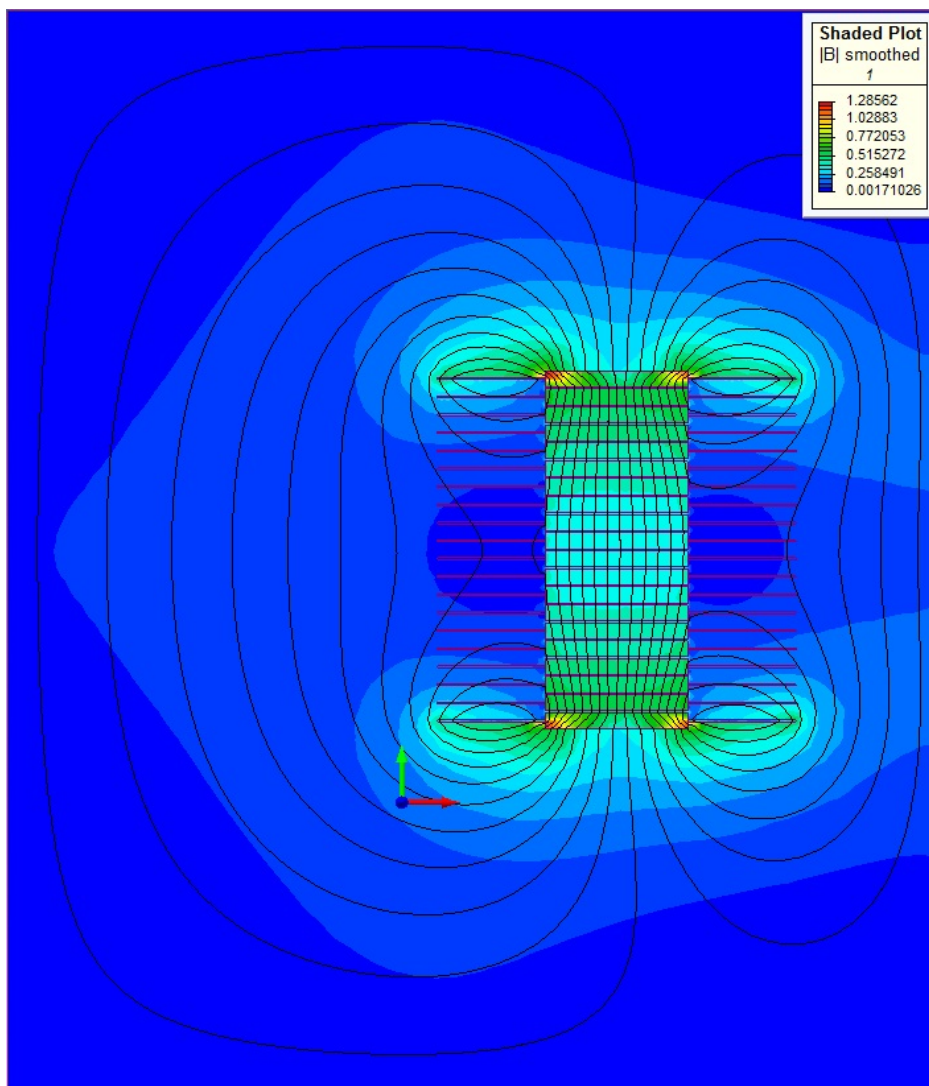


Figure 5.4 The flux flow around a 20 layer ICT with primary windings at the top and bottom.

Table 5.2 Flux linkage in a basic ICT with two primary windings.

Winding Number:	Flux Linkage (Wb-t):	Normalised Flux linkage:
1	0.386150222	100%
2	0.350179842	91%
3	0.319815811	83%
4	0.295547005	77%
5	0.276143045	72%
6	0.260837013	68%
7	0.249105073	65%
8	0.240587518	62%
9	0.235039907	61%
10	0.232310688	60%
11	0.232325476	60%
12	0.235090035	61%
13	0.240671529	62%
14	0.249223596	65%
15	0.260993149	68%
16	0.276343884	72%
17	0.295796652	77%
18	0.320127523	83%
19	0.350569786	91%
20	0.386689246	100%

5.1.2 Flux Diverters

One possible way to redirect magnetic flux is to use Flux Diverters (FD). These consist of additional loops of wire that encircle the flux path at regular intervals, as shown in Figure 5.5. When a current is passed through these loops, they form a magnetic field around themselves. These fields form a tunnel for the magnetic flux from the primary winding to pass through.

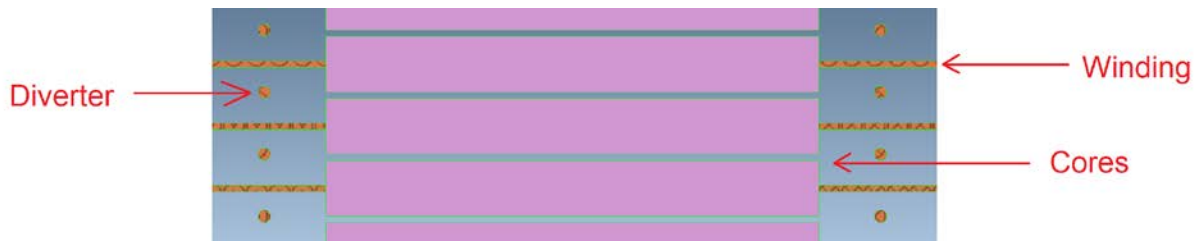


Figure 5.5 Flux diverters surrounding a stack of insulated cores.

For the sake of this preliminary simulation, important design challenges, such as how to power and insulate the FDs, are ignored. For the purposes of evaluating whether or not FD represent a viable solution to flux loss in a HV ICT, each FD is modelled as a winding with a single turn and driven by a current of 400 Amps. The effect this has on the flow of flux in a 10 stage ICT is shown in Figure 5.6 with the flux linkage recorded in each winding detailed in Table 5.3.

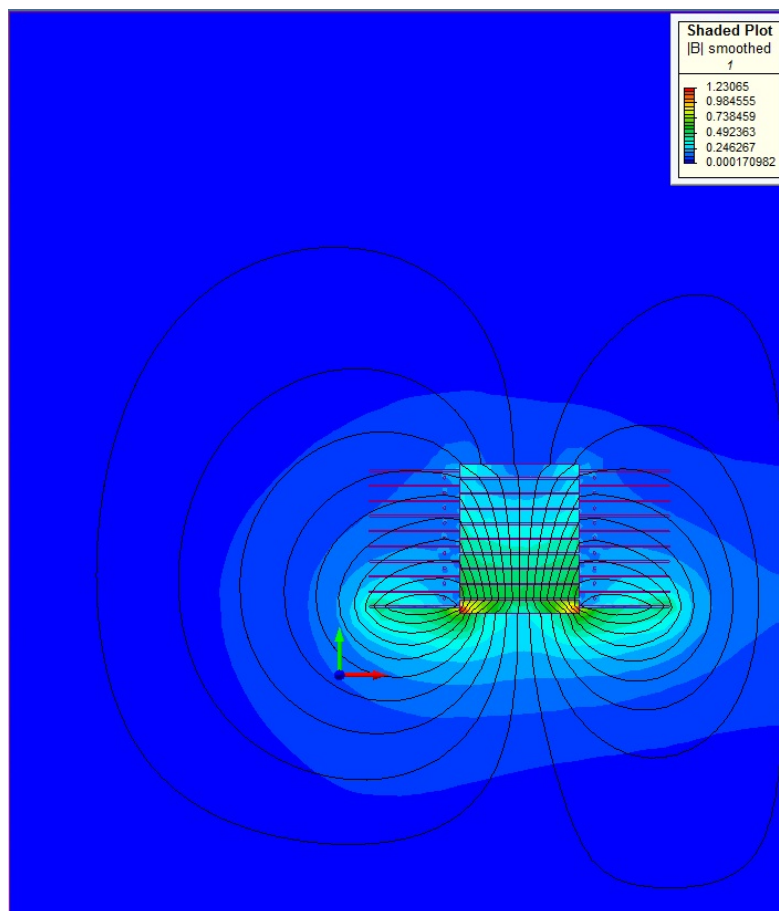


Figure 5.6 Flux flow around a 10 stage ICT with flux diverters.

Table 5.3 Flux linkage in a 10 layer ICT with flux diverters.

Winding Number:	Flux Linkage (Wb-t):	Normalised Flux linkage:
1	0.359635123	100%
2	0.319788822	89%
3	0.284048432	79%
4	0.253010963	70%
5	0.225371523	63%
6	0.200247058	56%
7	0.17696348	49%
8	0.154957654	43%
9	0.133740033	37%
10	0.112870507	31%

It was decided to try and drive the flux diverted ICT from two primary windings. The flux flow can be seen in Figure 5.7 and the flux linkage in each winding is recorded in Table 5.4.

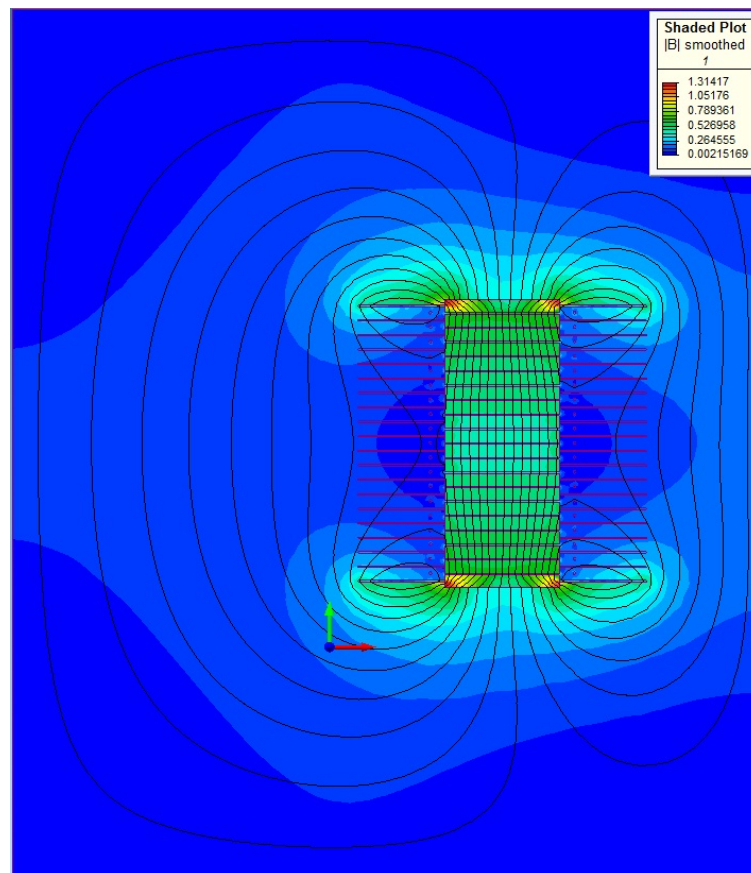


Figure 5.7 The flux flow around a 20 layer ICT with flux diverters, and primary windings at the top and bottom.

Table 5.4 Flux linkage in an ICT with flux diverters and two primary windings

Winding Number:	Flux Linkage (Wb-t):	Normalised Flux linkage:
1	0.412978232	100%
2	0.382265528	93%
3	0.356177286	86%
4	0.33546101	81%
5	0.318963482	77%
6	0.305985402	74%
7	0.296059332	72%
8	0.288862255	70%
9	0.284179154	69%
10	0.281876835	68%
11	0.281891351	68%
12	0.28422368	69%
13	0.288935924	70%
14	0.296162107	72%
15	0.306123542	74%
16	0.319135669	77%
17	0.335665955	81%
18	0.356415817	86%
19	0.382532351	93%
20	0.413276445	100%

5.1.3 Clamped Return Path

Both of the designs discussed above have suffered significant flux loss, in higher voltage windings, because there is no clear flux return path. As the air surrounding the ICT has a relatively low magnetic permeability, it can only sustain a low flux density. This forces the magnetic flux to fan out, as it passes through the ICT, as the air cannot conduct a high flux density return field. One possible solution to this would be to construct a metal flux return path around the ICT, effectively turning it into a shell core transformer with air gaps in one of the limbs. As the clamp must be grounded, the ICT must be constructed in the double stack layout described in Section 5.1.1. This design can be seen in Figure 5.8, with the flux flow shown in Figure 5.9. The recorded flux linkages are listed in Table 5.5.

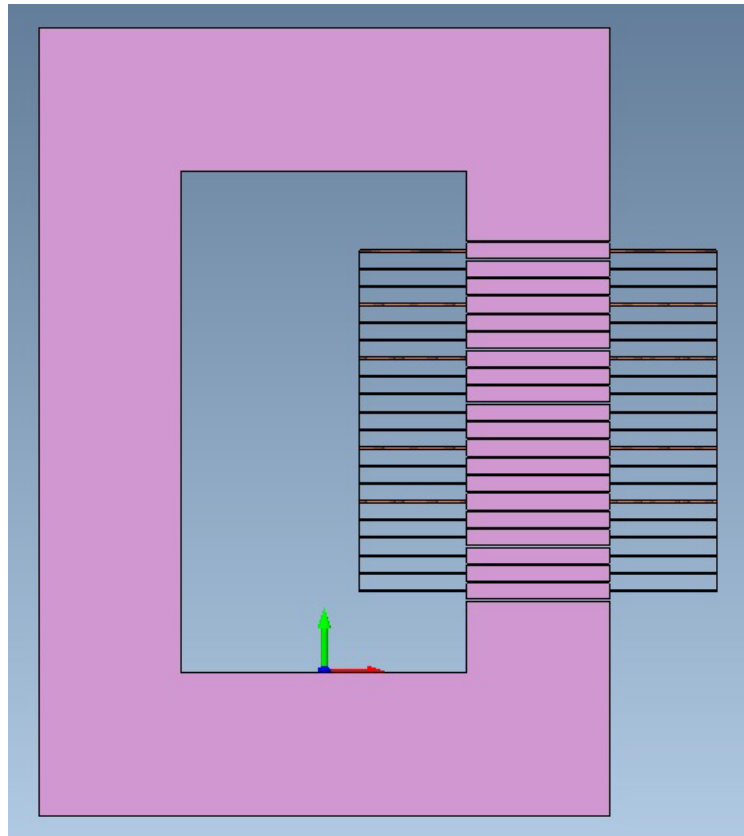


Figure 5.8 Layout of clamped flux return path ICT.

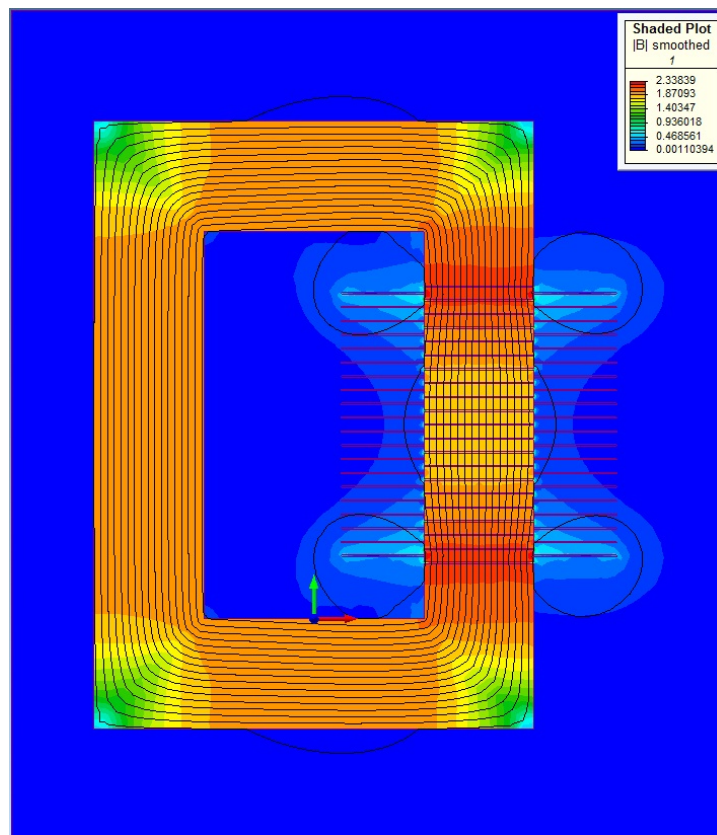


Figure 5.9 The flux flow around a 20 layer ICT with a flux return clamp, and primary windings at the top and bottom.

Table 5.5 Flux linkage in an ICT with flux return clamp and two primary windings

Winding Number:	Flux Linkage (Wb-t):	Normalised Flux linkage:
1	1.466440629	100%
2	1.406524633	96%
3	1.358069317	93%
4	1.31981425	90%
5	1.289508979	88%
6	1.265746028	86%
7	1.247601735	85%
8	1.234454045	84%
9	1.225900969	84%
10	1.221690915	83%
11	1.221700531	83%
12	1.225936067	84%
13	1.234516147	84%
14	1.247686173	85%
15	1.265858996	86%
16	1.289650179	88%
17	1.319983328	90%
18	1.358264174	93%
19	1.406756437	96%
20	1.466727434	100%

5.1.4 Partial Clamp Return Path

The major drawback of the flux return clamp is that it contains more metal than all of the insulated cores combined. This makes it exceedingly heavy and expensive to produce. It is possible that a partial flux return path will work nearly as well as a full flux return path, while not requiring as much material. A partial clamp design is suggested in Figure 5.10. In this case, the partial clamp consists of the two yokes of a shell type transformer core; only the second limb is missing. Other, more practical, designs can be proposed if this design shows promise. The flux flow in this configuration is shown in Figure 5.11. The recorded flux linkage in each winding is shown in Table 5.6.

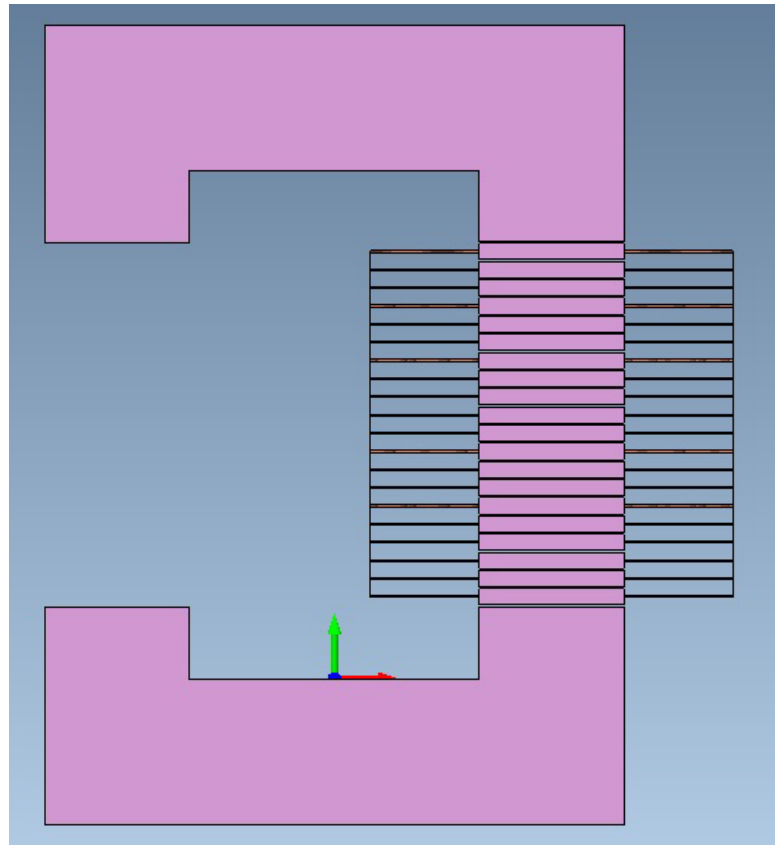


Figure 5.10 Layout of a partial flux return clamped ICT.

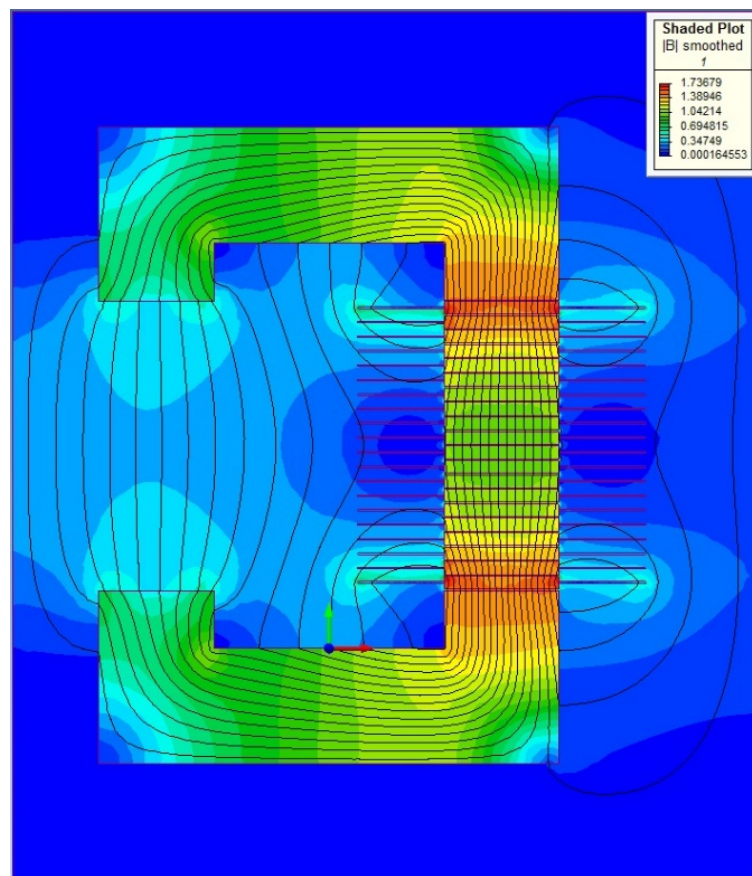


Figure 5.11 The flux flow around a 20 layer ICT with a partial flux return clamp, and primary windings at the top and bottom.

Table 5.6 Flux linkage in an ICT with partial flux return clamp and two primary windings.

Winding Number:	Flux Linkage (Wb-t):	Normalised Flux linkage:
1	0.951008112	100%
2	0.885214878	93%
3	0.829612527	87%
4	0.784195186	82%
5	0.747337859	79%
6	0.717940813	75%
7	0.695233087	73%
8	0.678658803	71%
9	0.66783778	70%
10	0.662523207	70%
11	0.66259111	70%
12	0.668051427	70%
13	0.67902158	71%
14	0.695740478	73%
15	0.718599717	76%
16	0.74814664	79%
17	0.785161332	83%
18	0.830740937	87%
19	0.886519019	93%
20	0.952532143	100%

5.1.5 Van De Graaff Layout

The first ICTs, as patented by Van de Graaff [45], consisted of a single stack of electrically insulated cores, effectively creating a bar core transformer. In order to prevent the magnetic flux from bypassing the HV cores completely, the stack is placed inside a metal, bell jar shaped container. This container is connected to the core around which the primary winding is wound, as seen in Figure 5.12. Flux can then bridge the gap between the top of the stack and surrounding container before completing the path to the primary winding, as seen in Figure 5.13. Because of its distinctive shape, this layout of core is commonly referred to as the Bell Dong ICT.

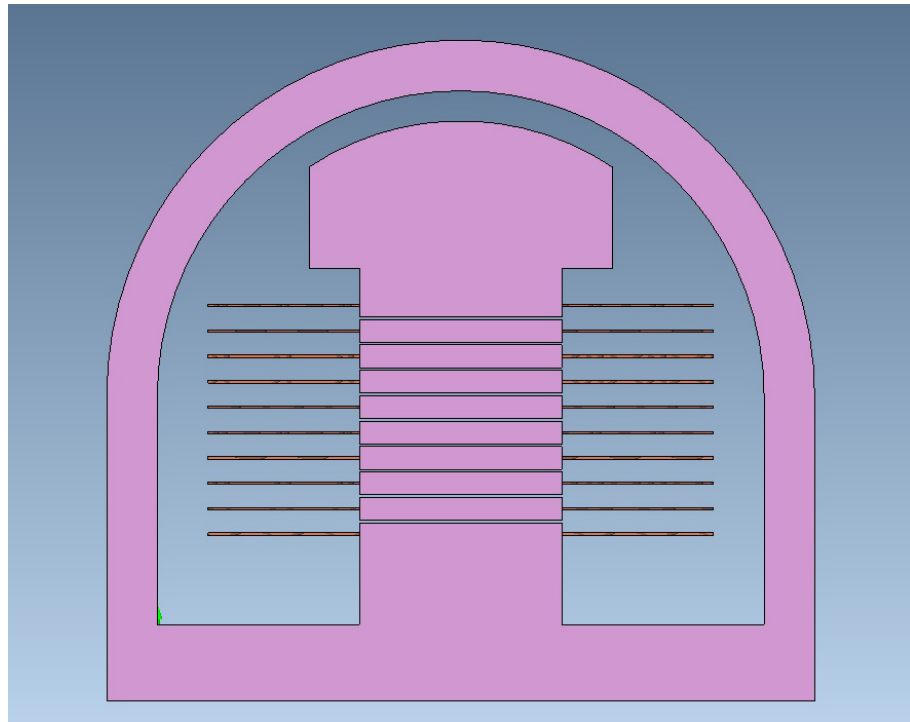


Figure 5.12 2D representation of the original Van De Graaff, or Bell Dong, ICT layout.

As the grounded bell jar has to be insulated from the total operational voltage of the device, it is necessary for a large gap to exist between the top of the stack and the container. This limits the flow of flux to the top of the stack. The recorded flux linkage in each winding, of such a device, is listed in Table 5.7.

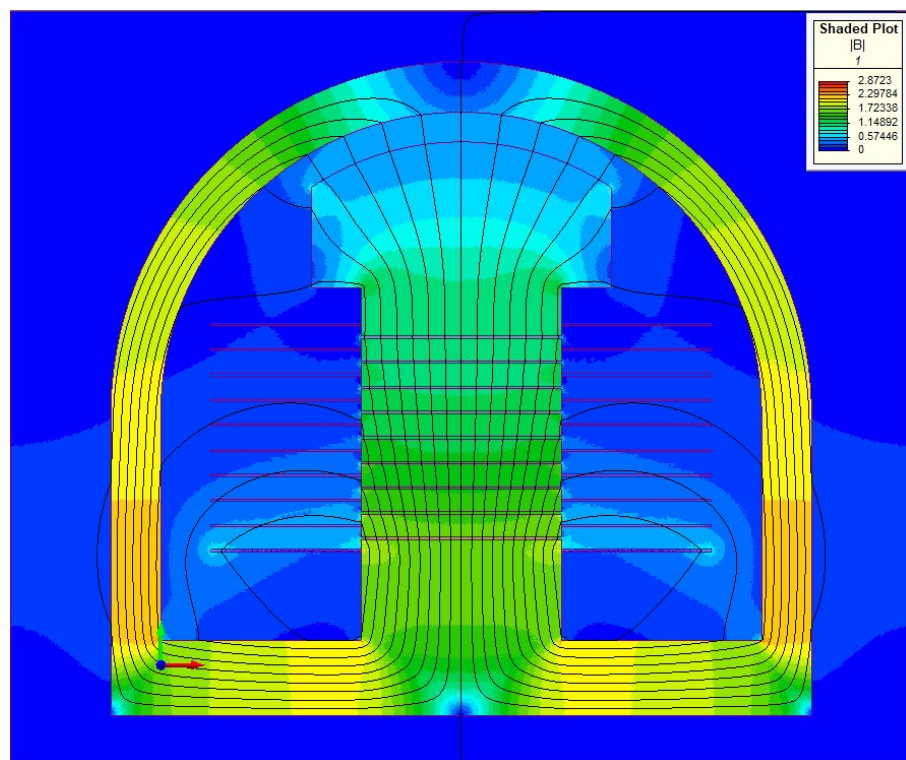


Figure 5.13 Flux flow within a Bell Dong Layout.

Table 5.7. Flux linkage in a 10 layer Bell Dong ICT.

Winding Number:	Flux Linkage (Wb-t):	Normalised Flux linkage:
1	1.074746	100%
2	1.000474	93%
3	0.936624	87%
4	0.882662	82%
5	0.836753	78%
6	0.79765	74%
7	0.764434	71%
8	0.736396	69%
9	0.712966	66%
10	0.693668	65%

5.1.6 Comparison of Different ICT Arrangements

The maximum flux linkages found in each ICT studied in the above sections, as well as the minimum flux linkage as a percentage of the maximum flux linkage, are recorded and shown in Figure 5.14. High peak flux linkage is ideal, as it reduces the number of turns needed to generate the same output voltage. In addition to this, as flux loss causes a reduction in output voltage, high flux retention is desirable. From Figure 5.14, it appears that there is a loose correlation between peak flux linkage and flux retention across an ICT design.

The simple stack of insulated transformer cores, driven by a single primary winding around the base core, had the lowest flux linkage, and greatest flux loss; flux diverters did little to improve this. Powering the stack, using a second primary winding, significantly reduced flux loss, but does little to increase the peak flux. However, providing a ferrous flux return path significantly increased both the peak flux and the flux retention. Accordingly, the biggest increase in peak flux linkage, and greatest reduction in flux loss, was brought about by combining these two methods in the form of the clamped return path.

There are both advantages and disadvantages to needing two windings per stage of an ICT. On the one hand, it drives up the cost of the design as twice as many cores and

windings are needed while, on the other, it effectively doubles the cross sectional area of the windings, which in turn increases the maximum current that can be drawn from the design.

The Bell Dong layout has a number of disadvantages, although it negates the expense of doubling the number of stages, as in the clamped return path layout, the bell jar will be incredibly complicated and expensive to construct. Furthermore, while the return clamp lends itself to being used in a multiphase system, as many phases can share the limb of the return clamp, the Bell Dong works exclusively with a single phase. This makes further development of this design challenging.

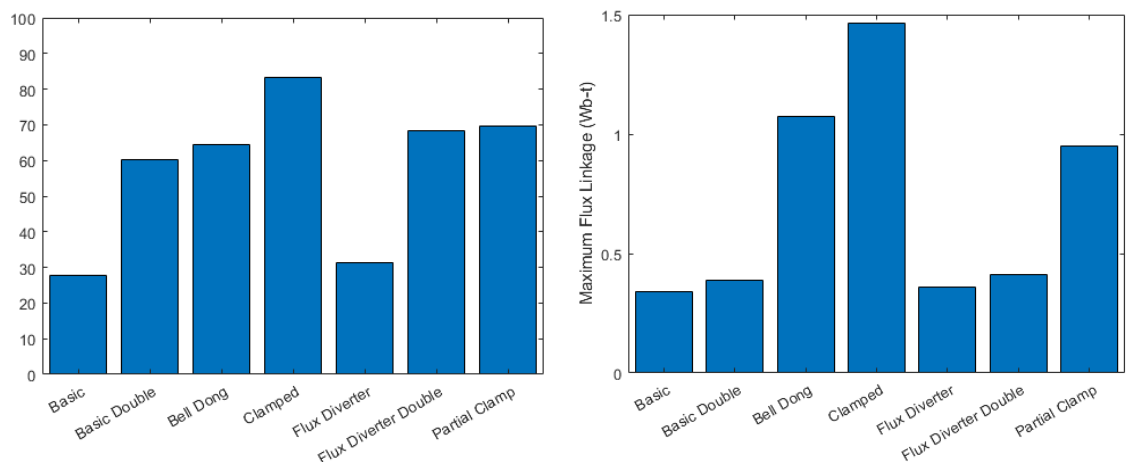


Figure 5.14 (LEFT) Minimum flux linkage found in each ICT as a percentage of the primary winding flux linkage and (RIGHT) maximum flux linkage in each design.

For these reasons, further work in this chapter will focus on designs that have a closed flux path constructed from soft magnetic material, similar in design to a conventional transformer.

5.2 Flux Path Layout

As already discussed, a necessity of creating a continuous flux path from soft magnetic material is that there needs to be two insulated cores operating at each voltage level. This is to stop the HV core needing to be insulated from the grounded primary winding. The Cross ICT [4], [5] achieved this by having two parallel insulated stacks connected, at the bottom, by a grounded core around which the primary winding is wound and, at the top, by another core section that would allow flux to pass between the two HV sections (Figure 5.15). This is an elegant solution as it means that the LV primary is at the bottom while the voltage in the stacks increases in the cores further away from the primary. However, there are problems with flux passing between the two stacks and being reluctant to change direction at the top of the design.

An alternative arrangement to this is one where a single stack is constructed that is driven by a primary winding at either end. These primary windings are electrically connected in parallel, meaning that they operate in phase with each other. The voltage increases towards the centre of the stack, where it is insulated from the LV winding at each end. Flux can then pass between the two windings via a solid clamp, as shown in Figure 5.16. This layout has the advantage that the magnetic flux has a straight path through the cores. In addition to this, having insulated gaps in a core effectively reduces the relative permeability of the core material. This means that the clamped system will reduce the amount of flux leaving the stack to return to the primary winding through the parallel flux path.

The relative flux path found in each layout was calculated and compared using a finite element analysis (FEA) model. In each case, an ICT was simulated with a core cross sectional area of 100 mm by 100 mm, and a thickness of 5.75 mm. There was a distance of 200 mm between the insulated stack and the return path, and a gap of 0.25 mm between each insulated core. Each core was surrounded by 100 turns. These parameters are reasonable as they are based on those commonly used in ICTs based on the Cross design [5]. ICTs with stack heights from 1 to 50 cores were simulated, in both layouts, and the minimum normalized flux in each system was recorded as shown in Figure 5.17.

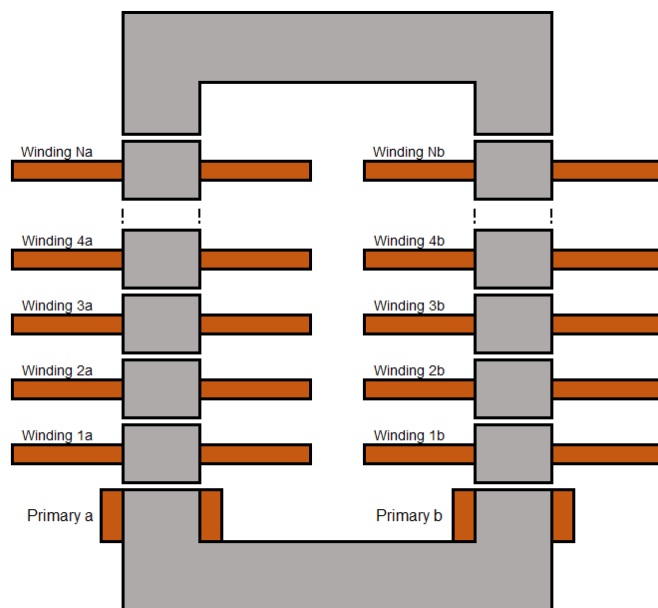


Figure 5.15 The traditional layout of the Cross type ICT.

From Figure 5.17, it can be seen that there is no significant difference between the flux losses obtained using either arrangement when the number of insulated cores is less than 30. For this reason, in a single phase ICT, a flux return clamped layout is inefficient as it effectively doubles the height and material cost of the design, without significantly reducing the flux loss. However, in designs that consist of multiple phases and a significant number of insulated cores (e.g. more than 40), the single stack configuration may prove advantageous. As the design, capable of

achieving the specifications outlined in the first chapter of this thesis, will require at least 50 cores, future work in this Chapter will focus on ICTs with a single stack configuration.

The flux loss predicted in these simulations, and detailed in Figure 5.17, is approximately half of that previously reported for an ICT [5] that was operating a higher voltage than used in this simulation study. The use of 2D simulation will lead to an underestimate of flux loss in the third dimension.

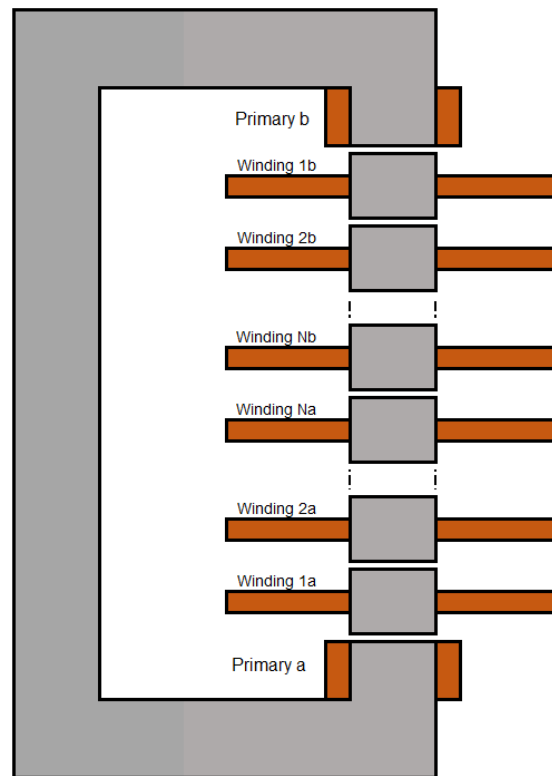


Figure 5.16 The proposed alternative layout of the Cross type ICT.

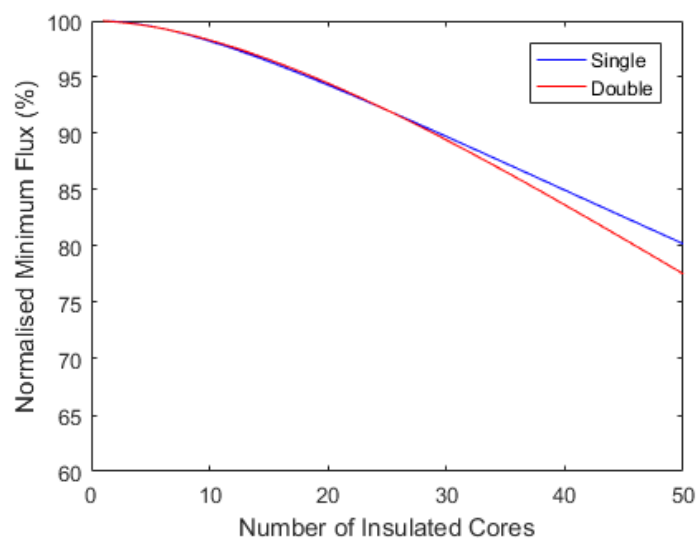


Figure 5.17 The minimum flux found in ICTs, arranged using both the traditional double stack layout and the proposed single stack layout, with a number of insulated cores ranging from 1 to 50.

5.3 Additional Improvements to Core

It is known that the biggest problem, with ICTs, is that magnetic flux tends to bypass the secondary windings. Flux is reluctant to cross the gaps between cores and so will instead return to the primaries via a more direct route. The most obvious route, for the flux, is to bridge the gap to one of the non-insulated limbs of the core; having bridged the air gap, it can enjoy an uninterrupted path to the primary.

There are two clear ways of reducing flux loss to the secondary windings: one is to reduce the number of gaps in the insulated section of the core; and the second is to increase the distance between the insulated stack and the return path.

5.3.1 Increase in Stage Sizes

It is not necessary for each secondary winding to be wrapped around an insulated core of its own. Flux loss might be reduced by grouping two or more secondary windings around each segment of insulated core to form a stage. This would reduce the number of necessary insulated cores, but require additional insulation between each stage as there will now be a greater potential acting on each section of insulated core. As well as this, the reluctance between each section of core and the flux return clamp will be reduced as each section will have to have a greater surface area to accommodate the additional windings.

A clamped return path ICT was constructed in MagNet, with 100 pairs of windings, with cores grouped into stages, so that multiple windings shared a core. The cross sectional area of the core was 80 mm by 80 mm, with each insulated stage being 9 mm thick, per winding. There was 1mm of insulation, between each stage, per winding. There was 160 mm between the core stack and the flux return clamp. The flux linkage found in the first 100 windings of a 200 winding ICT can be seen in Figure 5.18, for different stage sizes. It is impractical to have more than 20 stages per core, due to the difficulty in insulating the core from more than 200 kV.

The flux loss, in ICTs with larger stages, is noticeably reduced. Another interesting detail that can be seen in Figure 5.18 is that the flux linkage, in windings closest to gaps, is less than that in windings in the centre of stages. This is because the magnetic flux will fan out around gaps in the core, thus reducing the flux density passing through windings closest to the gaps. This phenomenon is shown in Figure 5.19.

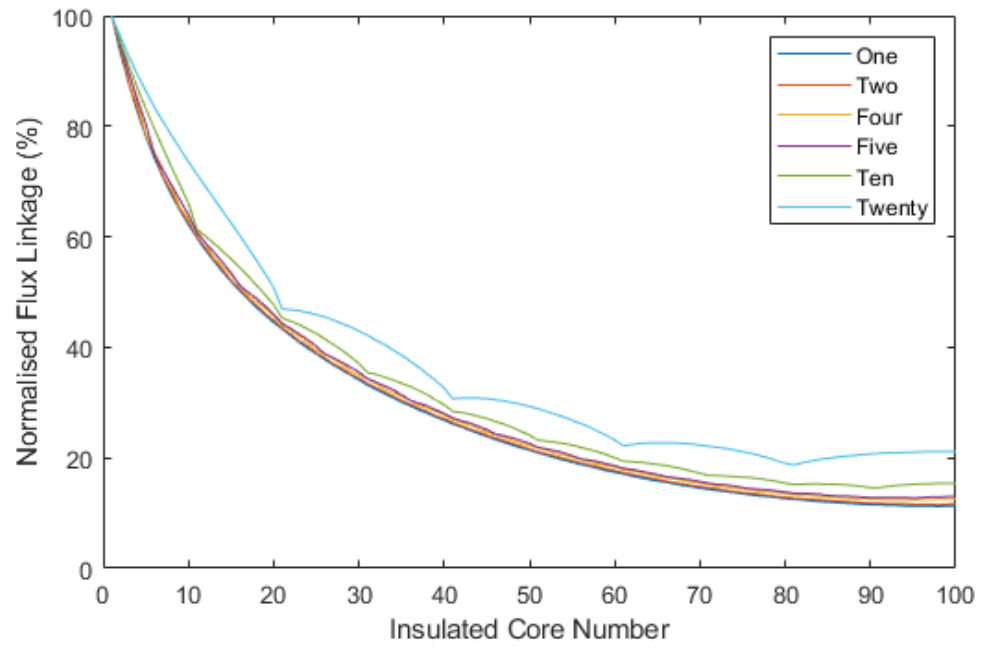


Figure 5.18 The flux linkage in the first 100 windings of a clamped return path ICT with various stage sizes, calculated using FEA.

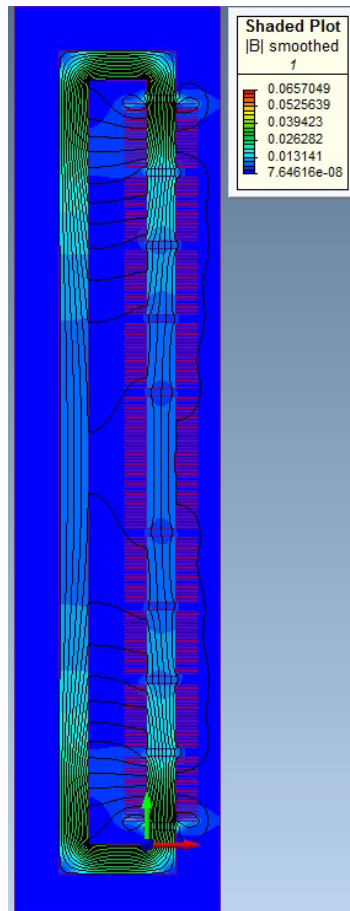


Figure 5.19 The flux contours in and around a clamped return path ICT with the 200 windings grouped around insulated cores in stages of 20.

5.3.2 Increasing Flux Path Length

The biggest source of flux loss in a clamped return path ICT is the reluctance between each insulated core and the return clamp. By this logic, it should be possible to reduce flux loss by increasing the reluctance between each insulated core segment and the return path. The easiest way to do this would be to extend the distance between the core stack and the return path.

An altered version of the clamped return path ICT was constructed in MagNet that had a 1.5 m gap between the insulated core column and the flux return path. This can be seen in Figure 5.20. The increased distance between the insulated core stack and the return path should make it more difficult for magnetic flux to cross from the insulated stack to the return path, thus reducing leakage flux.

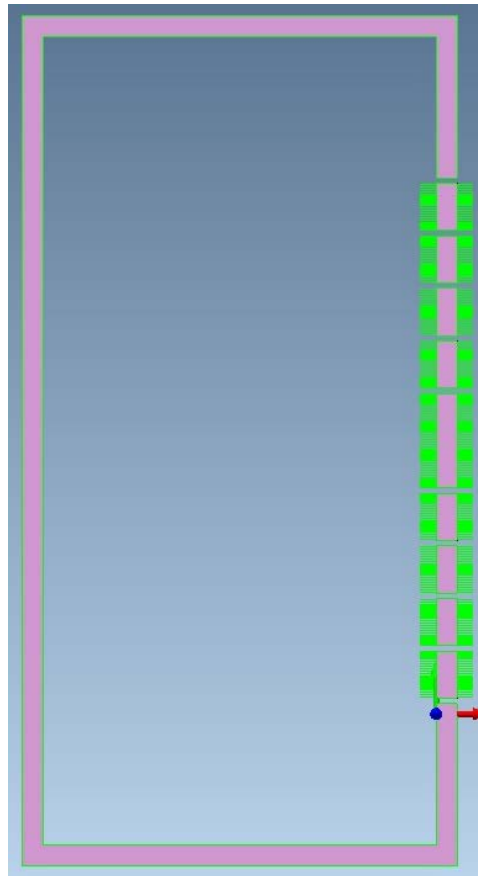


Figure 5.20 A clamped return path ICT with a stage size of 20. The distance between the insulated core stack and the return path is 1.5 m.

Again, a static simulation was performed and the flux linkage in each winding was recorded and normalised using a spreadsheet. The normalised flux linkage found in the first 100 windings can be seen in Figure 5.21.

A comparison of the minimum flux, in both the original and expanded core design, can be seen in Figure 5.22. The larger design consistently reduced the maximum flux loss by

between 16-17%. This is a relatively small improvement given the change in the size of the design. Figure 5.23 shows the flux contours inside the model of the enlarged clamped return path ICT and offers a clue as to why the difference in flux loss is so low. It can be seen that although a lot less flux bridges the return clamp, a noticeable amount of flux leaves the insulated core stack and passes through the air around it, re-entering the stack having passed around many of the centre windings.

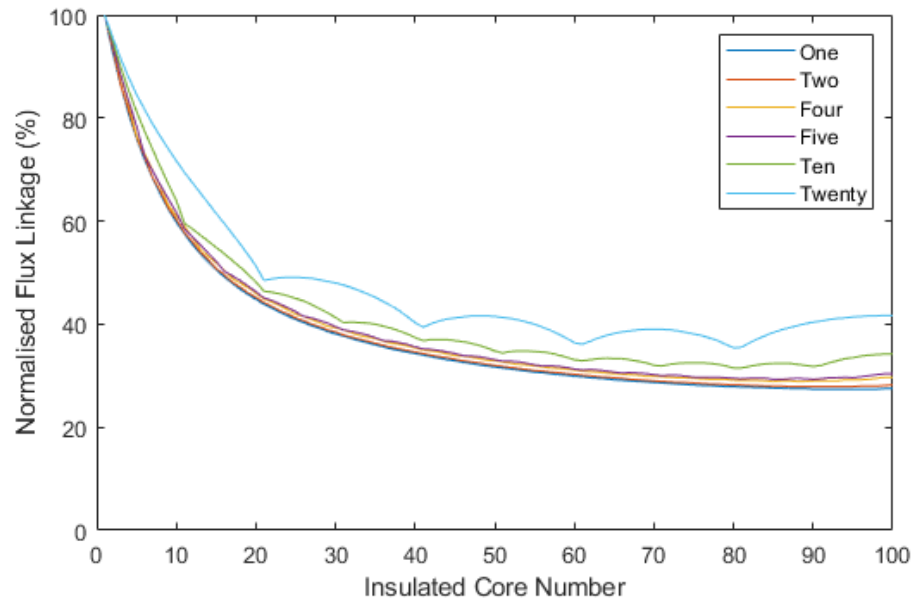


Figure 5.21 The flux linkage in the first 100 windings of a clamped return path ICT, with a distance of 1.5 m between the insulated core stack and the flux return path, with various stage sizes.

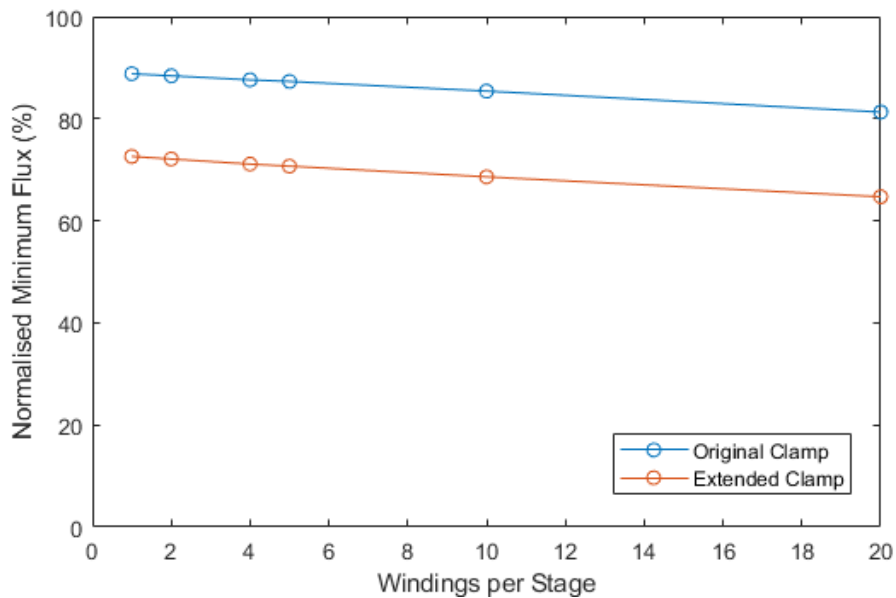


Figure 5.22 Minimum flux found in two clamped return path ICT, with 100 pairs of windings, with the stages grouped into different stage sizes, calculated using FEA.

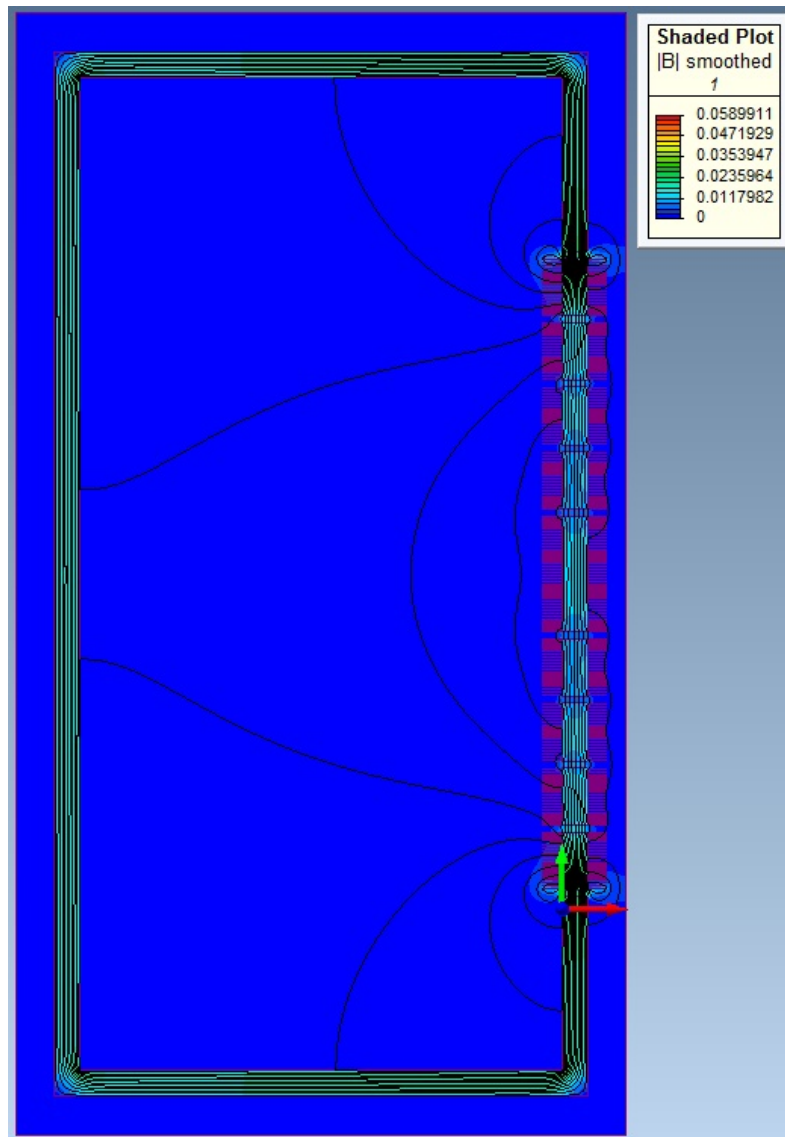


Figure 5.23 The flux contours around a clamped return path ICT with a stage size of 20. The distance between the insulated core stack and the return path is 1.5 m.

5.4 Benefits of Cross Core Technology

In addition to the closed flux path, there are several other appealing features of CTT over a conventional ICT. Most apparent is that the secondary windings are constructed from PCB windings [4],[5]. The HV power electronics are also surface mounted to these PCBs for reduced construction cost and complexity. An advantage of PCB printed transformer windings is that they consist of one or two layers of windings spiralling outwards; this makes very flat windings and has the benefit of reducing the thickness of each insulated core stage, therefore reducing the overall height of the design. However, a disadvantage of this technique is that it increases the surface area of each winding, thus increasing the parasitic capacitance between layers.

While conventional ICTs operate at single or three phase grid frequency, CTT uses power electronics and specialist core materials, such as nanocrystalline, to operate at a frequency close to 100 kHz. This significantly reduces the necessary size of the design, as well as the energy that must be stored in the voltage doublers to reduce ripple.

The key advantage of CTT is the use of tuned capacitors, connected across each secondary winding, to compensate for the flux lost between core slices [4]. A circuit diagram of the voltage doubler combined with flux compensation is shown in Figure 5.24.

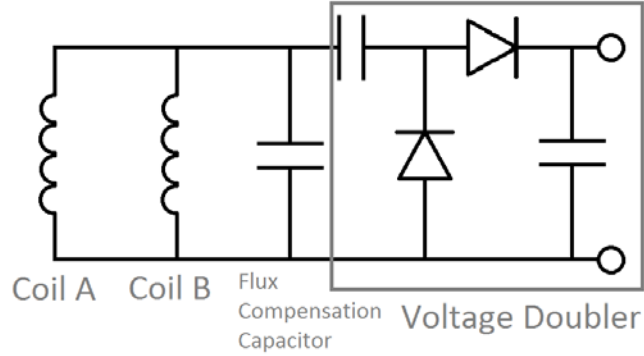


Figure 5.24 Circuit diagram of the secondary windings.

The capacitors are tuned to have a capacitance C_{flux} calculated using [5]

$$C_{flux} = \frac{l_g}{\mu_0 S_c N^2 (2\pi f)^2} \quad (5.1)$$

in which l_g is the length of the gap between insulated cores in meters; μ_0 is the permeability of free space; S_c is the cross sectional area of the gap between cores in meters squared; N is the number of turns around each core; and f is the operational frequency of the transformer.

An ICT, consisting of a stack of 50 cores, with the dimensions described in the previous section and a single core stack with clamped return path, was constructed in MagNet. The device was driven by a 500 Hz sinusoidal AC voltage source. Each secondary winding was connected in parallel with that of the other core acting at the same potential. The stack was driven by one of the secondary windings with a 100 V sinusoidal voltage acting upon it. A 1 k Ω resistor was connected across each set of secondary windings to draw an expected current of 100 mA. This design was simulated with and without a compensation capacitor, and the peak voltage found in each respective winding is shown in Figure 5.25.

From Figure 5.25, it can be seen that the inclusion of a flux compensation capacitor reduces the flux loss by around 10%, and also reduces the voltage drop per additional winding.

However, these simulations were carried out on a purely sinusoidal signal, which consists of a single frequency. In reality, an ICT that operates at high frequencies will likely be driven by pseudo square waves, which contain a large number of different frequencies. As the compensation capacitor can only be tuned to one frequency, it will add distortion to the overall signal. In order to evaluate this phenomenon, a single stack clamped return path ICT, with 50 pairs of secondary windings, each consisting of 100 turns, and driven by a pair of primary windings, each consisting of 4 turns, at either end of the stack, was constructed in MagNet. This ICT was simulated, with and without a flux compensation capacitor, while being powered by a sinusoidal signal with a frequency of 100 kHz and an amplitude of $400 V_{pk-pk}$. Figure 5.26 compares the voltage across the 50th windings of both of these simulations, with the ideal output, over the course of a power cycle. These simulations were repeated using square wave excitation, with the results being shown in Figure 5.27.

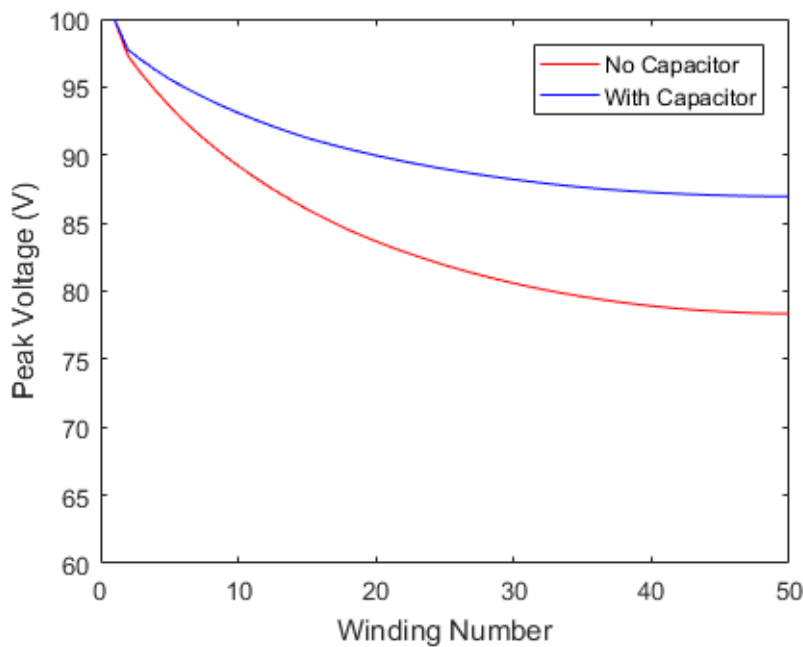


Figure 5.25 The peak voltage found in each secondary winding of an ICT, with 50 secondary circuits, with and without a flux compensation capacitor.

Figure 5.26 confirms the conclusions drawn from Figure 5.25; when sinusoidally excited, the flux compensation capacitor raises the output voltage by approximately 10%. However, there is no significant difference in terms of average voltage, between the waveforms in Figure 5.27. The results produced by the flux compensation capacitor are more distorted, including a peak that has an amplitude nearly twice that of the average voltage. This could lead to failure of the dielectric film used to isolate the stacks and make the quality of the output voltage difficult to control.

Two more techniques are employed, when manufacturing Cross type ICTs [5], to compensate for the effect that flux loss in the windings furthest from the primary winding has on the overall operational voltage of the design.

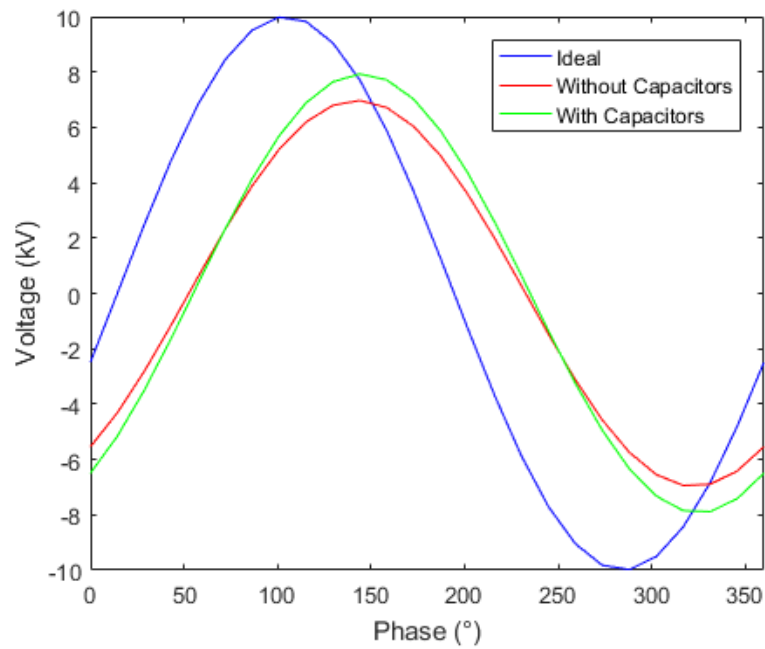


Figure 5.26 The 100 kHz voltage across the 50th pair of secondary windings, when excited by a sinusoidal signal with an amplitude of 400 V.

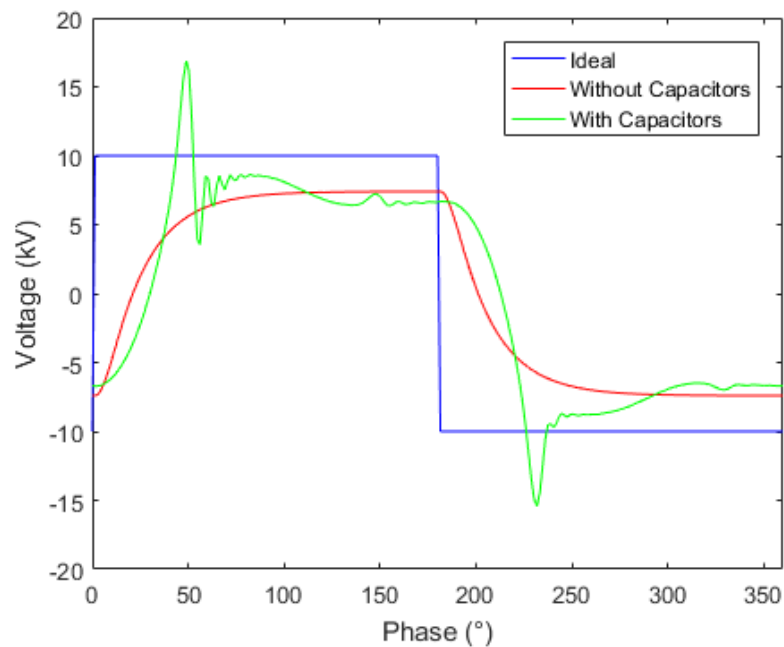


Figure 5.27 The 100 kHz voltage across the 50th pair of secondary windings, when excited by a square signal with an amplitude of 400V.

The first is to increase the voltage in the primary windings. This raises the voltage in each of the secondary windings, meaning that the lower secondary windings operate above their

nominal voltage to compensate for the voltage lost in the higher windings. However, operating the secondary windings at a voltage above what they were rated for comes with the risk of placing additional strain on the components, and may reduce the lifespan of the windings.

The other is simply to add additional cores to the top of the stack, each operating below their nominal voltage, until the desired overall voltage is reached.

5.5 Stored Energy

The use of capacitors, in flux compensators and voltage doublers, inherently stores energy in a system. The size of the capacitor C needed to reduce voltage ripple in a voltage doubler can be calculated using:

$$C = \frac{I}{2fV_{ripple}} \quad (5.2)$$

where I is the current drawn from the system; and V_{ripple} is the maximum allowable voltage ripple from the output voltage. The energy stored in each capacitor E_{stored} can then be calculated using:

$$E_{stored} = \frac{1}{2} CV^2 \quad (5.3)$$

Assuming each secondary winding produces 10 kV, doubled to 20 kV with a maximum allowable ripple of 0.5%, and operates at a frequency of 100 kHz, each capacitor will store 0.5 J. Multiplying this across all the capacitors in a stack means that the total stored energy per stack will be 50 J.

The energy stored in each compensation capacitor can be calculated using (5.2) and (5.3). Using the parameters described above, each capacitor will store 252 μ J of energy; meaning that, across the whole stack, they will store only 25 mJ. This is a negligible value and, hence, will be omitted from further calculations.

For reference, a Cockcroft Walton Generator, consisting of 10 stages, that produced 100 mA at 1 MV would need to store 1.1 MJ if operated at 50 Hz, or 550 J if operated at 100 kHz.

5.6 Circuit Equivalent Model (CEM) of Flux Loss

It has been suggested that the flux within a system can be modelled as a current in an electrical circuit [35]. This comparison is based on the fact that neither magnetic flux, nor electric current can have a non-zero value out of any closed surface. Although there are

many physical differences between current flow and magnetic flux, specifically that current in a circuit represents the constant flow of energy carrying electrons while the magnetic flux in a system is static, an equivalence exists between the two phenomena that allows the same principles to be used to calculate both the electrical potential in a circuit and the magnetic flux in a core.

There is a direct analogue between Electro Motive Force (EMF) and Magneto Motive Force (MMF), as well as resistance and reluctance. Using these basic components, a magnetic circuit can be constructed which can be used to model flux loss in a system, in the same way its electrical equivalent can be used to predict changes in potential difference.

The MMF in a system can be calculated using

$$MMF = iN \quad (5.4)$$

where i is the current in the windings around the core; and N is the number of turns of the winding around the core. The reluctance R_μ of the core can be calculated using

$$R_\mu = \frac{l_p}{\mu S_c} \quad (5.5)$$

where l_p is the length of part of the core, S_c is the cross sectional area, and μ is the permeability of the material. This is analogous to the resistance of a component, except that the conductivity is replaced by the permeability. In this way, a shell transformer core can be converted into a magnetic circuit, as seen in Figure 5.28, where the flux Φ in the system can be calculated using

$$\Phi = \frac{MMF}{R_\mu} \quad (5.6)$$

This is similar to Ohms Law, although resistance has been replaced by reluctance, and EMF has been replaced by MMF. In this analogy, magnetic flux is equivalent to electrical current.

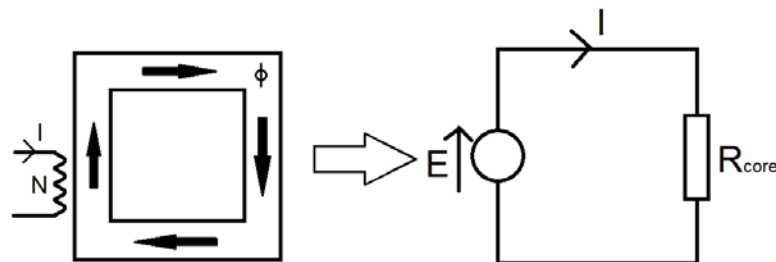


Figure 5.28 Magnetic flux loss in a core can be modelled as an electrical circuit.

This model can be extended further to calculate flux loss in insulated cores. If a small gap is placed in an otherwise closed magnetic core, the magnetic flux must cross this gap in order to complete the flux path. This gap can, therefore, be modelled as a reluctance in the closed magnetic circuit, as seen in Figure 5.29.

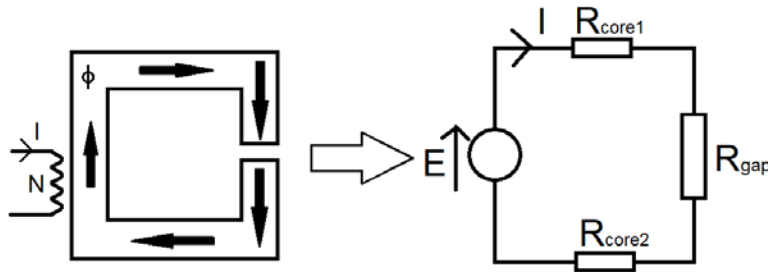


Figure 5.29 A gap in a magnetic core modelled as a resistance in a circuit.

If $\mu_{core} \gg \mu_{gap}$, then the reluctance of the core can be neglected, thus reducing the magnetic circuit seen in Figure 5.29 to the circuit seen in Figure 5.30.

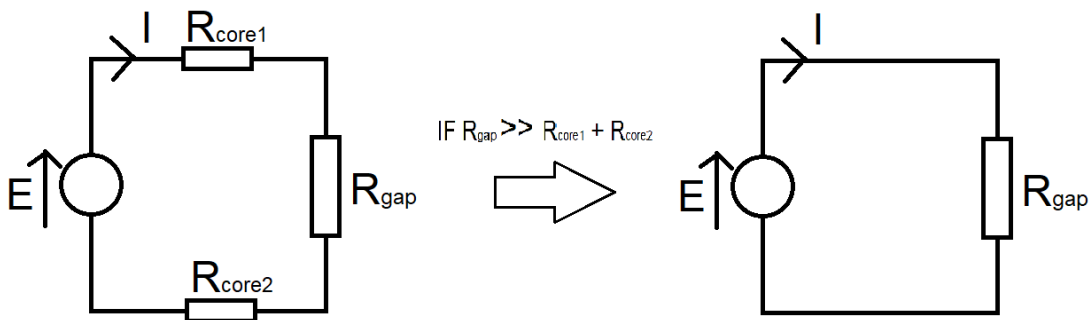


Figure 5.30 A simplification of the magnetic circuit shown in Figure 5.29.

This idea can be expanded on to make a model for a clamp flux return path ICT. Assuming that the gap between concurrent cores is relatively small and that the majority of the flux leaving the stack will do so by bridging the gap to the return clamp, then the whole core can be represented by a resistor ladder circuit. In this analogy, each section of core is represented by a single node and the flux return clamp is represented as the ground plane. As each of the gaps between each core, and the gaps between the cores and the flux return clamp, are the same, the whole ladder can be represented using only two resistor values. In this case, R_a will represent the gap between the cores and the clamp, while R_b represents the gap between cores. This circuit can be seen in Figure 5.31.

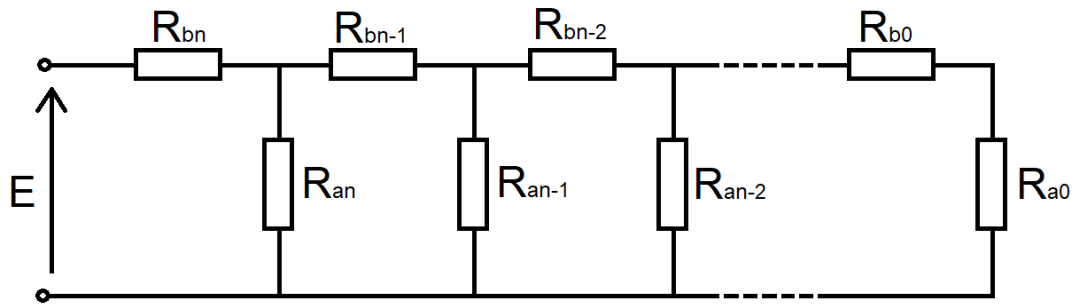


Figure 5.31 The flux circuit equivalent model of a clamped return path ICT.

The flux at any given point in the core can now be estimated much more easily using conventional circuit analysis. In this way, the flux loss in an ICT can be worked out by hand or, for larger cores, using a spreadsheet. If the flux in the system is then normalised so that the flux at the primary winding is unity, then the flux loss in one design can be compared to the loss in others. In the remainder of this section, the normalised flux loss of transformers with different numbers of secondary windings, different numbers of insulated core stages, and different shapes will be evaluated using this method. Results obtained using this approach can then be used to reduce the number of FEA based simulations required to optimise the magnetic design of an ICT against the given design specifications.

5.6.1 Stack Height

The height of a stack of insulated cores can be modelled, using the magnetic circuit analogy, by the number of resistors connected to the ladder. In this way, the maximum flux loss found inside ICTs of different heights can be predicted by simulating a resistor ladder using a spreadsheet. It is expected that the greatest flux loss will be seen in the middle of the stack as this is the furthest point from both primary windings. In order to find the minimum flux in the stack, as a proportion of the peak flux, one simply has to divide the MMF across the terminal reluctance by that at the input to the ladder.

Using this technique, the maximum flux loss was found for ICTs of various heights, up to 100 insulated cores, was estimated and normalised. The cross sectional area of the core was 100 mm by 100 mm, with each insulated stage being 5.75 mm thick. There was 0.25 mm of insulation, between each stage. There was 200 mm between the core stack and the flux return clamp. These are the same specifications used as in Section 5.2. The results of the CEM are compared, with the results obtained using FEA, in Figure 5.32.

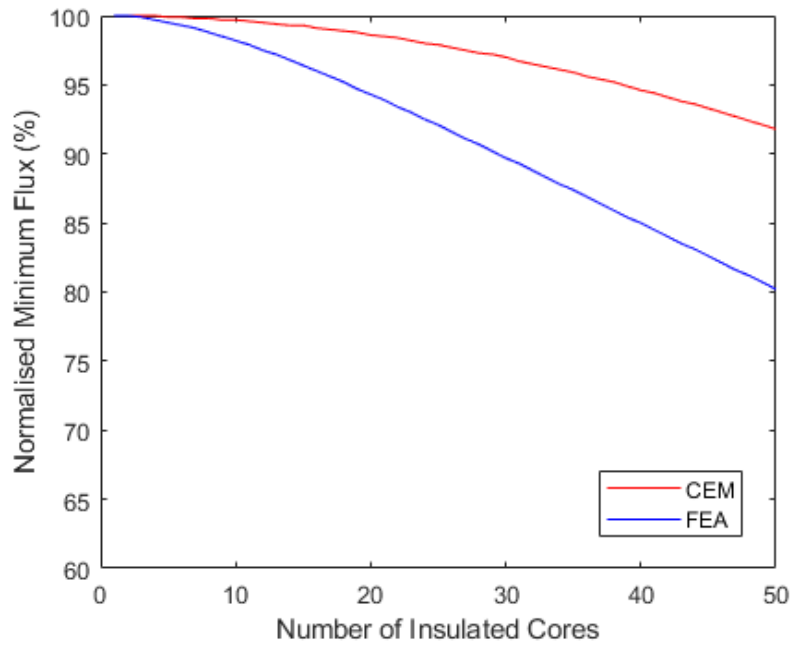


Figure 5.32 The minimum flux in an ICT, with different numbers of insulated cores, calculated using the circuit equivalent model, and finite element analysis.

5.6.2 Different Stage Sizes

The CEM was used to estimate flux loss in a system with increased stage sizes. The same dimensions were used, in this model, as in Section 5.3. The results of this can be seen in Figure 5.33.

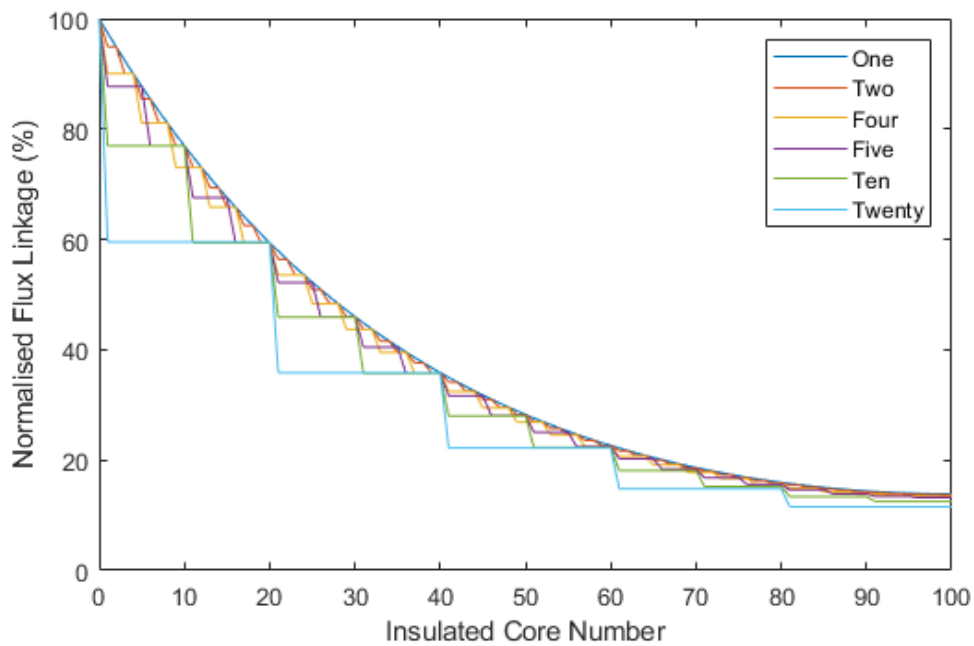


Figure 5.33 The normalised flux linkage in the first 100 windings of a clamped return path ICT with various stage sizes, calculated using the CEM.

Two features are noticeable in Figure 5.33. The first is that the flux linkage in all windings that share a stage is the same. This is because the CEM does not account for flux leakage within each stage. The second is that there is no difference in the overall flux loss, regardless of the stage size. As using a larger stage merely lumps circuit parameters together, the CEM predicts the same results only with varying levels of fidelity.

The results of the CEM were then compared with those obtained using FEA. Figure 5.34 shows a comparison of the flux linkage found in each winding of an ICT with a stage size of 20, calculated using the CEM and FEA.

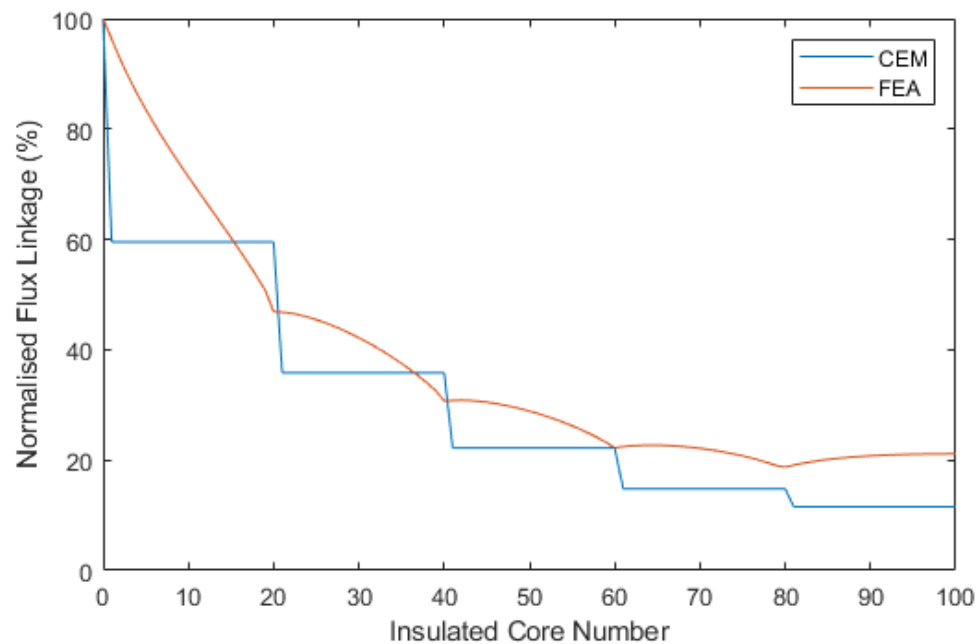


Figure 5.34 The normalised flux linkage in the first 100 windings of a clamped return path ICT, calculated using CEM and FEA.

From this, it can be seen that the two results are quite similar. However, the CEM overestimates the flux loss towards the centre of the stack and is more accurate towards the outside of the stack. This is because the error in calculating the flux in each stage adds up so that cores in the centre of the stack have a greater accumulation of errors. There is a 7.2% difference in the minimum flux linkage calculated using the two methods.

5.6.3 Extended Flux Path

The CEM was also used to evaluate the use of an increased flux path length. The results of this are compared, with the results obtained using FEA, in Figure 3.35, for systems with stage sizes of 1 and 20.

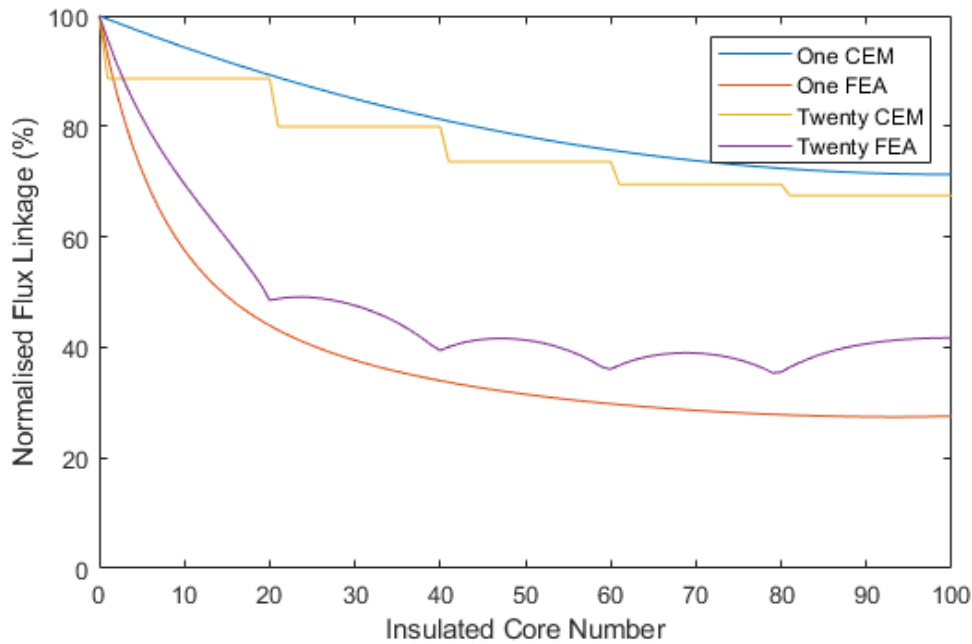


Figure 5.35 The normalised flux linkage in the first 100 windings of a clamped return path ICT with an extended flux path, with stage sizes of 1 and 20, calculated using both the CEM and FEA.

From Figure 5.35, it can be seen that the CEM grossly underestimates the flux loss in the cores. This is because, as the distance between the insulated core stack and the flux return clamp increases, the path of the flux loss becomes less predictable and does not conform to the simplified expectations used in the CEM. For example, the CEM could not predict the leakage flux returning to the insulated core stack, as was evidenced in results shown in Figure 5.23.

5.6.4 Evaluation of the Circuit Equivalent Model

The flux circuit model can be seen as a simple, static approximation of what actually happens inside and around an ICT. Many sources of loss are neglected in order to reduce the complexity of calculation. There is no reason why, for example, flux may not jump to the return clamp from the gap between insulated cores; it is merely assumed that, due to the relatively small size of the gaps, very little will do so compared to the amount of flux from the insulated cores themselves. This method also assumes there will be no crossover of flux between components. That is to say, that flux will pass from the insulated core to the flux return path at a tangent to the surface of the core as shown in Figure 5.36. In reality, it is known that the flux will not be constrained to the magnetic core.

The biggest limitation of this model is that it effectively creates a primitive simulation with very large mesh elements. The area between each insulated core and the flux return path as seen in Section 5.3.1, for example, is equivalent to a single mesh cell of $1,620 \text{ mm}^2$. It

stands to reason that, the larger the elements of the ICT are, the less accurate the model will become.

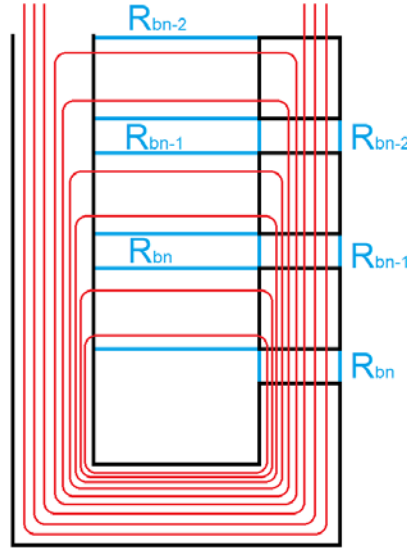


Figure 5.36 The flow of flux in a clamped return path ICT, as modelled by the Flux Circuit Equivalent Model.

For these reasons, the flux circuit model may be used as a tool for performing quick calculations of flux flow within a system, and may be used as a pilot study before employing computationally complex FEA, but should not be used in place of detailed simulation.

5.7 Increasing the Current Output

There are three factors that limit the current that can be drawn from an ICT. These are the flux density of the core, the power electronics and the winding thickness. The power electronics can, theoretically, be designed to accommodate any current, simply by selecting components rated to suitable specifications. The saturation of the core is more problematic in ICTs than in conventional transformers, as the relative permeability of the core material is effectively reduced by the insulated gaps. The saturation current becomes difficult to predict due to the non-linear nature of the insulated cores.

The limitations imposed by the winding thickness are easier to calculate as the largest current that can safely pass through the tracks of a PCB can be determined by the IPC- 2221 standard [115]. This standard dictates that the largest continuous current that can safely be used in a PCB can be calculated using:

$$I = k\Delta T^{0.44} S_{mil}^{0.725} \quad (5.7)$$

where I is the current passing through the track in Amperes; ΔT is the permissible change in temperature in $^{\circ}\text{C}$; S_{mil} is the cross sectional area of the track in mil^2 ; and k is a constant

determined by the IPC-2221. For tracks printed on the surface of a PCB, in atmospheric air, $k = 0.048$.

Assuming each PCB is printed on a board with a copper thickness of 0.305 kgm^{-2} (1 Ozft^{-2}), the most commonly used copper thickness in PCB design, and the tracks are printed with a width of 0.5 mm , then the maximum safe continuous current would be 1.46 A . This is even supposing that a maximum temperature increase of only $10 \text{ }^{\circ}\text{C}$ was imposed. Given the potentially dangerous nature of a fault in this project, it is not unreasonable to impose a large margin of error onto the maximum current, say, no more than half of the PCBs rated current may flow through the PCB windings during normal operation. This brings the effective rated current of each PCB down to 0.73 A , although because in this design, each winding is connected in parallel to another winding, the effective rated current of the stack once again becomes 1.46 A .

There are two ways in which the operational current of the ICT could be increased. The first is to increase the size of the single phase ICT, by widening the diameter of the tracks and the core. This will raise the saturation flux of the core and the current that can safely pass through the windings.

The second is to connect multiple stacks in parallel, as shown in Figure 5.37. This arrangement has the advantage that scaling up a design becomes a trivial exercise rather than having to redesign the whole design from first principles. To increase the operational current of the supply, one simply needs to add additional stacks to the existing design. Using multiple stacks also reduces voltage ripple, provided that each operates out of phase [26].

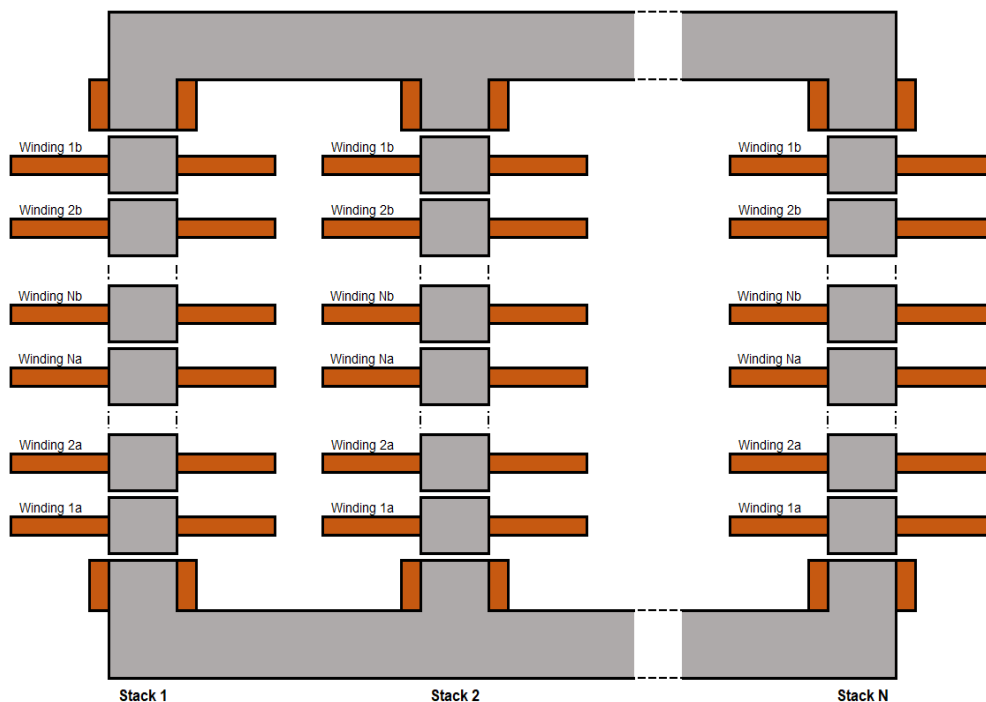


Figure 5.37 The layout of a multiphase ICT.

5.8 Possible Future Developments

It has been shown that an ICT can be used to produce 500 kV AC, which can then be doubled and rectified to produce 1 MV DC. It has also been shown that several of these ICTs can be connected in parallel to, theoretically, achieve any output current. The analysis in this Chapter indicates that a power supply, based on CTT, could be constructed to produce 2 A at 1 MV.

In order to evaluate whether this technology is suitable for future development, with the aim of creating a 5 MV power supply, the process that was carried out in Section 5.2 was extended to ICTs of up to 100 pairs of cores. Once again, the minimum normalized flux linkage in each model, calculated using FEA, was recorded and plotted in Figure 5.38.

From Figure 5.38, it can be seen that the minimum system flux drops significantly as the stack height is increased. Using the system parameters listed in Section 5.3, a roughly 40% flux loss is expected in the HV secondary windings of a 1 MV stack. Although this flux loss could conceivably be compensated for by having more windings around the higher voltage cores, given the exponential decline of flux linkage in higher stacks, it is unlikely that this technique could practically be applied to a 2.5 MV ICT with the intention of doubling this voltage to create a 5 MV power supply.

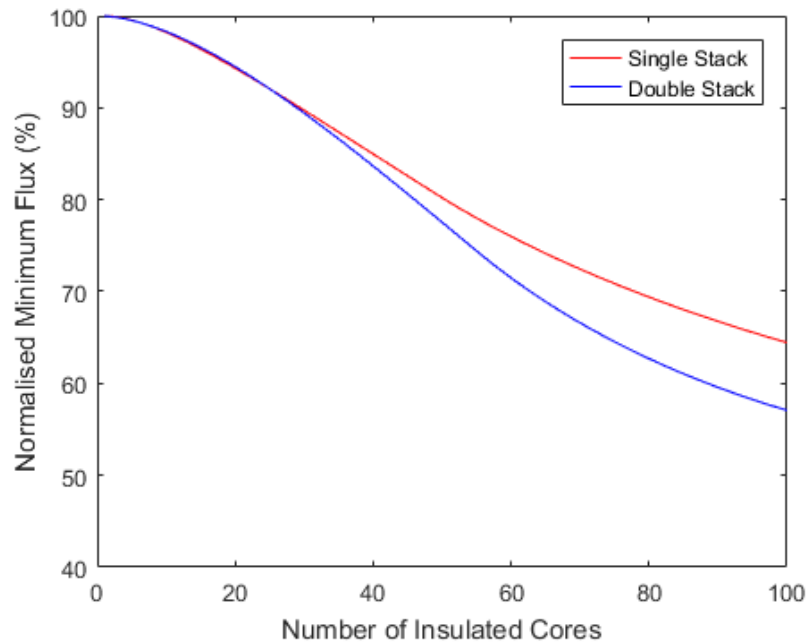


Figure 5.38 The minimum flux found in ICTs, arranged using both the traditional double stack layout and the proposed single stack layout, with a number of insulated cores ranging from 1 to 100.

5.9 Limitations of Simulations

The biggest limitation of the simulations, performed on the ICTs, is that they were carried out in only two dimensions. They, therefore, assumed that all flux would flow in a single plane. This assumption is provably false as it neglects the flux flow in the third dimension. In 2D, the flux flows in a straight line between the stack and the clamp while, in 3D, the flux fans out around the gap between the stack and the clamp. This essentially widens the cross sectional area of the flux path and reduces its reluctance; in turn, increasing the flux loss at each stage of the ICT.

To the author's knowledge, there is no simple way of estimating the flux loss in a 3D model based on the results of a 2D simulation, and so the only way of increasing the accuracy of the models would be to perform simulations on a 3D model. However, this would be very computationally intense, and each model would be so laborious in its construction that simulating hundreds of models using a macro, as was done with the 2D model, would not be possible over the time frame of this study.

Another limitation of the simulations undertaken in this study is that they do not take into account the environment around the ICT. In a practical system, the ICT will likely be held inside a metal tank that will contain an insulating medium. If the tank is constructed from a non-magnetic material, such as copper, then it will not have an effect on the flux flow in and around the core. However, if the core is made from steel, or some other soft magnetic material, then it will have an effect on the magnetic flux flow. A comparison of the flux flow around the ICT, both inside and outside the tank, can be seen in Figure 5.39.

Figure 5.39 shows a noticeable difference in flux flow induced by including a ferrous tank. The minimum flux linkage found in any winding in the ICT without a tank was 80.5% of the flux linkage in the primary windings, while the minimum flux linkage found in the ICT in the tank was 78.4% of the flux linkage found in the primary windings.

These differences are not important for this project, which merely seeks proof of concept. However, development of a prototype design will need to take each of these considerations into account.

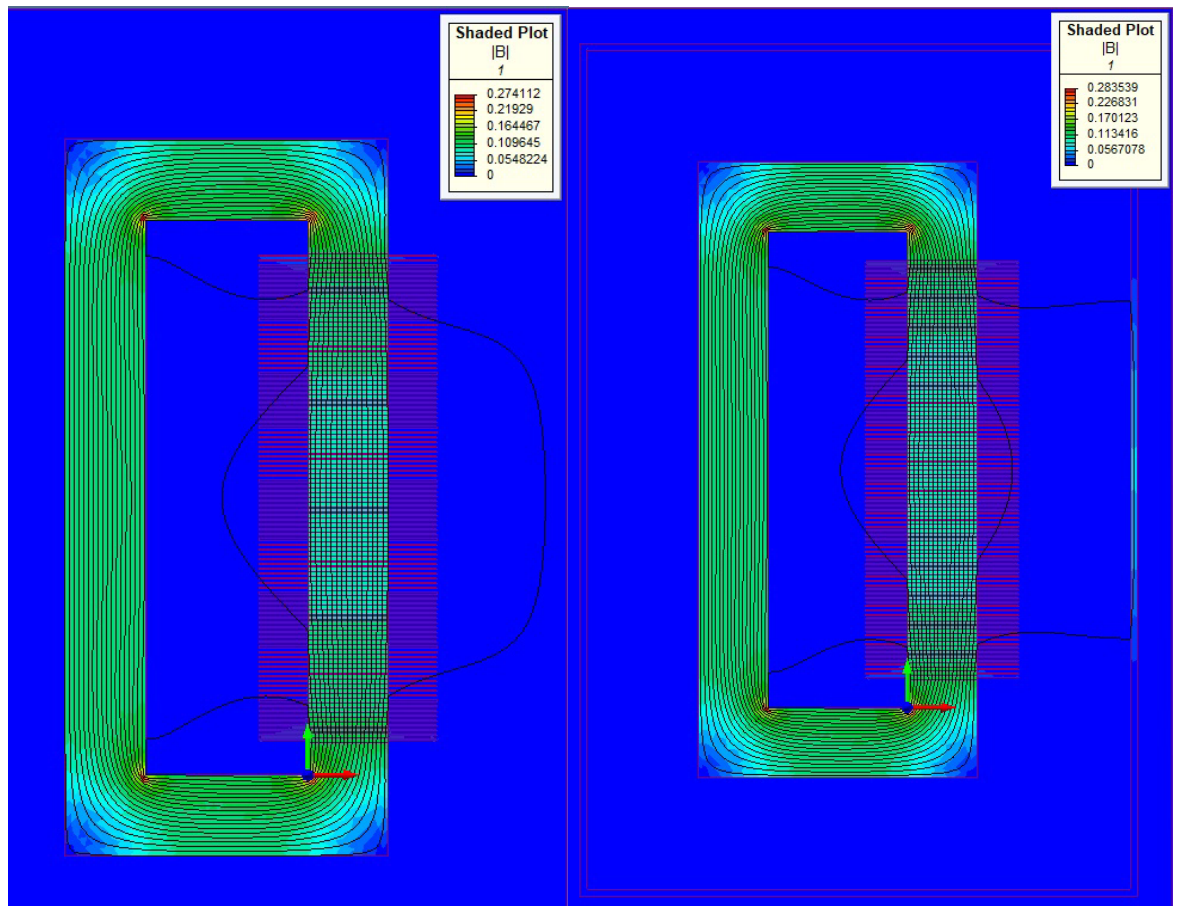


Figure 5.39 Flux flow around a clamped return path ICT (LEFT) outside of a ferrous container and (RIGHT) inside of a ferrous container.

5.10 Possible Improvements and Concluding Comments on ICTs

The effectiveness of ICTs in producing 500 kV, which can then be rectified and doubled using voltage doublers, has been evaluated, as well as a number of ways of reducing flux loss. It can be concluded that ICTs may be used as the basis of a 1 MV power supply that produces currents in the order of hundreds of milliamps. It was then shown, in Section 5.7, that by connecting multiple ICTs in parallel, the design could be expanded to produce outputs of an Ampere or more, with little voltage ripple. To meet the requirement of minimal stored energy, it is necessary to design a primary excitation source capable of switching mains voltages (e.g. 400 V) at as high a frequency as possible. This in turn has the effect of negating some of the advantages of using the flux compensation capacitors as the primary waveform is very likely to be non-sinusoidal.

It has been shown that, although ideal for a 1 MV power supply, ICT technology is currently not suitable to be scaled up to 5 MV. Further work will focus on investigating other promising

technologies that might facilitate scaling to 5 MV. It is possible that an ideal solution would be a combination of ICTs and another technology, for example the cascade transformer.

Chapter 6

Cascade Transformers

This chapter summarises an investigation into the suitability of a cascade transformer based power supply to meet the requirements outlined in Table 1.1. First, a brief overview is given of the principles of transformer design, with particular focus given to determining optimum core parameters. Then, attention is given to maximising the output voltage of the power supply. This involves modelling flux loss across the design using both 2D and 3D simulations. Through this work, a novel new core layout is proposed which potentially has a very high power density. Finally, the potential future development of this design is discussed.

6.1 Design Methodology

Much work has gone into developing techniques to determine the optimal design of a transformer [36]–[38]. These techniques usually consist of a number of steps which take a collection of design parameters, such as operating voltage and frequency, as well as the properties of the selected core material, and calculate the peak magnetic flux density B_{max} in the transformer core. This value can then be used to calculate the power loss in the transformer core and windings, and the overall efficiency of the design.

The suggested equations used to calculate B_{max} take into account the geometry of the core, as well as environmental factors such as ambient temperature, to predict the flux leakage in the design. These equations are often highly complex and involve arbitrary constants that are given with little explanation and are often based on the authors experience [36]. For these reasons, these complex equations are eschewed in favour of a simpler equation derived from first principles. As a significant proportion of this chapter is devoted to minimising flux loss, and each transformer will be in close proximity to other transformers, it is unlikely that the assumptions used in the literature will hold true for the purposes of this project.

In this section, the necessary steps will be undertaken to design the stages of a cascade transformer. This work will, then, be verified in simulations in the rest of this chapter.

6.1.1 Flux Equation

Faraday's Law can be used to derive

$$V = B_{max} k_v N_p S_c f \quad (6.1)$$

where V is the peak voltage in the core, k_v is a constant that converts frequency to angular velocity, it has a value of 4.44 for sinusoidal waveforms and 4 for square waves, N_p is the number of turns of the primary winding, S_c is the cross sectional area of the core, and f is the frequency of the primary current. This equation is useful for deciding the necessary cross sectional area of the core. If the frequency and primary voltage are stated design parameters, and if B_{max} is given by the core material, then S_c is inversely proportional to the number of turns.

6.1.2 Transformer Losses

The total loss in a transformer is the sum of the losses generated in the core and in the windings. Methods of estimating core losses have been discussed in Chapter 3, while winding losses were considered in Chapter 4. The total loss in the transformer can then be calculated using

$$P_{loss} = P_{fe} + P_{cu} \quad (6.18)$$

From this, the efficiency of the device η can be calculated using

$$\eta = \frac{P_{total} - P_{loss}}{P_{total}} \quad (6.19)$$

Where P_{total} is the total power inputted into the transformer.

There are several decisions to be considered when optimising the design of the transformer; one of which is the size of the core. Ideally, for the greatest power density, the core should be as small as possible. However, this might not produce the greatest efficiency from the transformer. There is also a practical limit to how small the core cross sectional area can be before the core becomes too brittle to be used in a practical transformer. For this reason, it might be necessary to increase the diameter of the core to a value that is wider than optimal.

6.1.3 Simulation Design

The remainder of this Chapter will focus on optimising a design based on a series of parameters that are detailed in this section. These parameters should help establish a proof of concept for a cascade transformer based power supply, and can be used as a template for a future prototype. Note that this chapter only examines the magnetic field around a cascade transformer, and does not consider electrical insulation. This is a practical issue that must be considered during the prototyping stage of this project and is, therefore, outside the scope of this thesis.

In order for the simulations to be consistent, it is important that each of the transformers being simulated have the same characteristics. For this reason, it was arbitrarily decided that the power supply would be constructed from sixteen phases, each consisting of a stack of 60 PCB based secondary windings acting out of phase with each other. Each stack would be excited by a primary winding with 4 turns and each secondary winding would have 100 turns and produce a voltage of 10 kV. The voltage per turn ratio of each transformer would be 100 Volts per turn. Each cascade would consist of three cores, each supporting two transformers acting 180° out of phase with each other, with the secondary windings divided equally between them. Eight such cascades will be connected in parallel.

In order to keep each core at a fixed potential, it is important that the secondary windings are not all connected in series, before being rectified by a single voltage doubler, as doing so would cause the potential of each core to fluctuate with the excitation voltage. This is not a problem in a single phase cascade transformer, however, if two or more phases were to share a core then the potentials in the higher cores would cancel each other out. This would negate the benefits of using a cascade transformer. Instead, the secondary windings around of each stage will be connected in series (in groups of 20), with a voltage doubler connected across each group of secondary windings. This arrangement rectifies the voltage after each stage, meaning that each transformer remains at a constant potential; this is shown in Figure 6.1. It is also possible to connect 60 voltage doublers across all 60 secondary windings individually, as was the arrangement used in the Cross ICT, and connect these voltage doublers in series. However, doing this would double the voltage applied across each core. Thus making this arrangement unsuitable for use in cascade transformers.

Assuming 100% flux efficiency of the design, the secondary windings in each stack should produce a total of 600 kV at 250 mA and 100 kHz. This can be processed, using voltage doublers, to produce 1,200 kV DC at 125 mA; thus producing a total of 2 A between the sixteen phases. The idealised voltage waveform between ground and the secondary windings, and between ground and the voltage doublers, are shown in Figure 6.2.

The output voltage has been deliberately selected to be more than the 1,000 kV required for this project, to allow for a certain amount of flux loss in the core. Not accounting for power loss, the input current for each stage of the stack is: 125 A for the top stage; 250 A for the middle stage; and 375 A for the bottom one. It was decided to use a simulated material with a relative permeability of 1,000. This is lower than would ideally be used in the real world, and so was selected to exaggerate the flux loss in the simulations.

Equation (6.1) was used to determine that, in order to create a flux density of unity, the minimum cross sectional area should be 225 mm^2 . Because this equates to a square core only 15 mm thick, which would likely be structurally unsound, it was decided to increase the area to the core to $1,600 \text{ mm}^2$, which equates to a thickness of 40 mm.

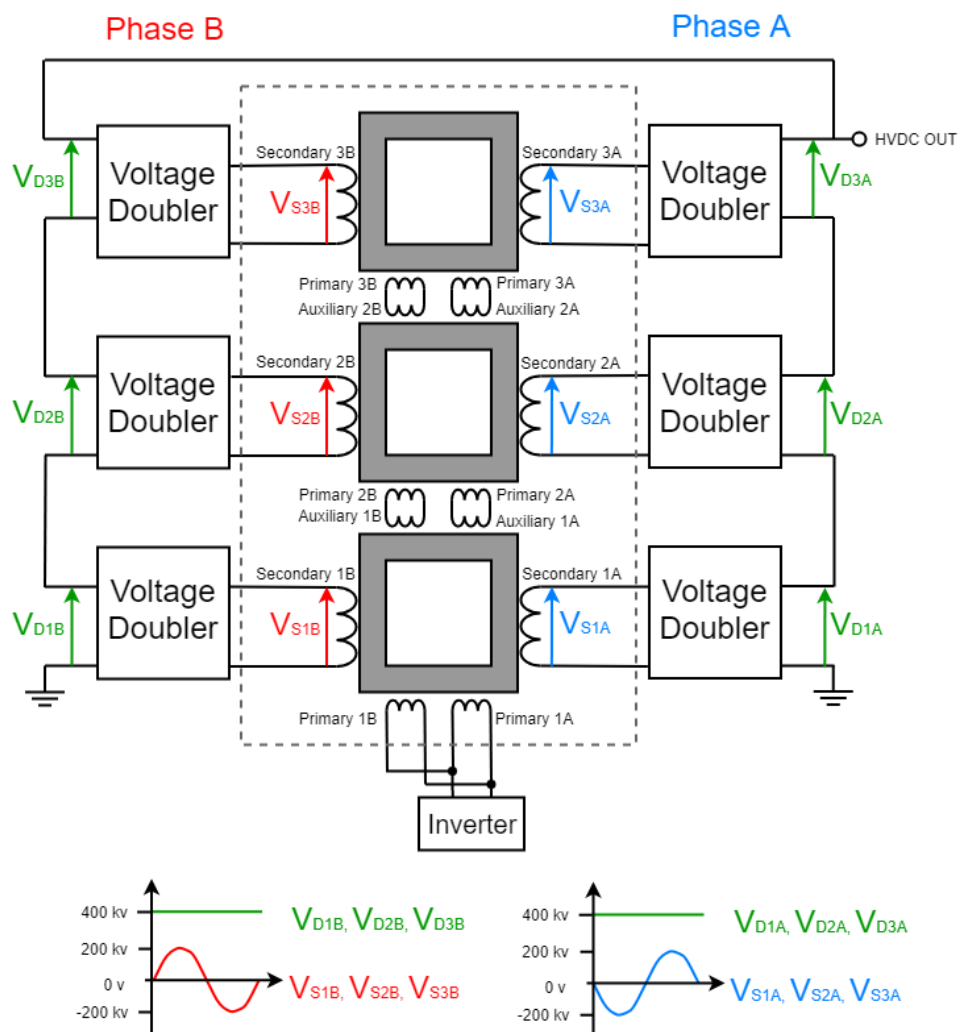


Figure 6.1. (TOP) A conceptual design of each three stage cascade transformer. Two phases share this cascade, A on the right and B on the left, with each having its own set of primary, secondary, and auxiliary windings. All of the secondary windings around each core are grouped into two phases. Voltage doublers are connected across each group of secondary windings. Note that only things inside the grey dotted line are actually modelled. (BOTTOM) The idealised voltage waveforms of the groups of secondary windings, and the outputs of the voltage doublers.

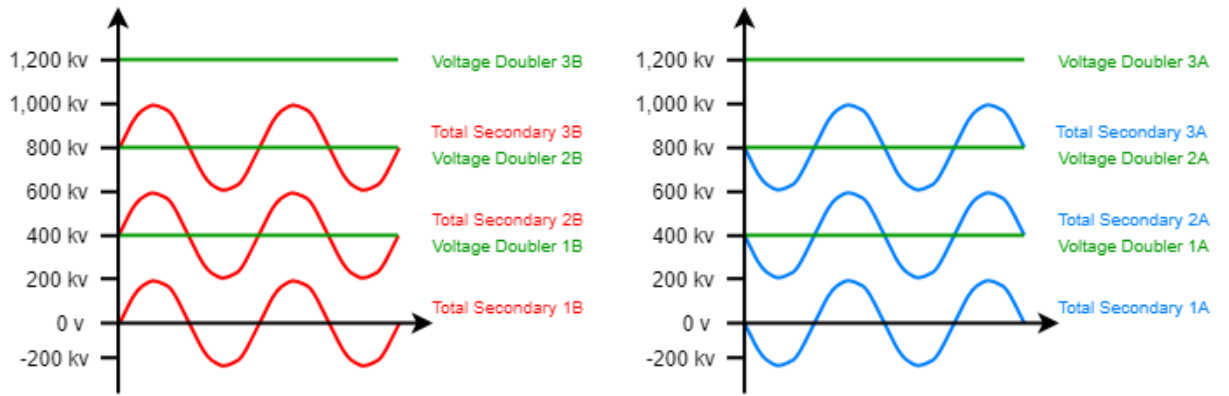


Figure 6.2. The idealised voltage waveforms of the grouped secondary windings, and voltage doublers, relative to ground.

6.2 2D Simulations

As in the case of ICTs, flux leakage will reduce the output voltage of the cascade. Although the design, outlined in the previous section, does allow for a certain amount of flux loss, it is desirable to keep this to a minimum in order to maintain voltage across the supply. For this reason, it was decided to find the arrangement of primary and auxiliary windings that suffered the lowest flux loss. A number of potential layouts were proposed, and simulated using MagNet. The voltages in the secondary windings were observed to determine the flux at different stages of the design.

In this section, the cascade transformer that was described in Section 6.1.3 is simulated, in order to determine the winding arrangement that retained the most flux. A number of different winding arrangements are simulated in 2D, with the most successful of these being simulated in 3D in the next section.

For consistency, the windings were all applied to cores with the same geometry. The dimensions of these cores are shown in Figure 6.3. The transformers are housed in the same tank, and supported by solid insulators. Neither of these are included in the simulations, as they will have a relative permeability of unity and, therefore, will not affect the magnetic flux flow around the cascade. The cores at the bottom of the cascade are larger to compensate for the increase in flux density caused by the higher current in the primary and auxiliary windings.

A 40 k Ω resistor is connected across the terminals of each secondary winding to model the load attached to the power supply. If there is 100% flux retention, each secondary winding will have a peak voltage of 10 kv, meaning that each resistor should draw a current of 250 mA. Each layout was simulated for 50 μ s, with a time step of 0.1 μ s, using a mesh with a maximum edge length of 15 mm.

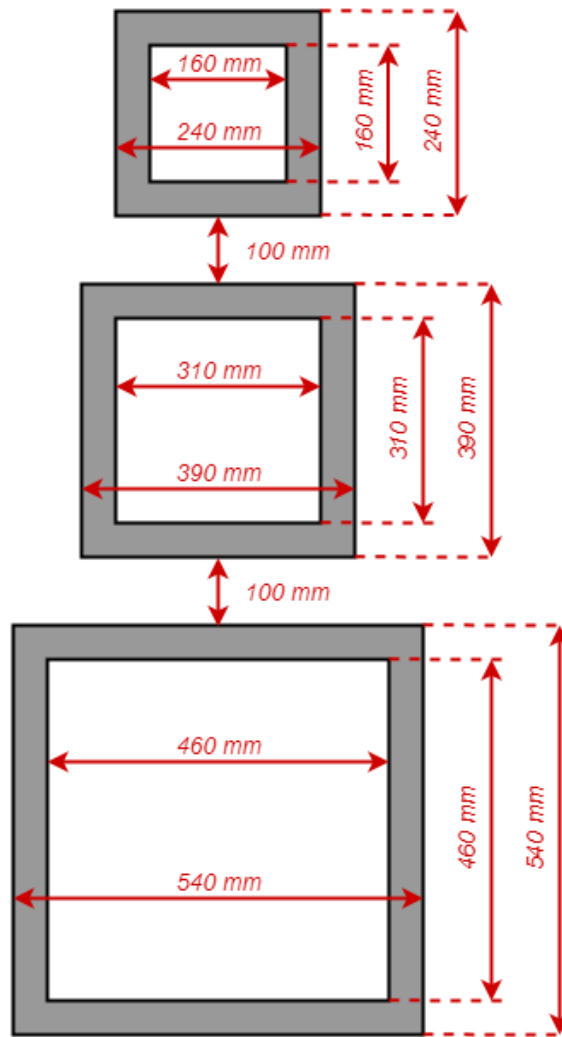


Figure 6.3. The dimensions of the cascade transformer modelled in this section. Each core has a cross section of 40 mm by 40 mm.

6.2.1 Optimal Winding Location

The first layout to be considered was to have the secondary windings centred around the vertical limbs of the core, with the primary and auxiliaries placed immediately above and below them. In Phase A, as labelled in Figure 6.1, the primary is placed above the secondaries, with the auxiliary below it, as shown in Figure 6.4. In Phase B, the position of the primary and auxiliary are reversed. This ensures the primaries are evenly spaced around the core, leading to a more even flux distribution.

This layout will henceforth be referred to as Layout 1, and can be seen in Figure 6.5. The flux flow around this layout can also be seen in Figure 6.5. From this, it can be seen that a significant amount of flux circumvents the secondary windings, or even jumps between cores. This leads to a voltage drop in the secondary windings, particularly in those wound around the higher cores. This can also be seen in the secondary winding voltages, as shown in Figure 6.6. Here it can be seen that there are a wide range of voltages in the windings

wrapped around the bottom two cores. This is caused by the flux leakage shown in Figure 6.5. There is a significant phase shift in the voltages in the higher cores, compared to the voltages measured in the bottom core. This is caused by the inductance in the transformer windings. Providing voltage doublers are applied across each core, the effects of this phase shift on the total supply voltage are negated. Assuming perfect rectification and voltage doubling between each transformer, the peak voltage measured across the whole design was 638 kV. This is significantly less than the desired 1,000 kV, and does not take into account voltage drop in the voltage doublers.

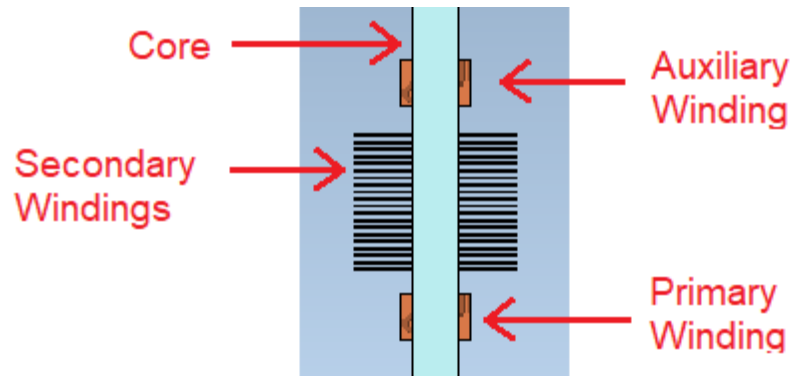


Figure 6.4. The windings around the core, as used in Layout 1.

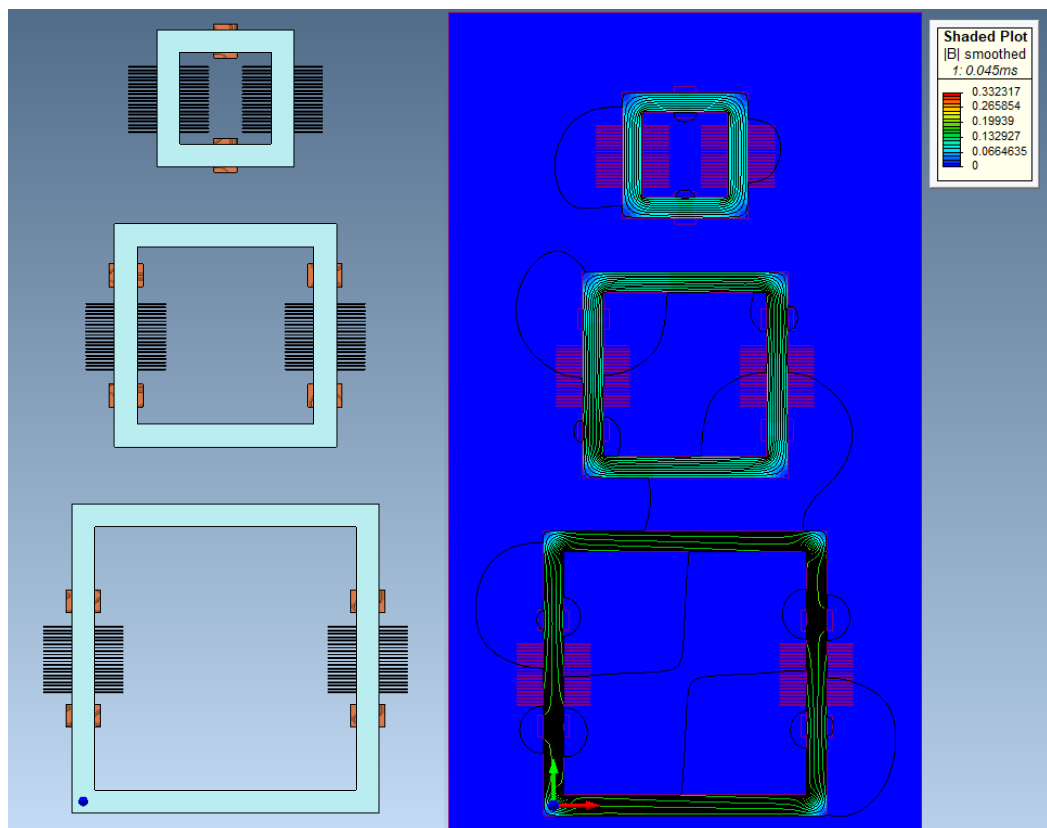


Figure 6.5 (LEFT) The two dimensional geometry of Layout 1. Note that associated pairs of primary and auxiliary windings are located on opposite sides of the secondary windings they are driving. (RIGHT) The magnetic flux flow, around Layout 1, 0.045 ms after the start of the simulation.

The second layout that was examined was similar to that proposed in Layout 1, with the notable difference being that the primary and auxiliary windings were moved to the horizontal yokes. This new layout, referred to as Layout 2, can be seen in Figure 6.7, and it appears that the magnetic flux in each stack of secondaries is more consistent; this is verified by the similarity of the voltages shown in Figure 6.8, though there is still noticeable flux leakage between cores. Assuming perfect rectification and voltage doubling between each transformer, the peak voltage measured across the whole design was 698 kV. This is an improvement on Layout 1, but still far below of the required voltage of 1,000 kV.

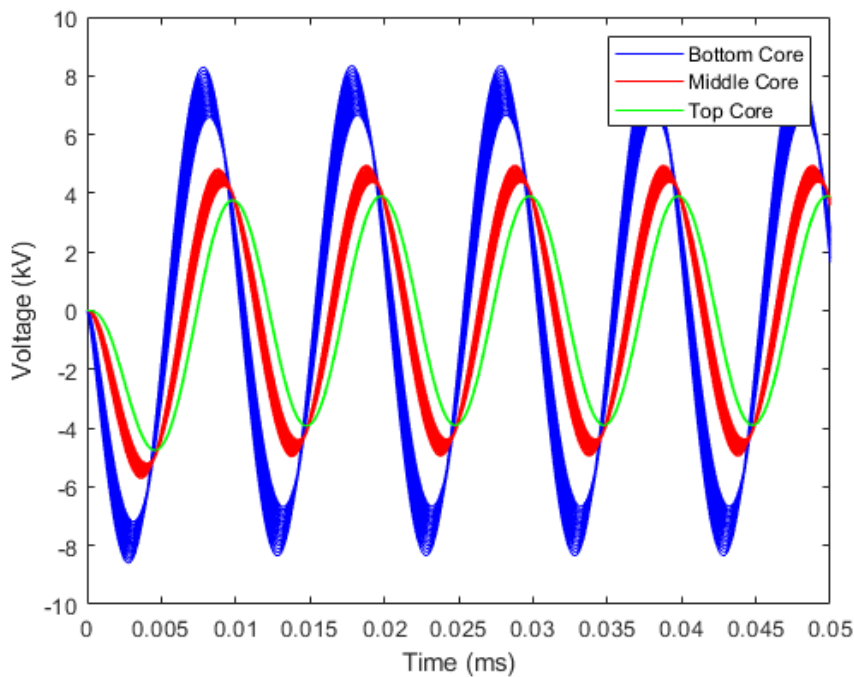


Figure 6.6 The computed voltages across the secondary windings of Layout 1. The voltages in the secondary windings surrounding the bottom core are shown in blue, windings around the middle core are shown in red, and windings around the top core are shown in green.

Layout 3 was similar to Layout 1, except that the auxiliary windings were moved to encompass their associated primary windings. This was to reduce the flux loss between stages. This layout, as well as the magnetic flux flow around it, can be seen in Figure 6.9. There is still flux leakage between cores and between windings; however, this is applied evenly. Figure 6.10 shows that, in every core, the voltages across all the secondary windings is nearly identical to that of all the other windings around that core. Assuming perfect rectification and voltage doubling between each transformer, the peak voltage measured across the whole design was 1,073 kV. This is a huge improvement on both Layout 1 and Layout 2, indeed the output voltage is greater than the 1,000 kV required from the supply. Although, for reasons already described, this is an optimistic estimate of the total system voltage.

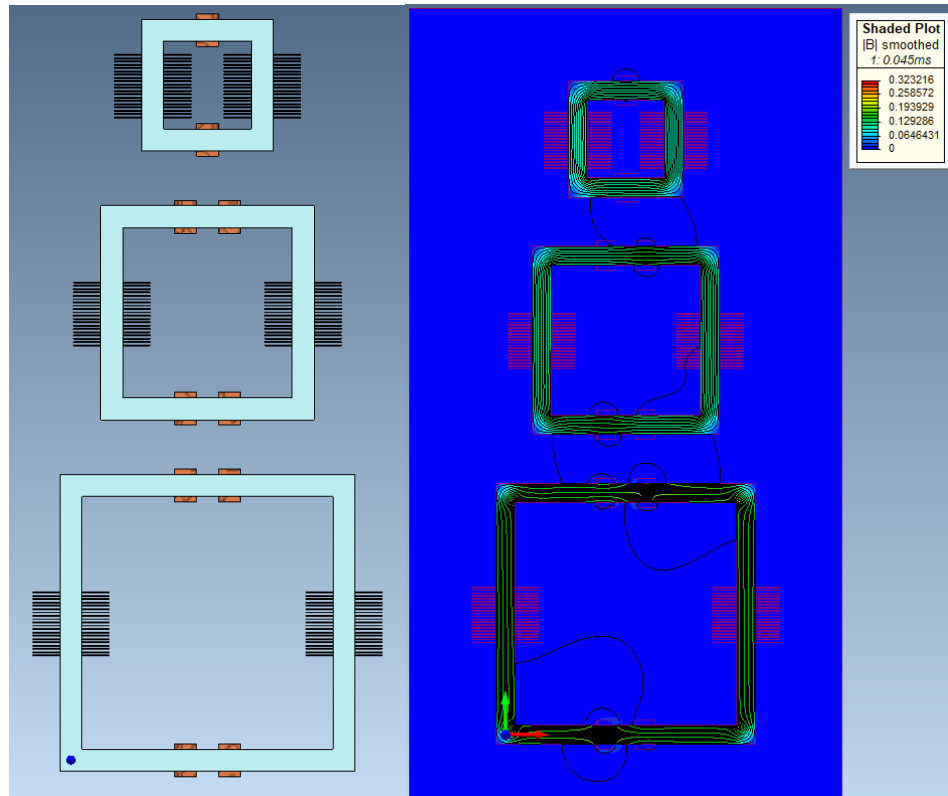


Figure 6.7 (LEFT) The two dimensional geometry of Layout 2. Note that associated pairs of primary and auxiliary windings are located on opposite yokes to each other. That is to say, in the bottom and middle cores, the primary winding driving the left hand secondary stack, and the auxiliary winding associated with the right hand stack, are wound around the lower yoke. The reverse is true for the upper yoke. (RIGHT) The magnetic flux flow around Layout 2, 0.045 ms after the start of the simulation.

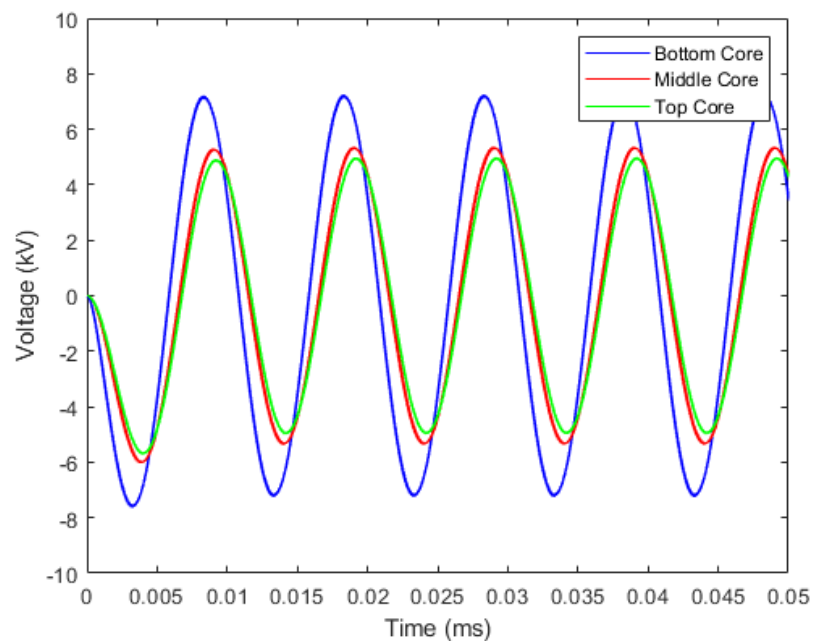


Figure 6.8 The computed voltages across the secondary windings of Layout 2. The voltages in the secondary windings surrounding the bottom core are shown in blue, windings around the middle core are shown in red, and windings around the top core are shown in green.

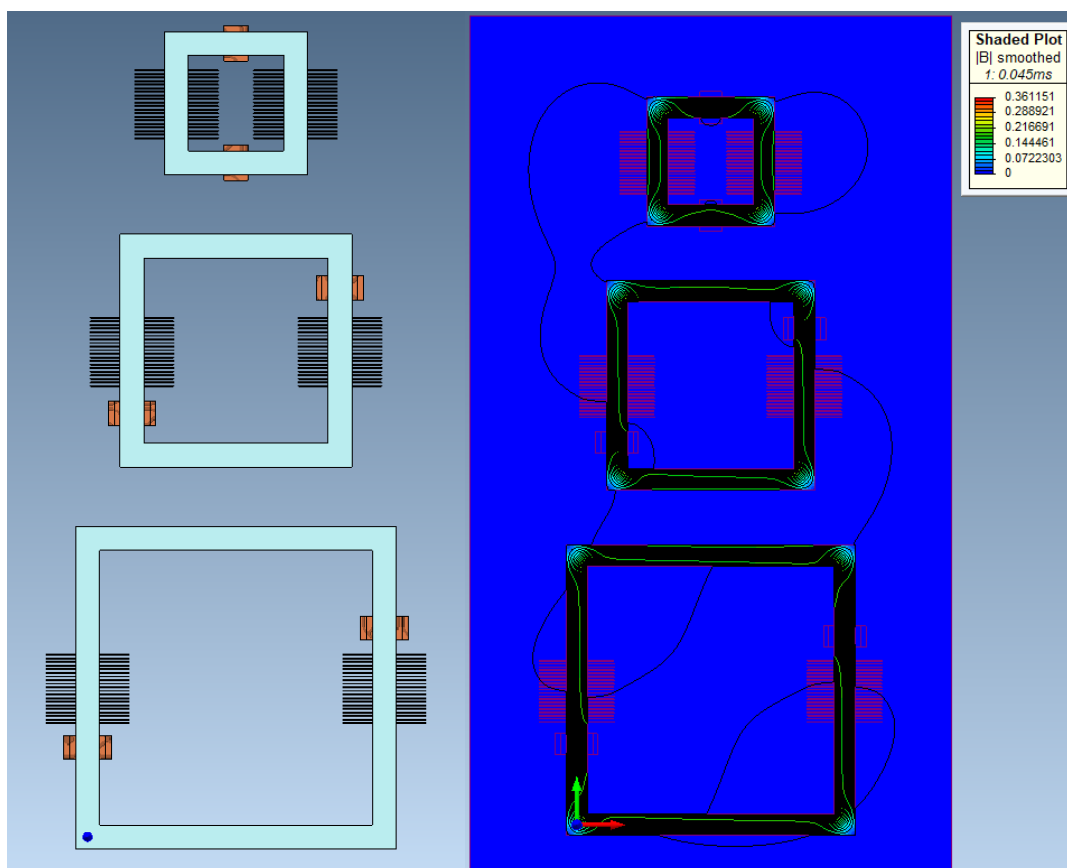


Figure 6.9 (LEFT) The two dimensional geometry of Layout 3. Note that each auxiliary surrounds the primary winding that is driving it. (RIGHT) The magnetic flux flow around Layout 3, 0.045 ms after the start of the simulation.

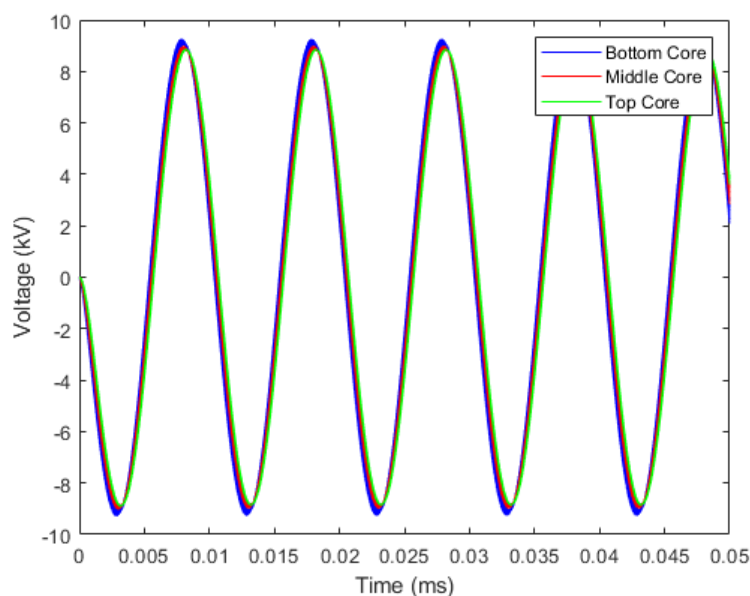


Figure 6.10 The computed voltages across the secondary windings of Layout 3. The voltages in the secondary windings surrounding the bottom core are shown in blue, windings around the middle core are shown in red, and windings around the top core are shown in green.

Layout 4 was essentially a combination of Layouts 2 and 3, in that the auxiliary windings encompassed the primaries and were wound around the centres of the horizontal yokes.

This layout, as well as the magnetic flux flow around it, can be seen in Figure 6.11. The secondary voltages, as shown in Figure 6.12, are almost identical, similar to those in Layout 3. Assuming perfect rectification and voltage doubling between each transformer, the peak voltage measured across the whole design was 990 kV. This makes this design less effective than Layout 3.

Finally, Layout 5, as well as the magnetic flux flow around it, is shown in Figure 6.13. In this case, a primary winding is wound around the vertical limbs of each core above and below the secondary windings stack. Auxiliary windings are then wrapped around the primary windings (as was done in Layouts 3 and 4). Each pair of primary and auxiliary windings were then connected in parallel in an arrangement similar to that used in the single stack ICT. This meant that each stack of secondary windings is driven from the top and bottom simultaneously. Figure 6.13 shows no flux leakage except in the top stage. The secondary winding voltages, shown in Figure 6.14 support this, as the output of each stage is nearly 10 kV. Assuming perfect rectification and voltage doubling between each transformer, the peak voltage measured across the whole design was 1,141 kV. This makes this the most effective layout examined thus far.

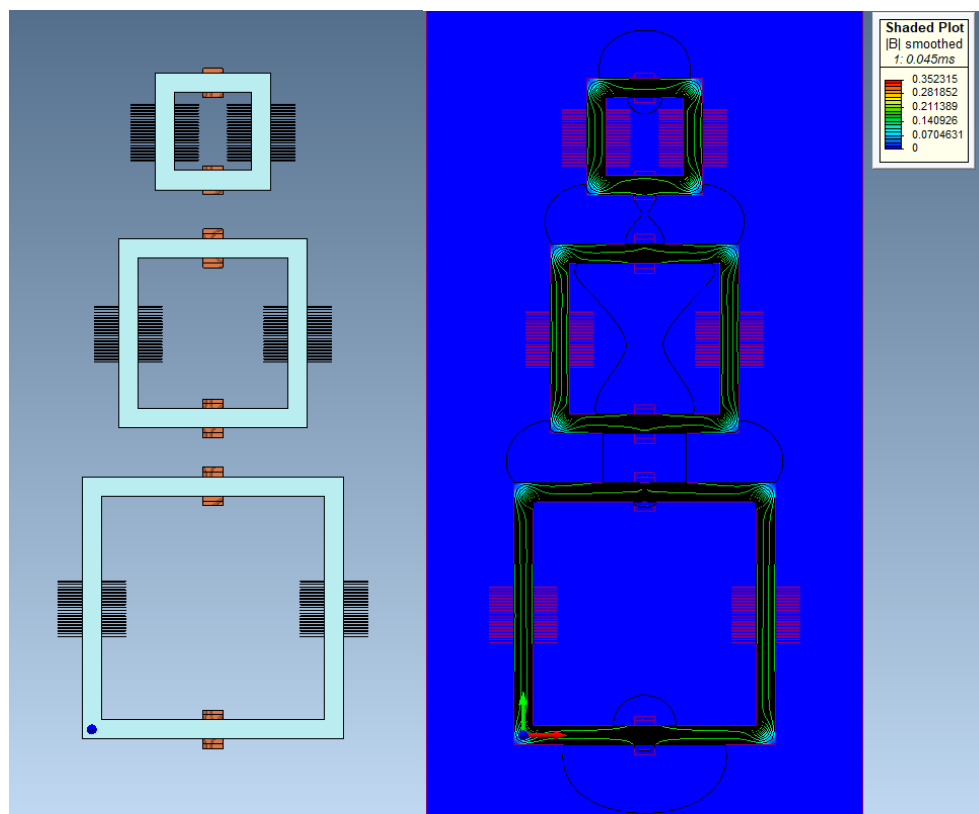


Figure 6.11 (LEFT) The two dimensional geometry of Layout 4. The auxiliary windings encompass the primaries, which are in turn wound around the centres of the horizontal yokes. (RIGHT) The magnetic flux flow around Layout 4, 0.045 ms after the start of the simulation.

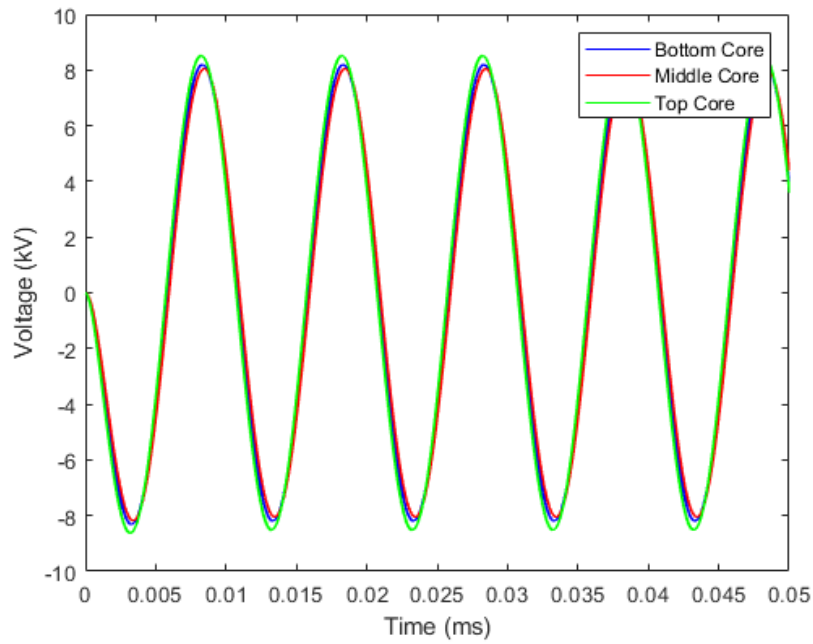


Figure 6.12 The computed voltages across the secondary windings of Layout 4. The voltages in the secondary windings surrounding the bottom core are shown in blue, windings around the middle core are shown in red, and windings around the top core are shown in green.

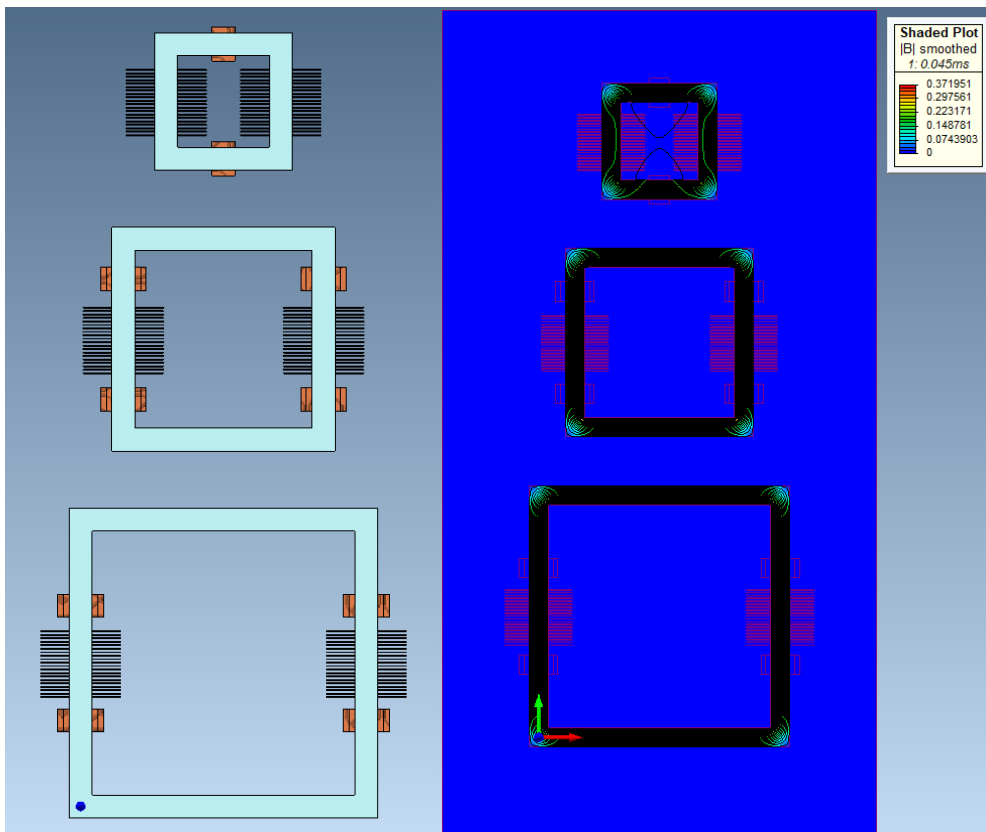


Figure 6.13 (LEFT) The two dimensional geometry of Layout 5. There is a primary and auxiliary winding at the top and bottom of each stack of secondary windings. (RIGHT) The magnetic flux flow around Layout 5, 0.045 ms after the start of the simulation.

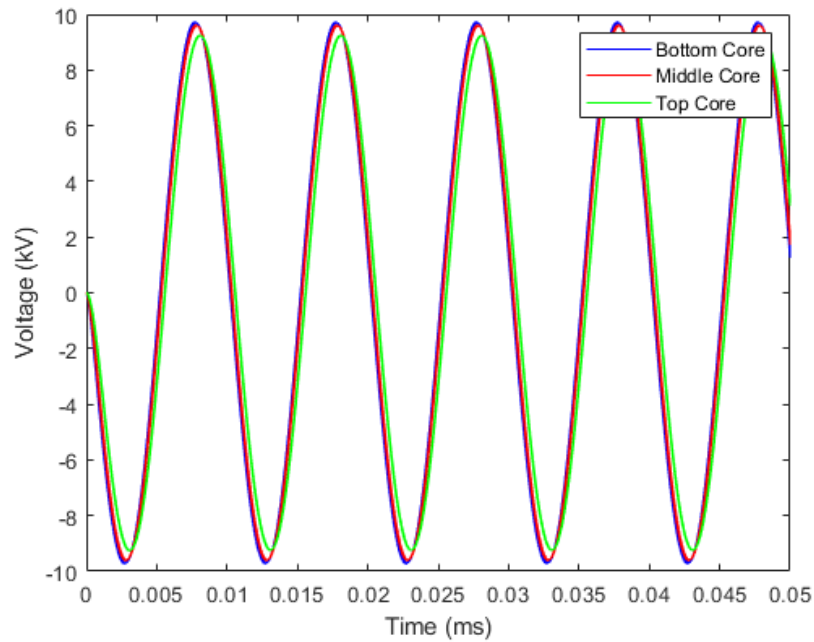


Figure 6.14 The computed voltages across the secondary windings of Layout 5. The voltages in the secondary windings surrounding the bottom core are shown in blue, windings around the middle core are shown in red, and windings around the top core are shown in green.

6.2.2 Concentric Transformers

It was shown, in the previous Section, that a design based on cascade transformers has potential for development into a working 1 MV power supply. However, possible improvements may be made in reducing the size of the design. As the windings take up relatively little space in relation to the cores of each transformer, the majority of the space inside the transformer core is left empty. In addition, as each core must be separated from the one above and/or below it, the overall size of the design will likely be several times greater than that of the bottom stage alone. A possible improvement on this would be to fit each core inside the one below it in the cascade, so that the middle core encompasses the top core, which is in turn encompassed by the bottom core, as shown in Figure 6.15. To do this would involve enlarging every core except the top one, in order to encompass the higher cores with additional room for windings and insulation. This will result in more wasted material as the flux density in the core will be less than optimal. Another problem with this proposed, concentric, design is flux leakage. One of the biggest causes of flux leakage in the cascade transformers, examined in the previous section, was flux bridging the gap between cores. In a cascade transformer, this could be reduced by simply moving the cores further apart. However, this would not be a possibility in a concentric design. For this reason, ways of reducing flux leakage in concentric transformers are now examined. The dimensions of the cores used in the following simulations are shown in Figure 6.15.

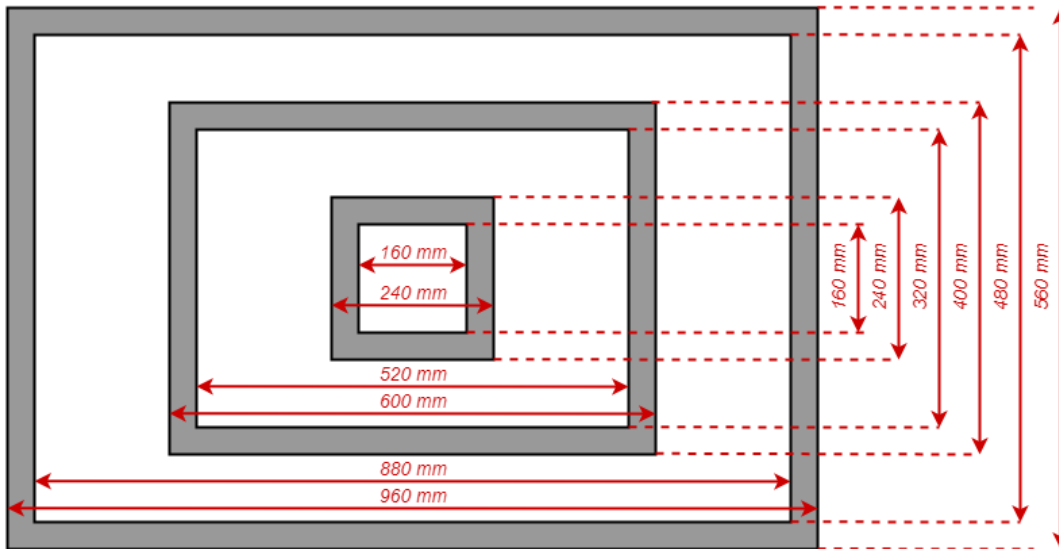


Figure 6.15. The dimensions of the concentric transformer modelled in this section. Each core has a cross section of 40 mm by 40 mm.

The first layout of concentric transformer to be examined is that shown in Figure 6.16, referred to as Layout 6. In this layout, the primary and auxiliary windings are placed as they are in Layout 1, with the primary and auxiliary windings located immediately above and below the stack of secondary windings. The flux flow around this layout is shown in Figure 6.17, with the secondary voltages shown in Figure 6.18. Both of these Figures imply a high flux leakage across the design. Assuming perfect rectification and voltage doubling between each transformer, the peak voltage measured across the whole design was 652 kV. This is 14 kV more than Layout 1, which had the same winding arrangement, suggesting that the Concentric Transformer might actually be a more flux efficient design than the Cascade Transformer.

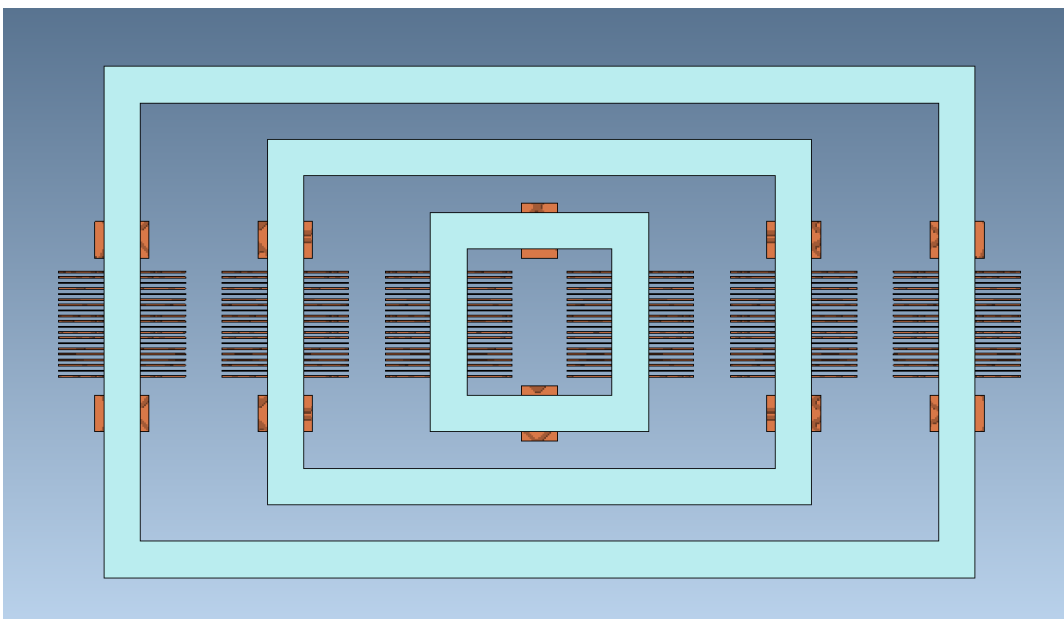


Figure 6.16 The two dimensional geometry of Layout 6.

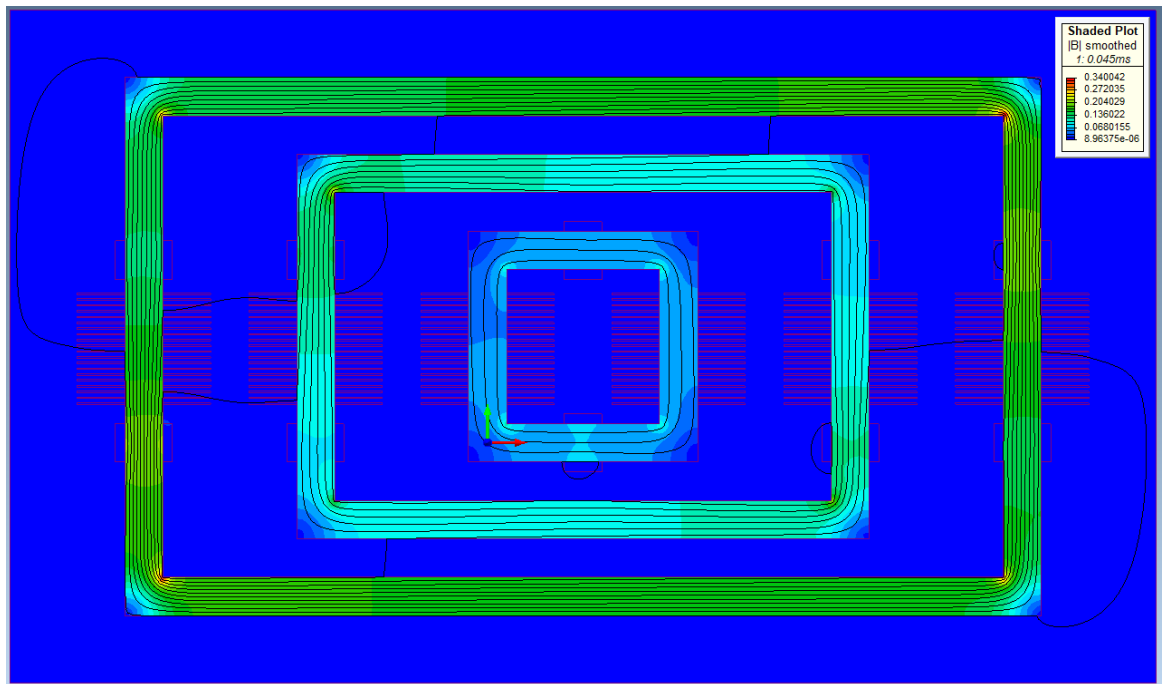


Figure 6.17 The magnetic flux flow around Layout 6, 0.045 ms after the start of the simulation.

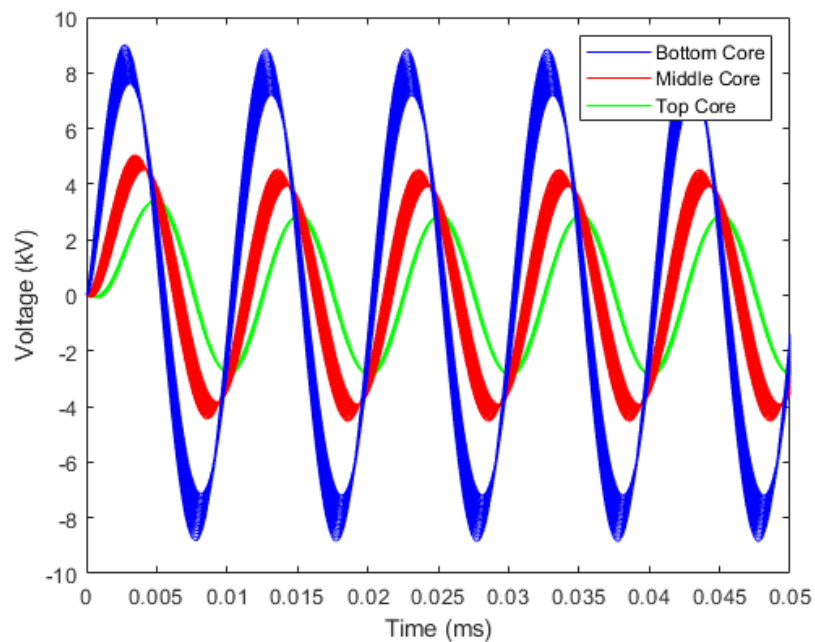


Figure 6.18 The computed voltages across the secondary windings of Layout 6. The voltages in the secondary windings surrounding the bottom core are shown in blue, windings around the middle core are shown in red, and windings around the top core are shown in green.

Layout 7 involves arranging the primary and auxiliary windings as they were in Layout 3, as shown in Figure 6.19. The flux flow around this layout can be seen in Figure 6.20, and the secondary voltages in Figure 6.21. The voltages are more consistent, which implies reduced flux loss in each core. However, there is still a noticeable flux loss between cores. Assuming perfect rectification and voltage doubling between each transformer, the peak

voltage measured across the whole design was 921 kV. This is a significant improvement on Layout 6.

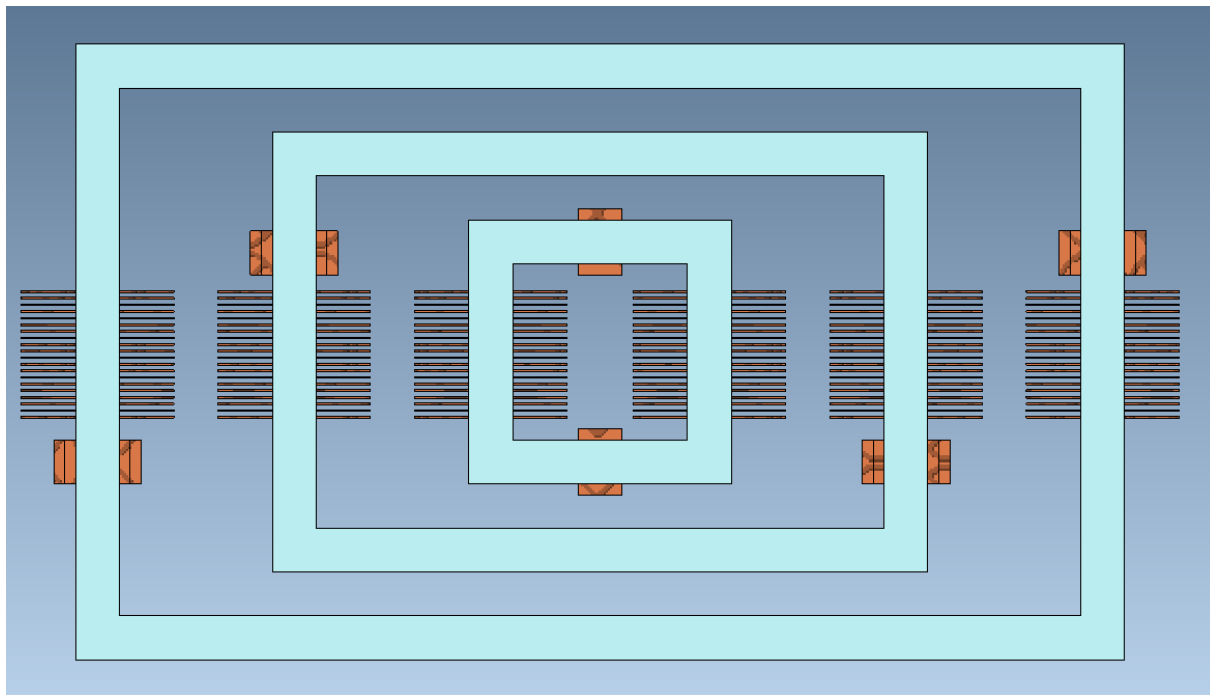


Figure 6.19 The two dimensional geometry of Layout 7.

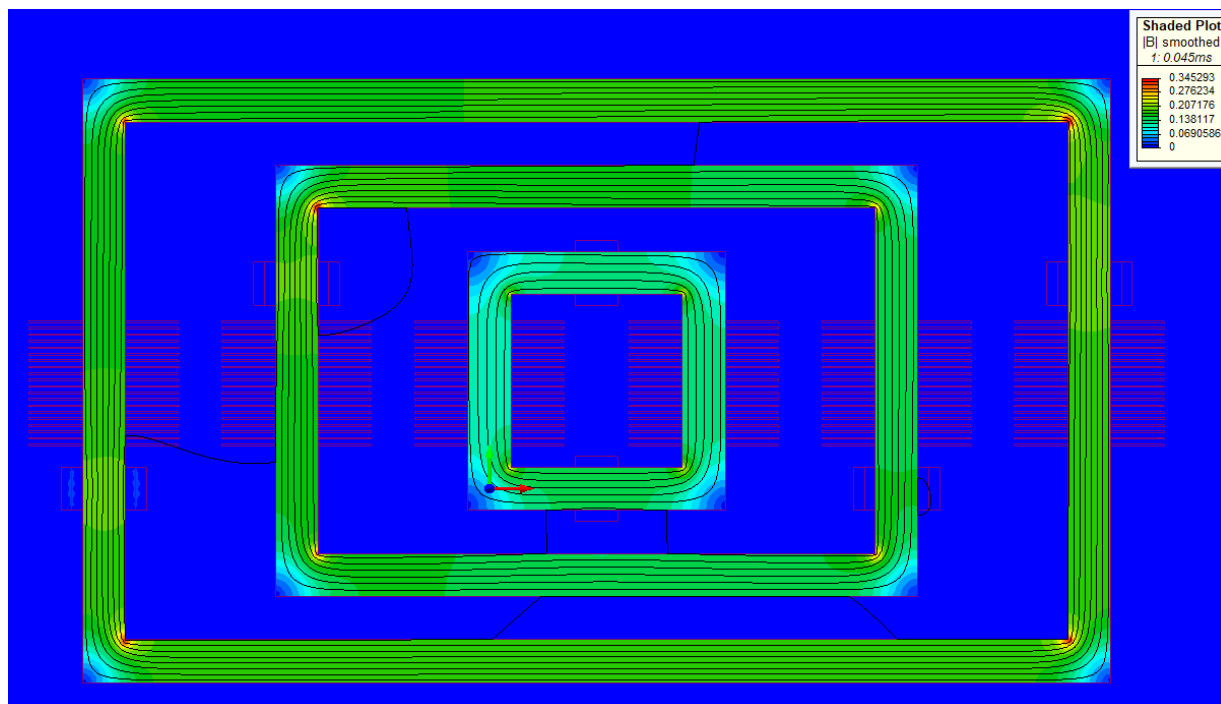


Figure 6.20 The magnetic flux flow around Layout 7, 0.045 ms after the start of the simulation.

Layout 8 imposes the windings of Layout 4 onto a concentric design and can be seen in Figure 6.22, with the flux flow shown in Figure 6.23. In order to allow sufficient space for the primary and auxiliary windings, the vertical limbs of the bottom and middle transformer were extended so that they now have outside lengths of 700 mm and 460 mm, respectively. Like

in Layout 8, there is no clearly visible flux leakage, in the bottom two stages. Figure 6.24 shows a slight voltage drop in the windings associated with the top core but the voltage produced from the bottom two cores is consistent. Assuming perfect rectification and voltage doubling between each transformer, the peak voltage measured across the whole design was 1,032 kV. This is greater than the 1,000 kV requirement, indicating that a concentric design is viable.

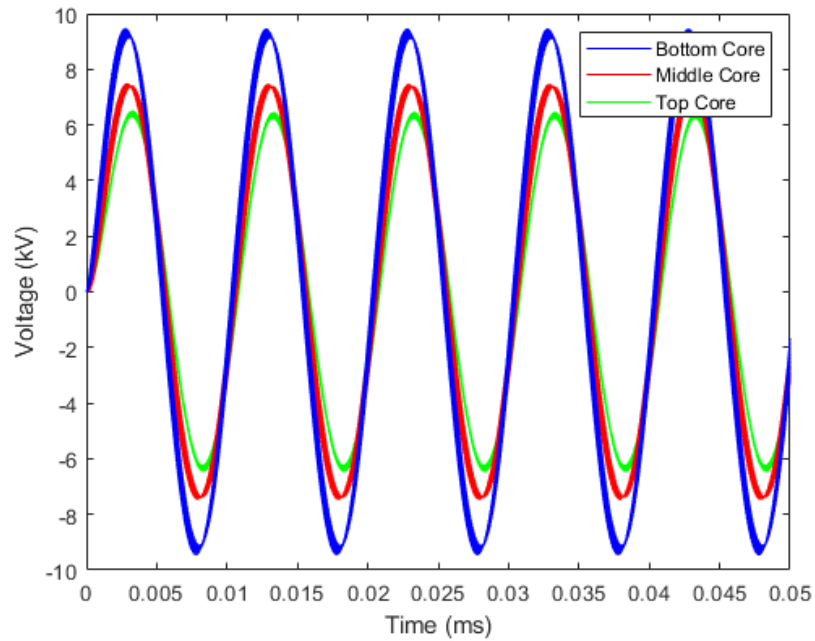


Figure 6.21 The computed voltages across the secondary windings of Layout 7. The voltages in the secondary windings surrounding the bottom core are shown in blue, windings around the middle core are shown in red, and windings around the top core are shown in green.

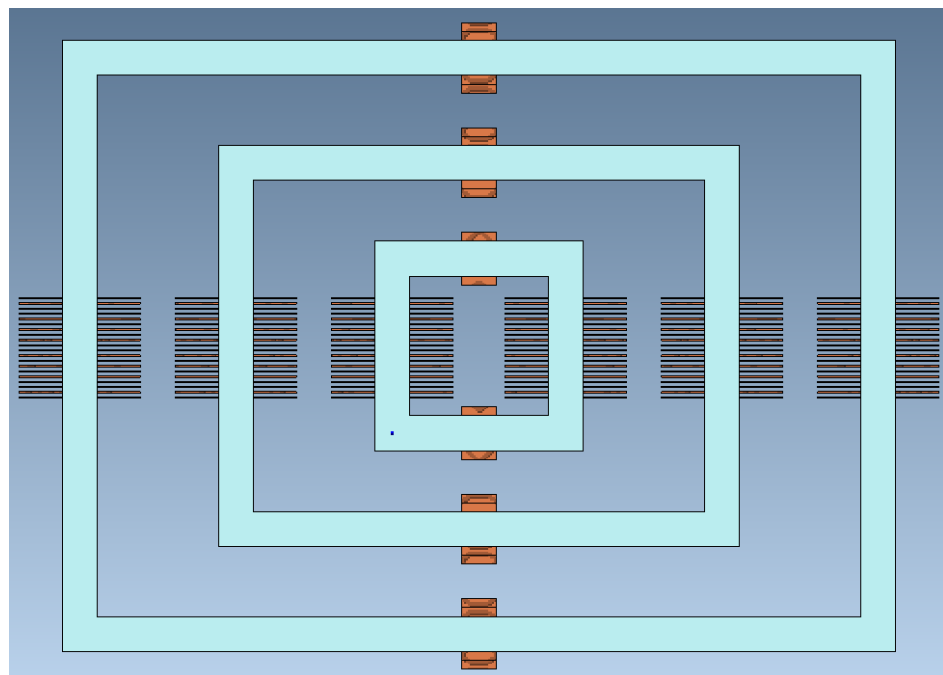


Figure 6.22 The two dimensional geometry of Layout 8.

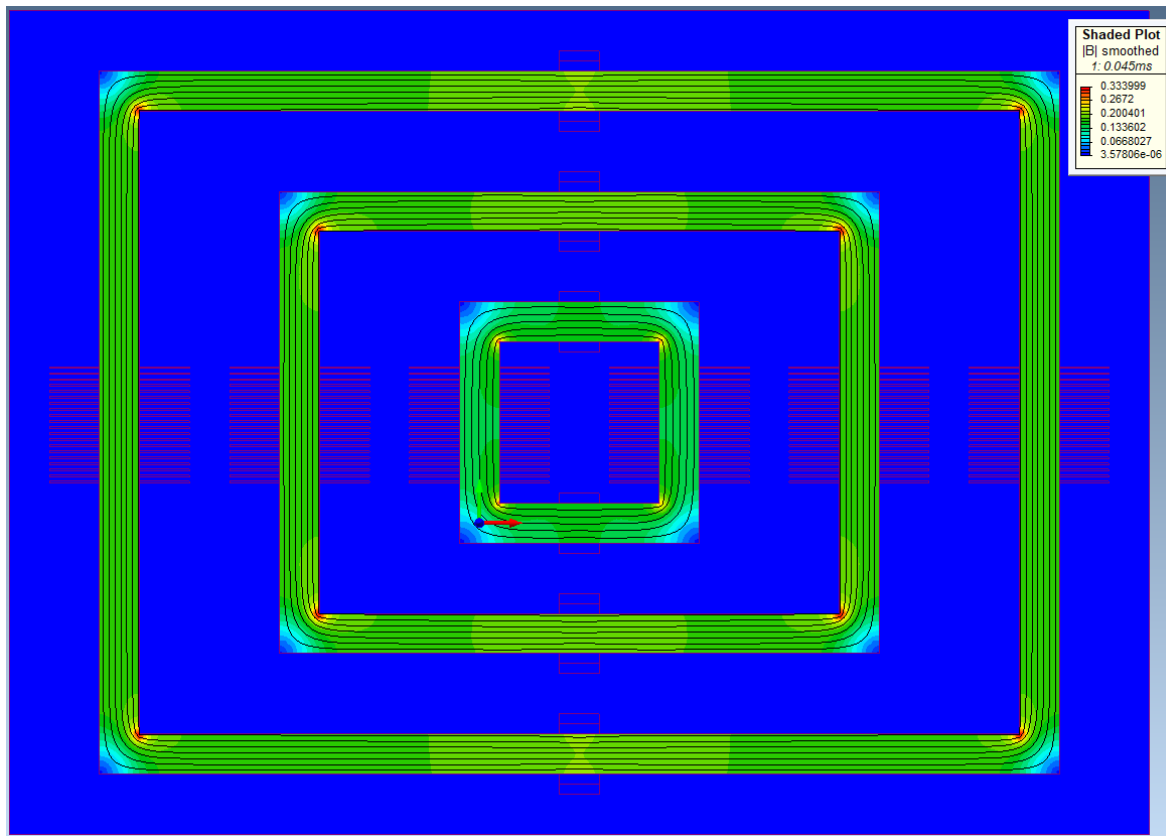


Figure 6.23 The magnetic flux flow around Layout 8, 0.045 ms after the start of the simulation.

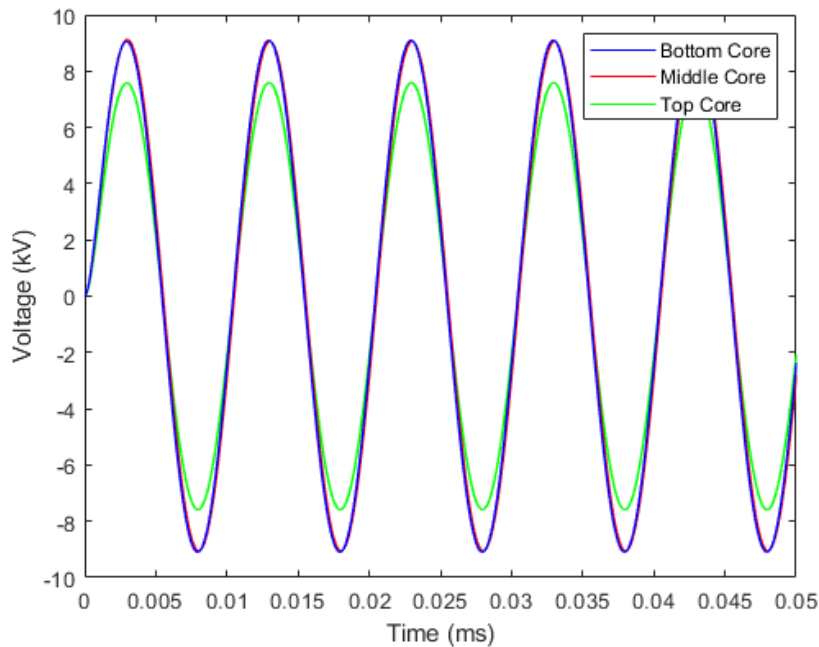


Figure 6.24 The computed voltages across the secondary windings of Layout 8. The voltages in the secondary windings surrounding the bottom core are shown in blue, windings around the middle core are shown in red, and windings around the top core are shown in green.

Finally, Layout 9 combines the winding positioning of Layout 5 with the concentric core arrangement, and can be seen in Figure 6.25, with the flux flow shown in Figure 6.26 and

the secondary voltages in Figure 6.27. From these, it can be seen that there is little flux leakage, except in the top stage. Assuming perfect rectification and voltage doubling between each transformer, the peak voltage measured across the whole design was 1,017 kV. Although not as high as Layout 8, this is still greater than the 1,000 kv objective. However, neither this layout nor Layout 8 produce a voltage as high as Layouts 3 and 5.

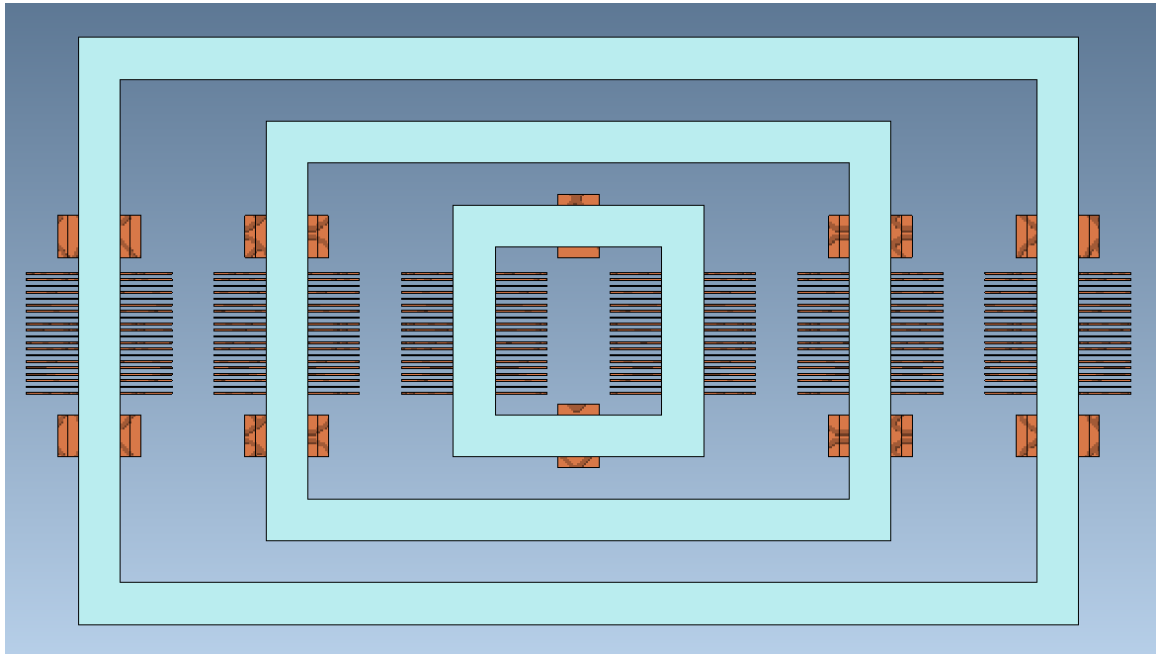


Figure 6.25 The two dimensional geometry of Layout 9.

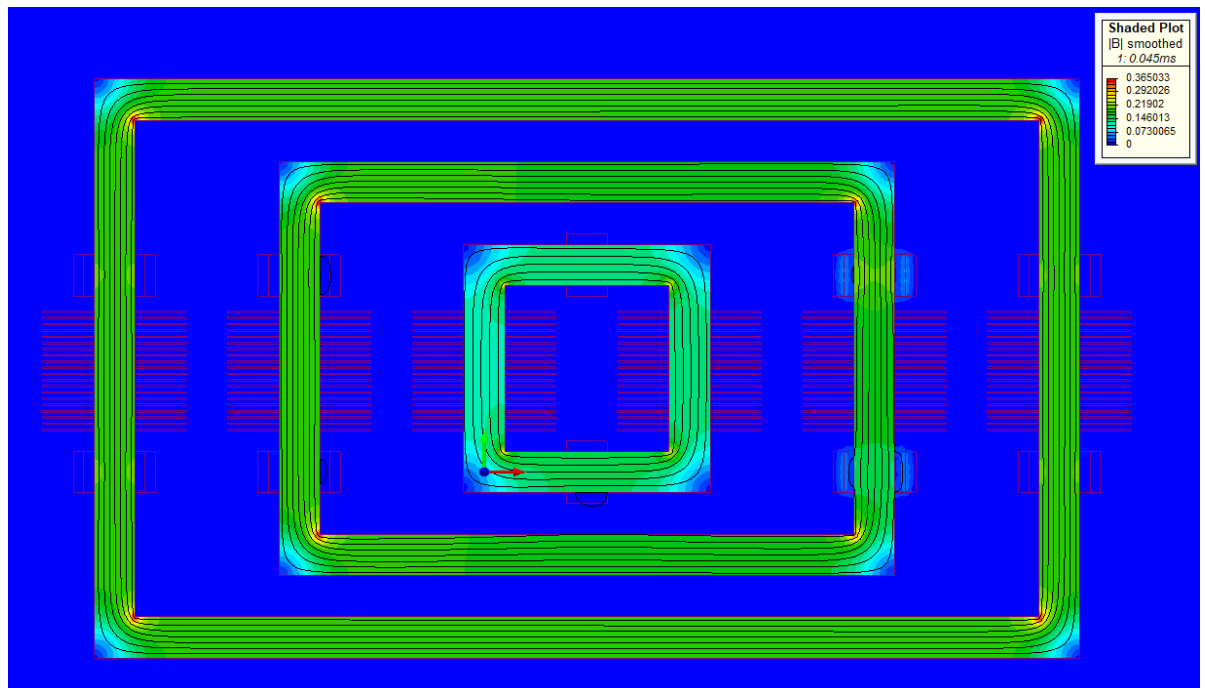


Figure 6.26 The magnetic flux flow around Layout 9, 0.045 ms after the start of the simulation.

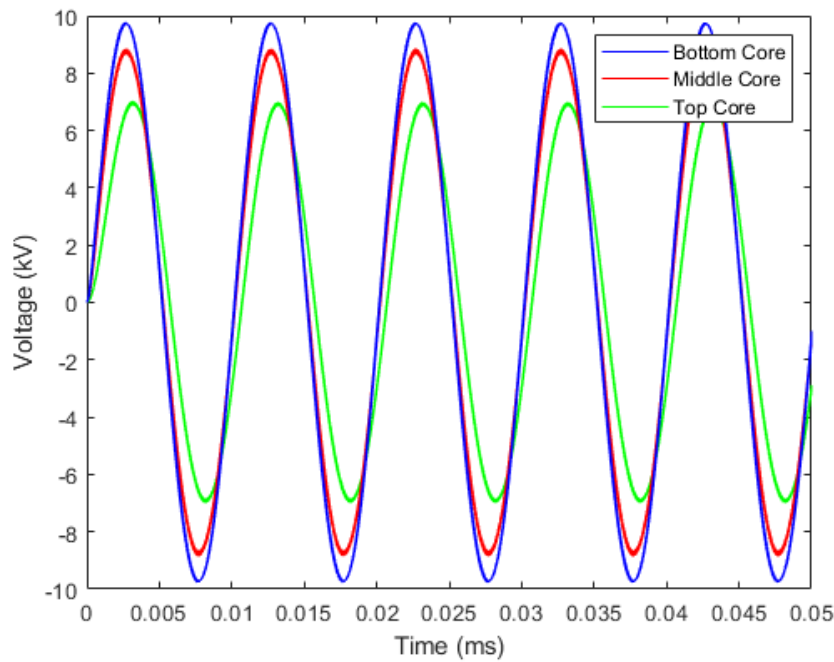


Figure 6.27 The computed voltages across the secondary windings of Layout 9. The voltages in the secondary windings surrounding the bottom core are shown in blue, windings around the middle core are shown in red, and windings around the top core are shown in green.

6.2.3 Comparison

The voltages that would be generated by power supplies, using all of the layouts in this section, have been collated and are listed in Table 6.1. From this, it can be seen that cascade transformers typically suffer from lower flux loss, when simulated in 2D, than concentric transformers. It can also be concluded that the winding arrangements that produce the lowest flux loss are those that either wrap the primary and auxiliary windings around the horizontal yokes of the transformer; or use two sets of primary and auxiliary windings, placed above and below the secondary winding stack.

Based on these conclusions, Layouts 4, 5, 8, and 9 will be simulated in 3D in the following section.

Table 6.1 Power supply voltages generated using different layouts and idealised voltage doubling.

Cascade Transformers		Concentric Transformers	
Layout 1	638.2 kV	Layout 6	652.5 kV
Layout 2	698.0 kV	Layout 7	921.2 kV
Layout 3	1,072.9 kV	Layout 8	1,032.0 kV
Layout 4	989.5 kV	Layout 9	1,016.6 kV
Layout 5	1,141.3 kV		

6.3 3D Simulations

Having established the most effective layouts for a cascade or concentric transformer, these layouts will now be evaluated using three dimensional finite element analysis. Each layout will be simulated for 50 μs , with a time step of 0.1 μs , using a mesh of maximum edge length of 15 mm. The dimensions of the transformer cores are the same as those used in the 2D simulations. Each design will be evaluated based on the voltage produced across their secondary windings.

6.3.1 Cascade Transformers

Layout 4 was simulated in 3D, as can be seen in Figure 6.28. The voltage measured in each winding is shown in Figure 6.29. Despite this layout producing one of the highest output voltages, when simulated in 2D, the total supply voltage calculated using 3D simulation was only 434 kV. This is even assuming perfect rectification and voltage doubling between each transformer.

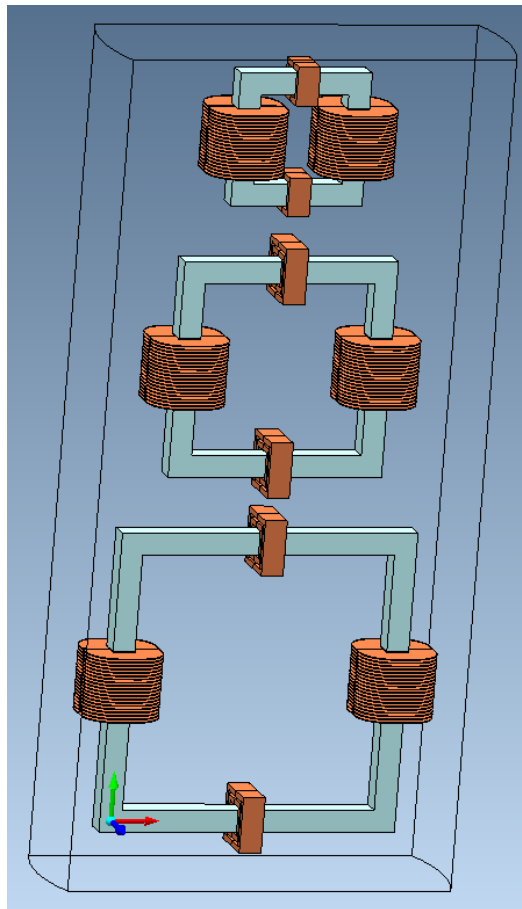


Figure 6.28 A 3D rendering of the Layout 4.

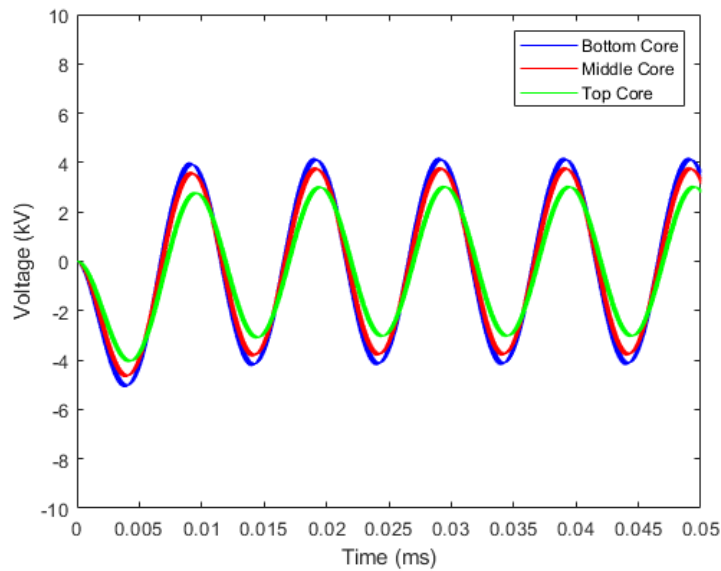


Figure 6.29 The computed voltage across the secondary windings in each stage of Layout 5 when simulated in 3D. The voltages in the secondary windings surrounding the bottom core are shown in blue, windings around the middle core are shown in red, and windings around the top core are shown in green.

Layout 5 was also simulated in three dimensions, as can be seen in Figure 6.30. The voltage measured in each winding is shown in Figure 6.31. Assuming perfect rectification and voltage doubling between each transformer, the total voltage measured across the whole design was 802 kV. Although this is a significant improvement on the voltage produced by Layout 4 in 3D simulation, it is still significantly less than the 1,141 kV predicted for Layout 5 using two-dimensional simulation.

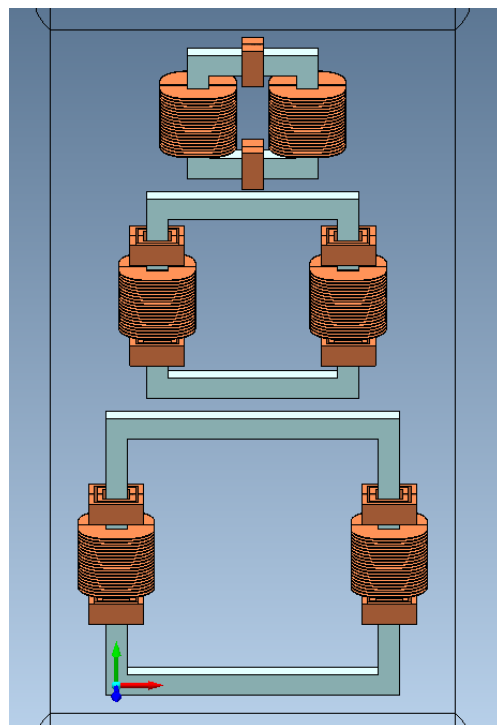


Figure 6.30 A 3D rendering of the Layout 5.

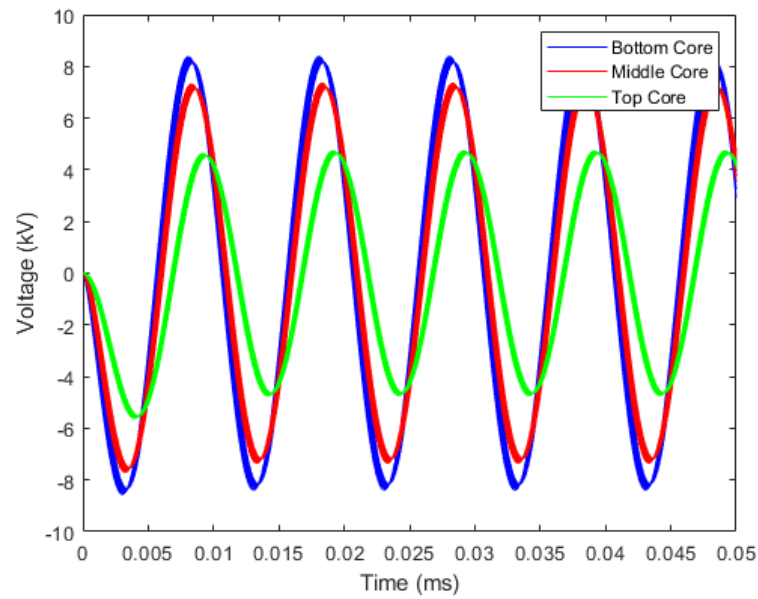


Figure 6.31 The computed voltage across the secondary windings in each stage of Layout 5 when simulated in three dimensions. The voltages in the secondary windings surrounding the bottom core are shown in blue, windings around the middle core are shown in red, and windings around the top core are shown in green.

6.3.2 Concentric Transformer

Layout 8 was simulated, in 3D, and can be seen in Figure 6.32, with the simulated secondary voltages shown in Figure 6.33. The close output voltages show that there is little flux loss in each stage. Assuming perfect rectification and voltage doubling between each transformer, the total voltage measured across the whole design was 506 kV. This is one of the lowest output voltage obtained yet, despite Layout 8 being the most promising arrangement based on 2D simulations.

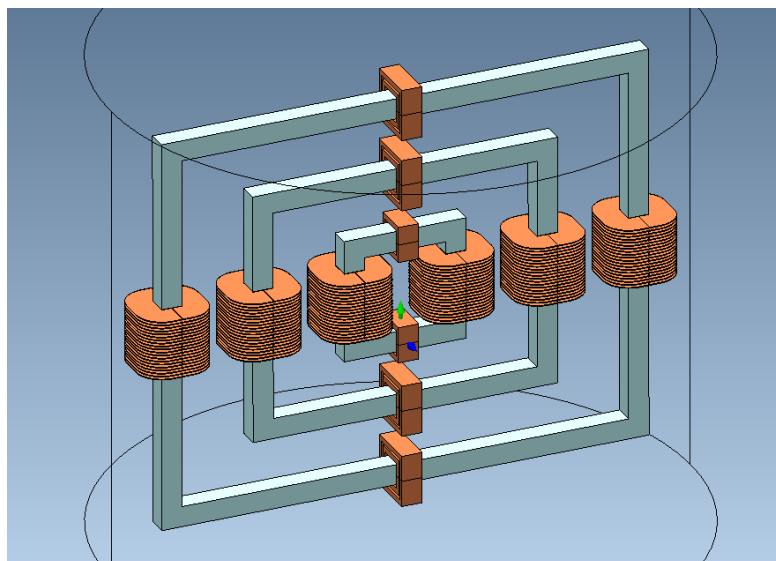


Figure 6.32 A 3D rendering of Layout 8.

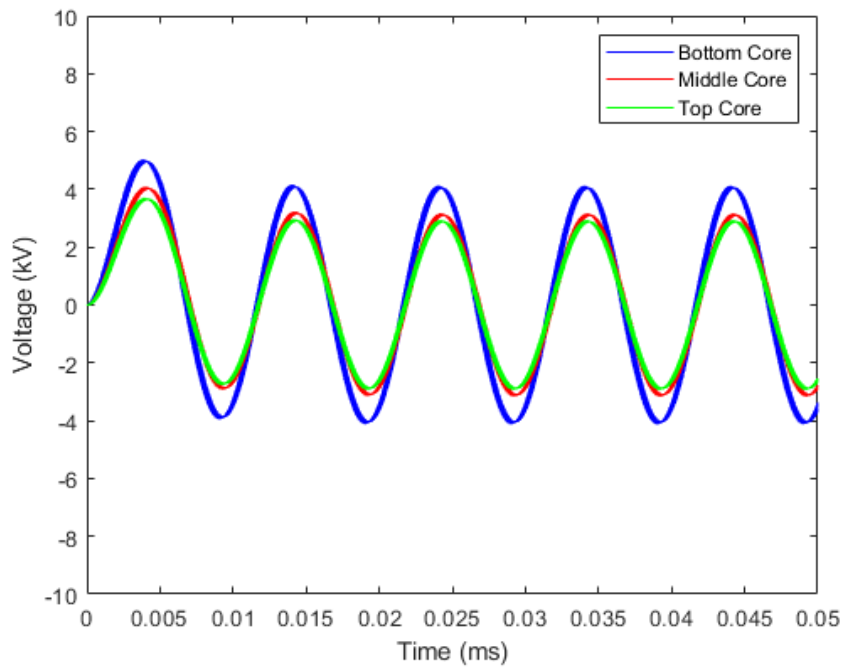


Figure 6.33 The computed voltage across the secondary windings in each stage of Layout 8 when simulated in three dimensions. The voltages in the secondary windings surrounding the bottom core are shown in blue, windings around the middle core are shown in red, and windings around the top core are shown in green.

Finally, Layout 9 was simulated in 3D, as can be seen in Figure 6.34. The voltage measured in each secondary winding is shown in Figure 6.35. The similarity of voltages in each stage, shows that there is little flux loss in each transformer. There is only a small drop in the voltages between the bottom two stages, implying little flux leakage between the stages. However, there is a much greater flux drop between the middle and top stages. Assuming perfect rectification and voltage doubling between each transformer, the total voltage measured across the whole design was 844 kV. This is close to the targeted 1,000 kV, which could easily be obtained by adding additional turns to the windings in higher stages. This is also significantly higher than the voltage achieved using a cascade design.

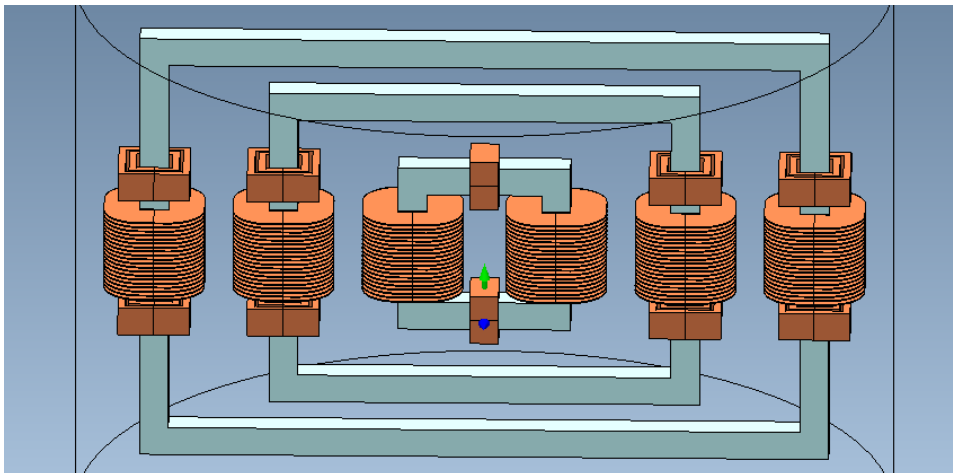


Figure 6.34 A 3D rendering of the Layout 9.

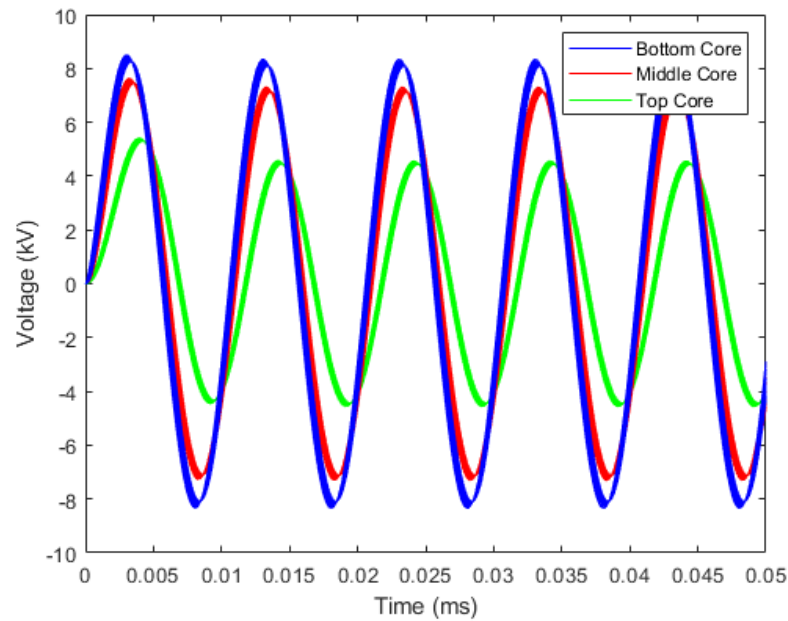


Figure 6.35 The computed voltage across the secondary windings in each stage of Layout 9 when simulated in three dimensions. The voltages in the secondary windings surrounding the bottom core are shown in blue, windings around the middle core are shown in red, and windings around the top core are shown in green.

From the studies examined in this section, two conclusions can be drawn: the first is that driving a transformer with two parallel primary windings produces a much higher voltage in the secondaries, than by driving it with a single winding. The second is that 3D simulations predict much greater flux loss than 2D simulations. It is also worth noting that, in this investigation, the concentric transformer designs performed slightly better than the cascade transformer designs. It is possible that, by increasing the distance between the cores of the cascade, the voltage output of the cascade can be increased. However, as power density is an important factor in this project, and the concentric transformer performed better in this comparison, the cascade transformer will not be investigated further in this work. Instead, the remainder of this chapter will focus solely on development of the Layout 9 concentric transformer.

6.3.3 Rotated Concentric Designs

3D analysis of concentric transformers predict a greater magnetic flux loss than 2D analysis of the same design. This is because the added dimension allows for flux to flow around the sides of the cores, while 2D analysis only allows for flux to flow in a flat plane. It is possible that the flux leakage could be reduced by rotating the centre cores. This may work for two reasons: the first is that the vertical limbs, around which the windings are wound, will be positioned further apart. In addition to this, it is possible that flux escaping around the outside core may be reclaimed as it passes through the windings of the inner cores.

In order to test this hypothesis, Layout 9 was constructed, and simulated under the same conditions as in the previous section, with each stage rotated, by a given angle, about the Y-axis. The first layout to be tested was one in which each stage was rotated 90° from the one below it, as is shown in Figure 6.36. The voltage across the secondary windings can be seen in Figure 6.37. This layout has a higher power density, than the case when each stage is laid flat, because the windings can be moved closer together thus reducing the overall size of the design. The downside of this is that the windings in the centre of the design are harder to access. This can be alleviated by, instead, rotating each stage by 120° as shown in Figure 6.38. This allows easier access to the centre windings as there is a wider gap between the outer cores, thus allowing more space for high voltage and high current carrying wires to pass between the top windings and the outside of the concentric transformer. The secondary voltages of the design shown in Figure 6.38 are shown in Figure 6.39. The total calculated voltage across the three designs, assuming perfect voltage doubling, are compared in Table 6.2.

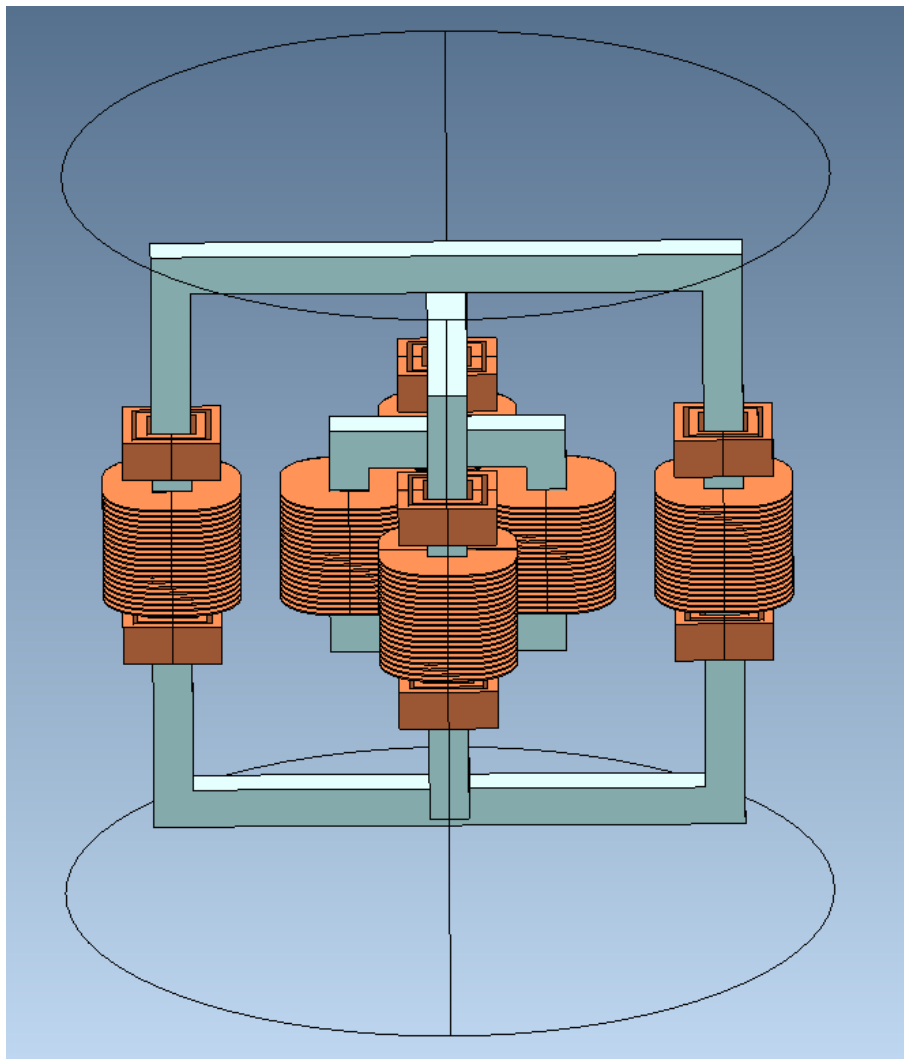


Figure 6.36 A variation on Layout 9 in which each stage is rotated 90° from the previous one.

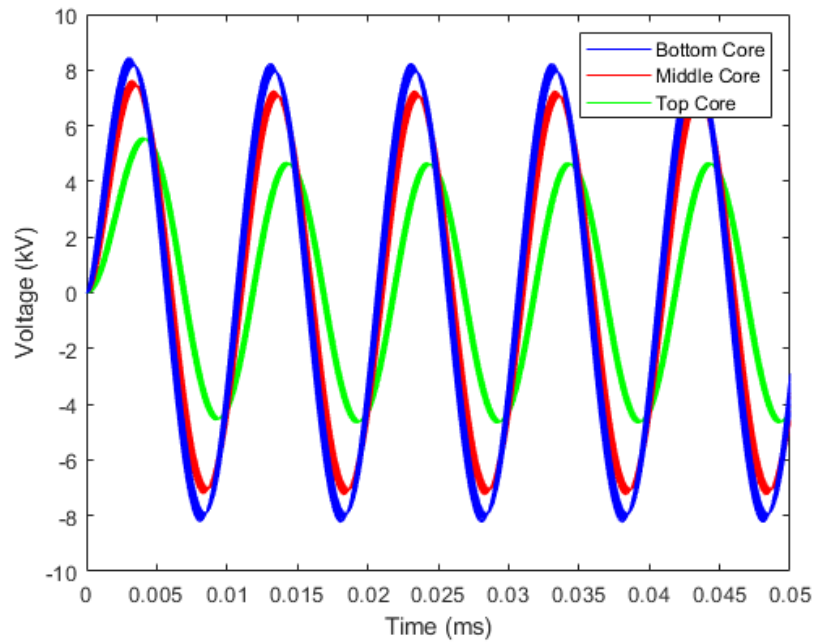


Figure 6.37 The computed voltage across the secondary windings in each stage of Layout 9 with each stage rotated 90° from the one below it. The voltages in the secondary windings surrounding the bottom core are shown in blue, windings around the middle core are shown in red, and windings around the top core are shown in green.

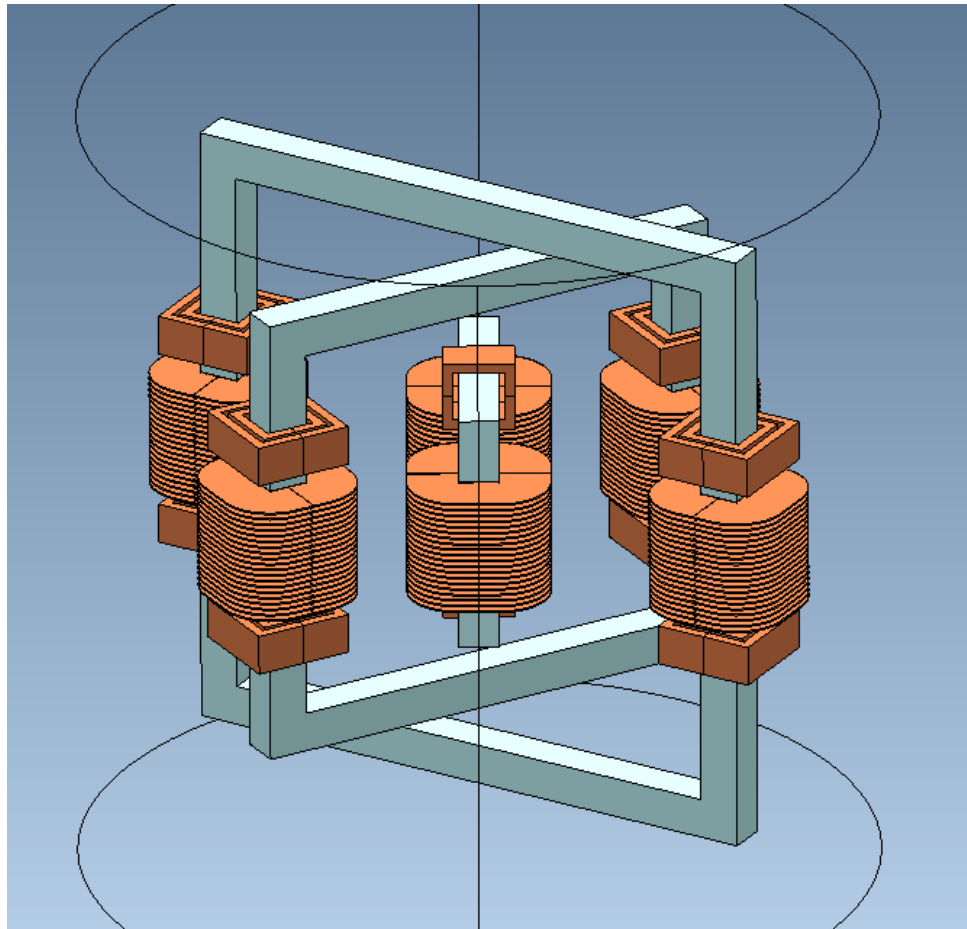


Figure 6.38 A variation on Layout 9 in which each stage is rotated 120° from the previous one.

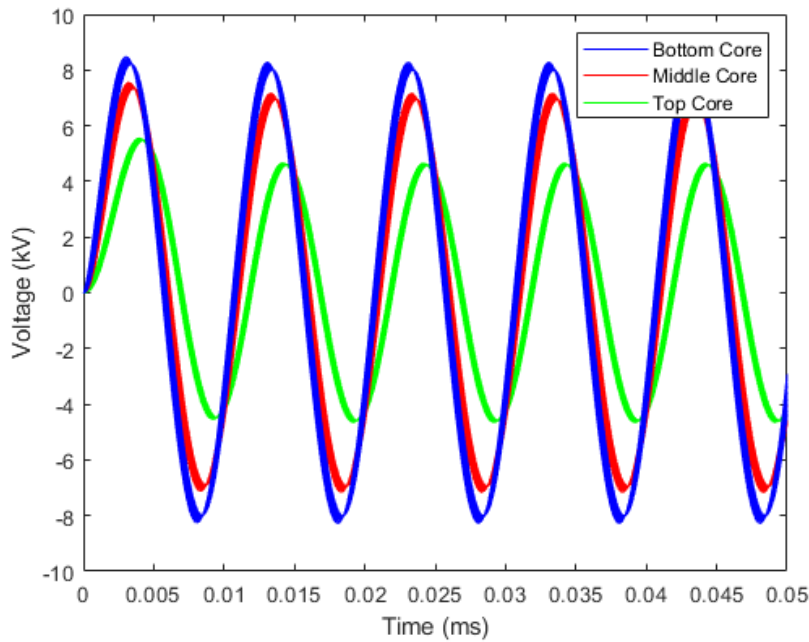


Figure 6.39 The computed voltage across the secondary windings in each stage of Layout 9 with each stage rotated 120° from the one below it. The voltages in the secondary windings surrounding the bottom core are shown in blue, windings around the middle core are shown in red, and windings around the top core are shown in green.

Table 6.2 The total output voltage of power supplies based on Layout 9, with different angles of rotation between transformer stages, assuming perfect voltage doubling.

Cascade Angle	Voltage
0° Rotation	844.3 kV
90° Rotation	847.6 kV
120° Rotation	845.3 kV

From Table 6.2, it can be seen that rotating the cores of a concentric transformer has little effect on flux loss. Indeed, there is less than 0.4% difference between the output voltages of each design. The fact that each core has a different yoke length may prevent leakage flux from being reclaimed by higher cores. If the flux path, of leakage flux travelling between stacks of windings, follows an arc with a fixed radius about the centre of the core, then it will not pass through any of the other stacks of windings as they have a different radius and do not fall in the flux path. To test this hypothesis, the concentric transformer, with 120° spacing, was remodelled with each stage having the same yoke length. This can be seen in Figure 6.40, with the secondary winding voltages shown in Figure 6.41. There is a significant drop in voltage between the middle and top stages, which reduces the total voltage to 746.3 kV.

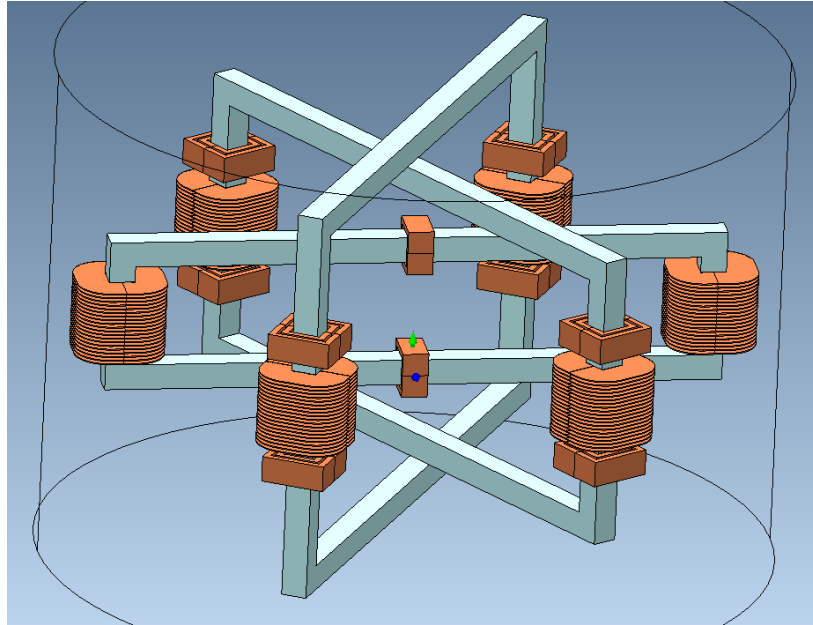


Figure 6.40 A variation on Layout 9 in which each stage is rotated 120° from the previous one and each yoke is the same length.

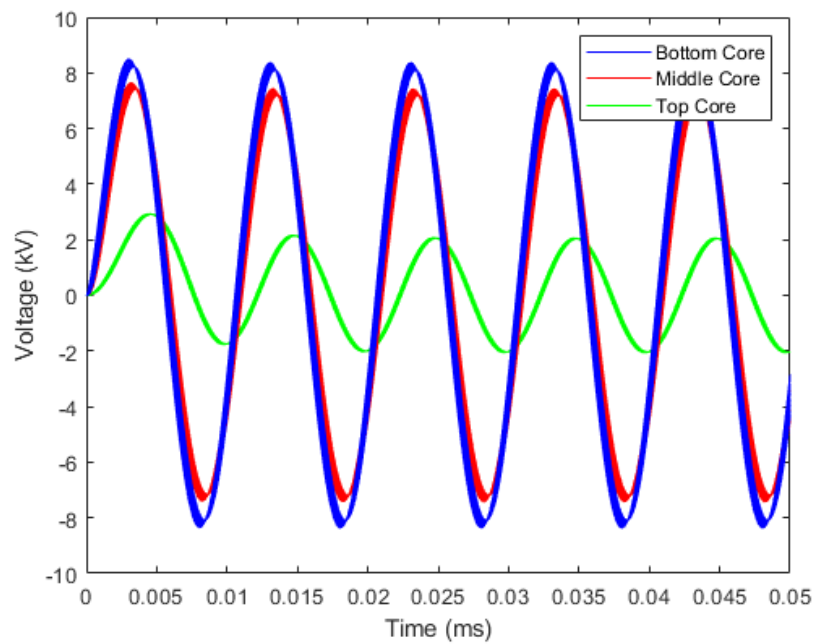


Figure 6.41 The computed voltage across the secondary windings in each stage of Layout 9 with each stage rotated 120° from the one below it and each yoke is the same length. The voltages in the secondary windings surrounding the bottom core are shown in blue, windings around the middle core are shown in red, and windings around the top core are shown in green.

It has been shown that the most effective design layout is that of the concentric transformer in which each stage is driven by two primary windings connected in parallel. This not only

produces a higher output voltage, implying a greater retention of magnetic flux, than any other layout but is also more compact than the conventional cascade transformer. It has also been shown that rotating the cores of a concentric transformer has no effect on the flux loss, though may be advantageous in changing the overall size and shape of the design. The rotated cores layout may be particularly useful if the insulating vessel they are to be kept in is cylindrical, as this would require less wasted space. Extending the yokes of the middle and top cores proved to increase flux leakage, particularly in the top core. This is likely because the lengthened yokes, running parallel to each other, increases the likelihood of flux passing through the air gap. For these reasons, work in the remainder of this chapter will focus on Layout 9 applied with no angle between stages of the core.

6.3.4 Square Wave Driven Design

All of the simulations so far have been applied to cascade and concentric transformers excited by sinusoidal waveforms. In most practical high frequency applications, however, the power supply is likely to be driven by a square wave. For this reason, Layout 9 was simulated using a square wave voltage source, with a frequency of 100 kHz. The voltage rise and fall times were both 0.1 ns. The simulated voltages across the secondary windings can be seen in Figure 6.42. The output voltages are not square because of the inherent inductance of the windings. Assuming perfect rectification and voltage doubling between each transformer, the total voltage measured across the whole design was 982.7 kV. This is higher than the output voltage produced using a sine wave, but comes at the cost of greater power loss, as will be discussed in the following section.

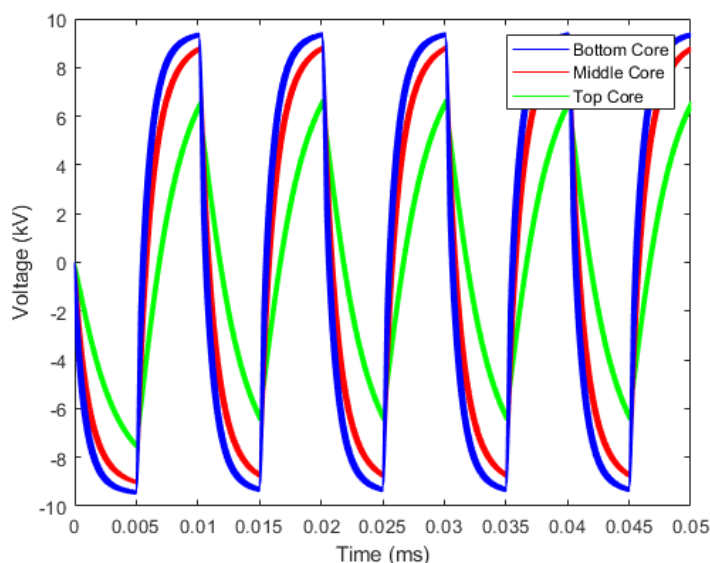


Figure 6.42 The voltage across the secondary windings in each stage of Layout 9 when excited by a square wave. The voltages in the secondary windings surrounding the bottom core are shown in blue, windings around the middle core are shown in red, and windings around the top core are shown in green.

6.3.5 Power Loss

As has already been stated, power loss is a significant concern in the field of power supply design as wasted power reduces supply efficiency, and generates heat that may damage components. In order to estimate the power loss in a concentric transformer, the core losses in Layout 9 were simulated in MagNet, in both 2D and 3D. It was excited using both a sinusoidal and square wave power source. The cores were constructed from a material with the same arbitrarily selected parameters that were used in Section 3.6.1. The core losses obtained from these simulations are compared to losses calculated using the Steinmetz Equation, in Table 6.3.

Table 6.3 Core losses under different forms of excitation.

	Top Core	Middle Core	Bottom Core	Total Loss
Sine Wave Excitation				
2D Simulation	39 W	167 W	297 W	502 W
3D Simulation	26 W	111 W	197 W	334 W
Steinmetz Equation	584 W	740 W	1,316 W	2,640 W
Square Wave Excitation				
2D Simulation	82.4 W	381 W	701 W	1,164 W
3D Simulation	51 W	231 W	442 W	724 W
Steinmetz Equation	652 W	826 W	1,468 W	2,946 W

Three things are interesting about the results shown in Table 6.3. The first is that the losses calculated for square wave excitation are noticeably bigger than those calculated for sinusoidal excitation. This is in line with what was predicted in Chapter 3. The second is that the SE predicts significantly greater losses than 2D and 3D simulations. This is likely the result of the SE assuming lumped parameters across whole cores, whereas simulations are able to estimate the losses in localised areas, and sum these together. Finally, 2D simulation predicts nearly twice as high losses as 3D simulation. Again, this is likely the product of using lumped parameters, as 2D simulations are forced to assume that all values are homogeneous in the third dimension.

Winding losses were calculated, using the methods described in Chapter 4, and are displayed in Table 6.4. Square wave excitation produces double the losses of that of a sine wave as the vast majority of the waveform is spent at peak amplitude, whereas, when calculating sinusoidal loss, the RMS current is used.

Table 6.4 Winding losses under different forms of excitation.

	Loss Per Winding	Total Loss
Sinusoidal Excitation	1.37 W	165 W
Square Wave Excitation	2.74 W	329 W

The total losses for each cascade are shown in Table 6.5. Both excitation waveforms produce close to 100% efficiency in simulation. In reality, this is unlikely to be the case as unforeseen factors cause additional loss. However, as a preliminary study, these values are sufficient to prove that a concentric transformer based design is a viable option for the development of a power supply that meets Specification 1, as defined in Table 1.1.

Table 6.5 Total losses calculated by summing the 3D simulation core losses in Table 6.3 and the winding losses in Table 6.4.

	Core Losses	Winding Loss	Total Loss	Efficiency
Sinusoidal Excitation	334 W	330 W	664 W	99.73%
Square Wave Excitation	724 W	658 W	1,382 W	99.45%

6.4 Future Scope of Design

As with the ICT, it is important to consider the future potential of the concentric transformer layout to be scaled up to produce 5 MV. To this end, a version of the concentric transformer was designed, which features six stages, with the same core and winding parameters as used in Section 6.3. This can be seen in Figure 6.43. Each stage is intended to produce 200 kV, which can then be doubled to 400 kV. The total voltage produced by the concentric transformer should be 1 MV, which can be doubled to 2 MV if 400 kV loss is allowed for.

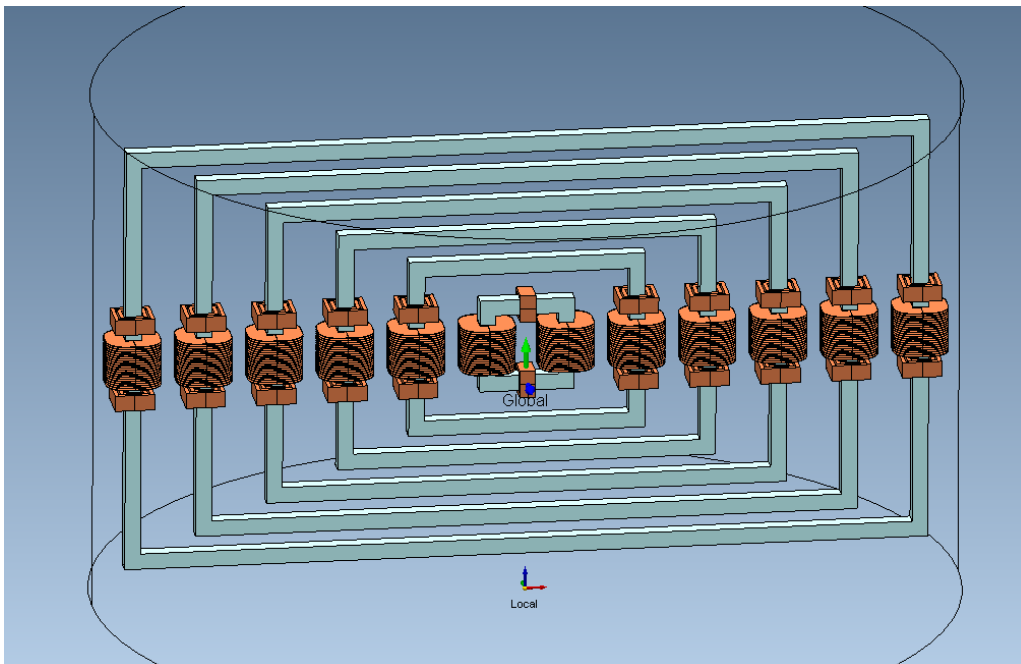


Figure 6.43 A 3D rendering of the concentric transformer with six stages.

The voltage output of the design is shown in Figure 6.44. Assuming perfect rectification and voltage doubling between each transformer, the total voltage measured across the whole design was 1,453 kV. This is just over two thirds of the voltage required. It can, therefore, be concluded that concentric transformers, on their own, have limited scalability. However, it may be possible to scale voltages by creating a cascade of concentric transformers. Providing enough distance is left between each concentric transformer, and each transformer is sufficiently insulated, this would allow the voltage to be scaled linearly.

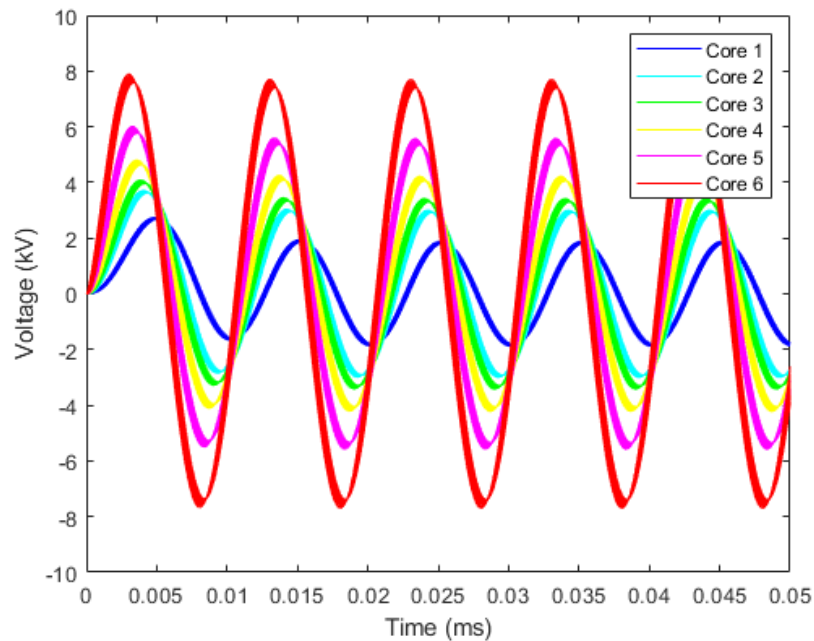


Figure 6.44 The computed voltage across the secondary windings in each stage of a concentric transformer with six stages. Core 1 is the innermost stage, as shown in Figure 6.43, while Core 6 is the outermost stage in the design

6.5 Summary

This chapter began by discussing methods of designing transformers, with a particular focus on obtaining the optimum core geometry based on circuit parameters and material characteristics. It was then decided to examine a number of potential arrangements of the windings around cascade transformers. It was concluded that using two sets of primary windings to drive the secondary stack from both ends, similar to the arrangement used in Chapter 5, was the best way of reducing flux leakage. A new type of power supply was then proposed, this being a variation of the cascade transformer, in which each stage is placed inside another in order to reduce the overall size and increase power density. This concentric transformer showed promise when investigated under 2D simulation, though it performed slightly worse than the conventional cascade transformer. This dynamic was reversed, however, when both designs were simulated in 3D and the concentric

transformer was shown to produce the higher output voltage. The concentric transformer was then assessed using the type of excitation waveform likely to be applied in real world applications.

The power loss in the design was then estimated using 2D and 3D simulations. It was shown that square wave excitation produced a power loss more than twice as great as that experienced under sinusoidal excitation. However, even this greater loss is sufficiently small for further development of this proposed design.

Chapter 7

Conclusions and Further Work

The aim of this thesis was to investigate potential designs for a new generation of high power density HVDC power supplies. A detailed literature survey was conducted, of existing HVDC power supplies, from which the most promising technologies were chosen for further study. It should be noted that there is limited information in the public domain about this area of HV technology as it is generally commercially sensitive. Of these technologies, the ICT and the cascade transformer, were selected because of their high power densities rather than their voltage output.

A way in which these technologies could be incorporated into a functioning power supply was then proposed; in which the ICT or cascade transformer would form a voltage increasing stage in a larger, modular design. It was decided that the most effective way to increase load current, while reducing voltage drop and voltage ripple, would be to connect multiple transformers in parallel. Each of these would be driven by an external, high frequency, power source that would power each transformer stage out of phase with each other, thus reducing voltage ripple even further. The output of the transformers would be rectified using voltage doublers. This would effectively half the voltage required from the rest of the design, while doubling the current requirement, effectively changing the problem into one that transformers are much better suited to solving.

Simulation studies were then carried out, on the two selected technologies, in order to determine the practical limits of their voltage output. It was discovered that the ICT would suffer from insurmountable flux loss if the voltage was raised significantly above 500 kV, though this could be doubled producing a 1 MV supply. The cascade transformer, on the other hand, could theoretically produce any required voltage providing sufficient electrical insulation and magnetic shielding was put in place between stages. During the course of this study, a new variation on the cascade transformer was proposed that showed merit for the applications of this project. In this design, successive cores were placed inside each other in a concentric layout; thus reducing the size of the overall design and therefore

increasing the power density. This was shown to perform sufficiently up to 500 kV, which could be doubled to 1 MV. However, increasing the size of the design led to diminishing returns for voltages above that.

In addition, an investigation was carried out into the viability of constructing transformer windings from PCBs. The current carrying capacity of the printed tracks was evaluated analytically and found to be sufficient for the few amps, divided across several transformers, required of this project. Simulations and experiments were used to test the breakdown voltage between parallel turns. It was shown that PCBs were sufficiently insulated to withstand the potential differences put upon them in a single winding configuration. However, they were not suitable for an interleaved winding configuration without significant modification.

7.1 Conclusions

Technologies based on transformers show the most promise for meeting the specifications of this project due to their high power density. In order to reduce the size of the design, it is important to reduce the voltage difference between the core and the windings so that the insulation can be minimised. There are two ways of doing this, either the core can be divided up into electrically insulated sections, as in the ICT, between which magnetic flux can pass or else a number of cores can be electrically connected as in a cascade transformer.

Simulations showed that both the ICT and the cascade transformer can be used to meet Specification 1, as outlined in Chapter 1, but the ICT is unsuitable to be scaled up to voltages above 1 MV. Conversely, there is no reason that a cascade transformer cannot be developed to generate voltages above 1 MV, provided the cores and windings of the lower cores were designed to be able to accommodate the high current required to power the higher transformers, although a significant program of research and development must be carried out to produce one that can operate at 5 MV. For this reason, any future work, developing a power supply that meets Specification 2, will have to be based on the cascade transformer. Concentric transformers can be used to generate voltages up to 1 MV, but appear to be limited above that.

PCB based transformer windings can conceivably be used in a practical design. There does not appear to be any ill effects associated with the frequency of operation. Although they are not the most space efficient winding method, they are ideal for prototyping as they form discreet windings that can easily be handled; rather than having to unwind each turn as in a conventional winding arrangement.

The main technical challenges, which have been overcome in this thesis, are magnetic flux loss, voltage drop and ripple under load, and power loss. Though further challenges have been identified that must be overcome before a working prototype can be constructed. These are electrical insulation and thermal considerations of the supply.

7.2 Future Work

The work in this thesis forms a good foundation for the development of the next generation of HVDC power supplies, but there is still a considerable amount of work that must be completed before a working prototype can be constructed. The steps necessary to complete this project are outlined briefly in this section. It is noted that designs based on resonant transformers and NHVGs have not been considered in this project, and there may be some merit in investigating these technologies to the same level of detail as the ICT and cascade transformer designs that have been investigated in this thesis.

There is still a lot of work that must be carried out before a PCB based winding can be reliably used in a HV power supply. First, more experiments need to be carried out to evaluate the performance of the windings under different frequencies. Initial findings do not indicate any significant relationship between frequency and breakdown voltage. However, it is possible that an increase in frequency of an order of magnitude or more might have a noteworthy effect on dielectric strength of the solder mask. In addition, all experiments to date have been conducted using a sinusoidal voltage source. It is of great importance to learn how the windings would react to square or trapezoidal waveforms, which are much more likely to be used in practical power supplies. A number of prototype windings must be fabricated, to verify the results found from carrying out experiments on smaller sections.

It is also important to determine how capable PCBs are of withstanding the environmental stresses that will be put upon them in a working power supply. For this, a test rig must be constructed, that can subject the boards to the insulating fluid and temperatures that they will be exposed to during power supply operation. Once the boards have undergone accelerated lifetime testing, they should be inspected for any signs of degradation. While in the rig, they should also be tested electrically to determine how well the windings handle a “worst case scenario”. The boards should be subjected to normal operating voltages for extended periods of time as well as impulse voltages, with amplitudes several times that expected to be experienced during normal operation, to evaluate the ability of the PCBs to withstand unforeseen transients.

Additional work should also be undertaken with the intention of optimising the design of the PCB windings. This thesis has not explored the potential of utilizing the internal layers of a PCB. Doing so could significantly reduce the size of the windings, potentially leading to a

reduction in the size of the overall design, leading to lower production costs. First, the withstand voltage of the internal insulation should be tested in a similar manner to that described in Section 4.3.2. Then, a number of prototype windings should be fabricated and subjected to severe environmental stress using the test rig. Finally, the prototypes should undergo electrical testing to ensure their withstand voltages are sufficient for the purposes of this project.

Another area in need of additional development, before being applied in a practical power supply, is that of insulation. This has not been investigated here in detail but is of critical importance if this work is to be investigated further. Firstly, a detailed review of possible insulating materials must be undertaken; after which a simulation study should be undertaken to optimise the transformer design so that excessively high electric field gradients are avoided. Areas with an unavoidably high electric field strength should be identified so that they can be strengthened with additional insulation in the design stage. The results of these simulations should be verified using practical experiments conducted on small sections of the overall design, in a similar manner to the way elements of PCB windings were tested in this thesis.

Once a design is settled upon that satisfies the magnetic, electrical, and insulation requirements of this project; a second simulation study must be conducted to investigate the heat flow of the power supply under constant operation. From this, it should be determined if passive cooling will be sufficient for regular operation, or if active cooling is required.

Eventually, construction of a prototype cascade can begin. This should undergo the same rigorous testing as the PCB windings. Provided the cascade is proven able to operate under extreme conditions, or else once the cascade has been redesigned to correct the problems experienced under testing, then work can begin constructing a complete power supply.

List of References

- [1] J. W. Coltman, "The Westinghouse Atom Smasher-An IEEE Historical Milestone," *IEEE Trans. Educ.*, vol. 30, no. 1, pp. 37–42, 1987.
- [2] High Voltage Engineering, "Tandetron Sales Brochure." .
- [3] "ITER Web Page." [Online]. Available: <https://www.iter.org/>.
- [4] J. D. Cross, "Modular High Voltage Power Supply with Integral Flux Leakage Compensation," Pat. No. US6026004A, 1998.
- [5] Kaiser, "Kaiser Technical Presentation," 2008. [Online]. Available: <https://www.jlab.org>.
- [6] R. J. Adler, "Private Conversation With Dr Richard Adler at the 2018 IPMHVC." 2018.
- [7] IEEE, "IEEE Transactions on Dielectrics and Electrical Insulation." [Online]. Available: <https://ieeexplore.ieee.org/xpl/RecentIssue.jsp?punumber=94>.
- [8] E. Schamiloglu, R. J. Barker, M. Gundersen, and A. A. Neuber, "Modern Pulsed Power: Charlie Martin and Beyond," *Proc. IEEE*, vol. 92, no. 7, pp. 1014–1019, 2004.
- [9] J. C. Martin, "Nanosecond Pulse Techniques," *Proceedings IEEE*, vol. 80, no. 6, pp. 934–945, 1992.
- [10] A. A. Neuber and J. C. Dickens, "Magnetic flux compression generators," *Proc. IEEE*, vol. 92, no. 7, pp. 1205–1215, 2004.
- [11] K. A. O. Connor, R. D. Curry, L. Altgilbers, and A. F. C. G. Simulator, "Investigation of a High Voltage , High Frequency Power Conditioning System for Use With Flux Compression Components," in *16th IEEE International Pulsed Power Conference*, Albuquerque, NM, USA, 2007, pp. 2007–2010.
- [12] P. S. H. Kim, H. Heo, S. H. Nam, S. S. Pohang, and S. T. Ko, "Development of Air Core Type 500 kV HV Pulse Transformer," in *IEEE Pulsed Power Conference*, Monterey, CA, USA, 2005, pp. 696–699.
- [13] J. O'Loughlin, G. J. Rohwein, and J. D. Sidler, "Air Core Pulse Transformer Design," in *IEEE Conference Record of the 1988 Eighteenth Power Modulator Symposium*, Hilton Head, SC, USA, 1988, pp. 325–330.
- [14] G. J. Rohwein, "A Low-Impedance, High-Voltage Direct Drive Transformer System," in *IEEE Conference Record of the 1988 Eighteenth Power Modulator Symposium*, Hilton Head, SC,

USA, 1988, pp. 331–335.

- [15] H. Ibaiondo and A. Romo, “Kinetic Energy Recovery on Railway Systems With Feedback to the Grid,” in *Proceedings of 14th International Power Electronics and Motion Control Conference EPE-PEMC 2010*, Ohrid, Macedonia, 2010, pp. 94–97.
- [16] D. Cornic, “Efficient Recovery of Braking Energy Through a Reversible DC Substation,” in *International Conference on Electrical Systems for Aircraft, Railway and Ship Propulsion, ESARS 2010*, Bologna, Italy, 2010, pp. 1–9.
- [17] M. Steiner and H. Reinold, “Medium Frequency Topology in Railway Applications,” in *2007 European Conference on Power Electronics and Applications, EPE*, Aalborg, Denmark, 2007, pp. 1–10.
- [18] “Magnetis Marelli - KERS.” [Online]. Available: <http://www.magnetimarelli.com/excellence/technological-excellences/kers>.
- [19] J. F. Smee, “A 700-kV Direct-Current Electrostatic Generator,” *J. Inst. Electr. Eng.*, vol. 91, no. 47, pp. 422–431, 1944.
- [20] R. J. Van De Graaff, “Electrostatic Generator,” Pat. No. US1991236A, 1935.
- [21] W. E. Shoupp, “The Electrostatic Generator Used in Nuclear Studies,” *Electr. Eng.*, vol. 67, no. 7, pp. 668–671, 1948.
- [22] B. R. L. Fortescue and P. D. Hall, “The High-Voltage Electrostatic Generator at the Atomic Energy Research Establishment,” *Proc. IEE*, vol. 96, no. 98, pp. 77–85, 1949.
- [23] R. Khalid, S. Shaheen, and A. Javed, “Van de Graaff Generator – A Cost Effective Solution,” in *2018 International Conference on Power Generation Systems and Renewable Energy Technologies (PGSRET)*, Islamabad, Pakistan, 2018, no. September, pp. 1–6.
- [24] E. Kuffel, W. Zaengl, and J. Kuffel, *High Voltage Engineering: Fundamentals*, 2nd ed. Oxford: Newnes, 2000.
- [25] F. H. Merrill, “The Van de Graaff Electrostatic Generator,” *Students Q. J.*, vol. 9, no. 35, pp. 124–127, 1939.
- [26] L. Katzir and D. Shmilovitz, “A Split-Source Multisection High-Voltage Power Supply for X-Ray,” *IEEE J. Emerg. Sel. Top. POWER Electron.*, vol. 4, no. 2, pp. 373–381, 2016.
- [27] I. Diversified Technologies, “Power Supply Sales Leaflet,” 2019. [Online]. Available: <http://www.divtecs.com/data/Root/HVPSDataSheet2018.pdf?rev=859B>.
- [28] E. Gates and L. Chartrand, *Introduction to Electronics*, 4th ed. Cengage Delmar Learning, 2000.

- [29] D. A. Spence, B. F. Gavin, R. Peters, L. L. Reginato, B. H. Smith, and R. C. Wolgast, "A 3-MV Injector For The Superhilac," *IEEE Trans. Nucl. Sci.*, vol. 18, no. 3, pp. 97–101, 1971.
- [30] M. R. Cleland and P. Farrell, "Dynamitrons of the Future," *IEEE Trans. Nucl. Sci.*, vol. 12, no. 3, pp. 227–234, 1965.
- [31] M. R. Cleland, R. A. Galloway, L. DeSanto, and Y. Jongen, "High-Current DC Proton Accelerator," Pat. No. US8148922B2, 2012.
- [32] D. J. W. Mous, "High Current Single-Ended DC Accelerator," Pat. No. US9084336B2, 2015.
- [33] R. Koudijs, A. Gott dang, and D. J. W. Mous, "Introduction Of The New High Voltage Engineering (HVE) Accelerator For High Energy/High Current Ion Implantation," in *Ion Implantation Technology. 2002. Proceedings of the 14th International Conference on*, Taos, New Mexico, USA, 2002, pp. 498–500.
- [34] J. P. O. Connor, M. S. Chase, S. L. F. Richards, N. Tokoro, and S. T. Drive, "Performance Characteristics of the Genus Inc. Tandetron™ 1520 MeV Ion Implantation System," in *Proceedings of 11th International Conference on Ion Implantation Technology*, Austin, TX, USA, 1992, pp. 454–457.
- [35] P. Hammond and J. K. Sykulski, *Engineering Electromagnetism Physical Processes and Computation*, 1st ed. Oxford: Oxford University Press, 1994.
- [36] W. G. Hurley and W. H. Wolfle, *Transformers and Inductors For Power Electronics*, 1st ed. Chichester: Wiley, 2013.
- [37] W. G. Hurley, W. H. Wölfle, and J. G. Breslin, "Optimized Transformer Design: Inclusive of High-Frequency Effects," *IEEE Trans. Power Electron.*, vol. 13, no. 4, pp. 651–659, 1998.
- [38] A. Van den Bossche and V. C. Valchev, *Inductors and Transformers for Power Electronics*, 1st ed. Taylor and Francis Group, 2005.
- [39] T. Xu and Z. Xu, "Flashover Characteristics of Artificial Polluted UHV AC Bushing Insulators," in *2013 Annual Report Conference on Electrical Insulation and Dielectric Phenomena Flashover*, Shenzhen, China, 2013, pp. 387–390.
- [40] X. She, A. Q. Huang, and R. Burgos, "Review of Solid-State Transformer Technologies and Their Application in Power Distribution Systems," *IEEE J. Emerg. Sel. Top. Power Electron.*, vol. 1, no. 3, pp. 186–198, 2013.
- [41] G. Ortiz, M. Leibl, J. W. Kolar, and O. Apeldoorn, "Medium Frequency Transformers for Solid-State-Transformer Applications - Design and Experimental Verification," in *IEEE International Conference on Power Electronics and Drive Systems (PEDS 2013)*, Kitakyushu, Japan, 2013, pp. 1285–1290.

- [42] C. Leung, S. Baek, S. Dutta, and S. Bhattacharya, "Design Considerations of High Voltage and High Frequency Three Phase Transformer for Solid State Transformer Application," in *2010 IEEE Energy Conversion Congress and Exposition*, Atlanta, GA, USA, 2010, pp. 1551–1558.
- [43] R. W. Sorensen, "Development and Characteristics of a 1,000,000-Volt Cascade Transformer at California Institute of Technology," *J. Am. Inst. Electr. Eng.*, vol. 44, no. 4, pp. 373–378, 1925.
- [44] A. Takahashi, T. Tanaka, K. Yamaguchi, H. Fujita, Y. Hiranuma, S. Ichimura, K. Watanabe, and M. Kashiwagi, "ITER NBI DC-1MV Ultrahigh Voltage Rectifier," in *2018 IEEE Energy Conversion Congress and Exposition*, Portland, OR, USA, 2018, pp. 4232–4237.
- [45] R. J. Van de Graaff, "High Voltage Electromagnetic Apparatus Having an Insulating Magnetic Core," Pat. No. US3289066A, 1965.
- [46] N. Tesla, "Apparatus For Transmitting Electrical Energy," Pat. No. US1119732A, 1914.
- [47] Y. Irani, A. Lapthorn, and P. Bodger, "Equivalent Circuit Model of Cascade Connected Partial Core Resonant Transformers," in *Australian Universities Power Engineering Conference*, Hobart, TAS, Australia, 2013, pp. 1–4.
- [48] H. Yamaguchi, Y. Sato, and T. Kataoka, "Conceptual Design of Air-Core Superconducting Transformer For 500 kV Cable Transmission System," *IEE Proc. - Gener. Transm. Distrib.*, vol. 142, no. 5, pp. 487–493, 1995.
- [49] H. L. Chan, K. W. E. Cheng, and D. Sutanto, "Superconducting Self-Resonant Air-Core Transformer," in *IEEE 31st Annual Power Electronics Specialists Conference*, Galway, Ireland, Ireland, 2000, pp. 314–319.
- [50] N. Zhu, J. D. Van Wyk, and F. Wang, "Design of Integrated Parallel Resonant Transformers," in *PESC Record - IEEE Annual Power Electronics Specialists Conference*, Recife, Brazil, 2005, pp. 1787–1792.
- [51] C. D. Meyer, S. S. Bedair, B. C. Morgan, and D. P. Arnold, "High-Inductance-Density, Air-Core, Power Inductors, and Transformers Designed for Operation at 100–500 MHz," *2010 IEEE Trans. Magn.*, vol. 46, no. 6, pp. 2236–2239, 2010.
- [52] J. C. Sprott, *Physics Demonstrations: A Sourcebook for Teachers of Physics*, 1st ed. Univ. of Wisconsin Press, 2006.
- [53] R. Adler and R. Richter-Sand, "High Voltage, High Power Nested High Voltage Accelerator," in *Conference Record of the 1991 IEEE Particle Accelerator Conference*, San Francisco, CA, USA, 1991, pp. 3201–3203.
- [54] R. J. Adler, "Comparison of DC and Pulsed Beams for Commercial Applications," in *10th*

International Conference on High-Power Particle Beams, San Diego, CA, USA, 1994, pp. 29–32.

- [55] R. J. Adler and R. J. Richter-Sand, “Advances in the Development of the Nested High Voltage Generator,” in *Proceedings of International Conference on Particle Accelerators*, Washington, DC, USA, 1993, pp. 1306–1308.
- [56] R. J. Adler, J. Gilbrech, K. Childers, and E. Koschmann, “A Compact Nested High Voltage Generator For Medium Pulse Duration Applications,” in *17th IEEE International Pulsed Power Conference*, Washington, DC, USA, 2009, pp. 913–917.
- [57] R. J. Adler, “Nested High Voltage Generator/Particle Accelerator,” Pat. No. US5124658A, 1992.
- [58] R. H. Potter, R. J. Adler, and J. M. Potter, “High voltage Generator With Multiple Inductive Couplings,” Pat. No. US8274806B1, 2012.
- [59] G. J. Rohwein and R. N. Lawson, “An Scr-Switched, High Voltage, High Gain Linear Transformer System,” in *7th Pulsed Power Conference*, Monterey, CA, USA, 1989, pp. 762–765.
- [60] S. Naidu, M and V. Kamaraju, *High Voltage Engineering*, 2nd ed. New York: McGraw-Hill, 1995.
- [61] T. Takuma, T. Kouno, and H. Matsuda, “Field Behavior Near Singular Points In Composite Dielectric Arrangements,” *IEEE Trans. Electr. Insul.*, vol. 13, no. 6, pp. 426–435, 1978.
- [62] E. Volpov, “Dielectric Strength Coordination and Generalized Spacer Design Rules for HVAC/DC SF 6 Gas Insulated Systems,” *IEEE Trans. Dielectr. Electr. Insul.*, vol. 11, no. 6, pp. 949–963, 2004.
- [63] L. Solymar, D. Walsh, and R. R. A. Syms, *Electrical Properties of Materials*, 9th ed. Oxford: Oxford University Press, 2014.
- [64] S. M. Harris and A. Mellinger, “Nitrogen and Air Paschen Curves for Dielectric Barrier Discharges in μm -Sized Voids,” in *2015 IEEE Conference on Electrical Insulation and Dielectric Phenomena (CEIDP)*, Ann Arbor, MI, USA, 2015, pp. 598–600.
- [65] M. McGrath, “Climate Change: Electrical Industry’s ‘Dirty Secret’ Boosts Warming,” *BBC News*, 2019. [Online]. Available: <https://www.bbc.co.uk/news/science-environment-49567197>. [Accessed: 13-Sep-2019].
- [66] D. Zheng, C. Chen, S. Lv, X. Zhai, and D. Zhao, “Experimental Research on Endurance Behaviors of the SF6/N2 Mixtures Under Impulse Voltage,” in *Proceedings of 2011 6th International Forum on Strategic Technology*, Harbin, Heilongjiang, China, 2011, pp. 166–168.

- [67] H. R. Hiziroglu and M. S. Dincer, "Calculation of Discharge Inception Voltages in Argon + SF₆ Mixtures Under Non-uniform Electric Fields," in *2000 Annual Report Conference on Electrical Insulation and Dielectric Phenomena*, Victoria, BC, Canada, 2000, pp. 426–429.
- [68] K. Mardikyan, O. Kalenderli, O. Ersen, and E. Canarslan, "AC Breakdown Strength of N₂, SF₆ and a Mixture of N₂ + SF₆ Containing a Small Amount of SF₆," in *IEEE International Symposium on Electrical Insulations*, Montreal, Quebec, Canada, 1996, pp. 763–765.
- [69] Y. Q. Xing, J. X. Jin, B. X. Du, R. M. Sun, X. Y. Chen, F. M. Li, Z. H. Chen, L. J. Ba, H. You, Z. Q. Jiang, Y. L. Wang, X. D. Liu, and Y. P. Zhu, "Influence of Flux Diverter on Magnetic Field Distribution for HTS Transformer Windings," *IEEE Trans. Appl. Supercond.*, vol. 26, no. 7, 2016.
- [70] F. Endo, T. Kichikawa, R. Ishikawa, and J. Ozawa, "Dielectric Characteristics of SF₆ Gas for Application to HVDC Systems," *IEEE Trans. Power Appar. Syst.*, vol. 99, no. 3, pp. 847–855, 1980.
- [71] A. De Lorenzi, L. Grando, A. Pesce, P. Bettini, and R. Specogna, "Modeling of Epoxy Resin Spacers for the 1 MV DC Gas Insulated Line of ITER Neutral Beam Injector System," *IEEE Trans. Dielectr. Electr. Insul.*, vol. 16, no. 1, pp. 77–87, 2009.
- [72] D. J. Swaffield, P. L. Lewin, G. Chen, and J. K. Sykulski, "Cryogenic Dielectrics and HTS Power Apparatus: Research at the University of Southampton," *IEEE Electr. Insul. Mag.*, vol. 22, no. 5, pp. 29–37, 2006.
- [73] P. C. S. Krishnayya, P. J. Lambeth, P. S. Maruvada, N. G. Trinh, G. Desilets, and S. L. Nilsson, "Technical Problems Associated with Developing HVDC Converter Stations for Voltages Above 600 kV," *IEEE Trans. Power Deliv.*, vol. 2, no. 1, pp. 174–181, 1987.
- [74] S. Menju and K. Takahashi, "DC Dielectric Strength of a SF₆ Gas Insulated System," *IEEE Trans. Power Appar. Syst.*, vol. 97, no. 1, pp. 217–224, 1978.
- [75] E. Volpov, "Electric Field Modeling and Field Formation Mechanism in HVDC SF₆ Gas Insulated Systems," *IEEE Trans. Dielectr. Electr. Insul.*, vol. 10, no. 2, pp. 204–215, 2003.
- [76] S. Matsumura, T. Tanabe, Y. Harumoto, S. Tominaga, H. Kuwahara, N. Nagai, and K. Tada, "New Approach to SF₆ Gas Insulated HVDC Converter Station," *IEEE Trans. Power Appar. Syst.*, vol. 102, no. 9, pp. 2871–2880, 1983.
- [77] T. Hasegawa, K. Yamaji, and M. Hatano, "Development of Insulation Structure and Enhancement of Insulation Reliability of 500 kV DC GIS," *IEEE Trans. Power Deliv.*, vol. 12, no. 1, pp. 194–202, 1997.
- [78] T. Ohga, K. Usui, K. Ohmori, K. Watanabe, K. Ohshima, T. Itoh, M. Kawai, and M. Kuriyama, "High Voltage Power Supply of Negative-Ion Based NBI for JT-60U," in *17th*

- [79] L. Boxman, R. M. Sanders, D. and J. Martin, P, *Handbook of Vacuum Arc Science and Technology Fundamentals and Applications*, 1st ed. Park Ridge, New Jersey: Moyes Publications, 1995.
- [80] D. Biswas, "A Universal Formula For The Field Enhancement Factor," *Phys. Plasmas*, vol. 25, no. 4, p. 043113 1-4, 2018.
- [81] J. Wu, Z. Zhang, B. Zhang, L. Zhang, and X. Zheng, "Effects of Degassing on DC Surface Flashover Property of Polyimide," in *2015 IEEE 11th International Conference on the Properties and Applications of Dielectric Materials (ICPADM)*, Sydney, NSW, Australia, 2015, pp. 504–507.
- [82] J. Wang, A. Q. Huang, W. Sung, Y. Liu, and B. J. Baliga, "Smart Grid Technologies: Development of 15-kV SiC IGBTs and Their Impact on Utility Applications," *IEEE Industrial Electronics Magazine*, 2009.
- [83] J. W. Palmour, J. Q. Zhang, M. K. Das, R. Callanan, A. K. Agarwal, and D. E. Grider, "SiC Power Devices for Smart Grid Systems," in *International Power Electronics Conference*, 2010, pp. 1006–1013.
- [84] Q. Zhang, R. Callanan, M. K. Das, S.-H. Ryu, A. K. Agarwal, and J. W. Palmour, "SiC Power Devices for Microgrids," *IEEE Trans. Power Electron.*, vol. 25, no. 12, pp. 2889–2895, 2010.
- [85] W. Sung, J. Wang, A. Q. Huang, and J. Baliga, "Design and Investigation of Irequency Capability of 15kV 4H-SiC IGBT," in *21st International Symposium on Power Semiconductor Devices & IC's*, 2009, pp. 271–274.
- [86] S. Mao, Z. Yao, D. Zhu, J. Popovic, and J. A. Ferreira, "A High Frequency 110kV Output-voltage, 8kW Output-power High Voltage Generator with Silicon Carbide Power Semiconductor Devices," in *21st European Conference on Power Electronics and Applications*, 2019.
- [87] J. Wang, G. Wang, S. Bhattacharya, and A. Q. Huang, "Comparison of 10-kV SiC Power Devices in Solid-State Transformer," in *2010 IEEE Energy Conversion Congress and Exposition*, 2010, pp. 3284–3288.
- [88] H. W. Beaty, *Electrical Engineering Materials Reference Guide*, 1st ed. McGraw-Hill, 1990.
- [89] S. Barg, K. Ammous, H. Mejbri, and A. Ammous, "An Improved Empirical Formulation for Magnetic Core Losses Estimation Under Nonsinusoidal Induction," *IEEE Trans. Power Electron.*, vol. 32, no. 3, pp. 2146–2154, 2017.
- [90] E. C. Snelling, *Soft Ferrites Properties and Applications*, 2nd ed. Butterworths, 1988.

- [91] C. P. Steinmetz, "On the Law of Hysteresis," *Trans. Am. Inst. Electr. Eng.*, vol. IX, no. 1, pp. 1–64, 1892.
- [92] J. Reinert, A. Brockmeyer, and R. W. De Doncker, "Calculation of Losses in Ferro- and Ferrimagnetic Materials Based on the Modified Steinmetz Equation," in *Conference Record of the 1999 IEEE Industry Applications Conference. Thirty-Forth IAS Annual Meeting*, Phoenix, AZ, USA, 1999, pp. 2087–2092.
- [93] J. Reinert, A. Brockmeyer, and R. W. A. A. De Doncker, "Calculation of Losses in Ferro and Ferrimagnetic Materials Based on the Modified Steinmetz Equation," *IEEE Trans. Ind. Appl.*, vol. 37, no. 4, pp. 1055–1061, 2001.
- [94] J. Li, T. Abdallah, and C. R. Sullivan, "Improved Calculation of Core Loss with Nonsinusoidal Waveforms," in *Conference Record of the 2001 IEEE Industry Applications Conference. 36th IAS Annual Meeting*, Chicago, IL, USA, 2001, pp. 2203–2210.
- [95] K. Venkatachalam, C. R. Sullivan, T. Abdullah, and H. Tacca, "Accurate Prediction of Ferrite Core Loss with Nonsinusoidal Waveforms Using Only Steinmetz Parameters," in *2002 IEEE Workshop on Computers in Power Electronics, 2002. Proceedings*, Mayaguez, Puerto Rico, USA, 2002, pp. 36–41.
- [96] J. Muhlethaler, J. Biela, J. W. Kolar, and A. Ecklebe, "Improved Core-Loss Calculation for Magnetic for Components Employed in Power Electronic Systems," *IEEE Trans. Power Electron.*, vol. 27, no. 2, pp. 964–973, 2012.
- [97] W. Shen, F. F. Wang, D. Boroyevich, and C. W. Tipton, "Loss Characterization and Calculation of Nanocrystalline Cores for High-Frequency Magnetics Applications," *IEEE Trans. Power Electron.*, vol. 23, no. 1, pp. 475–484, 2008.
- [98] "Beta Layout PCB Pool." [Online]. Available: <https://uk.beta-layout.com/pcb/configurator/>. [Accessed: 29-Aug-2019].
- [99] ELECTRA, "Technical Datasheet Carapace EMP110." [Online]. Available: <http://allenwoodsgroup.com/pdf/EMP110.pdf>.
- [100] D. N. Light and J. R. Wilcox, "Process Considerations in the Fabrication of Teflon Printed Circuit," in *1994 Proceedings. 44th Electronic Components and Technology Conference*, Washington DC, USA, 1994, pp. 542–549.
- [101] Autodesk, "Eagle Product Overview." [Online]. Available: <https://www.autodesk.com/products/eagle/overview>.
- [102] L. A. R. Tria, D. Zhang, and J. E. Fletcher, "Planar PCB Transformer Model for Circuit Simulation," *IEEE Trans. Magn.*, vol. 52, no. 7, pp. 1–4, 2016.
- [103] N. G. Trinh, "Electrode Design for Testing in Uniform Field Gaps," *IEEE Trans. Power*

Appar. Syst., vol. PAS-99, no. 3, pp. 1235–1242, 1980.

- [104] E. Tuncer, I. Sauers, D. R. James, and A. R. Ellis, “Electrical Insulation Characteristics of Glass Fiber Reinforced Resins,” *IEEE Trans. Appl. Supercond.*, vol. 19, no. 3, pp. 2359–2362, 2009.
- [105] F. Guastavino, L. Centurioni, G. Coletti, A. Ratto, and E. Torello, “Electrical characterization of multi-layered Printed Circuit Boards,” in *The 17th Annual Meeting of the IEEE Lasers and Electro-Optics Society, 2004. LEOS 2004*, Boulder, CO, USA, 2004, pp. 588–591.
- [106] J. Gerhold, “Cryogenic liquids - A Prospective Insulation Basis for Future Power Equipment,” *IEEE Trans. Dielectr. Electr. Insul.*, vol. 9, no. 1, pp. 68–74, 2002.
- [107] T. Xiong, Q. Zhou, T. Jiang, X. Li, and T. Yang, “Breakdown Characteristics of Printed Circuit Boards Under Pulsed Square Wave,” in *2017 International Symposium on Electrical Insulating Materials (ISEIM)*, Toyohashi, Japan, 2017, pp. 287–290.
- [108] S. Ui-haq and G. R. G. Raju, “Weibull Statistical Analysis of Area Effect on the Breakdown Strength in Polymer Films,” in *2002 Annual Report Conference on Electrical Insulation and Dielectric Phenomena*, Cancun, Quintana Roo, Mexico, 2002, pp. 518–521.
- [109] M. P. Wilson, M. J. Given, I. V Timoshkin, S. J. Macgregor, T. Wang, E. Engineering, G. Street, M. A. Sinclair, K. J. Thomas, H. Division, A. W. E. Aldermaston, J. M. Lehr, S. N. Laboratories, and P. O. Box, “Weibull Statistical Analysis Of Impulse-Driven Surface Breakdown Data,” in *2011 IEEE Pulsed Power Conference*, Chicago, IL, USA, 2011, pp. 218–222.
- [110] X. Du and Y. Gao, “Dielectric Breakdown of Printed Circuit Board Under Magnetic Field,” in *Proceedings of 2005 International Symposium on Electrical Insulating Materials, 2005*, Kitakyushu, Japan, 2005, pp. 308–311.
- [111] G. Meng, Y. Cheng, J. Song, Y. Liu, K. Wu, J. Dong, and A. S. Preparation, “Breakdown Characteristics of PCB Paralleled Traces Injected by Rectangular Pulse,” in *International Symposium on Electrical Insulating Materials*, Kyoto, Japan, 2011, pp. 144–147.
- [112] L. E. Reukema, “The Relation Between Frequency and Spark-Over Voltage in a Sphere-Gap Voltmeter,” *Trans. Am. Inst. Electr. Eng.*, vol. 47, no. 1, pp. 38–48, 1928.
- [113] J. A. Pim, “The Electrical Breakdown Strength of Air at Ultra-High Frequencies,” *Proc. IEE - Part III Radio Commun. Eng.*, vol. 96, no. 40, pp. 117–129, 1949.
- [114] A. Lieberman, M and J. Lichtenberg, A, *Principles of Plasma Discharges and Materials Processing*, 2nd ed. Hoboken: Wiley, 2005.
- [115] “IPC-2221.” [Online]. Available: <http://ch00fttech.com/wp-content/uploads/2016/12/IPC-2221-2.pdf>.

Appendix A Published Paper

The following pages contain a copy of a paper that was published in the IEEE Transactions on Dielectrics and Electrical Insulation (Volume: 26 , Issue: 2 , April 2019). The work in this paper was expanded to form the basis of Chapter 5 of this thesis.

An Investigation into the Suitability of Insulated Core Transformer Technology for an Ultra High Voltage Power Supply

R.E.P. Frost and P.L. Lewin

Electronics and Computer Science
University Of Southampton
Southampton, United Kingdom
SO17 1BJ

M. Spong

QinetiQ Group plc.
Cody Technology Park
Farnborough, United Kingdom

ABSTRACT

A growing area of interest is HVDC supplies. This paper represents an initial study into possible designs of HVDC transformers that could provide 2A at 1MV, with the added specification that any proposed technology should be scalable to 5A at 5MV. Insulated core transformers (ICTs) have been initially selected as a potentially suitable technology. Careful design of the ICT magnetic core is required to ensure that flux loss is limited so that higher voltages are achievable. Simulation studies have shown that the voltage produced in an ICT does not scale linearly, meaning that there is an effective limit to the voltage that they can produce. In addition to this, a technique is proposed to increase the available current output of an ICT. The full analysis is presented in this paper.

Index Terms — HVDC, transformer, insulated core transformers, simulation, magnetic flux

1 INTRODUCTION

THERE is currently growing interest in both academia and industry for a power supply capable of producing 2A continuous DC current, at 1MV, with a maximum voltage ripple of 0.5%. Any design must be as compact as possible; ideally able to fit inside a three-meter cube, and should store limited energy of the order of hundreds of joules or less. This final requirement is a safety measure, as a fault in the HV circuits of a supply that stores a lot of energy could be catastrophic and irreparable. At the same time there is also interest in developing such a supply further in the future, to ultimately be able to generate 5A continuous DC current at 5MV.

Several technologies are currently used ubiquitously in compact HV power supply design, most notably the Cockroft Walton (CW) Generator. These are popular, in no small part, due to their simplicity; they can easily generate several megavolts

using relatively few components. However, they suffer from severe voltage drop under heavy load, and require a large amount of stored energy [1].

For this reason, other technologies with a higher power density are being investigated. Amongst the most promising are resonant transformers (RTs), cascade transformers (CTs), and insulated core transformers (ICTs). The aim of the work reported in this paper is to examine the feasibility of using an ICT based design for this particular application.

This work is based on assuming the limitations of current insulating film technologies. That is to say, the simulation studies do not anticipate any significant developments in core electrical properties of thin film insulation materials. All designs assume that insulation of the individual cores is achieved using a 250 micron thick film of a commonly used solid insulator such as mylar, teflon, or kapton.

2 CORE LAYOUT

The first ICTs, as patented by Van de Graaf [2], consisted of a single stack of electrically insulated cores, effectively creating a bar core transformer. In

order to prevent the magnetic flux from bypassing the HV cores completely, the stack was placed inside a metal container. This container was connected to the core around which the primary winding was wound. Flux could then bridge the gap between the top of the stack and surrounding container before completing the path to the primary winding.

As the grounded container had to be insulated from the total operational voltage of the device, it was necessary for a large gap to exist between the top of the stack and the container. This limited the flow of flux to the top of the stack. The reduction in flux, reaching the higher cores, reduced the operational voltage of secondary windings further away from the primary.

Soon a three-phase variant of the ICT was developed for high power applications [3], thus eliminating the need for the grounded container, by providing a complete flux path between phases. This worked in the same way as a three-phase transmission, or distribution, transformer.

Van de Graaf sought to get around the voltage drop associated with flux loss by wrapping more windings around cores situated further away from the primary. This however, adds complexity to the system design as the windings around each insulated core have to be unique. A more economical design would have identical windings around each core to reduce system cost and complexity. In addition to this, there is a practical limit to the voltage that can be obtained using a single stack, as increasing the height of the stack will soon yield diminishing returns, in terms of voltage, as the flux loss becomes too great.

A number of different core configurations were examined in [4] and it was concluded that the most effective way of reducing flux loss is, as with a conventional transformer, to create a closed flux path from soft magnetic material. This technique was employed, amongst others, by Cross, who patented an ICT that produced 375 kV. That was then doubled to 750 kV using power electronics [5], at several hundred milliamps. This design has since been scaled up to 1 MV [6].

A necessity of creating a continuous flux path from soft magnetic material is that there needs to be two insulated cores operating at each voltage level. This is to stop the HV core needing to be insulated from the grounded primary winding. The Cross ICT achieved this by having two parallel insulated stacks connected, at the bottom, by a grounded core around which the primary winding is wound and, at the top, by another core section that would allow flux to pass between the two HV sections (Figure 1). This is an elegant solution as it means that the LV primary is at the bottom while the voltage, in the stacks, increases in the cores further away from the primary. However, there are problems with flux passing between the two stacks and being reluctant to change direction at the top of the stacks.

In this paper, the authors have investigated an alternative arrangement in which a single stack is constructed that is driven by a primary winding at either end. These primary windings are electrically

connected in parallel, meaning that they operate in phase with each other. The voltage increases towards the center of the stack, where it is insulated from the LV winding at each end. Flux can then pass between the two windings via a solid clamp, as seen in Figure 2. This layout has the advantage that the magnetic flux has a straight path through the cores. In addition to this, having insulated gaps in a core effectively reduces the relative permeability of the core material. This means that the clamped system will reduce the amount of flux leaving the stack to return to the primary winding through the parallel flux path.

The relative flux path found in each layout was calculated and compared using a finite element analysis (FEA) model. In each case, an ICT was simulated with a core cross sectional area of 100 mm by 100 mm, and a thickness of 5.75 mm. There was a distance of 200 mm between the insulated stack and the return path, and a gap of 0.25 mm between each insulated core. Each core was surrounded by 100 windings. These parameters are reasonable as they are based on those commonly used in ICTs based on the Cross design [6]. ICTs with stack heights from 1 to 50 cores were simulated, in both layouts, and the minimum normalized flux in each system was recorded as shown in Figure 3.

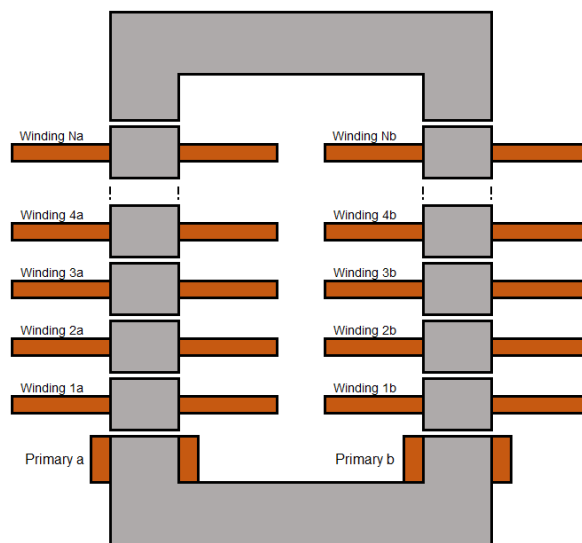


Figure 1. The traditional layout of the Cross type ICT.

From Figure 3 it can be seen that there is no significant difference between the flux losses obtained using either arrangement when the number of insulated cores is less than 30. For this reason, in a single phase ICT, a flux return clamped layout is inefficient as it effectively doubles the height and material cost of the design, without significantly reducing the flux loss. However, in designs that consist of multiple phases and a significant number of insulated cores (e.g. more than 40), the single stack configuration may prove advantageous; this is discussed further in Section 4.

The flux loss predicted in these simulations, and detailed in Figure 3, is approximately half of that previously reported for an ICT [6] that was operating at a higher voltage than used in this simulation study.

The use of 2D simulation will lead to an underestimate of flux loss in the third dimension.

3 BENEFITS OF CROSS CORE TECHNOLOGY

In addition to the closed flux path, there are several other appealing features of Cross transformer technology (CTT). Most apparent is that the secondary windings are constructed from PCB windings [5]. The HV power electronics are also surface mounted to these PCBs for reduced construction cost and complexity. An advantage of PCB printed transformer windings is that they consist of one or two layers of windings spiraling outwards; this makes very flat windings and has the benefit of reducing the thickness of each insulated core stage, therefore reducing the overall height of the design. However, a disadvantage of this technique is that it increases the surface area of each winding, thus increasing the parasitic capacitance between layers.

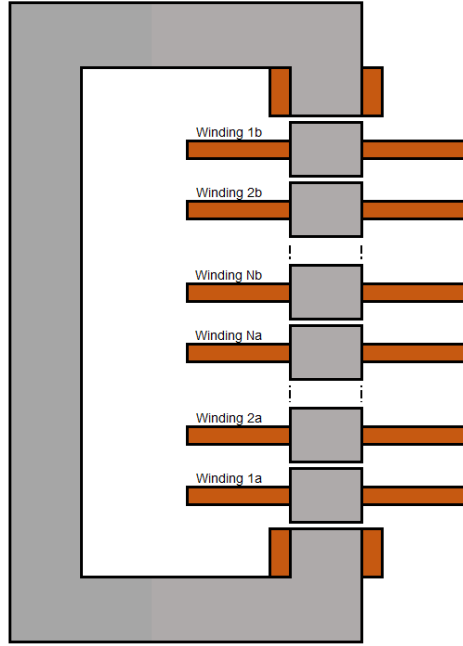


Figure 2. The proposed alternative layout of the Cross type ICT.

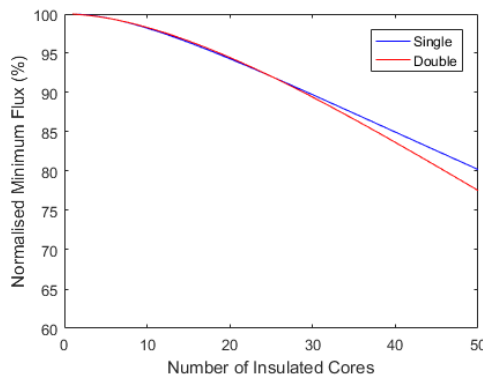


Figure 3. The minimum flux found in ICTs, arranged using both the traditional double stack layout and the proposed single stack layout, with a number of insulated cores ranging from 1 to 50.

While conventional ICTs operate at single or three phase grid frequency, CTT uses power electronics and specialist core materials, such as nanocrystalline, to operate at a frequency close to 100 kHz. This significantly reduces the necessary size of the design, as well as the energy that must be stored in the voltage doublers to reduce ripple.

The key advantage of CTT is the use of tuned capacitors, connected across each secondary winding, to compensate for the flux lost between core slices [5]. A circuit diagram of the voltage doubler combined with flux compensation is shown in Figure 4.

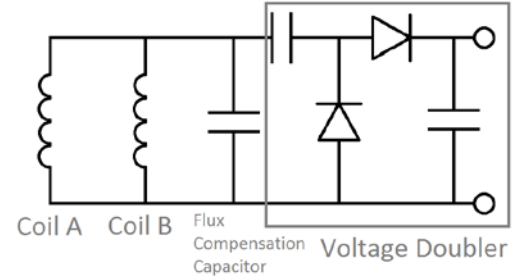


Figure 4. Circuit diagram of the secondary windings.

The capacitors are tuned to have a capacitance, C_{flux} , calculated using:

$$C_{flux} = \frac{l}{\mu_0 AN^2 (2\pi f)^2} \quad (1)$$

in which l is the length of the gap between insulated cores in meters; μ_0 is the permeability of free space; A is the cross sectional area of the gap between cores in meters squared; N is the number of windings around each core; and f is the operational frequency of the transformer.

An ICT, consisting of a stack of 50 cores, with the dimensions described in the previous section and a single core stack with clamped return path, was constructed in an FEA software package. The device was driven by a 500 Hz sinusoidal AC voltage source. Each secondary winding was connected in parallel with that of the other core acting at the same potential. The stack was driven by one of the secondary windings with a 100 V sinusoidal voltage acting upon it. A 1 k Ω resistor was connected across each set of secondary windings to draw an expected current of 100 mA. This design was simulated with, and without a compensation capacitor, and the peak voltage found in each respective winding is shown in Figure 5.

From Figure 5, it can be seen that the inclusion of a flux compensation capacitor reduces the flux loss by around 10%, and also makes the output voltage more consistent.

However, these simulations were carried out on a purely sinusoidal signal, which consists of a single frequency. In reality, an ICT that operates at high frequencies will likely be driven by square waves, which contain a large number of different

frequencies. As the compensation capacitor can only be tuned to one frequency, it will add distortion to the overall signal. In order to evaluate this phenomenon, a single stack clamped return path ICT, with 50 pairs of secondary windings, each consisting of 100 turns, and driven by a pair of primary windings, each consisting 4 turns, at either end of the stack, was constructed in MagNet. This ICT was simulated, being powered by a sinusoidal signal, with a frequency of 100 kHz and an amplitude of $400 V_{pk-pk}$, with and without a flux compensation capacitor. Figure 6 compares the voltage across the 50th windings of both of these simulations, with the ideal output, over the course of a power cycle. These simulations were repeated using square wave excitation, with the results being shown in Figure 7.

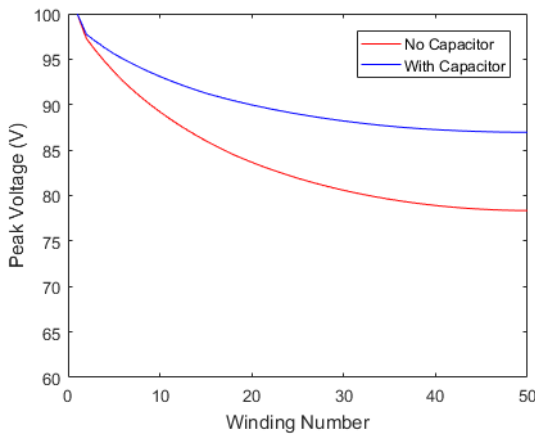


Figure 5. The peak voltage found in each secondary winding of an ICT, with 50 secondary circuits, with and without a flux compensation capacitor.

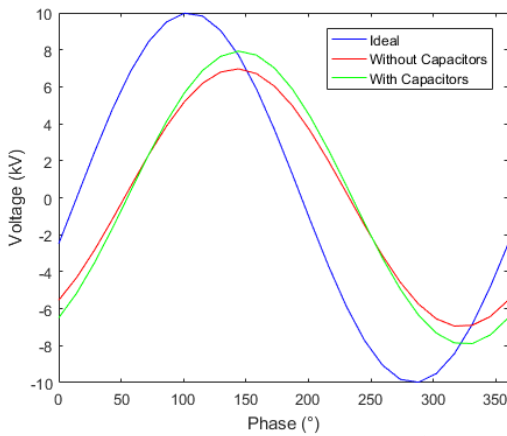


Figure 6. The 100 kHz voltage across the 50th pair of secondary windings, when excited by a sinusoidal signal with an amplitude of 400 V.

Figure 6 confirms the conclusions drawn from Figure 5; when sinusoidally excited, the flux compensation capacitor raises the output voltage by approximately 10%. However, there is no significant difference in terms of average voltage, between the waveforms in Figure 7. The results produced by the flux compensation capacitor are more distorted, including a peak that has an amplitude nearly twice that of the average voltage.

This could lead to failure of the dielectric film used to isolate the stacks and make the quality of the output voltage difficult to control. Practical experiments, verifying the results of these simulations, are currently being undertaken.

Two more techniques are employed, when manufacturing Cross type ICTs [6], to compensate for the effect that flux loss in the windings furthest from the primary winding has on the overall operational voltage of the design.

The first is to increase the voltage in the primary windings. This raises the voltage in each of the secondary windings, meaning that the lower secondary windings operate above their nominal voltage to compensate for the voltage lost in the higher windings. However, operating the secondary windings at a voltage above what they were rated for comes with the risk of placing additional strain on the components, and may reduce the lifespan of the windings.

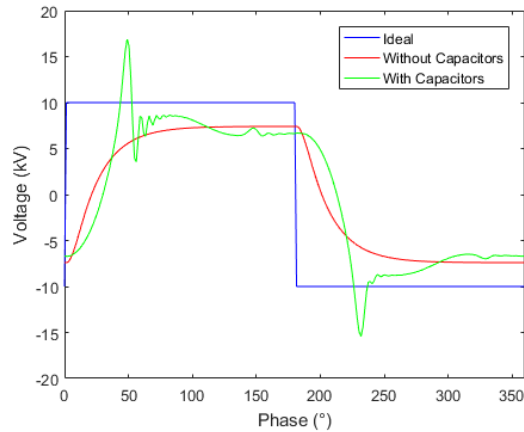


Figure 7. The 100 kHz voltage across the 50th pair of secondary windings, when excited by a square signal with an amplitude of 400V.

The other is simply to add additional cores to the top of the stack, each operating below their nominal voltage, until the desired overall voltage is reached.

4 STORED ENERGY

The use of capacitors, in flux compensators and voltage doublers, inherently stores energy in a system. The size of the capacitor, C , needed to reduce voltage ripple in a voltage doubler can be calculated using:

$$C = \frac{I}{2fV_{ripple}} \quad (2)$$

where I is the current draw from the system; and V_{ripple} is the maximum allowable voltage ripple from the output voltage. The energy stored in each capacitor, E , can then be calculated using:

$$E = \frac{1}{2} CV^2 \quad (3)$$

Assuming each secondary winding produces 10 kV, doubled to 20 kV with a maximum allowable ripple of 0.5%, and operates at a frequency of 100 KHz, each capacitor will store 0.5 J. Multiplying this across all the capacitors in a stack means that the total stored energy per stack will be 50 J.

The energy stored in each compensation capacitor can be calculated using (1) and (3). Using the parameters described above, each capacitor will store 252 μ J of energy, meaning that across the whole stack, they will store only 25 mJ. This is a negligible value and hence will be omitted from further calculations.

For reference, a Cockcroft Walton Generator, consisting of 10 stages, that produced 100 mA at 1 MV would need to store 1.1 MJ if operated at 50 Hz, or 550 J if operated at 100 kHz.

5 INCREASING THE CURRENT OUTPUT

There are three factors that limit the current that can be drawn from an ICT. These are the flux density of the core, the power electronics, and the winding thickness. The power electronics can, theoretically, be designed to accommodate any current, simply by selecting components rated to suitable specifications. The saturation of the core is more problematic in ICTs than in conventional transformers, as the relative permeability of the core material is effectively reduced by the insulated gaps. The saturation current becomes difficult to predict due to the non linear nature of the insulated cores.

The limitations imposed by the winding thickness are easier to calculate as the largest current that can safely pass through the tracks of a PCB can be determined by the IPC-2221 standard [7]. This standard dictates that the largest current that can safely be used in a PCB can be calculated using:

$$I = k\Delta T^{0.44} A_{track}^{0.725} \quad (4)$$

where I is the current passing through the track in Amperes; ΔT is the permissible change in temperature in $^{\circ}\text{C}$; A_{track} is the cross sectional area of the track in mil^2 ; and k is a constant determined by the IPC-2221. For tracks printed on the surface of a PCB, $k = 0.048$.

Assuming each PCB is printed on a board with a copper thickness of $0.305 \text{ kg}/\text{m}^2$, the most commonly used copper thickness in PCB design, and the tracks are printed with a width of 0.5 mm, then the maximum safe current would be 1.46 A. This is even supposing that a maximum temperature increase of only 10°C was imposed. Given the potentially dangerous nature of a fault in this project, it is not unreasonable to impose a large margin of error onto the maximum current, say, no more than half of the PCBs rated current may flow through the PCB windings during normal operation. This brings the effective rated current of each PCB down to 0.73 A, though because in this design, each winding is

connected in parallel to another winding, the effective rated current of the stack once again becomes 1.46 A.

There are two ways in which the operational current of the ICT could be increased. The first is to increase the size of the single phase ICT, by widening the diameter of the tracks and the core. This will raise the saturation flux of the core and the current that can safely pass through the windings

The second is to connect multiple stacks in parallel, as shown in Figure 8. This arrangement has the advantage that scaling up a design becomes a trivial exercise as, rather than having to redesign the whole design from first principles, to increase the operational current of the supply, one simply needs to add additional stacks to the existing design. Using multiple stacks also reduces voltage ripple, providing they each operate out of phase [8].

The stacks can be driven out of phase using a circuit, similar to the one in Figure 9, to power the primary windings. In this case, V_{in} can be provided by a rectified, three phase mains outlet and can be treated as a 400 V busbar. The switches, which would be replaced by MOSFETs in a practical circuit, can be operated in pairs to create a H-bridge. In this way, the voltage across the primary windings can be alternated, from +400 to -400 V, at a frequency determined by a microcontroller. The circuit shown in Figure 9 is designed for an ICT consisting of four stacks, but can be expanded to accommodate any even number of stacks.

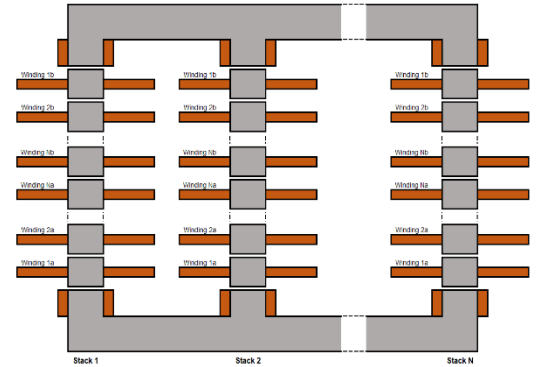


Figure 8. The layout of a multiphase ICT.

6 POSSIBLE FUTURE DEVELOPMENT

It has been shown that an ICT can be used to produce 500 kV AC, which can then be doubled and rectified to produce 1 MV DC. It has also been shown that several of these ICTs can be connected in parallel to, theoretically, achieve any output current. Thus, a power supply, based on CTT, could be constructed to produce 2 A at 1 MV.

In order to evaluate whether this technology is suitable for future development, with the aim of creating a 5 MV power supply, the process that was carried out in Section 2 was extended to ICTs of up to 100 pairs of cores. Once again, the minimum normalized flux linkage in each model, calculated using FEA, was recorded and plotted in Figure 10.

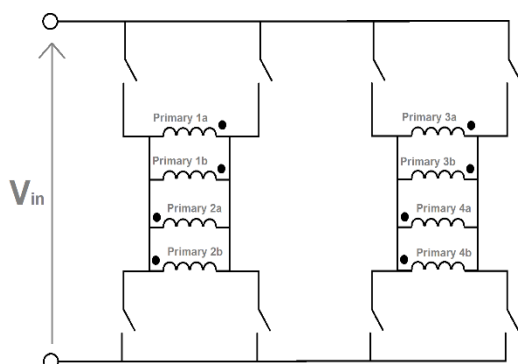


Figure 9. Diagram of the primary circuit for a four stack ICT.

From Figure 10, it can be seen that the minimum system flux drops significantly as the stack height is increased. Using the system parameters listed in Section 2, there is expected to be roughly 40% flux loss in the HV secondary windings of a 1 MV stack. Although this flux loss could conceivably be compensated for by having more windings around the higher voltage cores, given the exponential decline of flux linkage in higher stacks, it is unlikely that this technique could practically be applied to a 2.5 MV ICT.

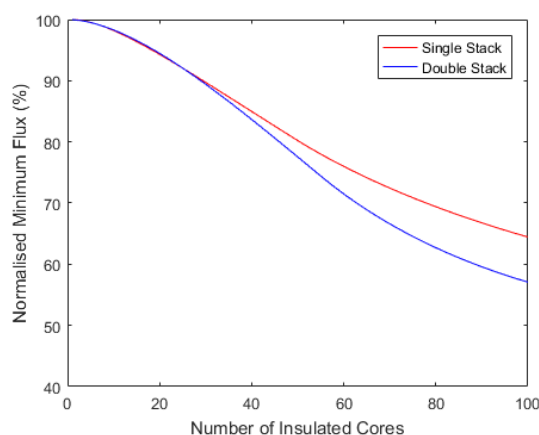


Figure 10. The minimum flux found in ICTs, arranged using both the traditional double stack layout and the proposed single stack layout, with a number of insulated cores ranging from 1 to 100.

7 CONCLUSIONS

The effectiveness of ICTs in producing 500 kV, which can then be rectified and doubled using voltage doublers, has been evaluated, as well as a number of ways of reducing flux loss. It can be concluded that ICTs may be used as the basis of a 1MV power supply that produces currents in the order of hundreds of milliamps. It was then shown, in Section 5, that by connecting multiple ICTs in parallel, the design could be expanded to produce outputs of an Ampere or more, with little voltage ripple. To meet the requirement of minimal stored energy, it is necessary to design a primary excitation source capable of switching mains voltages (e.g. 400 V) at frequencies of 100 kHz or higher. This in turn has the effect of negating some of the advantages of using the flux compensation

capacitors as the primary waveform is very likely to be non-sinusoidal.

Finally, it has been shown that, although ideal for a 1 MV power supply, ICT technology is currently not suitable to be scaled up to 5 MV. Further work will focus on investigating other promising technologies. It is possible that an ideal solution would be a combination of ICTs and another technology, for example the cascade transformer.

ACKNOWLEDGMENT

The authors would like to thanks QinetiQ Group plc. For providing funding and technical support for this project.

REFERENCES

- [1] E. Kuffel, W. Zaengl, and J. Kuffel, High Voltage Engineering: Fundamentals, 2nd ed. Oxford: Newnes, 2000.
- [2] R. J. Van de Graaff, "High Voltage Electromagnetic Apparatus Having an Insulating Magnetic Core," 3289066, 1965.
- [3] L. Cao and J. Yang, "Linear Circuit Model of the Three-phase Insulated Core Transformer Power Supply," in IEEE Transactions on Nuclear Science, vol. 63, no. 1, pp. 288-296, Feb. 2016.
- [4] R. E. P. Frost, J. A. Pilgrim, P. L. Lewin and M. Spong, "An Investigation into the Next Generation of High Density, Ultra High Voltage, Power Supplies," 2018 IEEE International Power Modulator and High Voltage Conference (IPMHVC), Jackson, WY, USA, 2018, pp. 156-161.
- [5] J. D. Cross, "Modular High Voltage Power Supply with Integral Flux Leakage Compensation," US6026004A, 1998.
- [6] Kaiser, "Kaiser Technical Presentation," 2008. [Online]. Available: <https://www.google.com/url?sa=t&rct=j&q=&esrc=s&source=web&cd=1&ved=2ahUKEwigvPfa8NXcAhXCmLQKHWT4AJ8QFjAAegQIABAC&url=https%3A%2F%2Fwww.jlab.org%2Fconferences%2Fpesp2008%2FThursday%2FUhmeyer%2520KSI%2520PESP%25202008-10-02.ppt&usq=AOvVaw1KdbD63tNLOSa6Xh76OSdw>.
- [7] "IPC-2221." [Online]. Available: <http://ch00ftech.com/wp-content/uploads/2016/12/IPC-2221-2.pdf>.
- [8] L. Katzir and D. Shmilovitz, "A Split-Source Multisection High-Voltage Power Supply for X-Ray," IEEE J. Emerg. Sel. Top. POWER Electron., vol. 4, no. 2, pp. 373-381, 2016.



numerical modeling.

Russell E. P. Frost (S'18) was born in Salisbury, Wiltshire, in 1993. He received the B.Eng. (Hons) degree from the University of Southampton, in 2016, and is currently working on a Ph.D. in High Voltage Electrical Engineering at the same University. He has previously interned at National Grid plc. His research interests include high voltage plant, partial discharge analysis, power system stability, and



Prof. Paul L. Lewin (M'05-SM'08-F'13) was born in Ilford, Essex in 1964. He received the B.Sc. (Hons) and Ph.D. degrees in electrical engineering from the University of Southampton, UK in 1986 and 1994, respectively. He joined the academic staff of the University in 1989 and is Head of Electronics and Computer Science, where he is also Director of

the Tony Davies High Voltage Laboratory. His research interests are within the generic areas of applied signal processing and control. Within high voltage engineering this includes condition monitoring of HV cables and plant, surface charge measurement, HV insulation/dielectric materials and applied signal processing. Since 1996 he has received funding and grants in excess of £30M, supervised 47 graduate students solutions for government and industry.

to successful completion of their doctoral theses and published over 500 refereed conference and journal papers in these research areas. He is a Chartered Engineer, a Fellow of the IET, and former president of the IEEE Dielectrics and Electrical Insulation Society.



Matt Spong was born in Wokingham, Berkshire in 1972. He completed an MOD Apprenticeship in 1992 in Electrical Power and has worked for research establishments in Government and Industry. Interests include UHV DC power supplies, large HV machines and physics research. He has a broad range of knowledge and experience of delivering cutting-edge

novel research and engineering

Appendix B Derivation of Equation 4.3

First it is assumed that the windings can be represented by a number of concentric tracks encompassing the core, as shown in Figure B. 1. Each of these tracks can be split into four straight sections, and four curved sections that would form a circle if laid out together. Both of these sections are discussed individually in the following two sections, and then combined in the final section of this appendix.

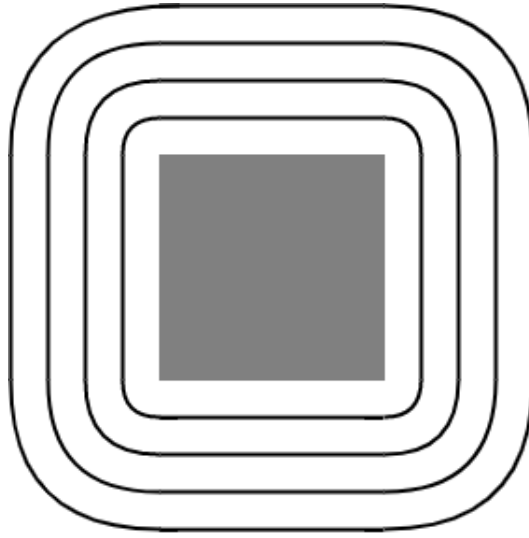


Figure B. 1. A near exact approximation of the windings around a square core, as viewed from above.

B.1 Straight sections

Regardless of the distance between these lengths of track and the core, the lengths of these sections will be the same as the circumference of the core. Assuming that a square core is used, this will be equivalent to four times the thickness of the core t_c . The total length of the straight sections of track $l_{straight}$ will, therefore, be the product of the number of turns N and the circumference of the core. This is shown in

$$l_{straight} = 4Nt_c \quad (B.1)$$

B.2 Curved Sections

The curved sections can be expressed as a series of N concentric circles, the circumference of which can easily be calculated by multiplying the radius by 2π . The radius of each circle is the sum of the distance between the core and the innermost turn r ; the sum of the widths of all the tracks between the core and the turn in question w ; and the sum of the gaps between all the turns inside the turn in question g . Thus the total length of all curved sections l_{curved} can be expressed as

$$l_{curved} = 2\pi r + 2\pi\{r + (g + w)\} + 2\pi\{r + 2(g + w)\} + \dots \quad (\text{B.2})$$

which can, more succinctly, be expressed as

$$l_{curved} = N \cdot 2\pi r + 2\pi \sum_{j=1}^{N-1} j(g + w) \quad (\text{B.3})$$

Taking the sum of this series gives

$$l_{curved} = N \cdot 2\pi r + \frac{2\pi N(N-1)}{2} (g + w) \quad (\text{B.4})$$

which can be reduced to

$$l_{curved} = 2\pi N \left\{ r + \frac{(N-1)(g+w)}{2} \right\} \quad (\text{B.5})$$

However, this is only applicable if all the windings are on a single layer. If the winding is spread over multiple layers then each instance of N must be divided by the number of layers N_L , and this total be multiplied by N_L , as shown in

$$l_{curved} = 2\pi \frac{N}{N_L} N_L \left\{ r + \frac{\left(\frac{N}{N_L}-1\right)(g+w)}{2} \right\} \quad (\text{B.6})$$

which cancels to produce

$$l_{curved} = 2\pi N \left\{ r + \frac{\left(N/N_L-1\right)(g+w)}{2} \right\} \quad (\text{B.7})$$

B.3 Total Length

The total length of all the turns in a winding l is simply the sum of the lengths of the straight and the curved sections, as in

$$l = l_{straight} + l_{curved} \quad (\text{B.8})$$

In this case that is equivalent to

$$l = 4Nt_c + 2\pi N \left\{ r + \frac{\left(N/N_L-1\right)(g+w)}{2} \right\} \quad (\text{B.9})$$

Appendix C Experimental Breakdown Voltages

Table C.1. Breakdown voltages of initial sample breakdown.

Breakdown (kv)			
Narrow Straight:	Wide Straight:	Wide Curve:	Tight Curve:
4.497	6.655	3.957	4.856
4.856	6.655	4.136	3.597
4.497	5.936	3.417	4.136
4.677	5.936	5.036	7.015
5.036	5.756	4.856	3.957
4.136	6.655	5.576	5.396
4.136	6.116	5.035	5.036
3.957	6.475	6.295	5.936
4.677	5.936	5.756	5.936
4.497	5.756	3.777	5.756
4.856	6.836	6.836	6.295
4.677	7.015	3.777	6.295
4.136	6.295	5.756	5.576
4.136	6.116	5.936	4.136
4.497	6.655	3.417	5.396
4.856	6.475	6.475	6.295
4.856	6.116	6.295	5.756
4.677	6.295	4.856	4.677
4.497	6.295	5.576	6.116
4.497	6.475	4.136	5.576
4.856	6.295	5.227	5.576
4.497	6.655	5.576	6.836
4.856	6.655	5.677	6.295
4.317	6.836	6.116	5.576
5.216	6.655	7.015	5.936
4.677			

Table C. 2. Breakdown voltage after initial sample breakdown

Breakdown (kv)			
Narrow Straight:	Wide Straight:	Wide Curve:	Tight Curve:
2.877	6.475	3.597	3.957
2.877	7.015	3.417	3.417
2.877	5.936	3.237	3.597
3.417	6.295	3.957	3.777
2.697	5.756	3.417	3.957
3.057	5.756	4.677	3.417
3.417	5.216	3.057	4.16
2.697	4.497	3.237	3.957
3.057	5.756	3.057	3.777
3.597	5.576	3.77	3.733
3.057	7.735	4.107	3.417
3.237	6.295	3.413	4.107
3.237	6.116	3.417	3.057
3.417	5.936	3.057	3.957
3.417	5.936	3.057	3.777
3.057	7.555	4.136	3.733
3.777	5.576	3.417	3.777
3.057	6.295	3.52	2.877
2.697	6.295	2.697	3.777
2.877	6.655	3.597	3.417
3.057	5.576	3.957	3.417
2.877	5.756	3.77	3.947
2.697	6.295	2.697	3.573
3.573	2.036	3.68	2.877
	6.295	3.777	3.777

Table C. 3. Breakdown voltage at different frequencies

Initial Breakdown:		Post Initial Breakdown:	
Frequency (Hz)	Breakdown (kv)	Frequency (Hz)	Breakdown (kv)
1000	4.497	1000	2.877
1000	4.856	1000	2.877
1000	4.497	1000	2.877
1000	4.677	1000	3.417
1000	5.036	1000	2.697
1000	4.136	1000	3.057
1000	4.136	1000	3.417
1000	3.957	1000	2.697
1000	4.677	1000	3.057
1000	4.497	1000	3.597
1000	4.856	1000	3.057
1000	4.677	1000	3.237
1000	4.136	1000	3.237
1000	4.136	1000	3.417
1000	4.497	1000	3.417
1000	4.856	1000	3.057
1000	4.856	1000	3.777
1000	4.677	1000	3.057
1000	4.497	1000	2.697
1000	4.497	1000	2.877
1000	4.856	1000	3.057
1000	4.497	1000	2.877
1000	4.856	1000	2.697
1000	4.317	1000	3.573
1000	5.216	100	3.677
1000	4.677	100	3.777
100	4.677	2000	3.057
100	5.576	2000	3.057
100	5.068	2000	3.417
2000	5.216	5000	3.777
2000	5.756	5000	3.417
2000	5.396	5000	3.957
5000	5.216	100	3.237
5000	3.957	100	3.417
5000	4.136	2000	2.877
100	4.856	2000	2.697
100	5.576	5000	3.777
2000	4.497	5000	3.777
2000	4.856	5000	3.597
5000	3.597		
5000	4.136		
5000	3.597		

